Crystallographic aspects of deformation microstructures in metals

Author:
Afrin Zinnia, Nasima

Publication Date:
2014

DOI:
https://doi.org/10.26190/unsworks/16702

The University of New South Wales

UNSW
AUSTRALIA

Faculty of Science
School of Materials Science and Engineering

Crystallographic aspects of deformation microstructures in metals

A thesis submitted in complete fulfilment of the requirements for the award of the degree of

DOCTOR OF PHILOSOPHY

in

Materials Science and Engineering

Nasima Afrin

August, 2013

PLEASE TYPE

THE UNIVERSITY OF NEW SOUTH WALES
Thesis/Dissertation Sheet

Surname or Family name: **Afrin Zinnia**

First name: **Nasima** Other name/s: **N/A**

Abbreviation for degree as given in the University calendar: **PhD**

School: **Materials Science & Engineering** Faculty: **Science**

Title: **Crystallographic aspects of deformation microstructures in metals.**

Abstract 350 words maximum: (PLEASE TYPE)

The deformation structures that form in 10–30% channel–die plane strain compressed Goss–oriented Ni single crystals and 50–75% cold–rolled polycrystalline interstitial free (IF) steel were characterized by two and three dimensional electron backscatter diffraction and transmission electron microscopy. In the 30% deformed Ni sample the microband boundary surfaces are found to be largely planar and crystallographically aligned over large distances, but frequently interrupted by local distortions and undulations due to interactions between intersecting, non–coplanar microbands. The non–crystallographic origins are explained from the varying fractions of slip on a given {111} planes as a result of ±7.5° orientation oscillations towards RD during deformation. Transmission electron microscopy study on the dislocation structures in a 10% deformed Ni crystal revealed that mesh, cell and dense dislocation walls form prior to the microband formation. The cells are initially equiaxed but later many such cell boundary segments constitute denser segments of dislocation walls, from which microbands form by splitting into a pair of dislocation walls at ~1μm spacing. Microbands also form in series on one set of dense dislocation walls parallel to their second set. These boundaries then propagate into two walls to generate microband channels.

At any stage of deformation, microband boundaries are generally regarded as low–angle deformation features. However, unusual high orientation differences of up to 20° across microband boundaries was found in {111}<110>–oriented grains in a 50% cold rolled IF steel. Despite their high angle nature, the microband interfaces maintain their well–known crystallographic characteristics through a rigid body rotation around the interface normal between adjacent microband lattices.

To realize the complex role of the grain boundaries in the generation of deformation and recrystallization textures, the structures across ~{111}<112>– and ~{111}<110>–oriented grains in a 75% cold rolled IF steel were studied. The coexistence of several deformation features both near to and on the boundaries, such as steep orientation gradients up to 5°/μm, high angle boundary networks and numerous thin, elongated blocks on their surface, reveal the complex, irregular and diffuse nature of grain boundaries and why they are excellent sites for nucleation of recrystallization.

Declaration relating to disposition of project thesis/dissertation

I hereby grant to the University of New South Wales or its agents the right to archive and to make available my thesis or dissertation in whole or in part in the University libraries in all forms of media, now or here after known, subject to the provisions of the Copyright Act 1968. I retain all property rights, such as patent rights. I also retain the right to use in future works (such as articles or books) all or part of this thesis or dissertation.

I also authorise University Microfilms to use the 350 word abstract of my thesis in Dissertation Abstracts International (this is applicable to doctoral theses only).

Nasima Afrin ....15/08/2013.....

Signature Witness Date

The University recognises that there may be exceptional circumstances requiring restrictions on copying or conditions on use. Requests for restriction for a period of up to 2 years must be made in writing. Requests for a longer period of restriction may be considered in exceptional circumstances and require the approval of the Dean of Graduate Research.

FOR OFFICE USE ONLY Date of completion of requirements for Award:

THIS SHEET IS TO BE GLUED TO THE INSIDE FRONT COVER OF THE THESIS

Originality Statement

I hereby declare that this submission is my own work and to the best of my knowledge it contains no materials previously published or written by another person, or substantial proportions of material which have been accepted for the award of any other degree or diploma at UNSW or any other educational institution, except where due acknowledgement is made in the thesis. Any contribution made to the research by others, with whom I have worked at UNSW or elsewhere, is explicitly acknowledged in the thesis.

I also declare that the intellectual content of this thesis is the product of my own work, except to the extent that assistance from others in the project's design and conception or in style, presentation and linguistic expression is acknowledged.

Signed 
Nasima Afrin Zinnia

Date ……15/08/2013…….....

Copyright Statement

I hereby grant the University of New South Wales or its agents the right to archive and to make available my thesis or dissertation in whole or part in the University libraries in all forms of media, now or here after known, subject to the provisions of the Copyright Act 1968. I retain all proprietary rights, such as patent rights. I also retain the right to use in future works (such as articles or books) all or part of this thesis or dissertation.

I also authorise University Microfilms to use the 838 word abstract of my thesis in Dissertation Abstract International.

I have either used no substantial portions of copyright material in my thesis or I have obtained permission to use copyright material; where permission has not been granted I have applied/will apply for a partial restriction of the digital copy of my thesis or dissertation.

Signed 
Nasima Afrin Zinnia

Date ……15/08/2013……

Authenticity Statement

I certify that the Library deposit digital copy is a direct equivalent of the final officially approved version of my thesis. No emendation of content has occurred and if there are any minor variations in formatting, they are the result of the conversion to digital format.

Signed …….....

Nasima Afrin Zinnia

Date ……15/08/2013……

Acknowledgement

First of all, I would like to express my sincere gratitude to my supervisor, Professor Michael Ferry, for his invaluable advices, everlasting encouragements and persistence guidance throughout the course of this degree. Without his supervision and suggestion this thesis would not have been possible. I also want to express thanks, with all the sincerity, to my co-supervisor Professor Paul R. Munroe for his supportive discussions and continuous encouragement.

I am particularly thankful to Prof. Julian Driver and Dr. Adeline Albou of Ecole des Mines des St Etienne, France for cutting and deforming the Ni single crystal sample. I also like to thank A/Prof. Lori Bassman and her team members from Harvey Mudd college, California, USA for helping during manual 3D EBSD data acquisition which requires continuous operational engagement with the machine for several days.

Thanks must go without a shadow of doubt to Dr. George Yang of sample preparation laboratories of Materials Science school and Dr. Charlie Kong, Dr. Aron Dodd and Mr. Sean Lim of Electron Microscope unit for their effort to teach me TEM and dual beam FIB. I also like to take the opportunity to thank all my fellow group mates, Kevin, Martin, KD, Karl, Jack, John, Olga, Yi, Michael and anyone omitted by mistake for their friendly attitude, support, understanding and cooperation over the years.

I gratefully acknowledge the Australian Research Council (ARC) for financing this work through the Discovery Projects (grants no. DP0556927, DP0986600). I also acknowledge the Australian Microscopy and Microanalysis Research Facility (AMMRF) for providing access to cutting edge equipments to conduct this research.

I acknowledge the encouragements and generous supports of my family members and relatives. My departed beloved father would have been very happy seeing this achievement. Finally I am grateful to almighty God to make this achievement possible in my life.

List of publications

The following publications were generated throughout the course of the thesis:

Journal papers:

1. N. Afrin, M.Z. Quadir and M. Ferry: *A three dimensional EBSD study on a γ/γ grain boundary in a 75% cold rolled IF steel*. **Scripta Materialia** (under review).

2. N. Afrin, M.Z. Quadir, M. Ferry and P. Munroe: *Unusual high angle microband boundaries in {111}<110> orientated grains in a 50% cold rolled interstitial free (IF) steel*. **Metallurgical and Materials Transactions A** (under review).

3. N. Afrin, M.Z. Quadir and M. Ferry: *On the complexities of microband interactions in a cold deformed Goss-oriented Ni single crystal*. **Metallurgical and Materials Transaction B**, DOI: 10.1007/s11663-013-9827-7.

4. N. Afrin, M.Z. Quadir, W. Xu and M. Ferry: *Spatial orientations and structural irregularities associated with the formation of microbands in a cold-deformed Goss-oriented Ni single crystal*. **Acta Materialia**, Vol. 60 pp. 6288-6300 (2012).

5. N. Afrin, M.Z. Quadir, L. Bassman, J.H. Driver, A. Albou and M. Ferry: *The three-dimensional nature of microbands in a channel die compressed Goss-oriented Ni single crystal*. **Scripta Materialia**, Vol. 64 (3), pp. 221-224 (2011).

Conference papers:

6. N. Afrin, M.Z. Quadir, L. Bassman, J.H. Driver, A. Albou and M. Ferry, *On the bumps and curves in the microband boundaries in a channel-die compressed Goss-oriented Ni single crystal*, **Materials Science Forum**, 702-703, pp. 101-104 (2012). 16th Int. Conf. on Textures of Materials, 12-17 Dec 2011, Bombay, India.

7. L. Bassman, C.George , M. Z. Quadir , N. Afrin, B. Liu, B. Soe and M. Ferry, *Study of the True Nature of Microband Boundaries in Aluminum with 3D EBSD*, **Materials Science Forum**, 702-703, pp. 558-561 (2012). 16th Int. Conf. on Textures of Materials, 12-17 Dec 2011, Bombay, India.

8. M. Ferry, W. Xu, M. Z. Quadir, N. Afrin, K. Laws, N. Mateescu, L. Robin, L. Bassman, J. Cairney, J. Humphreys, A. Albou, J. Driver: *3D-EBSD Studies of Deformation, Recrystallization and Phase Transformations*, 4th International Conference on recrystallization and Grain Growth, Sheffield, UK, 4-9th July (2010).

9. B. Liu, D. Bolton-Haughton, C. George, C. McMahon, M. Z. Quadir; N. Afrin, W. Xu, M. Ferry, L. Bassman: *Three-Dimensional Reconstruction of Microband Boundaries in FCC Metals*, TMS 2010 Annual Meeting & Exhibition, Seattle, USA, 14-18th February (2010).

Abstract

In this thesis, the deformation structures that form in 10–30% channel–die plane strain compressed Goss–oriented Ni single crystals and 50–75% cold–rolled polycrystalline interstitial free (IF) steel were characterized by two and three dimensional electron backscatter diffraction (2D– and 3D–EBSD) and transmission electron microscopy (TEM). Emphasis was given to understand the evolution sequence of microbands via a detailed characterization of dislocation structures and crystallographic aspects of their boundaries. In the IF steel, both microband structures and the deformation morphology near grain boundaries were studied.

Microbands are well–known deformation features that form in the deformation microstructures of many medium to high stacking fault energy metals and alloys. The crystallographic nature of microband boundaries was investigated in a 30% deformed Ni crystal using the foregoing analysis techniques. When viewed in the three orthogonal sections, microband boundary traces were classically aligned in the normal direction (ND)–rolling direction (RD) section at an acute angle from the RD, but appear wavy in the RD–transverse direction (TD) section. The latter observation may lead to the conclusion that microband boundaries are non–crystallographic. The use of 3D–EBSD to reconstruct actual microbands in a volume of deformed material revealed significant new information about their morphology. Here, microband surfaces are largely planar over large distances, but frequently interrupted by local distortions and undulations due to interactions between intersecting, non–coplanar microbands. The overall investigation has revealed that microband boundaries are aligned close to active {111} slip planes (*i.e.* they are crystallographic) but the bumps and distortions they contain are non–crystallographic in the sense that they deviate away from these slip planes. The non–crystallographic features of microbands (as revealed by their wavy structure in the RD–TD section) may be explained by the crystallographic oscillations of up to ±7.5° towards RD that occur during deformation. Such oscillations result in varying fractions of slip on a given {111} plane, thereby resulting in varying degrees of interaction between the two sets of non–coplanar microbands. These local and intense microband interactions result in the deviation away from their active slip planes.

The dislocation structures associated with early microband evolution in a 10% deformed Ni crystal was investigated by 2D–EBSD and TEM. A discrepancy was found

between EBSD and TEM measurements in the included angle between two intersecting dense dislocation walls (DDWs), *i.e.* the EBSD– and TEM–measured angles were 90° and 70°, respectively. After 10% strain, the spacing between DDWs are larger (average ≥5 μm) than the spacing between microband boundaries (average ≈1μm) after 30% strain. The dislocation structures between two DDWs comprise both mash and cell structures. In the former, it is possible to identify individual dislocations whereas, in the latter, dislocations obtain a denser distribution within ~150 nm thick boundaries and their interiors contain very few dislocations. The cells are initially equiaxed but eventually their boundaries orient along the existing DDWs. Subsequently, many such cell boundary segments constitute denser segments of dislocation walls, from which microbands form by splitting into two DDWs at ~1μm spacing. Microbands also form in series on one set of DDWs parallel to a second set of DDWs. These boundaries then propagate into two walls to generate microband channels. Once a DDW forms it may propagate into dislocation–free regions trailing behind a microband channel through splitting events.

Microband boundaries are generally regarded as low-angle deformation features that accommodate a small crystallographic rotation in the range 1–4°. In this part of the thesis, EBSD/TEM revealed unusual orientation differences of up to 20° across microband boundaries in {111}<110>–oriented grains in a 50% cold rolled IF steel. Despite their high angle nature, the microband interfaces maintain their well–known crystallographic characteristics, that is, they are aligned closely with highly stressed slip planes. Rigid body rotations are argued to take place around the interface normal between adjacent microband lattices, thereby generating the unusual microstructure containing alternating microband boundaries that are oriented in equal and opposite relative angles and produce an array of orientation pairs in their spatial distributions.

Grain boundaries play an important role in the formation of deformation and recrystallization textures in steels. In this second study using 3D–EBSD, microtexture distributions across a complex boundary between ~{111}<112>– and ~{111}<110>–oriented grains in a 75% cold rolled IF steel were studied. The coexistence of several deformation features both near to and on the boundaries, such as steep orientation gradients up to 5°/μm, high angle boundary networks and numerous thin, elongated blocks on their surface, reveal the complex, irregular and diffuse nature of grain boundaries and why they are excellent sites for nucleation of recrystallization.

Table of contents

Chapter 1

Introduction

Conventional two dimensional (2D) microstructural characterization techniques have been the primary metallographic tool for a very long time. In a given material, the structural features can range in size from hundreds of microns to the nano–scale. Depending on the feature size and characterization objective various 2D techniques have been deployed, namely optical microscopy, scanning electron microscopy (SEM) and transmission electron microscopy (TEM). Although the use of these 2D techniques as a research tool is widespread in materials science, there are some situations where they yield insufficient information for addressing some vital phenomena. As a classical example, one can recall the challenges in determining the true size and shape of grains by 2D methods due to the well–known sectioning effects. To address the problem, stereological methods have been developed over the years for transforming 2D data into 3D. These mathematical transformations are based on a range of assumptions and still do not provide unambiguous information concerning the actual structure in 3D.

The ability to observe the 3D structure of an opaque solid is of great importance in understanding its true nature, as it eliminates speculation about the spatial distribution of features associated with conventional 2D imaging techniques. This is a crucial step in exploring microstructure–property relationships relating to many metallurgical problems such as the nucleation of recrystallization in deformed metals, intergranular corrosion, fracture processes etc. since most practical materials have a complex, polycrystalline structure and most features affecting material properties are three dimensional. The relatively low resolution serial sectioning technique utilizing optical microscopy and standard polishing and grinding methods has been used for a number of years to create microstructures in 3D. Unfortunately, this laborious technique provides very little information on the crystallographic aspects of features of interest in the material. There have been recent significant advances in the development of higher resolution 3D techniques, including: 3D X–ray diffraction (3D–XRD) [Poulsen 2002], 3D secondary ion mass spectrometry (3D–SIMS) [Hutter 1992], 3D–TEM [Midgley *et al.* 2001], 3D focused ion beam (3D–FIB) [Inkson *et al*. 2001a] and 3D atom probe tomography (3DAP or APT) [Miller 2000, Gault *et al.* 2012]. Each technique has its advantages and limitations and, therefore, is suitable depending on the application.

Among the aforementioned 3D techniques, 3D–XRD and 3D–TEM are capable of providing crystallographic information about the structures of interest, with APT

recently demonstrating similar capabilities. In 3D–TEM, the feature size is limited to the foil thickness of ~100 nm. Other limitations of this technique, such as diffraction–related image contrast challenges and the long acquisition times to acquire a 3D dataset, are obstacles for its use as a routine characterization tool. In recent times, 3D–electron backscatter diffraction (EBSD) has been developed into a highly effective automated method for generating 3D crystallographic information in reasonably large volumes of most types of crystalline material. This technique utilizes a FIB as an accurate serial sectioning device for cutting parallel slices of material with a site–specific accuracy of 50 nm; each consecutive slice is mapped by high resolution EBSD and combined using advanced computer algorithms to generate the crystallographic volumes of material.

3D–EBSD has recently yielded excellent outcomes in our understanding of the crystallographic nature of both the deformed and annealed states of metals and alloys (see e.g. [Konrad *et al.* 2006]). For example, the technique revealed curved surfaces of microbands in the deformation microstructure of cold rolled interstitial free (IF) steel, although such features were largely aligned with the likely crystallographic slip planes. This finding reconciles the controversial argument that microbands appear straight along slip planes when viewed in the section containing the normal direction and rolling direction (i.e. ND–RD section) but appear wavy in the transverse direction (TD)–RD section [Quadir *et al.* 2007]. In another study, Xu *et al*. [2007b] generated information on the actual shape and orientation spread of the deformation zones that form around coarse (>1 μm), non-deformable particles of a cold deformed Ni alloy. This study also demonstrated the excellent propensity for particle stimulated nucleation of recrystallization at these important sites in a particle-containing alloy. These foregoing examples have generated new information on deformation and recrystallization not achievable by conventional 2D–EBSD.

The aim of this thesis is to investigate the true crystallographic nature of microbands in the cold deformation microstructures of a face centred cubic (fcc) Ni single crystal and body centred cubic (bcc) IF steel using a combination of 2D–TEM and 2D– and 3D–EBSD. These techniques are also used to investigate the deformation microstructure and texture in the vicinity of an important type of grain boundary in the IF steel.

Chapter 2

Literature review

2.1 Introduction

An understanding of deformation microstructures is of major interest to material scientists and engineers. This is due to two broad reasons: (i) the deformation structures provide a clue to the failure mechanism(s) and the events that sequentially occur during material processing, and (ii) the deformation microstructure provides important information on the origin of thermally activated restoration events (recovery and recrystallization) during subsequent heat treatments. In this chapter various important microstructural features that develop during deformation are described. The techniques for both measuring and representing deformation textures in cubic crystalline metals are also described.

2.2 Deformation microstructures

In cubic metals there are two principal modes of deformation. One is slip on crystallographic planes and the other is twinning. The operative deformation mode depends largely on the stacking fault energy (SFE) of the alloy of concern. In low SFE materials deformation primarily occurs by twinning. This is because cross slip is difficult in these metals and, therefore, slip alone cannot accommodate the required shape change, such that deformation by twinning becomes inevitable [Humphreys and Hatherly 2004]. In contrast, slip is the preferable deformation mode in a large variety of engineering materials within the medium to high SFE materials category. Many Fe, Al, Ni, Cu, Ag and their alloys fall within this category. In most cases slip takes place on the most densely packed planes and directions. In face centered cubic (fcc) metals slip occurs along <110> directions on {111} planes, and in body centred cubic (bcc) metals it occurs along <111> directions in {110}, {112} and {123} planes. The choice of slip plane in bcc metals is governed by the processing conditions (e.g. temperature) [Humphreys and Hatherly 2004, Backofen 1973, Watanabe 2006]. Pencil glide is often observed as a commonly operative mechanism whereby the deformation direction remains the same to switch between slip planes [Rosenberg 1971, Piehler 1967, Parniere and Sauzay 1976]. The operating slip system in a given grain primarily depends on the grain orientation in relation to the stress coordinates.

In metals, deformation changes the internal microstructure in several ways: the grains experience shape changes, grain boundary area increases and internal substructures are generated within each grain. These features involve dislocation generation and their rearrangements [Humphreys and Hatherly 2004]. When an original hot–band grain deforms, the dislocations evolve and decorate themselves into low energy configuration structures, *i.e.* there is an accumulation into various dislocation made boundaries.

According to the dislocation rearrangement in the deformed substructures of high SFE materials, they are broadly classified into two categories: incidental dislocation boundaries (IDB) and geometrically necessary boundaries (GNB). IDBs are generated by statistical trapping of dislocations and, in microstructures, these dislocations are found in a random distribution. The GNB formation starts with the evolution of cell blocks. Later, these blocks subsequently transform into various other dislocation composed structures. There is a long list of nomenclature of the deformation structural elements. So far, the commonly known nomenclatures are given by researchers in the Risø National Laboratory, Denmark. These are known as cell blocks, subgrains, microbands, kink bands, S–bands, shear bands and lamellar bands. These structures form at various levels of deformation.

2.2.1 Cells and subgrains

At low strains ($\varepsilon < 0.3$) the statistically trapped dislocations generate mesh structures, whereby individual dislocations create networks without forming any particular shape or pattern. These dislocations later rearrange into equiaxed cell structures. The cells have almost dislocation free interiors of ~0.5–1μm in size. The cell boundaries are made of dense packing of dislocations [Kuhlmann–Wilsdorf and Hansen 1991]. Across the cell walls there are small orientation differences which are often measured below 2° [Humphreys and Hatherly 2004]. A classical example of the cell structure is shown in Figure 2.1. The shape and misorientation of cell structures do not vary with deformation and, therefore, they are considered as transient features of microstructure [Humphreys and Hatherly 2004].

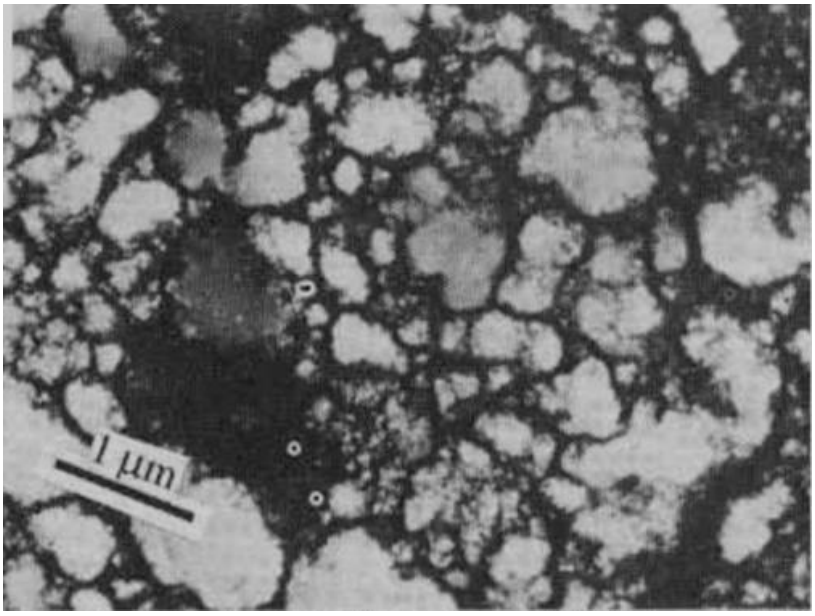

Figure 2.1: Bright field TEM micrograph of cell structures in a 25% cold rolled copper sample [Hatherly and Malin 1979].

2.2.2 Microbands

On further straining, thin channel–like structures evolve on the cell matrix structures. These channels are 1–1.5 μm thick and enclosed by dense dislocation walls (DDWs); a distinctive microstructural feature which is commonly known as microbands. With continuing deformation, the DDWs appear at about 1–1.5 μm repeat distances. Microbands are generated in a wide range of metals and alloys (e.g. Fe, Al, Cu, Ni, Ag, etc.) after deformation by rolling, compression, tension, etc. they are easily recognizable by optical microscopy and SEM from their characteristic lamellar appearances, that are found to be inclined at 25–35° to RD when viewing along the RD–ND cross sections [Humphreys and Hatherly 2004]. Typical microband structures are shown in Figure 2.2. The misorientations across these walls are low in the range of 2–8°. Within a given microband channel the misorientation across the thickness direction is also low (<0.5°). Microband boundaries are often found to be aligned along a trace of a potential slip plane and, thus, are known as crystallographic features [Hansen and Juul Jensen 1992]. At higher strain ($0.3 < \varepsilon < 0.9$), microbands are often found to be intersected by thin shear–, S– or deformation banding structures [Hughes and Hansen 1993, Kuhlman-Wilsdorf and Hansen 1991, Bay *et al.* 1992].

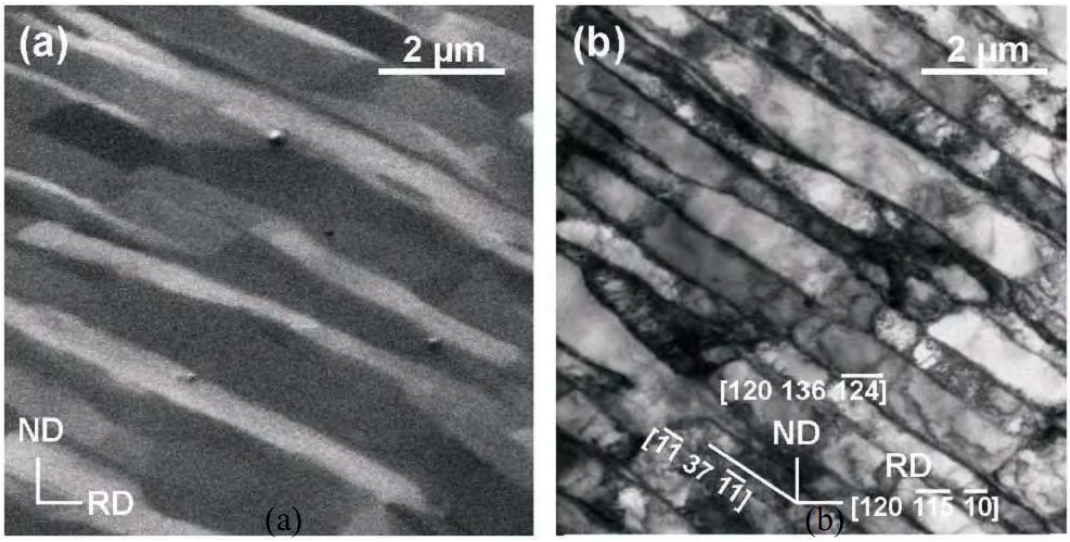

Figure 2.2: (a) Ion channelling contrast micrograph and (b) bright field TEM image of microband structures in ND–RD section in a 40% cold rolled IF steel [Quadir *et al.* 2007].

Crystallographic Vs non–crystallographic debate of microband structures

The "Microband" nomenclature was introduced by researchers at Risø National Laboratory. Early microband characterizations were done by SEM and TEM based techniques [Bay *et al.* 1992, Hughes and Nix 1989, Hughes and Hansen 1993, Huang and Hansen 1991, Hansen and Juul Jansen 1992, Winther *et al.* 1997, Winther *et al.* 2000]. A major finding of these investigations was that the microband boundaries are aligned closely with highly stressed slip planes and, based on this observation, microbands were concluded to be a crystallographic entity [Godfrey *et al.* 1998, Winther *et al.* 2004, Lin *et al.* 2009]. The majority of the early characterizations were conducted in fcc metals. Therefore, a large gap remains in the understanding on microbands in bcc metals (such as irons and steels) until the detailed investigation undertaken by the research team lead by Duggan at the University of Hong Kong [Chen *et al.* 2003, Tse *et al.* 1999, Duggan and Tse 2004, Quadir and Duggan 2006, Chen *et al.* 2006]. The crystallographic identity of microbands remains valid in their study. The following points stand in favour of the crystallographic nature of microbands:

- *Orientation dependency:* In polycrystalline samples, finding microband structures depends on the crystallographic orientation of the parent grain. In other words, microbands form in grains having a certain orientation, while some other oriented

grains remain microband free, even after large deformations. The cold rolling microstructure in steels is the best example to represent this phenomenon, whereby the grains having {111} planes parallel to the rolling plane comprise microband structures and the grains having <110> direction parallel to the rolling directions remains microband free. This finding has been unanimously reported in numerous investigations. Shen and Duggan [2007] and Chen *et al*. [2003] worked out the origin of microband structures in terms of grain orientation dependent crystallographic slip. It has been found that in microband containing grains slips are restricted within a few systems, whereas in microband free grains, there are many slip systems readily available to participate in the deformation process. A similar finding has been reported in fcc metals *i.e.* certain oriented grains comprise microband structures after deformation although this phenomenon is less distinctive in metals with this crystal structure.

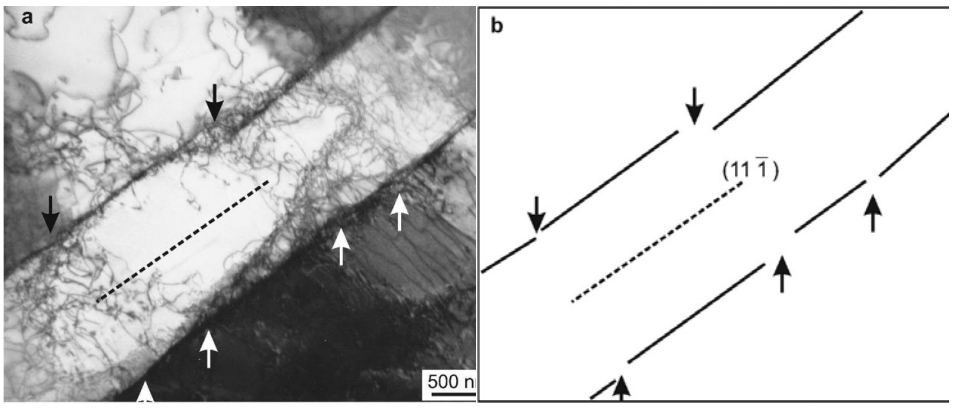

Figure 2.3: An edge–on image of two GNBs of a microband taken in the beam direction [$1\bar{2}\bar{1}$]. The presence of small steps (indicated by arrows) associated with the GNBs. The dashed line marks the trace of the primary slip plane ($11\bar{1}$). (b) A sketch showing an approximately parallel relationship between the straight segments forming the GNBs and the trace of the ($11\bar{1}$) plane that lies in the beam direction, suggesting that the GNB plane is close to the ($11\bar{1}$) [Huang and Winther 2007].

- *Microband alignment in TEM investigations:* TEM provides direct evidence of microband boundary alignments with potential crystallographic slip planes. This has been observed in both fcc and bcc metals. Figure 2.3 shows the dislocation structures of microband boundaries in a commercially pure aluminum alloy that was deformed by tensile loading [Huang and Winther 2007]. This image was

captured after tilting the sample to make the microband boundary projections as thin as possible, *i.e*. the edge–on condition of the boundary along the electron beam. In the image a dotted line is drawn along the trace of a {111} plane and thus it becomes obvious that microband boundaries are closely aligned along the $(11\bar{1})$ crystallographic plane. A similar finding has been presented for bcc metals, whereby freshly formed microband boundary interfaces were found to have close alignment with {110} planes [Chen *et al*. 2003].

- *3D–EBSD investigations:* Quadir *et al*. [2007] conducted 3D serial sectioning and EBSD investigations to find microband boundary inclinations in three dimensional spaces in a cold rolled ultra low carbon steel. The overall alignment of microband boundaries was found to match well with potential slip planes. However, many disturbances in microband boundary interfaces, in the form of curves and bumps, deviate short segments of boundaries from perfect crystallographic alignments. It should be noted that there are two limitations in their study: they analyzed a small volume of material that only covered few microband boundaries and bcc metals have many potential slip systems that may lead to ambiguous conclusions.

Other researchers have indicated that microband boundaries may be non–crystallographic [Hurley *et al.* 2003, Humphreys and Bate 2007, Albou *et al.* 2010, Borbély *et al.* 2007]. They arrived to this conclusion after conducting high resolution EBSD investigations, in two contiguous planes at right angles (RD–ND and RD–TD), in a Al–0.13% Mg alloy that was cold rolling to 65% reductions. The major points in favor of non–crystallographic arguments are summarized below:

- In the rolling plane (RD–TD) section the traces of microband boundaries are not straight although they appear straight in the RD–ND section. In local scale in this plane, they were found to be in irregular and jagged appearances, although on average they were oriented within 10–20° with TD. Therefore, it was concluded that microband interfaces do not lie on a common crystallographic plane of a given grain. Figure 2.4 shows the differences in their structure across these two contiguous planes.

- It was found that when microbands form in two grains of similar orientation, they do not necessarily have a general alignment along a common crystallographic plane. However, it is expected that similar orientations have similar operative slip systems and should yield similar dislocation structures and, hence, microband boundaries. The grain size of the sample is important in this regard, since in small grain aggregates grain boundary have large influence on the structures. The grain size prior to the rolling deformation was not noted in this report [Hurley *et al.* 2003].

- As a generic test, the traces of planar dislocation boundaries that form in several hundred grains were observed in both RD–ND and RD–TD sections. The resulting trace analysis data was divided into two groups corresponding to the major texture component found in the sample. Irrespective of the grain orientation, the traces are distributed in a bell–shaped manner, having peaks at 35–40° to RD in RD–ND section and 0° to TD in the RD–ND section. This is presented in Figure 2.5 and 2.6.

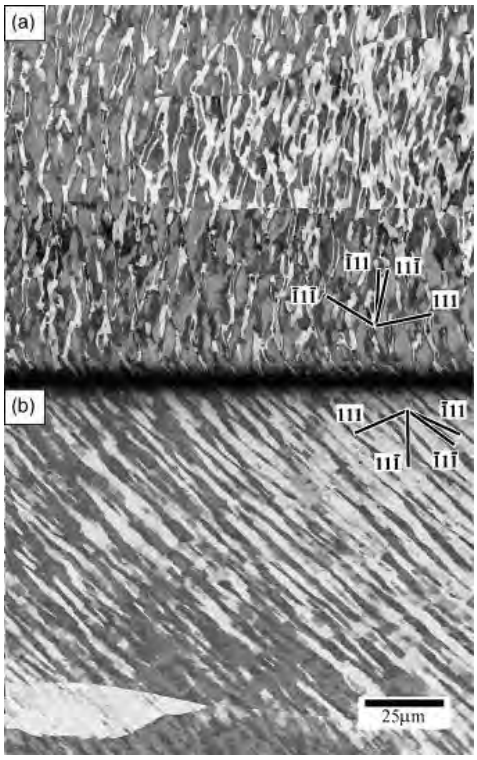

Figure 2.4: Backscattered electron image showing a grain located along the edge of a sample in which both (a) the rolling plane (RD–TD section); and (b) the longitudinal plane (RD–ND section) have been analyzed by EBSD and the {1 1 1} traces are shown in each case [Hurley *et al.* 2003].

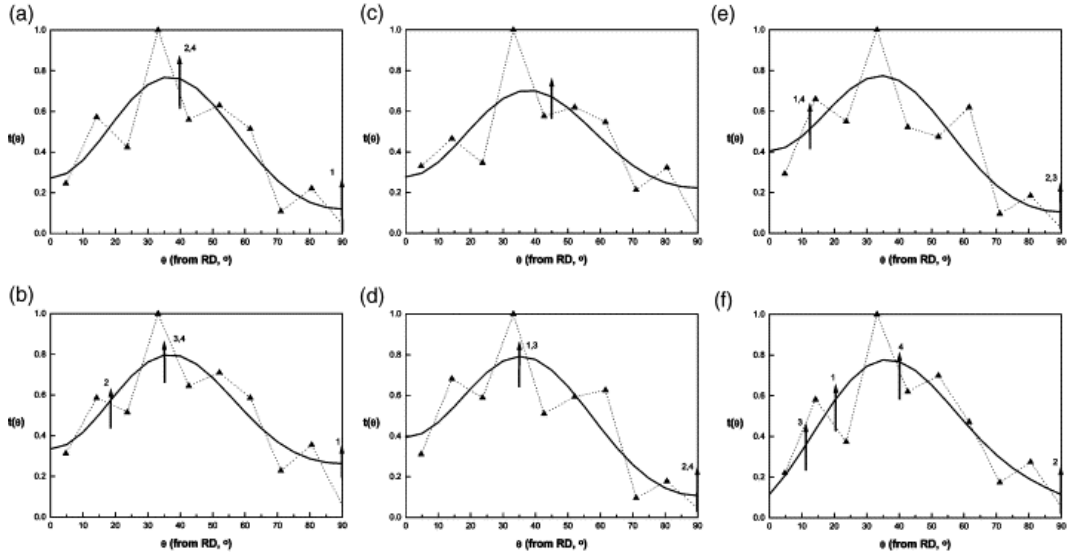

Figure 2.5: The summed trace distributions measured from grains analysed in the longitudinal plane (RD–ND) with orientations within 20° of (a) brass (b) copper (c) cube (d) Goss (e) P and (f) S ideal texture components in rolled Al–0.13% Mg microstructures. The unbroken lines represent the fitted Fourier curves. The traces of the {1 1 1} planes for each ideal orientation are shown as arrows [Hurley *et al.* 2003].

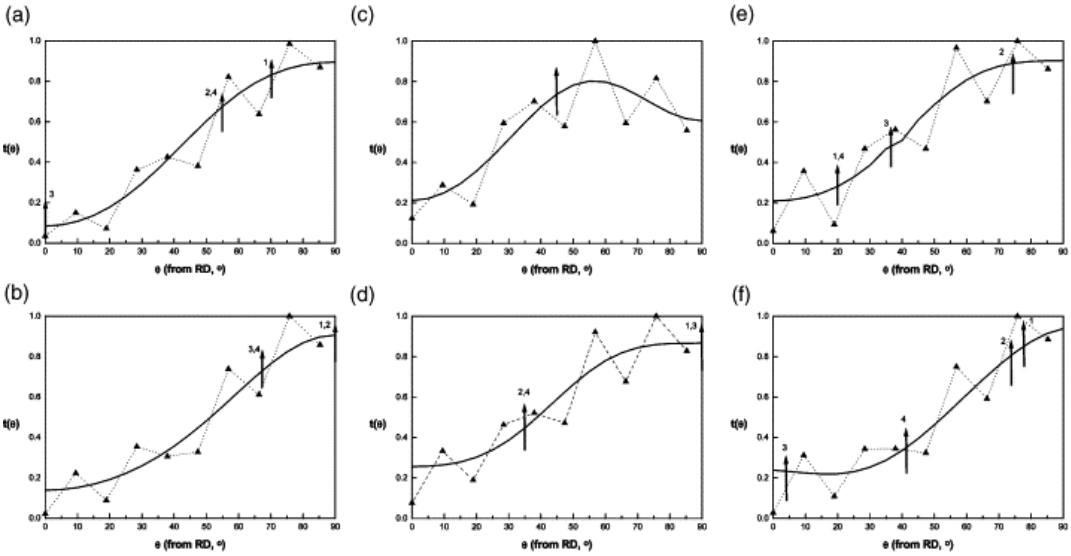

Figure 2.6: The summed trace distributions measured from grains analysed in the rolling plane (RD–TD section) with orientations within 20° of (a) brass (b) copper (c) cube (d) Goss (e) P and (f) S ideal texture components in rolled Al–0.13% Mg microstructures. The unbroken lines represent the fitted Fourier curves. The traces of the {1 1 1} planes for each ideal orientation are shown as grey arrows [Hurley *et al.* 2003]

Theories of microband formation:

There are two models to describe microband formation mechanisms: Jackson's double cross−slip model [Jackson 1983a and 1983b] and Hansen's boundary splitting model [Hughes and Hansen 1991, Hughes and Hansen 1993, Hughes and Nix 1989]. The principal difference between these two lies in the evolution sequence of the two boundaries that enclose a microband channel. In the double cross−slip model, these walls evolve continuously during cross−slipping arrays of dislocations and, in the splitting model, they evolve by splitting the existing dense dislocation walls. These models are now described briefly;

Double cross−slip model: The double cross−slip model was developed based on the early finding that shows isolated slip bands in the polished surfaces in a copper crystal [Kosel and Washburn 1970]. It was found that slip on the (111) plane is associated with a pair of dislocation "mats", separated at ~0.5 μm. The mats were misoriented with the matrix by small angles and the main Burgers vector in the mats laid on the cross−slip plane. From the similarity of microband structures with that of slip bands observed by Kosel and Washburn [1970] Jackson assumed that they have the same origin. It was also assumed that a microband originates from the instability of dislocation structures: as the crystal rotates during deformation and slips on the existing planes do not remain anymore viable. Therefore, further glide on the existing slip plane is likely to become unstable and cross−slip become inevitable. Cross−slip may transfer segments of gliding dislocations onto the cross−slip planes where they can glide along the slip directions. These segments will provide nuclei for the formation of dipole dislocation structures as glide continues. Thus, cross−slip produces characteristic double sheets of microband. However, the model does not explain the origin of the distance between microband boundary at <1 μm. A schematic of the model is shown in Figure 2.7. The important features of the model are given below:

- Successive cross−slip of dislocations in a procession produces a pair of dislocation boundaries of a microband channel, parallel to the active slip plane.
- When dislocation sheets form by cross−slip the materials between the sheets rotate around a specific axis.

- Cross–slip in a procession transfers slip to a set of closely spaced plane and therefore the corresponding shear is distributed over a band of neighboring plane.

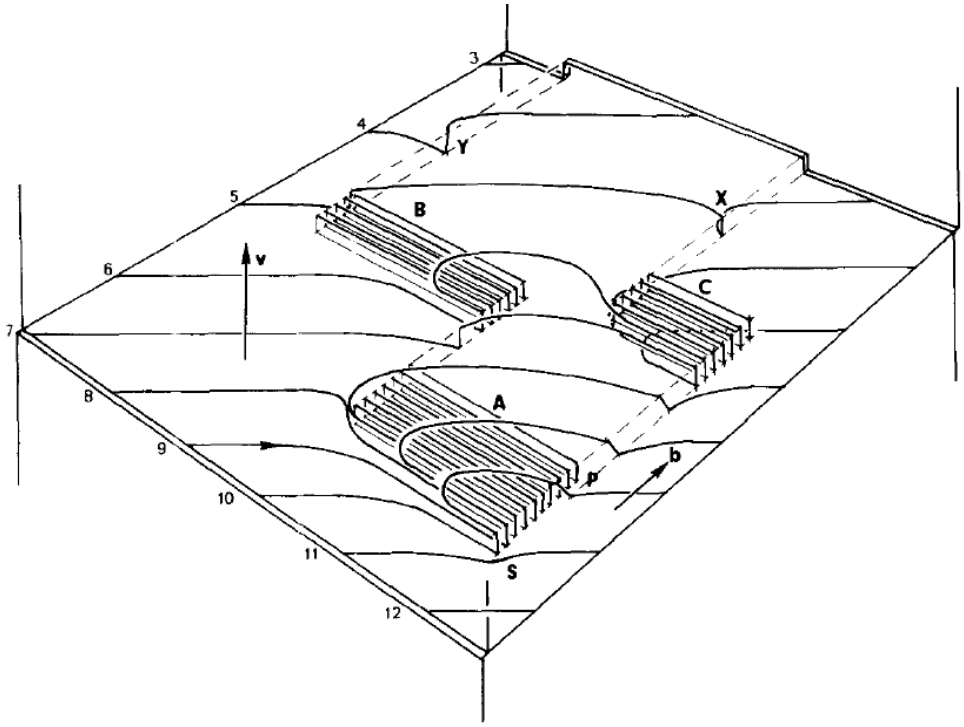

Figure 2.7: Schematic diagram showing how prismatic dislocation arrays may form by cross–slip in procession. The arrays A and B are interstitials and C is vacancy type. It is supposed that a group of dislocations (3–12) are moving across a glide plane, along ν, and that cross–slip started when a jog was trapped at P on the first dislocation, which has now left the crystal. Dislocations 6–10 are depositing dipoles at existing arrays. The eleventh dislocation is about to cross slip at S, and further slip will produce new arrays at X and Y, where jogs are being trapped [Jackson 1983a-b].

Boundary splitting model: This model is based on the sequential development of microstructures during deformation. It has been well documented that, in high SFE materials, dislocation arranges in cell structures at small strains. These cell structures are predominantly of equiaxed shape, although other shapes are possible, such as parallelograms and checkerboards. In many cases these cell structures line up and share a common dislocation wall. These walls have several attributes that distinguish them from the other commonly found cell boundaries. They have higher dislocation density, extended lengths of 5–50 μm and geometric orientation with the sample axes. These

boundaries are known as the so–called dense dislocation walls (DDWs). At the early deformation stages only few sparsely distributed walls of this kind are visible in the matrix of the cell structures in TEM observation. These walls separate regions of differing slip and they store dislocations from either side having dissimilar Burgers vectors. DDWs density increases as deformation proceeds. Figure 2.8a shows two intersecting sets of DDWs across a grain boundary.

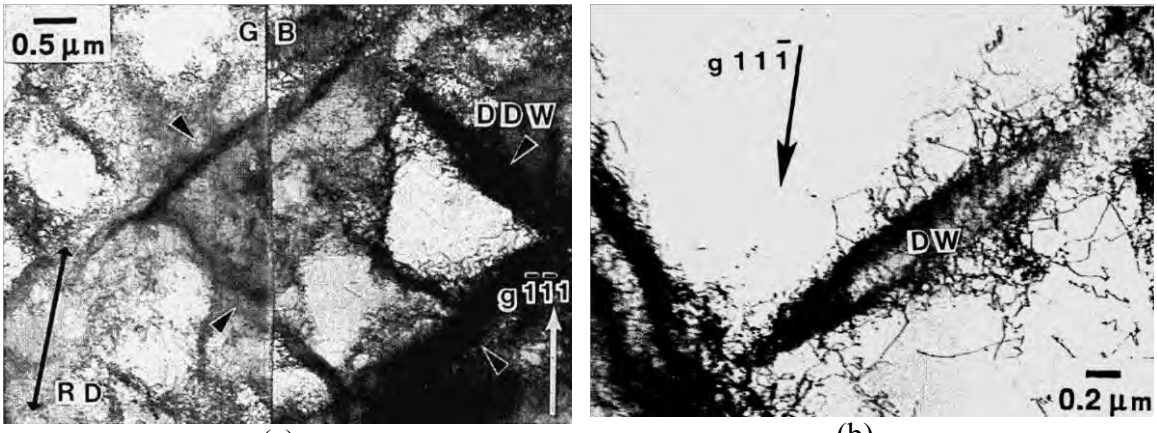

(a) (b)

Figure 2.8: Bright field TEM image showing: (a) an example of spatial organization of discontinuous DDWs, where two intersecting sets line up across grain boundary (GB) along the direction of applied shear stress in 10% cold rolled pure nickel, and (b) formation of microband channel by splitting a DDW [Hughes and Hansen 1991].

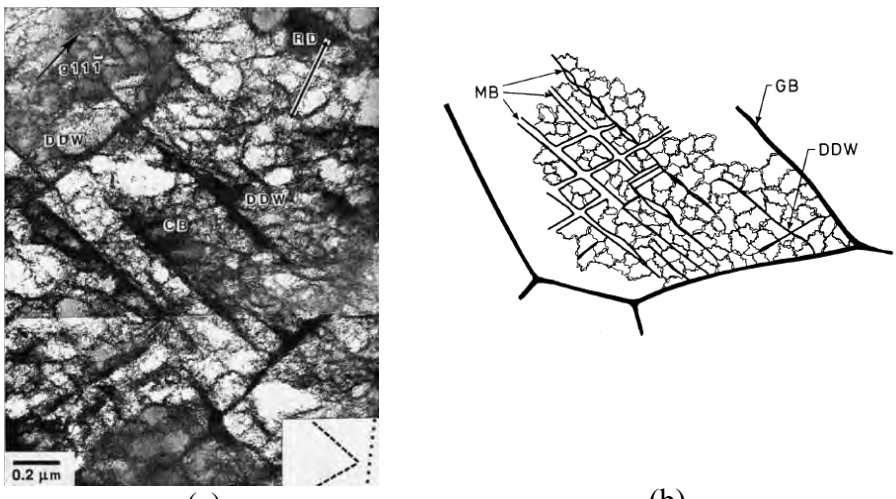

(a) (b)

Figure 2.9: (a) Bright field TEM image of intersecting DDWs is cell matrix structures showing that the microband and DDWs form parallel to a {111} plane in a 10% deformed pure Ni sample, and (b) a schematic diagram showing how the DDWs lead to the microband formations by boundary splitting mechanism [Hughes and Hansen 1991].

In boundary splitting model, the formation of DDWs is regarded as a precursor to microband evolution. During subsequent deformation the DDWs split apart and give rise to the formation of microband channels. One such example is shown in Figure 2.8b. Splitting occurs for two reasons. One, by generating the microband channel the material have new misoriented regions to accommodate further strain and two, the energy of a DDW can be minimized by the formation of two walls. In some cases, more than two walls form to generate a microband channel, but most commonly it remains at two. Figure 2.9a shows a bright field TEM image of intersecting DDWs in cell matrix structures to show that the microband and DDWs form parallel to a {111} plane in a 10% deformed pure Ni sample. The schematic diagram in Figure 2.9b shows how the DDWs lead to microband formation by boundary splitting. It is to be noted that, like the double cross–slip model, this models also does not account for the <1μm separation distance between the dislocation boundary pair in a microband channel.

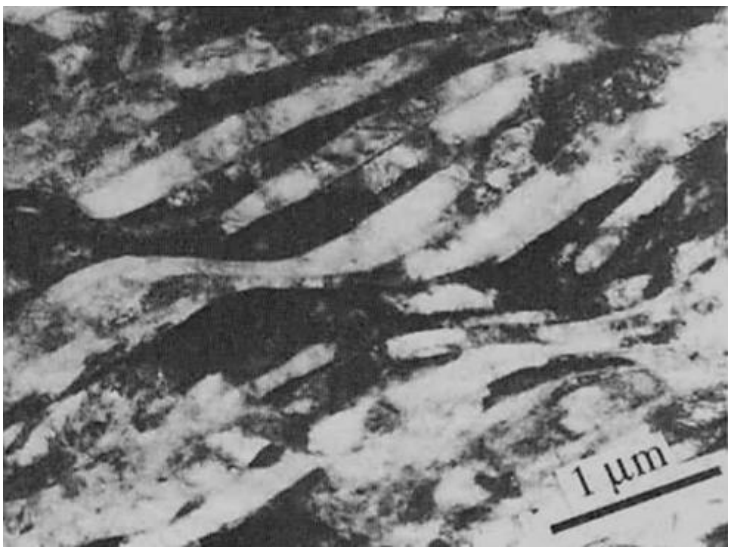

Figure 2.10: TEM micrograph of 85% cold rolled iron showing micro–shear bands in ND–RD section. (1μm marker is parallel to rolling direction) [Willis 1979].

2.2.3 Shear bands

At higher strains ($\varepsilon \sim 0.9$), another type of inhomogeneous structure evolves in microband containing grains. These structures accommodate highly localized flow and are commonly known as micro–shear bands [Duggan *et al.* 1978, Dillamore *et al.* 1979, Lee and Duggan 1993, Aghan and Nutting 1980]. A typical example of micro–shear banding structure is shown in the RD–ND section of 85% cold rolled iron in Figure

2.10. Along the micro–shear band the microband channels become narrowed because of intense shear strains, the magnitude of which may be as high as 3–4. Micro–shear bands form parallel to the second set of microbands and, therefore, they are also recognized as sheet like structures. These shear bands are of identical thickness to the microband channels and are found to be aligned with the highly stressed crystallographic slip planes and therefore are also considered to form from crystallographic origin. It is understood that when crystallographic slip process become restricted because of the obstacles induced by the dense dislocation boundaries of microband structures, the operation of micro–shear bands becomes inevitable to continue deformations.

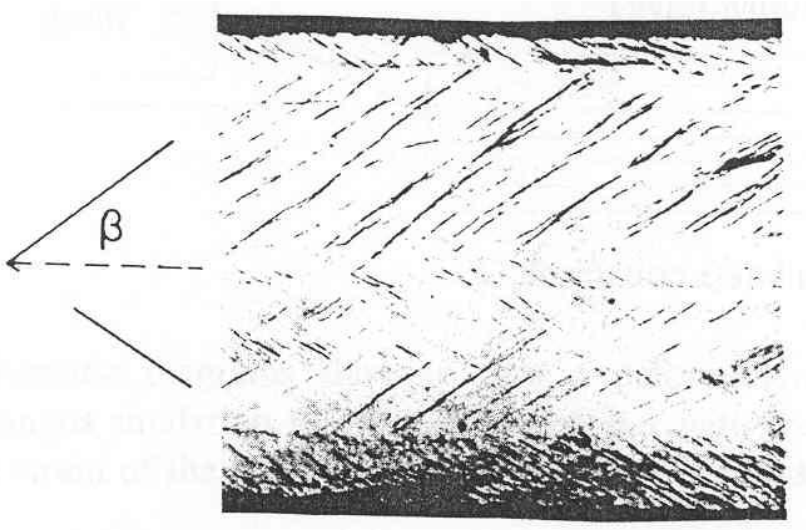

Figure 2.11: Microstructure of macro–shear bands formed following 70% rolling reduction in a pre–polished surface of Al–4.75%Cu alloy (Rolling direction horizontal, rolling plane normal is vertical). [Dillamore *et al*. 1979].

Under the optical microscope, micro–shear bands appear as dark etching lines parallel to the second set of microbands within original hot band grains. There are considerable displacements at the grain boundaries where the shear band interacts. Using high resolution SEM, EBSD and TEM, it has been found that the subgrains within shear bands are more elongated than the matrix. It is to be noted that there are another kind of shear band structure that passes through the whole sample thickness. These are known as macro–shear banding or sample scale shear banding (Figure 2.11). Macro–shear bands are 4–10 times thicker than micro–shear bands and usually align along the highest resolved shear stress directions. Preferential recrystallization has been found to take place along shear band structures due to their higher stored energy than

the surrounding matrix. Hence, macro–shear bands are more effective than micro–shear bands for nucleating recrystallized grains, shear bands can be an effective means of controlling recrystallization textures in metals.

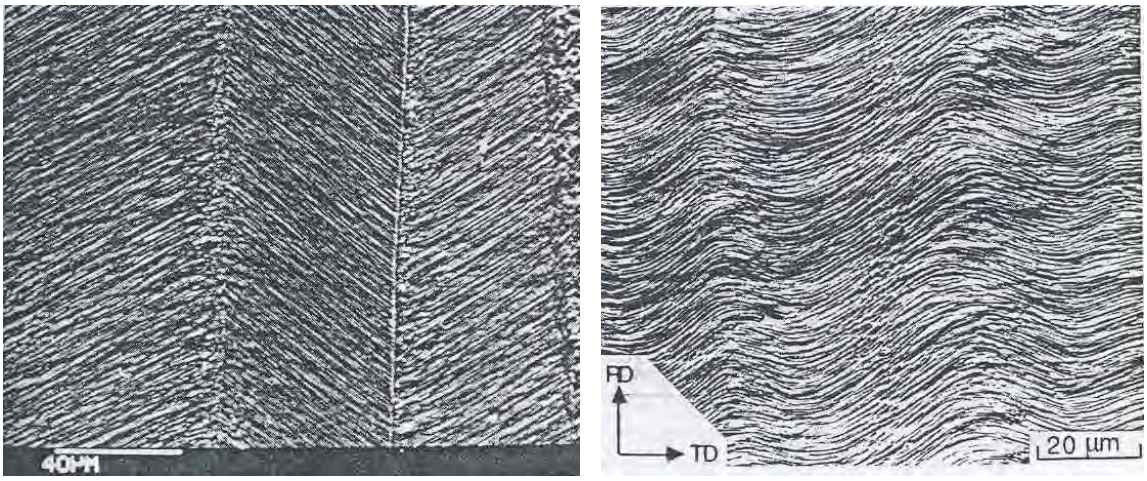

(a) (b)

Figure 2.12 Two types of deformation bands in 70% cold rolled coarse grained copper (a) with sharp boundary and (b) with diffuse boundary [Lee and Duggan 1991].

2.2.4 Deformation bands

During deformation some grains become divided into regions, each of which adopt unique deformation modes. The dividing boundary line between the zones are known as deformation banding structures. Among the early examples, deformation banding structures have been found in aluminum [Barrett 1939, Barrett and Massalski 1966] and low carbon steel [Hu 1963] after compression and tension. Among recent examples, Lee and Duggan [1993] found these features in coarse grained copper and Tse and Duggan [1999] found them in cold and warm rolled IF steels. Lee and Duggan [1991] demonstrated that larger grains are more susceptible to deformation banding structures. Deformation bandings may appear in two forms. In one, a sharp boundary forms between two differently oriented regions. In the other, a thin transition band form between the splitted regions. The second type of deformation banding was observed in cold rolled copper. Both kinds of deformation banding structure may act as preferred recrystallization sites during annealing and, therefore, have a pronounced influence in the development of recrystallization textures. Examples of sharp and gradual deformation banding structures are shown in Figure 2.12a and b, respectively.

2.2.5 Lamellar bands

At very high rolling strains, lamellar band structures was found to form all over the RD–ND section of the sample. Lamellar bands are also plate–like structures. However, unlike microbands lamellar bands are not crystallographic *i.e.* they align along RD irrespective of their orientations. Another major difference between microband and lamellar band is in the misorientation angles: the misorientations across microband boundaries are low, but are high across lamellar band boundaries [Quadir *et al.* 2007a]. As a result microband do not participate in the recrystallization events but in lamellar band structures recrystallization occurs by bulging their boundaries. A typical example of a lamellar band structure is shown in Figure 2.13 [Malin and Hatherly 1979, Hughes and Hansen 1997].

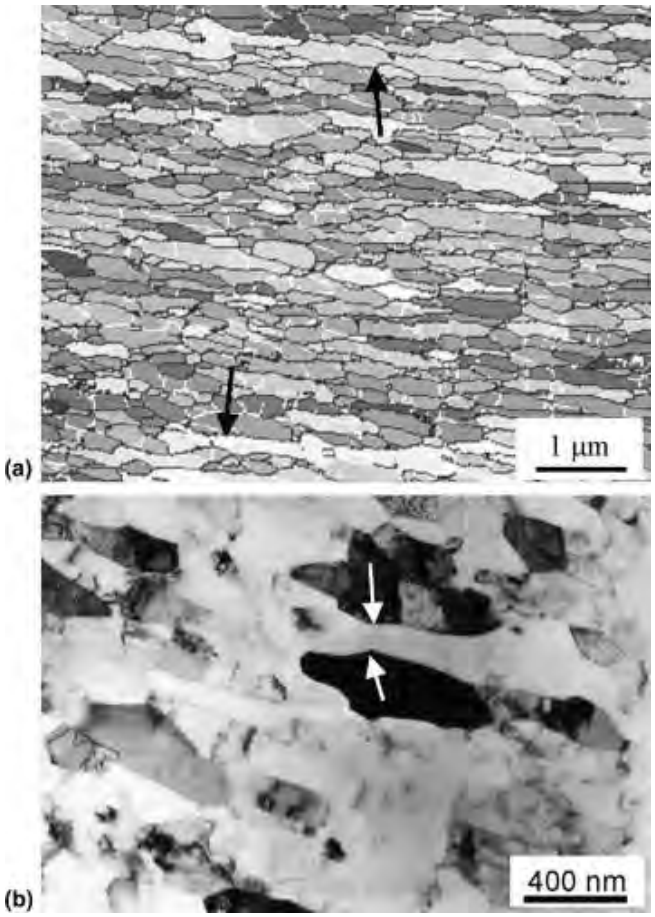

Figure 2.13. The lamellar band structure in the Al–0.13%Mg alloy after deformation to a strain of ε_{vm}~10: (a) an EBSD map, cleaned only with high and low angle boundaries as black and white lines, and (b) a TEM image.

2.3 Deformation textures of cubic metals

Common industrial alloys are composed of polycrystalline aggregates, whereby each crystal is commonly known as a grain. In terms of the grain orientations, two extreme situations can be imagined. In case one, each grain may have a particular crystallographic direction/plane oriented along a common sample axis, such as along RD, TD or ND in a rolled sample. In this situation, the sample is described as highly textured. In the other extreme, each of the grains may have a different orientation to generate what is termed a random texture. In commercial metals these extreme situations are unlikely to occur. Generally, if a large number of grains have a particular pattern in orientation it is known as a textured sample. A common example of this kind is grain oriented silicon steel, in which >90% grains have their {110} plane lie parallel to the rolling plane and <001> direction orient parallel to the rolling direction *i.e.* {110}<001> texture. Textured sample may also have several orientation components instead of a single orientation. For example, after rolling the orientations in Table 2.1 and 2.2 were found in fcc and bcc single phase metals [Hatherly and Hutchinson 1979].

Table 2.1: Rolling texture components in fcc metals.

Orientation component	{hkl}|| ND	<uvw>||RD	Euler angle		
			Φ_1	Φ	Φ_2
Cube	001	100	0	0	0
Goss, G	011	100	0	45	0
Brass, B	011	211	35	45	90
Copper, C	112	111	90	35	45
S	123	634	59	37	63

Table 2.2: Rolling texture components in bcc metals.

Orientation component	{hkl}|| rolling plane	<uvw>||rolling direction	Euler angle		
			Φ_1	Φ	Φ_2
γ–fibre orientations components	111	112	90	55	45
	111	110	90	55	45
	111	123	80	55	45
α–fibre orientation components	100	110	0	0	45
	113	110	0	25	45
	112	110	0	35	45
	111	110	0	55	45
Other orientation components					
Goss	110	001	0	45	0
Cube	001	100	0	0	0

For a given strain and deformation mode, the texture strength and the balance between the various texture components depend on materials variables *i.e.* grain size and shape, presence of second phase particles, initial crystal orientation and stacking fault energy [Hansen and Juul Jensen 1991, Hirsch and Lücke 1988a–b]. The processing conditions (deformation temperature, strain rate, extent of deformation, etc.) also have strong influences on the texture generation. Furthermore, the grain boundaries also play significant roles in texture formations.

2.3.1 Texture measuring techniques

There are various techniques for measuring textures. Some of them are suitable for samples having a large number of grains, whereby data statistics is important. Some are suitable for microstructural area specific regions. Among the quantitative techniques, the most widely used method is X–ray diffraction, by which a global picture of the orientation can be sought out and, therefore, is very suitable for knowing the orientations of grains in bulk samples. Neutron diffraction also operates on a similar

principle. However, in various scientific and technical researches, the orientation of a particular microscopic area is often important. In these situations texture measurement by SEM– and TEM–based techniques are commonly used. These methods are generally known as microtexture determination techniques. The TEM–based techniques are less attractive than the SEM–based EBSD technique, due to difficulties in sample preparation, data analysis and limitations in data statistics. In this thesis, both EBSD and TEM methods are used extensively and, hence, they are now described in further detail.

Electron backscatter diffraction (EBSD)

EBSD is a SEM–based microtexture determination technique. It is also capable of measuring quantitative texture [Maitland and Sitzman 2007, Prior *et al*. 1999, Randle 2004]. The technique involves automated computer based detection and analysis of Kikuchi patterns, which generate from the region where the electron beam of the SEM impinges on the crystalline surface of a sample. A point–by–point data acquisition over a selected area of a sample can thus yield a crystallographic orientation map of the entire area. The current EBSD detection systems are fast and, hence, capable of acquiring a vast amount of data within a short period of time.

A typical EBSD system comprises a backscatter diffraction camera with a phosphor screen and an image processing system for pattern averaging and background subtraction. A schematic of this process is shown in Figure 2.14. In the SEM chamber the EBSD detector aligns approximately horizontal, which is 90° to the electron beam column. During EBSD data acquisition, the sample surface is tilted ~70° with the beam axis so that the sample surface nearly faces the EBSD detector. The primary purpose of this arrangement is to enhance the diffraction pattern signal gain to the detector. The diffraction signal arrives at the camera as Kikuchi patterns, in which each parallel line represents a parallel set of crystallographic planes and the intersections of them are the zone axis of those planes. After capturing the pattern an automated computerized system indexes each of them, measures orientation data and stored the data as numerical values. Orientation detections are generally accurate to within ~1°, with a repeatability of <0.1°, depending on the conditions of the experiment [Humphreys 2001]. The spatial resolution of the EBSD measurement depends on the size of the electron probe and the nature of the material [Humphreys and Hatherly 2004]. In modern SEMs fitted with a

high resolution field emission gun, grain measurement down to 20 nm in size is possible with reasonable accuracy [Maitland and Sitzman 2007].

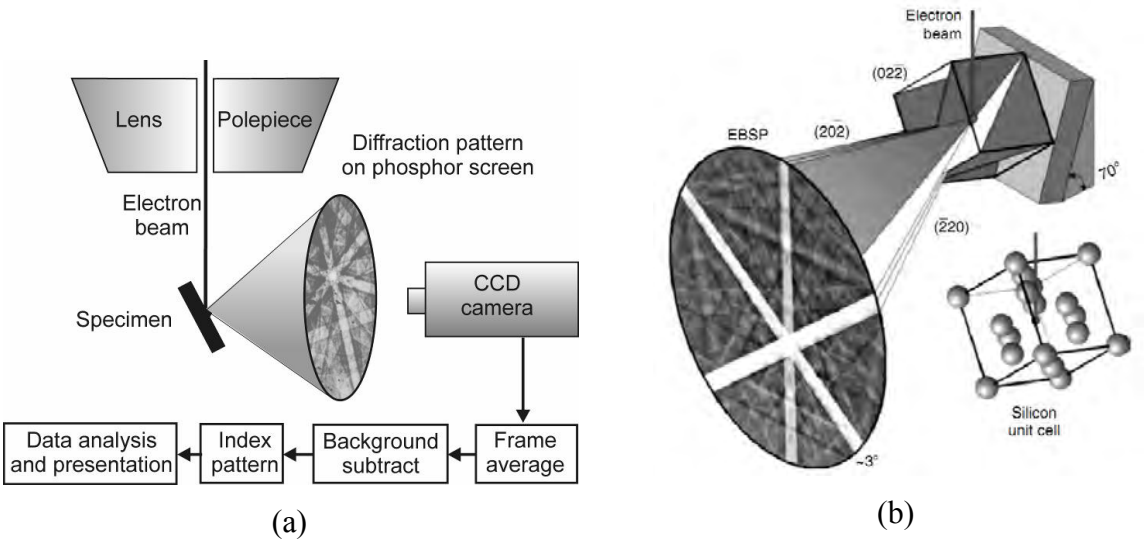

Figure 2.14: (a) Typical EBSD configuration in a SEM chamber, showing a Kikuchi EBSD pattern impinging on a phosphorous screen from a point on the sample surface [Humphreys and Hatherly 2004]. (b) Electron interaction with a crystalline material to generate the Kikuchi pattern [Day *et al.* 2004].

EBSD has been commonly used to generate orientation maps from selected areas in sophisticatedly polished sample surfaces. Such as acquired data set can then be plotted in color coded pixilated maps with the data processing software. In a map each pixel represents an orientation data [Humphreys 2001]. A typical orientation map is shown in Figure 2.15. Nowadays, the EBSD data analysis software is rather powerful to plot a wide variety of maps, charts and plots. Therefore, EBSD has been recognized as the most powerful tool for conducting wide range of investigations aimed at studying orientation relationships between phases, grain sizes and their distribution, phase identification, kinetic of phase transformations, crystallographic relationships between phases, and recrystallization and grain growth [Gourgues–Lorenzon 2007, Baba–Kishi 2002].

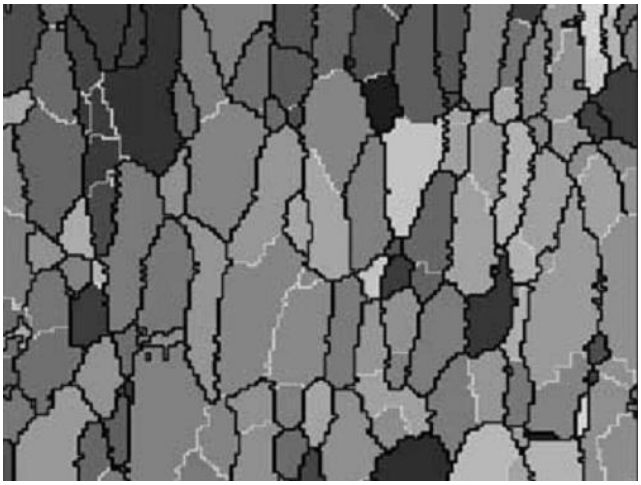

Figure 2.15: EBSD orientations map of a deformed aluminium alloy (high angle (>15°) and low angle (<15°) boundaries are marked with black and white color, respectively) [Humphreys 2001].

Transmission electron microscopy (TEM)

TEM uses a high energy electron beam to transmit and/or diffract through a very thin segment of a sample to image the microstructure to atomic−scale resolution. The electron beam is focused with a series of electromagnetic lenses to project the structural features on a fluorescent screen. The images can be readily recorded on film. Nowadays, a high resolution digital camera is commonly in use. A typical beam geometry of a TEM is shown in Figure 2.16.

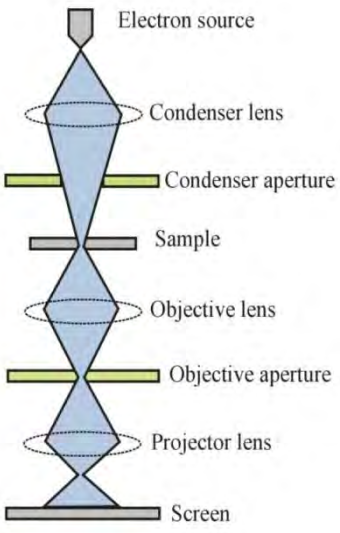

Figure 2.16: The schematic outline of a TEM.

It is possible to obtain orientation information from a region of interest from TEM generated diffraction patterns. The microscope operates in two common diffraction modes: selective area electron diffraction (SAED) and convergent beam electron diffraction (CBED). In SAED mode, parallel electron beam is directed through a small aperture on a small area of the sample and the orientation data is recorded in the form of spot patterns. Therefore, SAED provides information of a finite area from several hundred nanometres to microns, depending on the size of the aperture used. The angular resolution of diffraction spots are usually in the range of 2–5° [Duggan and Jones 1977]. An example of SAED pattern is shown in Figure 2.17b. In the CBED method, the electron beam is converged onto a very small region of the sample (e.g. 10nm) to generate a Kikuchi diffraction pattern. An example of CBED generated Kikuchi pattern is shown in Figure 2.17c. This method yields very accurate relative orientation measurements (~0.1° angular resolution). However, due to errors in sample cutting and loading into TEM holder, there is a ~5° uncertainty in the absolute orientation measurement.

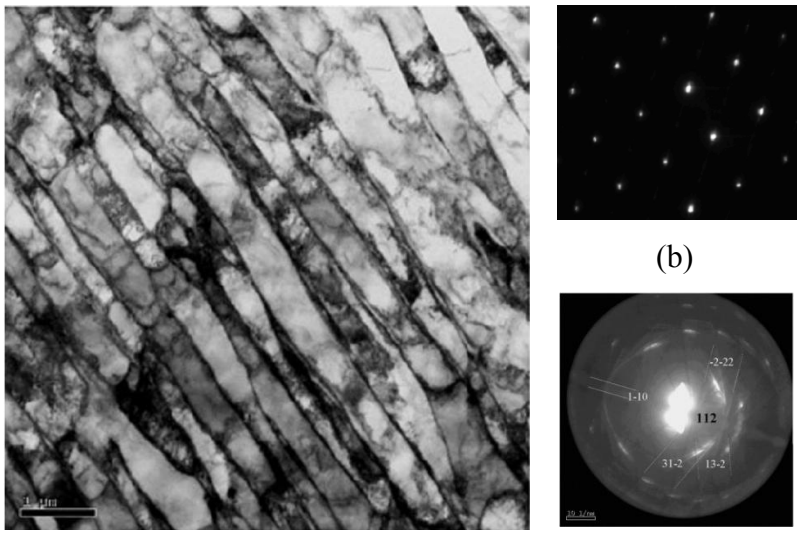

(a) (b) (c)

Figure 2.17: (a) Bright field TEM micrograph showing the formation of microband structures in a 50% cold rolled IF steel [Quadir and Duggan 2006]; (b) SAED electron diffraction pattern of a Si sample [Muller 2008], and (c) CBED diffraction pattern from a steel sample [Chen *et al.* 2006].

Beside many other advantages of TEM, it also provides image at atomic resolution, to reveal crystal structures, orientations, phases, compositions and magnetic

properties. Most modern TEMs operate in Scanning Transmission Electron Microscopy (STEM) mode. This is often used for elemental analysis (i.e. chemical information). In recent times, TEM has been used to obtain three dimensional information within the sample thickness of 50–150 nm. Here, a series of two dimensional images are recorded at small intervals in a wide range of tilt angles. Then an object can be reconstructed from these images to obtain 3D morphology. Another TEM–based microtexture determination method has been developed by Humphreys [1983] and Schwarzer [1990] to generate EBSD–like orientation maps at higher resolution (~2 nm) [Humphreys and Hatherly, 2004]. This technique is particularly suitable for highly deformed materials and regions around second phase particles. The recently developed transmission EBSD mode in the SEM also allows the generation of orientation maps at higher resolution (~2 nm) from transmitted electron beams in a TEM sample [Trimby 2012].

2.3.2 Representation of texture data

Crystallographic textures are usually represented by pole figures, inverse pole figures and orientation distribution functions. A brief description of each representation method is given below:

Pole figures

A pole figure is a simple stereographic projection that shows the distribution of particular crystallographic directions of the assembly of grains in a polycrystalline block of material [Humphreys and Hatherly 2004]. How the crystallographic orientation of single crystal, sitting within the rolling direction (RD), transverse direction (TD) and sheet plane normal direction (ND) reference frame of a sheet, can be plotted in a pole figure is simplified in Figure 2.18. In Figure 2.18a the sample is considered to sit at the centre of a stereographic sphere. The orientation of a single grain (*i.e.* a crystal) in the sample can be represented by plotting the three <100> poles. Here, the normal of each {100} plane is drawn where they intersect at three points on the surface of the sphere. A projection of those intersecting points to the bottom pole of the sphere shows them cutting through three points in the circle of the hemisphere (*i.e.* the equatorial plane). This hemispherical plane also comprises the projections of the three reference axes RD,

TD and ND, and thus represented as a stereographic projection, as shown in Figure 2.18b.

Therefore, the <100> pole plot, in Figure 2.18b, shows the orientation of a single grain with respect to RD, TD and ND reference axes of the sheet. For a polycrystalline material, practically many grains contribute three such <100> poles (in cubic system). A combined plot of many differently oriented grains therefore makes the pole figure crowded, as shown in Figure 2.18c. In practice, the points are presented as intensity contours, as shown in Figure 2.18d.

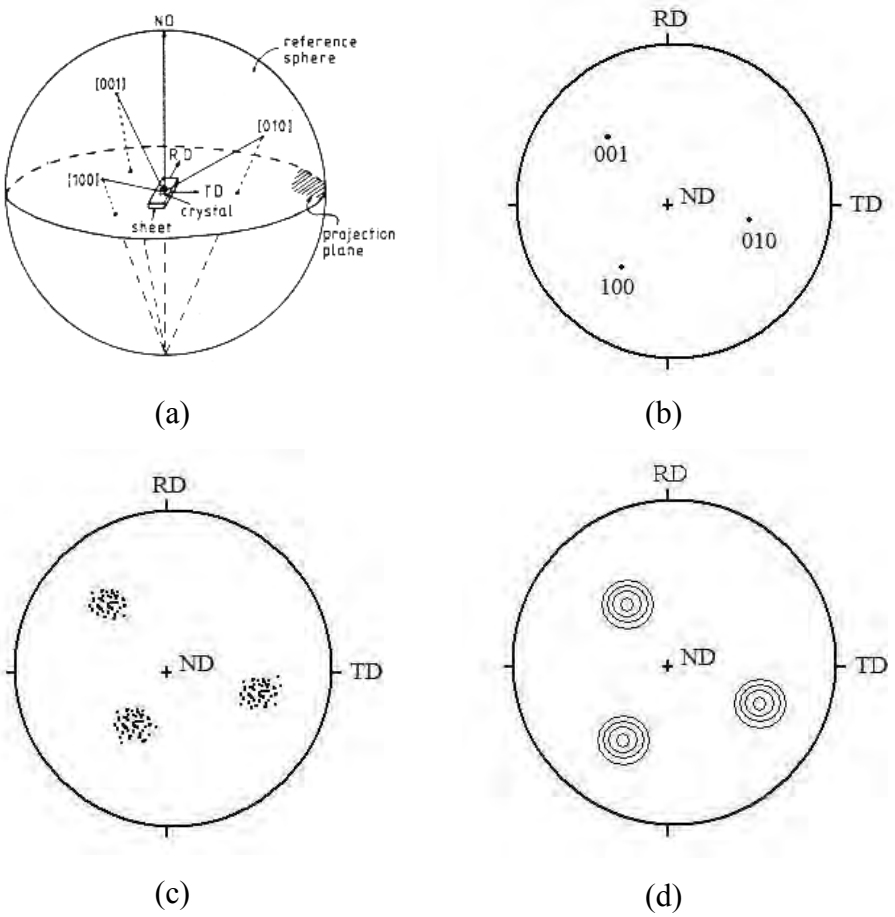

Figure 2.18: (a) Projection sphere and reference direction, (b) projection of poles for single and (c) textured grains, and (d) contour map of pole density [Hatherly and Hutchinson 1979].

Inverse pole figures

Inverse pole figures (IPF) are usually suitable for showing axisymmetric textures that generate through axisymmetric deformation processes (e.g. tension, wire drawing, extrusion, etc). In IPF, a particular reference axis of the sample is plotted in a single triangle of a stereographic projection, which is representative of the 24 equivalent triangles that compose the entire pole figure in cubic crystal system. A schematic representation of an inverse pole figure is shown in Figure 2.19, whereby the ND plot in an inverse pole figure triangle is shown.

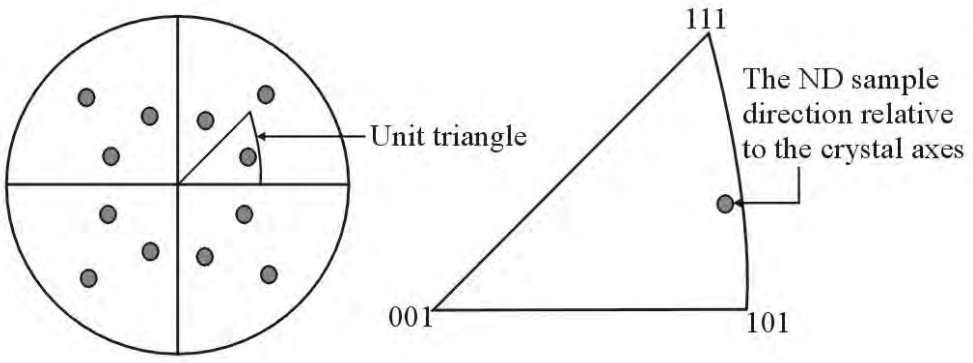

Figure 2.19: Schematic representation of an inverse pole figure.

Orientation distribution function (ODF)

The orientation distribution function (ODF) is suitable for representing quantitative textures and visualizing orientation relationships between texture components. It was originally developed for materials with cubic crystal structures and orthorhombic sample symmetry, *i.e.* for sheet products [Humphreys and Hatherly 2004]. The orientation data between ODF and pole figures are interchangeable. Physically, the ODF is based on the value of three rotation angles that bring the sample reference coordinates into coincidence with the crystal coordinates. These are known as Euler angles [Randle and Engler 2000]. There are several notations for representing Euler angles. The most common are those described by Bunge [1966 and 1982]. The other notations are also equivalent to Bunge's notations. A schematic description of the three rotation angles are shown in Figure 2.20, whereby the operation sequence of ϕ_1, ϕ and ϕ_2 angles are described,

ϕ_1 about the normal direction ND, transforming the transverse direction TD in to TD′ and rolling direction RD in to RD′.

ϕ about the axis RD′ (in its new orientation)

ϕ_2 about ND″ (in its new orientation)

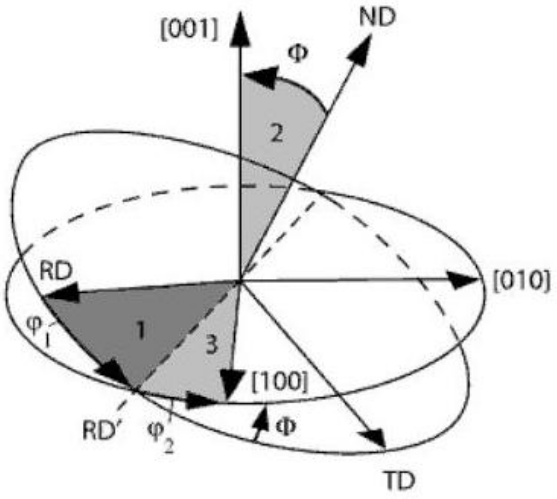

Figure 2.20: A schematic diagram showing descriptions of the Euler angles (in order 1, 2 and 3 as shown) that brings the specimen and the crystal axis in coincidence [Randle and Engler 2000].

Since three variables have been used to define a crystallographic orientation by ODF, an orientation can be displayed in 3D orientation space, whereby the Euler angles represent three axes in the cube (Figure 2.21a). Any point in the cube has three Euler angles and is representative of an orientation. In bcc and fcc sheets, rolling generates orientations distributed along strings. A plot of these orientations shows the connectivity in the form of orientations fibres. The ODF has been realized as a convenient method for visualizing these fibres. For example, the fcc rolling texture usually contains three prominent fibres connecting the principal orientations; these are known as α, β and τ fibres. The position of the α– and β–fibres are shown in the 3D orientation space in Figure 2.21b. Likewise, there are two principal orientation fibres in bcc rolling texture: the α– and γ–fibres. Positions of these fibres are also shown in Figure 2.21c. In routine practice, texture is presented as a series of slices taken through ODF space, for example at ϕ_2 = 0, 5, 10….90°. Because of symmetry the same orientation appears in different ODF sections. However, there are some prominent sections containing the principal orientation components of bcc and fcc rolling textures,

which have been in use by the research community for many years. For bcc and fcc materials, it is the ϕ_2=45° and ϕ_2=0° ODF sections, respectively. The principal orientations in these sections are shown in Figure 2.22.

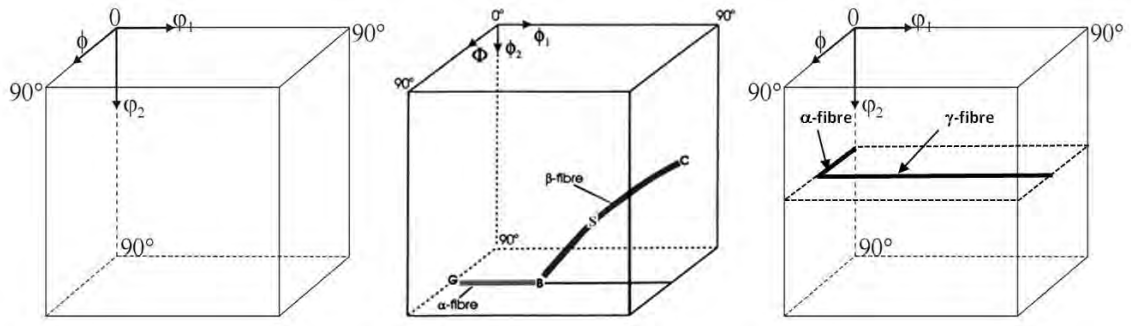

(a) (b) (c)

Figure 2.21: (a) Three dimensional orientation space of Euler angles and therein the positions of orientation fibres: (b) α– and β–fibres in fcc and (c) the α– and γ–fibres in bcc.

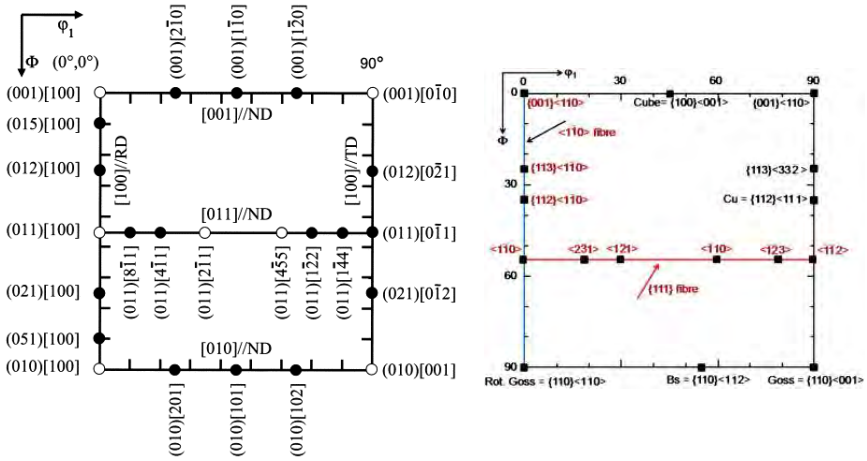

(a) (b)

Figure 2.22: (a) ϕ_2=0° ODF section showing the orientation positions of the main rolling texture components for fcc metals [Guzzo *et al*. 2000]. (b) ϕ_2= 45° ODF section showing the positions of the α– (<110>–) and γ– ({111}–) fibre rolling textures.

2.4 Three dimensional microstructural determination techniques

Scientists have been attempting to develop 3D analysis techniques for almost a century. For example, in 1918 Foresman [1984] painstakingly built a 3D cardboard model of pearlite lamellae by a serial sectioning technique. He utilized standard metallographic polishing method to remove material from the sample surface and

photographed the planer sections. Later, Hillert and Lange [1962], Hopkins and Kraft [1965], Rhines *et al.* [1976], DeHoff [1983], Rosier [1968], Rosner *et al* [2002] and Hull *et al.* [1991] have made modifications to Foresman's method to improve accuracy in serial sectioning and reconstruction. In 1990's a number of 3D experiments were conducted. For example, Mangan and Shiftlet [1994] reconstructed a pearlite colony through micromilling serial sectioning and secondary electron microscope (SEM) imaging, Figure 2.23. In another example, the distribution of cementite precipitates in a hypereutectoid steel were reconstructed by Kral and Spanos [1999]. Furthermore, 3D distribution of Al and Ti in a Si semiconductor material was obtained by Dunn and Hull [1999].

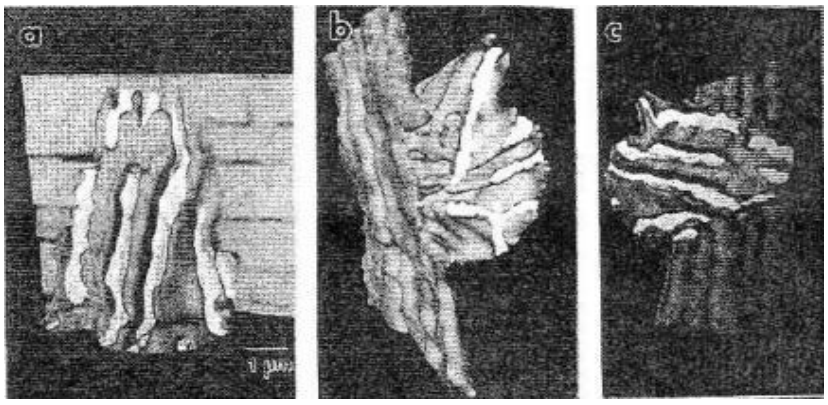

Figure 2.23: Reconstruction of a pearlite colony originated from a prior austenite grain boundary [Mangan and Shiflet 1994].

In recent times, there have been some milestone achievements in 3D crystallography using XRD and EBSD. Among them the work done by the researchers at Risø National Laboratory [Nielsen *et al.* 2001] to investigate the real time nucleation and growth behavior of individual grain using 3D XRD technique is worth noting. In this work the progression of nucleation with time was monitored in 3D space and, therefore, this type of study work has been recognized as 4D microscopy. Following this work, 3D recrystallization quickly become an attractive field of study by many researchers [Fu *et al.* 2003, Poulsen 2004, Schmidt *et al.* 2004, Larsen, Poulsen *et al*. 2005]. In 2006, Raabe and co−workers successfully conducted a 3D−EBSD study to investigate the microstructural development around non−deformable particles in a warm rolled Fe_3Al intermetallic [Konrad *et al*. 2006]. One of their outcomes is presented in Figure 2.24, whereby the distribution of texture components around a particle is

revealed. Currently, there are several research groups adopting 3D–EBSD in their laboratories and undertaking investigations in various areas of materials science. Among them, the 3D–EBSD group UNSW has made several achievements in the advancement in data acquisition and segmentation methods.

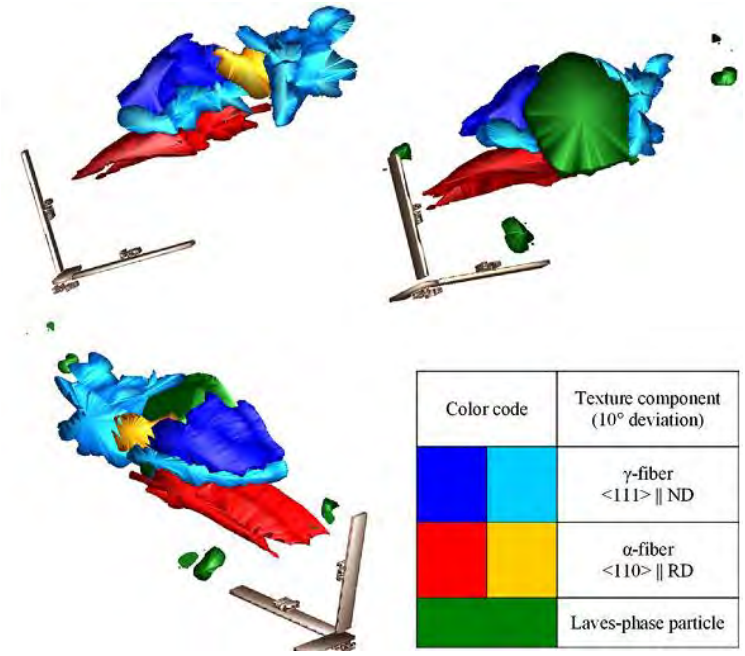

Figure 2.24: 3D visualization of the topography of the main texture components surrounding the Laves particles in a warm rolled Fe_3Al intermetallic compound [Konrad *et al.* 2006].

On a finer scale, the TEM (3D-TEM) and 3D Atom Probe Tomography (3D–APT) based techniques are well recognized. The precursor to the modern 3D atom probe instrument was first constructed by Miller in 1935. Thereafter, through a series of technological developments the first fully operational instrument, known as position sensitive atom probe, was established in 1988 by Cerezo *et al.* [1989] at the University of Oxford. This machine enabled building a 3D aggregate of atoms within few nanometer dimensions. The APT group at University of Sydney has made significant contributions in the latest developments of the technique [Gault *et al.* 2012, Sluytman *et al.* 2010, Tang *et al.* 2010]. The diffraction information generated from the atom probe data has been recognized as a fascinating development. The 3D TEM investigation is based on 2D TEM imaging at a wide range of sample holder's tilt conditions of the objects within the film thickness.

The principal 3D techniques are listed below;

- 3D X–ray Diffraction (3D–XRD)
- 3D Secondary Ion Mass Spectrometry (3D–SIMS)
- 3D Transmission Electron Microscopy (3D–TEM)
- 3D Focused Ion Beam (3D–FIB)
- 3D Atomic Probe Tomography (3D–APT)
- 3D Electron Backscatter Diffraction (3D–EBSD)

Based on resolution limits, the aforementioned techniques may be divided into two broad groups: low resolution (resolution >1μm) and submicron resolution techniques. This is presented in a schematic diagram in Figure 2.25, which might be utilized as a guide for selecting an appropriate technique for a particular application. A brief description of the 3D–EBSD technique is given below for being the extensively utilized technique in this thesis.

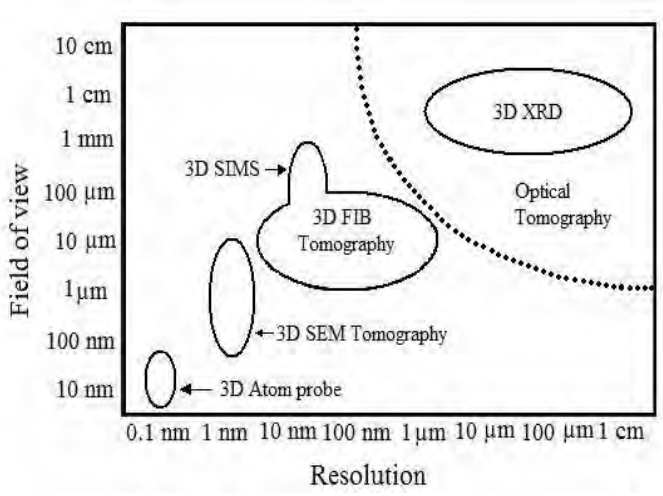

Figure 2.25: Schematic view of the 3D techniques according to their resolution.

2.4.1 Three dimensional electron backscatter diffraction (3D–EBSD)

3D–EBSD is recognized as a powerful method for generating 3D crystallographic information of a material of volumes up to 50×50×100 μm^3. Over time, the resolution of the technique has been improving, where it is now possible to acquire data at ~50 nm resolution. This method is suitable for finding the spatial distribution of various crystallographic features, determining orientation relationships between phases

and characterizing grain boundary features in various research areas, such as solid–state phase transformations, and recrystallization and grain growth etc.

This technique utilizes a high resolution field emission SEM, fitted with a focused ion beam (FIB) device, to acquire crystallographic information in 3D. The technique involves the successive removal of thin slices of material (minimum thickness ~50 nm) from the surface of a cubic block by sputtering with a high–energy ion beam (Ga^+ source) and then rotating the ion milled surface to the required EBSD position for acquiring an orientation map of the surface. The 3D dataset can then be reconstructed to generate detailed crystallographic information on a given feature. 3D–EBSD has the same general requirements as the 2D technique, whereby the features of interest should be at least a few hundred nanometres in size and any FIB beam surface damage should not cause problems with the 3D analysis. A schematic diagram of the sample set up with respect to FIB source and EBSD detector is shown in Figure 2.26.

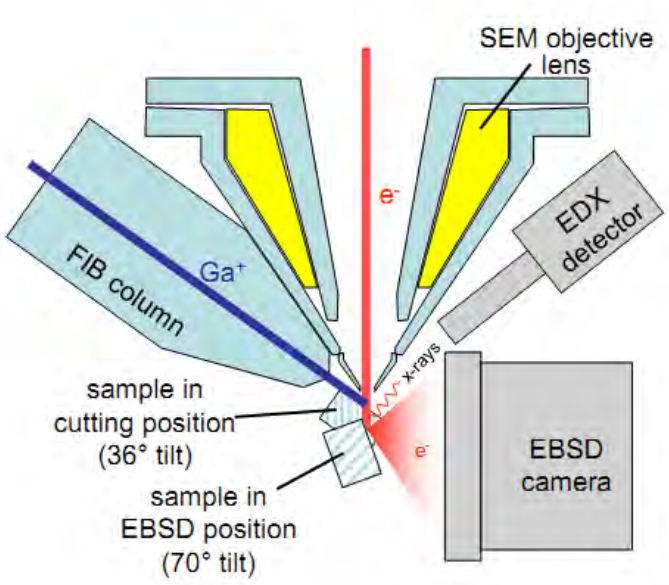

Figure 2.26: Schematic view of the 3D-EBSD set up showing the instrument chamber, the milling position and EBSD position [Zaefferer *et al.* 2008].

The 3D–EBSD technique was developed by Raabe and co–workers for investigating crystallographic distributions around non–deformable Laves particles in a warm rolled Fe_3Al intermetallic [Konrad *et al*. 2006]. The reconstructed 3D data revealed a considerable amount of useful information of the spatial distribution of matrix orientations surrounding the particles. Rowenhorst *et al.* [2006] also utilized the

technique to investigate the 3D crystallography of coarse martensite in a high strength low alloy steel. There have been a number of subsequent innovative inclusions made to this technique by different research groups to ease the challenges of reconstruction and improve accuracy. The works by Konrad *et al.* [2006], Ferry *et al.* [2006], Zaafarani *et al.* [2006], Xu *et al.* [2007a], Lee *et al.* [2007], Zaefferer *et al.* [2008], Prangnell *et al.* [2004] are worth noting in this regard.

2.4.2 Some milestone applications of 3D–EBSD

Among the various 3D techniques, 3D–EBSD is particularly suitable for displaying the distribution of micro–scale crystallographic features in single– and multi– phase materials. Currently, resolution of this techniques relies on the FIB resolution of ~50 nm. A number of structural studies have now been carried out using this technique, with some notable examples described below.

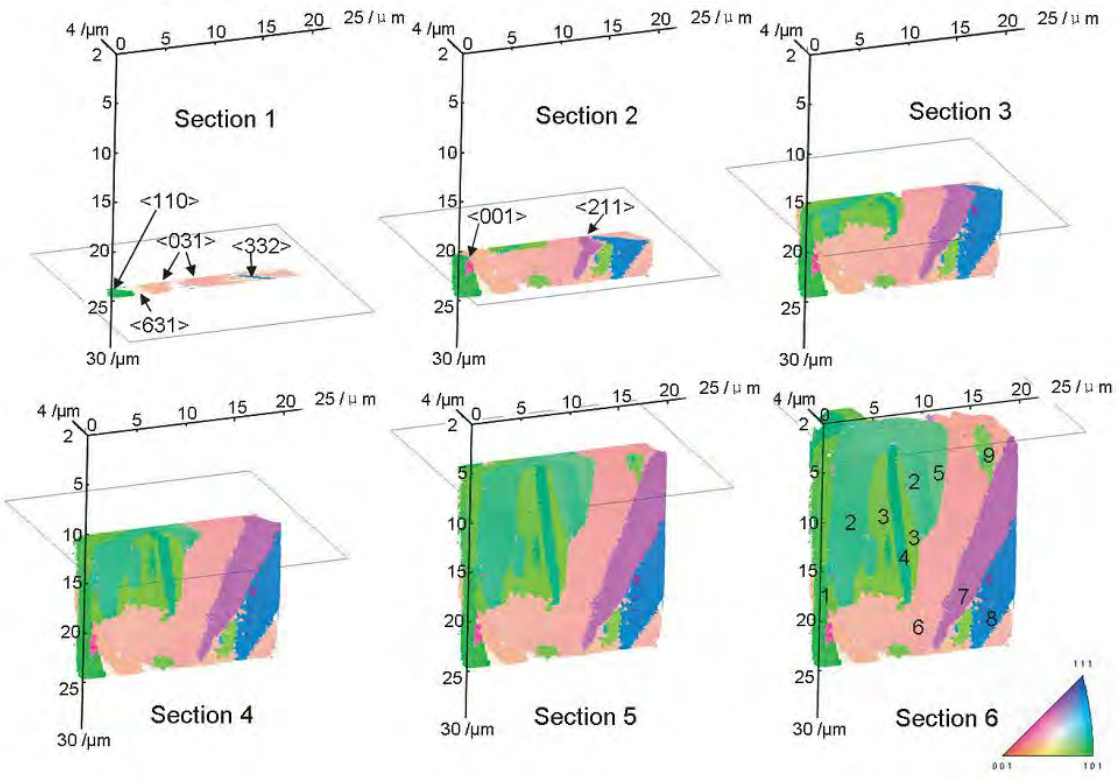

Figure 2.27: 3D orientation maps at different sections on 6 different planes perpendicular to the growth direction of crystals forming in a chemical vapor deposited diamond thin film. Section 1 is close to the nucleation zone and section 6 is the final growth front [Liu *et al.* 2008].

Liu *et al*. [2008] utilized 3D–EBSD to investigate the growth morphology of crystals in a chemical vapor deposited diamond thin film. In their study the nucleation to growth termination stages were delineated in 3D space. They found that the nucleation stage is predominated by twin formations. Thereafter, <110> orientations started prevailing because of their higher growth rate. It was also concluded from the growth kinetic study that growth along <110> and <031> directions produces fewer defects and are more stable than in the other directions, such as <332> and <211>. An example of their finding is shown in Figure 2.27.

In another 3D–EBSD study, He *et al.* [2012] investigated the actual microstructural features in terms of morphology, crystallographic orientation, grain size and arrangement of α and β phases in a near α titanium alloy. Their results indicated that the coarse primary α grains indeed consist of long and thick plates in a 3D. The second α lamellae are finer and have a parallel arrangement. These two types of α grains are connected to each other. The second α lamellae appear to have lower orientation gradients than the primary α grains. The retained β phase was revealed as continuous network structures in 3D.

Another noteworthy 3D–EBSD study was conducted by Raabe, Rollett and co–workers to investigate the crystallographic characteristics of grain boundary planes in an ultra–fine grained Cu+0.17%Zr alloy that was processed by equal channel angular pressing and annealed for 10 minutes at 650 °C [Khorashadizadeh *et al.* 2011]. The experimental data was analyzed in three different methods, namely, the line segment method, the stereological method, and the triangular surface mesh method. The line segment and triangular surface mesh methods yielded identical outcome *i.e.* there is 7% area fraction of coherent twins in the microstructure. Thus Khorashadizadeh *et al.* highlighted the importance of using right data analyzing method in 3D–EBSD.

Extensive research using 3D–EBSD has been carried out Ferry and his co–workers at UNSW. They investigated the deformation and annealing characteristics of a cold rolled nickel alloy containing coarse (>1μm) silica particles [Xu *et al*. 2007b, Xu *et al*. 2007c]. This study highlighted the deformation structures surrounding non–deformable particle and their influence during recrystallization. The study also analyzed recrystallization in terms of particle stimulated nucleation (PSN), twin

formation during PSN and the growth behavior of various types of grain boundaries (an example is shown in Figure 2.28). In another study, the effect of material as a variable to ion beam damage was studied by recording EBSD pattern quality [Mateescu *et al.* 2007, 2008]. It was found that a relatively poor quality EBSD patterns was generated from metals of low atomic number after exposing to FIB damage of identical set of parameters. 3D–EBSD was also used to investigate the deformation [Quadir *et al.* 2007] and recrystallization [Xu *et al.* 2009] behaviour of IF steels.

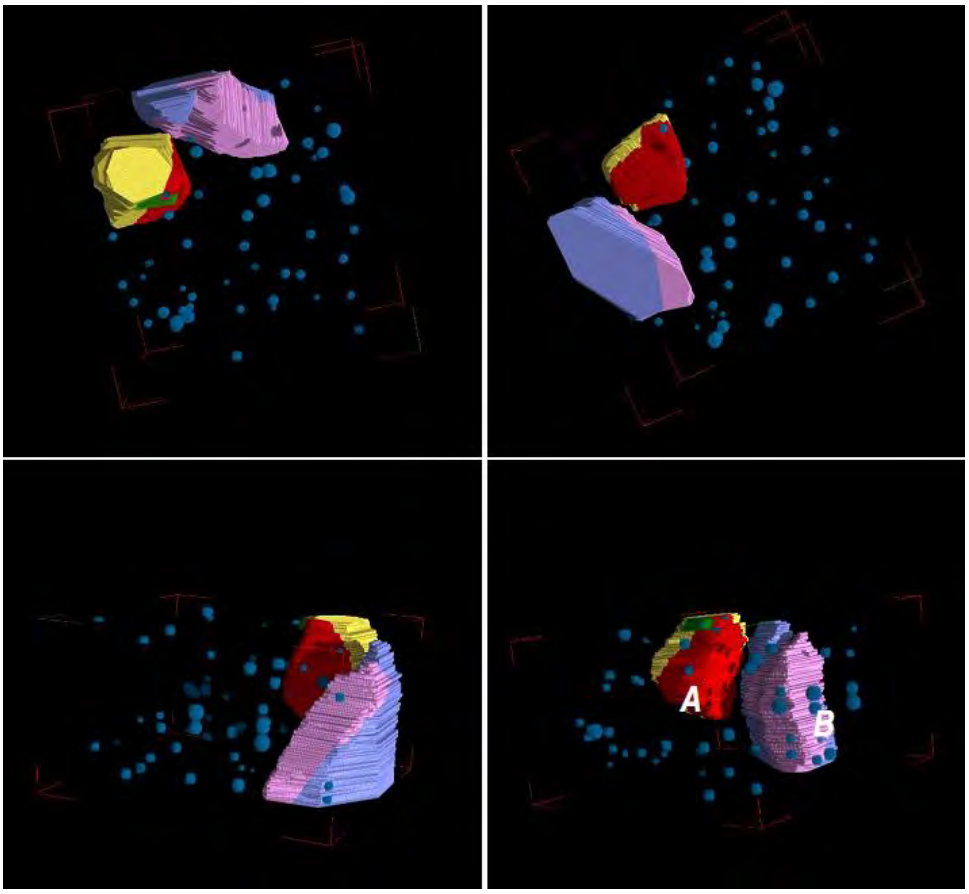

Figure 2.28: Reconstructed 3D–EBSD micrograph showing the spatial distribution of spherical silica particles and two groups of twinned grains (A and B) containing faceted interfaces, deformation substructure stripped for clarity [Xu *et al*. 2007c]

Very recently, Saowadee *et al.* [2012] investigated the effect of FIB current and accelerating voltage on EBSD pattern quality on yttria–stabilized zirconia and Nb–doped strontium titanate. These understandings were then utilized to optimize data quality and acquisition time for conducting 3D–EBSD experiments. They found that

reducing both FIB current and voltage significantly improved EBSD pattern quality (as shown in Figure 2.29). However, the effect was found to be very small for yttria–stabilized zirconia. As a final example, the 3D characteristics of fatigue crack growth in a titanium alloy were investigated by Birosca *et al*. [2009]. This investigation was coupled with x–ray tomography to identify the effect of prior β grain boundaries and crystallographic orientation of α lamellae on the crack trajectory. Figure 2.30 shows the 3D reconstructed images of cracks. In recent times, several research teams are trying to generate computer based automated code to handle huge amounts of data generated by 3D–EBSD. The work by the teams of Ghosh and Uchic [Groeber *et al.* 2008a–b], Bassman [King *et al*. 2009] and Rollett *et al.* [2007] are worth noting in this regard.

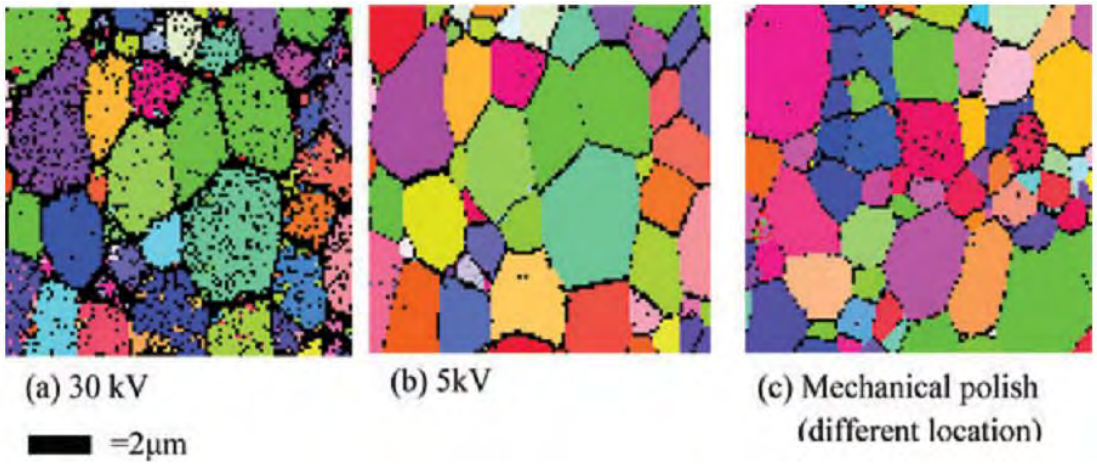

Figure 2.29: Inverse pole figure map of surfaces in the yttria–stabilized zirconia sample after milling with 30 kV and 5 kV FIB (without noise reduction). The non–indexed points (black dots) after milling by the 5 kV beam are almost only at grains boundaries. In the sample milled by 30 kV beam there are non–indexed points both at grain boundaries and inside the grains [Saowadee *et al*. 2012].

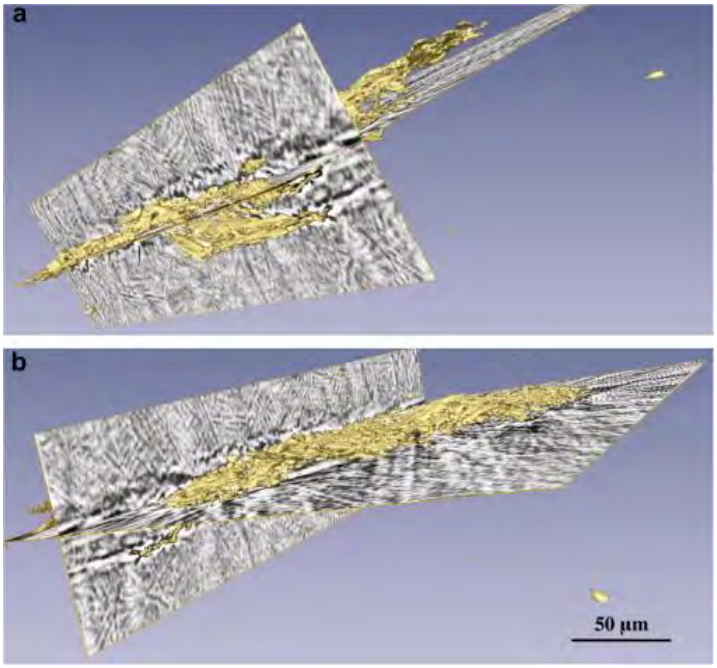

Figure 2.30: Ortho−slices showing microstructure Ti−6264 alloy in two dimensions with iso−surface to highlight the crack in three dimensions at different viewing angles in a and b [Birosca *et al*. 2009].

2.5 Summary and scope of thesis

3D structural analysis techniques are becoming increasingly important due to their capability to represent the true nature of a feature in an otherwise opaque material and eliminating speculation on how 2D images are translated into actual 3D structures. Among the various 3D techniques, 3D−EBSD has been shown to be an excellent tool for understanding the deformation and annealing behavior of metals. This technique utilizes a dual−beam platform consisting of a FIB and FEGSEM, including high resolution EBSD, to generate 3D crystallographic information within small volumes of material. Here, FIB is used for serial sectioning with a site−specific accuracy of ~50 nm with each consecutive ion milled layer mapped by EBSD. Using advanced computer algorithms, the entire EBSD dataset can be converted into 3D crystallographic volumes at submicron resolution. The major objective of this thesis is to utilize 3D−EBSD to intensively characterize the crystallographic nature of the deformation microstructures in high purity (fcc) nickel and IF steel (bcc). These metals were selected due to the extensive 2D literature base of their deformation behaviour.

In chapter 3, the experimental procedures is described, including the initial material processing methods and 3D–EBSD experimentation, *i.e.* sample preparation, data collection and 3D reconstruction. The 2D characterization methods used throughout the thesis, namely electron channeling contrast imaging (ECC), electron back scattered diffraction (EBSD) and transmission electron microscopy (TEM), are also described in this chapter.

The experimental results are divided into four chapters. Chapter 4 describes the 3D characterization of crystallographic orientations and structural irregularities of microband boundaries in a 30% plane strain compressed Goss–oriented Ni single crystal. Chapter 5 focuses on the early stages of microband formation in the same Ni single crystal but after PSC to a lower plastic strain (ε~10%). Chapter 6 reports the results of unusual characteristics of microband arrays in a 50% cold rolled IF steel, with Chapter 7 demonstrating the powerful use of 3D–EBSD in the study of the distribution of fragmented structures in grain boundary regions in the IF steel rolled to 75% reduction. Each chapter concludes with a detailed discussion of the results with Chapter 8 providing a concluding summary of all the major findings of the thesis.

Chapter 3

Experimental procedures

3.1 Introduction

This chapter describes the material processing methodologies and microstructural characterization techniques used in this thesis. This includes the methods for producing Ni and steel samples and deformation experiments, sample preparation methods, 2D– and 3D–EBSD data acquisition methods and 3D data reconstruction, and TEM characterization.

3.2 Sample processing and preparations

3.2.1 Goss-oriented Ni single crystals

Single crystal rods of high purity Ni (99.999 wt.% purity) were grown from the melt from <001>–oriented seed crystals using the modified Bridgman technique. The crystal orientations were confirmed by back reflection Laue X–ray diffraction to be within 2° from the ideal Goss orientation, *i.e.* {110}<001>. The crystals were carefully machined and ground to produce rectangular blocks of approximately 12×6×8 mm^3, and then were fitted into a channel die and deformed by Plane Strain Compression (PSC) at room temperature to 10% (ε=0.10) and 30% (ε=0.35) reduction in thickness. During deformation, the <110> and <001> directions of the crystal were aligned within ~2° to the compression and extension axis, respectively. The samples were deformed to their total strains in 5% increments using a combination of Teflon and MoS_2 as lubricant during each reduction. The deformation coordinates for PSC are equivalent to rolling, *i.e.* the normal direction (ND) and rolling direction (RD) of rolling are comparable to the compression and extension axes of PSC. Therefore, these rolling reference axes are used throughout the thesis, *i.e.* RD, ND and TD. A schematic view of the crystal orientation in the channel die is shown in Figure 3.1.

The as–deformed crystals were sectioned through their centre line along ND–RD plane using a low speed diamond saw. These surfaces were then ground on successively finer grades of SiC paper, followed by polishing with 3 μm and 1 μm diamond paste. Then, electropolishing was conducted at –20 °C in a solution containing 20% nitric acid in methanol using a DC voltage of ~17 V.

Samples for TEM were produced from the same section of the crystal by a two stage polishing method: mechanical thinning and electrolytic thinning. The mechanical thinning was done to produce 50–60 μm thick foils by polishing on successively finer grades (e.g. 1200) of SiC paper. Thin foils of 3 mm in diameter were punched with a Gatan disc punch device. The foils were then further thinned at –20 °C in the aforementioned solution using a TenuPol–5 electropolishing unit operating at 28V.

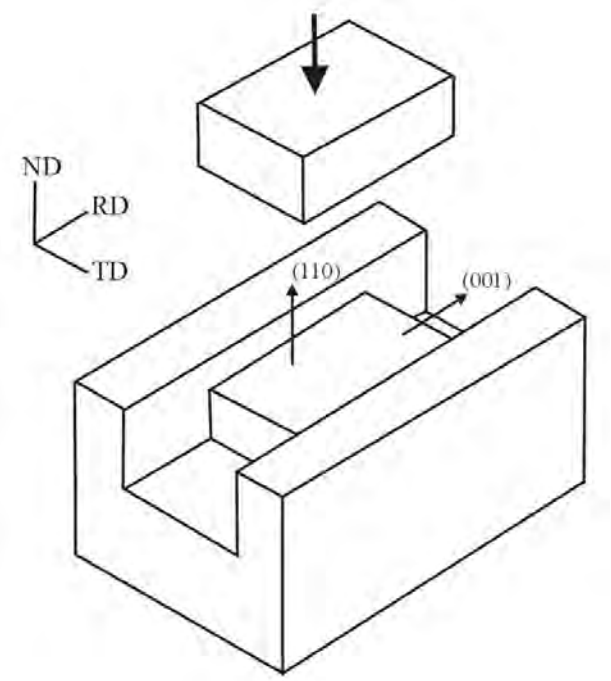

Figure 3.1: Schematic view of the Goss oriented crystal in the channel die.

3.2.2 Interstitial free steel

Interstitial free (IF) steel hot band of the chemical composition shown in Table 3.1 was homogeneously deformed under lubrication (10% reduction at each step) at room temperature to 50% and 75% reduction in thickness. The equiaxed grain structure of the hot band had an average grain size of 50 μm.

Table 3.1: Chemical composition of IF steel (wt.%).

C	Si	P	S	Mn	Ti
0.002	0.005	0.01	0.01	0.15	0.08

For microscopic characterizations, the polishing procedure was similar to that described for the Ni sample, *i.e.* the as–deformed sample was sectioned along the RD–ND plane and then mechanically polished followed by electrolytic polishing. The electrolytic polishing was carried out in a solution containing 10% perchloric acid and 90% acetic acid at –30° C and ~25 V.

3.3 3D–EBSD techniques

3.3.1 Selecting an area of interest

Prior to each 3D–EBSD investigation, the RD–ND section of the electropolished samples were thoroughly investigated by conventional EBSD to select a technically suitable area close to the edge of the sample. EBSD was conducted at 0.1 µm step size using a JEOL 7001 FEGSEM fitted with TSL EBSD detector, at 15 kV accelerating voltage, 2.1 nA beam current and 15 mm working distance. The acquired data was analyzed using TSL OIM^{TM} Data Analysis software.

3.3.2 Fabricating protrusion

For each selected area of interest, a rectangular protrusion was generated by FIB milling, for conducting FIB serial sectioning and concomitant EBSD. An outline of the procedure for fabricating a protrusion is given below:

The sample was mounted on a 45° pre–tilted holder using conductive silver paint. Prior to ion milling, the sample was tilted to 7° and focused at 5 mm working distance, where the eucentric height was also adjusted. Eucentric height is the height adjustment at which the sample's feature of interest remains focused (and almost no displacement occurs) when the stage is tilted or rotated. It is very important to achieve a good eucentric height set up, otherwise the beam will not be aligned correctly and the ion milling will not be done accurately.

The milling was conducted in several steps according to the schematic diagram shown in Figure 3.2. At the first stage, the surrounding material enclosed within the dotted lines in Figure 3.2a was removed using 20 nA milling current and 30 kV accelerating voltage. The accelerating voltage remains constant for remaining milling

steps. In the next stage, 7 nA milling current was used to remove material from the top surface and both sides of the area of interest, as shown in Figure 3.2b. The material from the bottom of the sample was then milled away using the same milling parameters. Overall, a considerable amount of surrounding material was removed for minimizing shadowing effects during EBSD mapping at the required tilt angle, *i.e.* 70°. After material removal, both the side walls and top surface of the protrusion were cleaned by 3 nA beam current. Three fiducial marks were milled on the side walls for enabling accurate stacking of the consecutive EBSD maps.

After shaping the pillar, 1 μm thick platinum layer was deposited on the surface facing the ion beam (purple colour in Figure 3.2c). The platinum layer helps to protect the sample from generating waterfall marks during milling on the EBSD surfaces. The deposition was done at 0.5 nA beam current. Prior to the platinum deposition, the eucentric height was rechecked. A FIB milled column is shown in the SEM micrograph in Figure 3.3, whereby the slicing direction and fiducial marks are indicated.

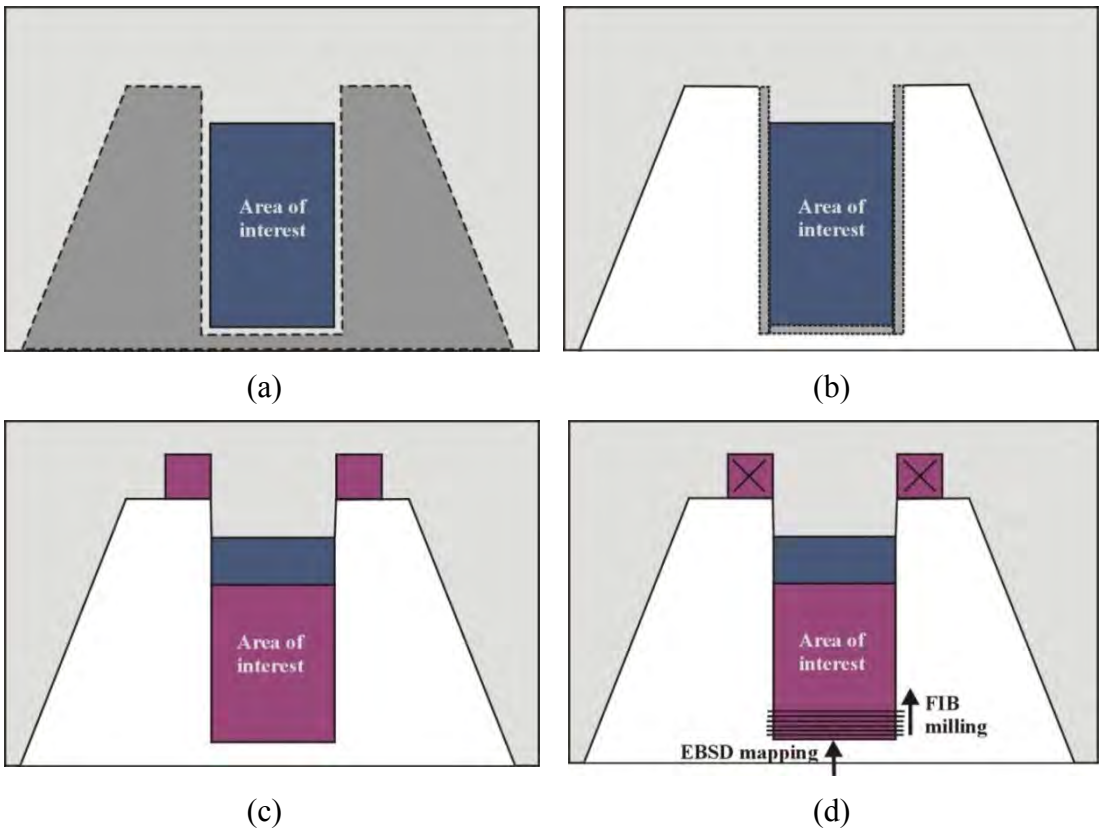

Figure 3.2: Schematic representation of the steps in fabricating a protrusion for 3D-EBSD.

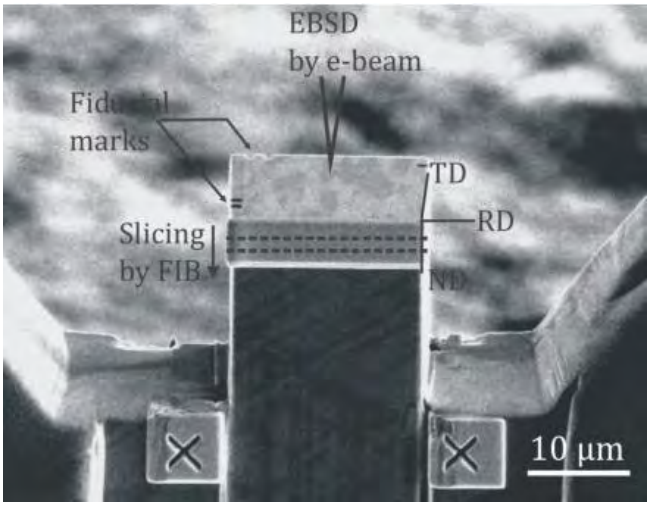

Figure 3.3: SEM micrograph of the protrusion showing the EBSD surfaces, the direction of slicing and fiducial marks on the side walls.

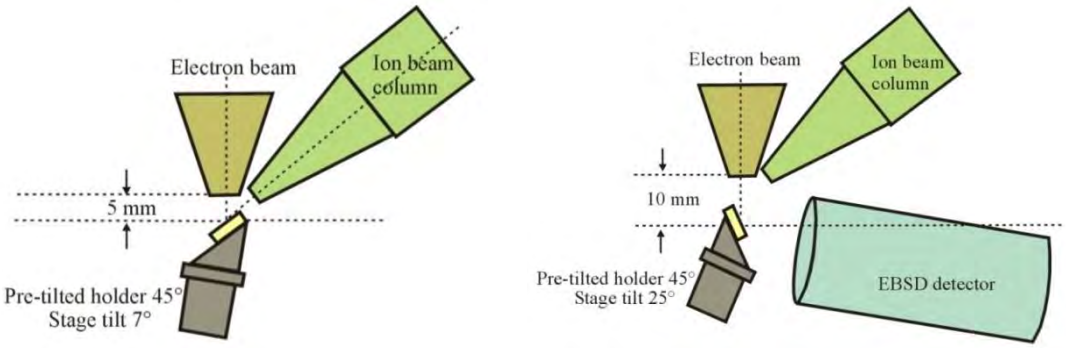

(a) (b)

Figure 3.4: Schematic diagram showing the: (a) FIB milling, and (b) EBSD data acquisition positions of the sample with respect to the ion beam and electron beam. [Mateescu *et al.* 2007].

3.3.3 Serial sectioning and EBSD data acquisition

Two 3D–EBSD experiments were conducted. The first one was done in a FEI Nova NanoLab 200 DualBeam™ platform interfaced with a TSL EBSD facility to investigate the 3D crystallographic features in microband boundaries in a Goss oriented Ni single crystal. The other investigation was done with the recently installed Carl Zeiss Auriga® Cross Beam® machine interfaced with a HKL EBSD system to investigate the deformation features across grain boundaries in a 75% cold rolled IF steel sample. This system is fully automated for acquiring 3D–EBSD data from many layers. In contrast,

conducting experiments with the FEI Nova NanoLab 200 DualBeam^{TM} required an in house computer script to be developed for establishing automatic movement of the sample between FIB and EBSD operation positions. The schematic diagrams in Figure 3.4 show the relative positions of the sample with the FIB and SEM beam, at the slicing (by FIB milling) and EBSD data acquisition positions. Two markers (crosses) were also milled for accurate positioning through image recognition capability of the system. Between two consecutive EBSD scans, milling was carried out by removing 0.1±0.01 μm material by a FIB which operates at 30 kV accelerating voltage, 3 nA current and 5 mm working distance. The sample was then rotated to 180° and tilted 25° to orient the milled surface at 70° to the electron beam for EBSD data acquisition. The EBSD acquisition was conducted at 0.1 μm step size, 10 kV accelerating voltage, 2.1 nA beam current and 10mm working distance. This cycle was repeated to produce 68 and 45 data slices for the Ni and IF steel sample, respectively. The series of ion beam micrographs are shown in Figure 3.5; these were taken after every 15 cycle milling operations on the Ni sample during serial sectioning.

3.3.4 3D reconstruction of EBSD slices

The EBSD data acquired from the aforementioned method were analysis using TSL OIM^{TM} data analysis software. The orientation maps of each slice were further processed in Corel draw to plot the misorientation boundaries in 2D. During Corel manipulation, special care was taken to maintain the dimensions of all the slices in terms of size and shape. Thus the pixel size (size/resolution) for each processed image was kept consistent. The slices were also stacked very carefully by placing the fiducial marks on the top of the preceding slice. Using Avizo Fire 7.0 software the Corel processed slices were reconstructed in 3D. The 3D reconstructed micrographs and movies were recorded from different angles and with different clipping planes and trajectories.

3.4 Microstructural Analysis

3.4.1 Scanning electron microscopy (SEM)

Two dimensional SEM analyses were carried out using a JEOL 7001F FEGSEM, which also has a TSL EBSD detector. The SEM samples were prepared by conventional metallographic techniques, as described in sections 3.2.1 and 3.2.2. High resolution SEM images were recorded in electron channeling contrast (ECC) imaging mode. In ECC mode the electron signal varies as a function of crystallographic orientation and, as a result, an image appears in gray scale contrast [Knudsen 2008, Prior *et al.* 1999, Day *et al.* 2004]. The ECC images were used for selecting suitable areas for orientation measurement by EBSD scanning. EBSD was conducted at 10–15 kV accelerating voltage and 15 mm working distance. The acquired EBSD data was analyzed using TSL OIM™ 5.2 analysis software. Prior to each analysis, a data cleaning procedure was used to remove orientation noise and non-indexed points.

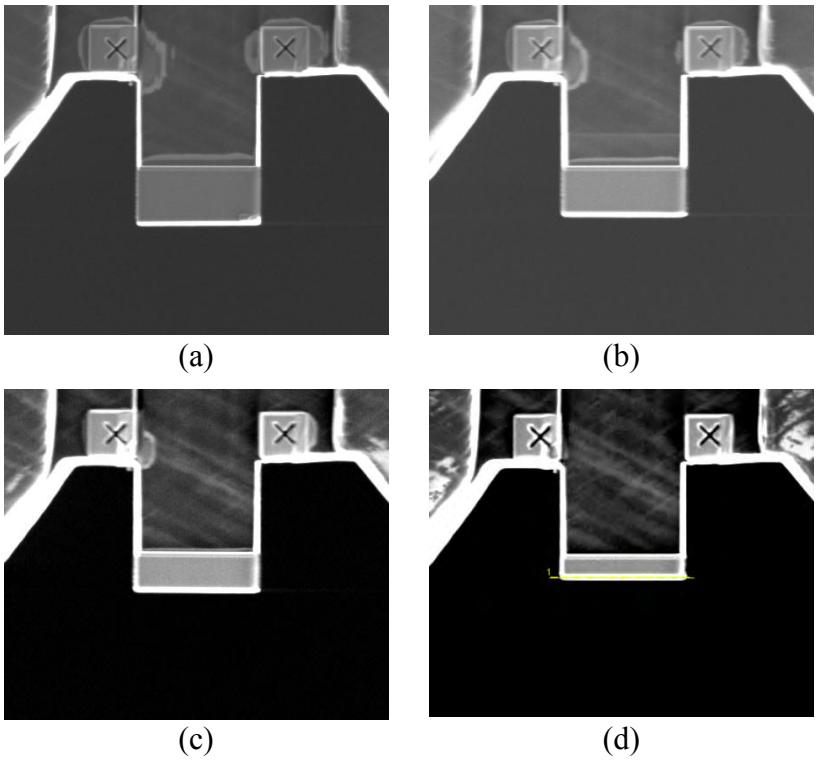

Figure 3.5: FIB micrographs of the protrusion showing the precision of milling after: (a) 15, (b) 30, (c) 45, and (d) 60 milling cycles.

3.4.2 Transmission Electron Microscopy (TEM)

TEM investigations were carried out in Philips CM 200 and FEI Tecnai G2 20 machines, operating at 200 kV accelerating voltage. Both microscopes were equipped with double tilt sample holders with ±30° tilting capacity. Orientation measurements were achieved using the appropriate diffraction techniques: convergent beam electron diffraction (CBED) and selected area diffraction (SAD) [Knudsen 2008].

Chapter 4

Result and Discussion–Part I

Crystallography of microband structures in a deformed Goss–oriented Ni single crystal

4.1 Introduction

As discussed in section 2.2.2, a microband (MB) is a lenticular–shaped microscopic feature that evolves by arranging the deformation–induced dislocations into wall–like structures [Humphreys and Hatherly 2004]. These walls take a parallel arrangement at ~1 μm repeat distances and, between them, the material is almost dislocation free [Hughes and Hansen, 2000]. Microbands have been characterized in substantial detail by the Risø group [Bay *et al.* 1992, Hughes and Nix 1989, Hughes and Hansen 1993, Huang and Hansen 1991, Hansen and Juul Jansen 1992, Winther *et al.* 1997, Winther *et al.* 2000] where a major finding is the alignment of their boundaries with highly stressed slip planes. This observation has been made in many alloys systems [Godfrey *et al.* 1998, Winther *et al.* 2004, Lin *et al.* 2009] thereby leading these workers to conclude that microbands are crystallographic in nature. Other researchers [Chen *et al.* 2003, Jackson 1983] have investigated fundamental aspects of microband formation by studying the dislocation configurations at low strains with their results supporting the Risø findings. However, other studies using EBSD have indicated that microband boundaries may be non–crystallographic [Hurley *et al.* 2003, Humphreys and Bate 2007, Albou *et al.* 2010]. Here, microband boundary traces were rarely found to resemble perfectly aligned crystallographic parallel lines but, instead, 5–10° deviations between the boundary traces and the nearest crystallographic slip planes were found. Another anti–crystallographic argument arose from the observation that microband boundaries appear wavy when viewed in the RD–TD section [Hurley *et al.* 2003, Humphreys and Bate 2007]. Based on crystallographic arguments, however, it was shown that microbands are closely aligned with a crystallographic slip plane in a cold rolled sample and, with increasing deformation, they rotate away around the TD [Huang and Winther 2007, Winther and Huang 2007].

Recent developments in 3D–EBSD have enabled these deformation features to be reconstructed within a 3D volume, hence, their crystallographic nature can be better understood. This chapter is focused on a 3D–EBSD investigation of microband structures in a Goss–oriented Ni single crystal deformed at room temperature by PSC to $\varepsilon = 0.35$ (30% reduction in thickness).

The type of metal, crystal orientation and deformation mode were selected due to the following advantages:

- Goss–oriented face centred cubic (fcc) crystals deform on four well characterized {111}<110> slip systems [Dorner *et al.* 2007, Liu *et al.* 2001];
- the substructure in Ni remains stable at this low homologous temperature, since dynamic/static recovery is not prevalent [Humphreys and Hatherly 2004], and
- there are no neighboring grains that can affect the mode of deformation [Humphreys and Hatherly 2004].

4.2 Two dimensional EBSD study

Figure 4.1a presents a typical electron channeling contrast (ECC) micrograph of the RD–ND section of the as–deformed crystal showing two sets of intersecting microbands in grey scale contrast. One set of microbands is more predominant in the micrograph with both sets inclined at ±30±5° to the RD. For both sets of microbands, there are offsets in the boundaries thereby indicating that the most predominant set has formed earlier in the evolution sequence. The microband boundaries are more defined in the first set with the boundaries of the second set more smeared due to the action of the former. An EBSD map was generated and shown in Figure 4.1b. The black lines along the microband boundaries correspond to orientation differences between two points on each side of the microbands greater than 1.5°, and small segments of these boundaries are misoriented up to 12° although, in general, there are distinguishable lengths (4–5 μm) remaining below 3°. The less predominant set of microbands do not have well–defined boundaries resulting in a gradual orientation profile. It is notable that the superimposed alternating solid and dotted lines are parallel to the second weaker set of microbands. The dotted line intersecting the first set of microband boundary segments have misorientations less than 1.5°, whereas the solid line intersecting the microband boundaries have misorientations greater than 1.5°.

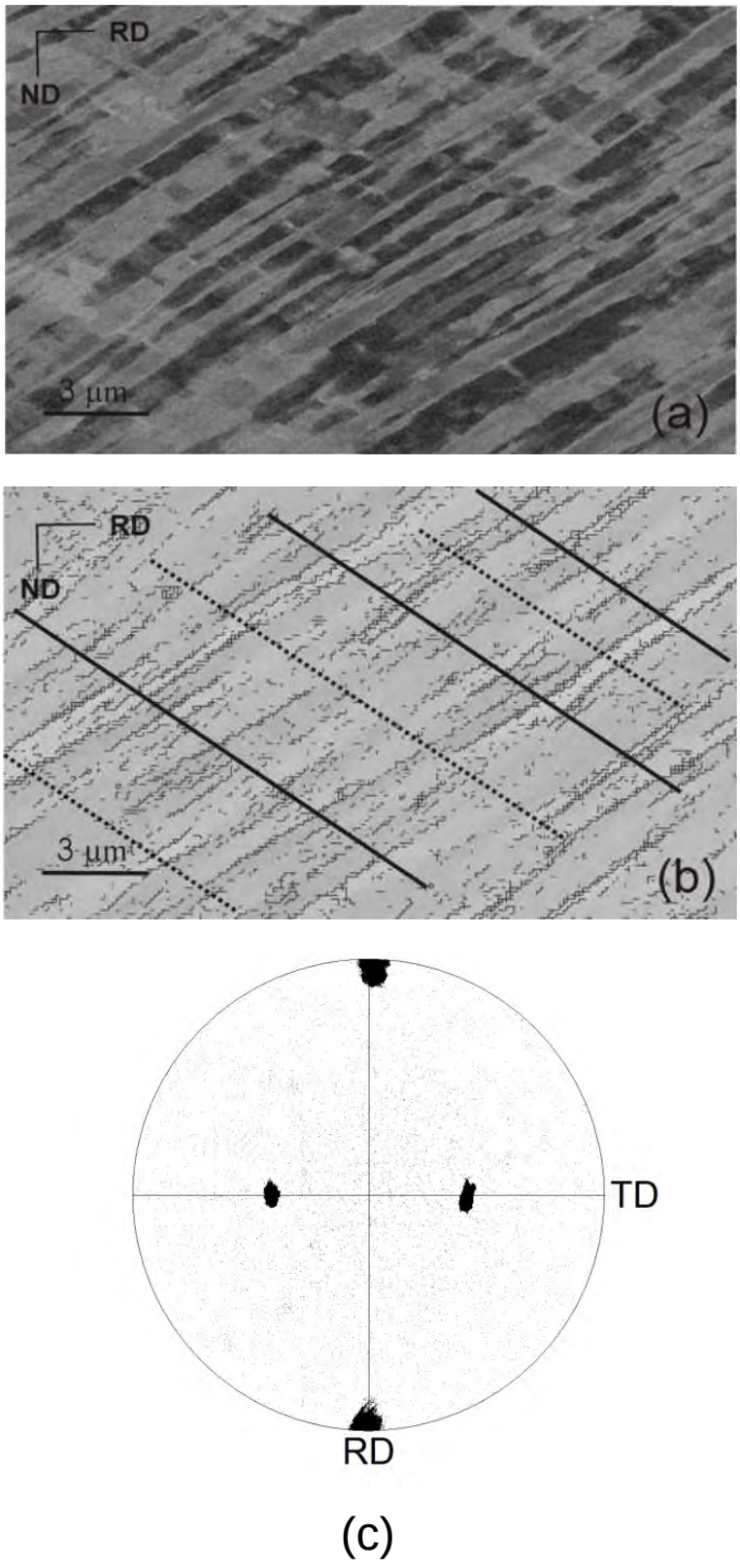

Figure 4.1: (a) SEM channelling contrast micrograph and (b) EBSD micrograph of the RD–ND section of 30% deformed Goss-oriented Ni crystal showing typical microband structures. (c) <001> pole figure of the orientations of the scanned area shown in (a).

A plot of the <001> pole figure showed that the average orientation of the EBSD map is centered at Goss with a spread of ±3.5° along the ND–TD trace and ±7.5° towards the RD (see Figure 4.1c). It is well known that microband boundaries are the principal features for accommodating the measured orientation spread in this type of deformation microstructure. There is also a small variation in orientation within the width of a typical microband, as observed by both EBSD and convergent beam electron diffraction (CBED) in TEM. However, there is significant orientation variation along the length of a given microband, as shown in Figure 4.2a where the orientation change along the length of the microband (see inset) is plotted. Here, orientation varies periodically along the microband length with a maximum range of ~4°. The distance between peaks also varies, with Figure 4.2a showing peaks at intervals of 14 and 32 μm, respectively.

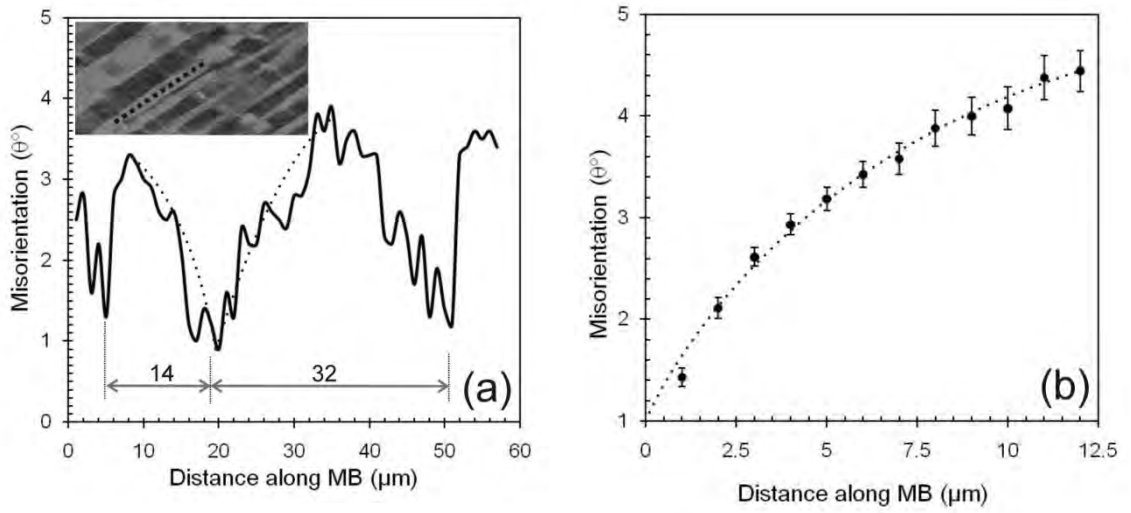

Figure 4.2: (a) Orientation profile (cumulative misorientation) along the length of a microband, and (b) the average profile of 100 microbands in which the misorientation gradually builds up (the error bars represent the standard deviation).

Within a cycle there are also smaller cycles accommodating orientation changes of less than 0.5° and these are likely to be the interior cell boundaries observed in the complementary TEM investigation. In Figure 4.2a, the dotted lines denote the trend between the peaks and troughs in orientation along the microband. This type of analysis was carried out for 100 microbands and plotted in Figure 4.2b showing clearly the general trend of cumulative misorientation along the microband length. In this plot, the

number of data points varies significantly with increasing distance along the microband. For distances greater than 6–7 μm, the number of data points is considerably reduced, thereby indicating that this trend generally continues in 6–7 μm along the microband length.

4.3 Three dimensional EBSD study

4.3.1 General structure and three dimensional features in microbands

In a typical EBSD slice, when viewing the RD–TD surface, the microband boundaries appear as curved profiles in short segments (Figure 4.3a). The deviations of the short segment boundaries are up to ±15° from the TD, although, on average, they are aligned parallel to the TD in low magnification images. These observations are consistent with other investigations on steel, Ni and Al(Si) alloys [Hansen and Juul Jensen, 1992, Hurley *et al.* 2003, Duggan and Tse 2004, Quadir *et al.* 2007]. Once again, similar to Figure 4.1c, the largest deviation from the ideal Goss orientation was ±8°, as shown in the combined (all 68 slices) <100> pole figure in Figure 4.3b, in which only a single <100> pole is shown for clarity. The ±8° orientation spread from a single point in the pole figure is generated during deformation and is accommodated by the deformation microstructures containing microband interiors and their boundaries. A careful analysis of all slices showed that the misorientations along microband boundaries are generally in the range 1–4°, with some rare cases of misorientations up to 7°.

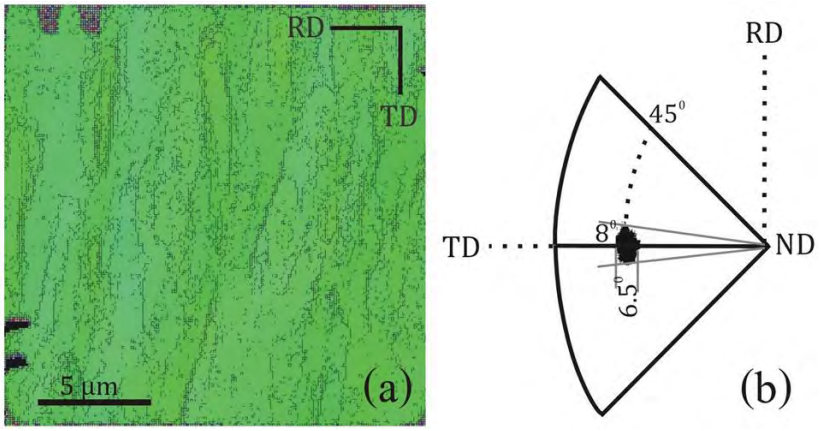

Figure 4.3: (a) EBSD map of a typical RD–TD section showing the ≥1° misorientation boundaries, and (b) a [100] pole of a combined <100> pole figure from the 68 slices showing the maximum orientation spread due to channel die PSC.

For 3D reconstruction, the analyzed EBSD maps were processed in Corel draw to plot the boundaries in 2D. Using Avizo Fire 7.0, which is capable of stacking the slices precisely in 3D, the Corel processed slices were reconstructed. The resulting volume of microstructure is shown in Figure 4.4, from which the newly reconstructed ND–RD and ND–TD cross sections are shown. It can also be seen that the pair of fiducial marks are well aligned after 3D reconstruction of the dataset. The microbands in this section are aligned parallel to TD with some deviations, as found elsewhere [Chen *et al.* 2006, Quadir and Duggan 2006]. It is pertinent to note that, in the ND–TD section, the microbands have a complex arrangement and, therefore, is not the ideal section for analyzing their boundary alignment [Winther *et al.* 2004]. It is significant to note that, in the ND–RD reconstructed section (Figure 4.4), the microbands show their classical form consisting of straight edges aligned ~35° to RD.

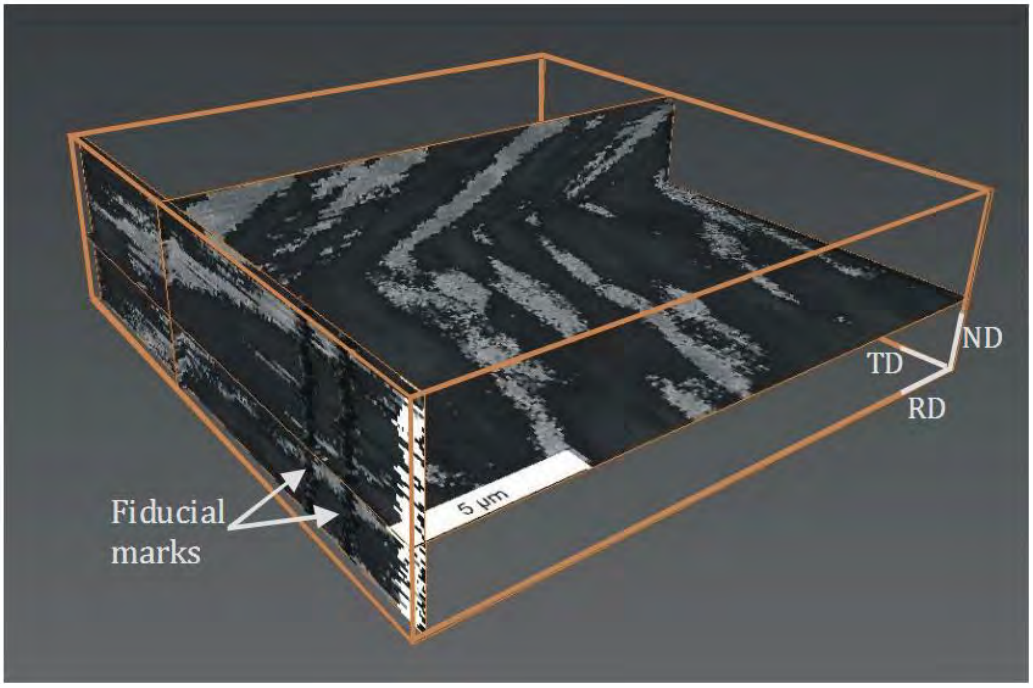

Figure 4.4: 3D reconstruction showing well–aligned fiducial markers and microband boundaries in their typical alignments with RD.

Reconstructing a given microband within the analyzed volume was found to be challenging because, in many cases, only short segments of each boundary were well–defined. Here, the boundaries often merged/split or changed into boundaries across which the misorientation is not sharp and in those locations it was difficult to delineate the boundaries in the consecutive EBSD slices. It is also to be noted that a

small orientation gradient (<3°) was found along the width of the microband. A part of which might arise from the angular resolution limit (~1°) of the EBSD technique. That is why the misorientation between the centre points of two neighboring microbands was measured higher than the misorientation across the separating boundary between them. The centre–to–centre orientation varied in the range 2.5–7°, whereas the misorientation of the boundaries was varied in 2–5°. During the process of finding a boundary both centre–to–centre and across the boundary was considered.

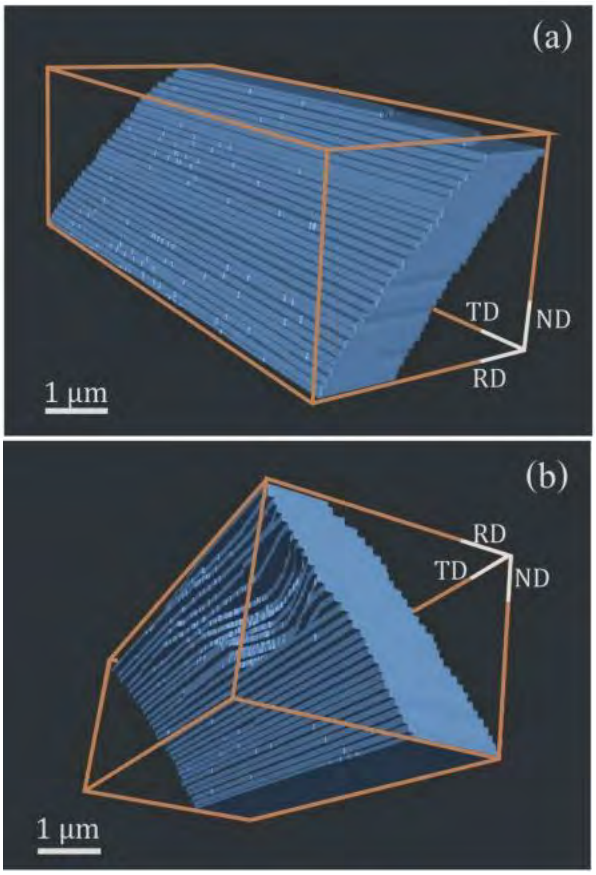

Figure 4.5: 3D image of the (a) front and (b) rear projection of a reconstructed microband in ND–RD section.

Two well–defined microband boundaries (microband 1 and 2) were selected for detailed analysis and the results of one microband (in Figure 4.5a) shows its surfaces to be largely planar (the surface steps are caused by the serial sectioning procedure where only low–level smoothing was carried out). An interesting feature of Figure 4.5b is the indented region on the flat surface of microband 2. Sectional view of that microband in Figure 4.6a–c is showing that the large curved segment is present in Figure 4.6a which

is gradually diminished in the later segments in Figure 4.6b–c. In Figures 4.6d–f, cross–sectional images of another microband are shown to demonstrate that curving in the microband boundary is common, although these are less intense in this microband surfaces. An investigation of the contiguous 2D–EBSD maps showed that this indented region corresponds to the curved profile boundaries in RD–TD sections.

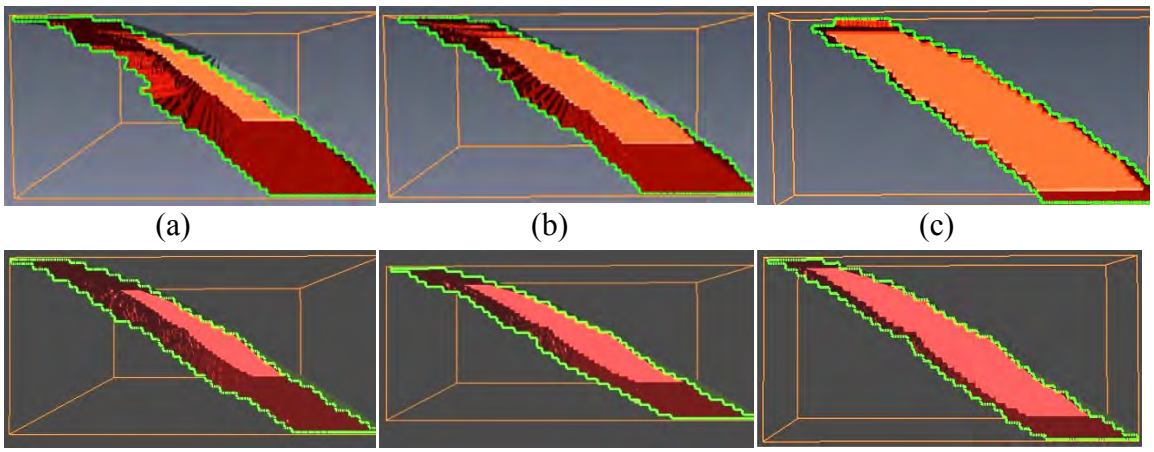

Figure 4.6: The edges of the reconstructed microband boundaries are shown in various segments in the 3–D skeletons. RD→ and ND↑.

The angle of inclination of the microband surfaces with respect to the crystal axes were found to vary from 37 to 45° with RD, Figure 4.7a–d. Part of this variation is probably due to the difficulty of EBSD in identifying the very low angle boundaries (<1°) between the two boundaries, at the merging/splitting locations. This is because when a boundary divides in two, one of them was often found to be of very low angle, as confirmed by a complementary TEM investigation. Recovery may also be a major reason for the deviation from the straightness of a boundary. The indented region of Figure 4.5b is probably relevant to the curving of microband boundaries by the operation of a second set of slip systems, which turns the existing set of microband into its operation direction. It is noted earlier, both (111) and $(11\bar{1})$ planes are predicted to be equally operative in a perfectly–oriented crystal of Goss orientation during PSC [Humphreys and Hatherly 2004, Ferry and Humphreys 1996a–b]. However, a slight deviation of the crystal from the ideal orientation resulted in preferential slip on one of the two possible {111} planes.

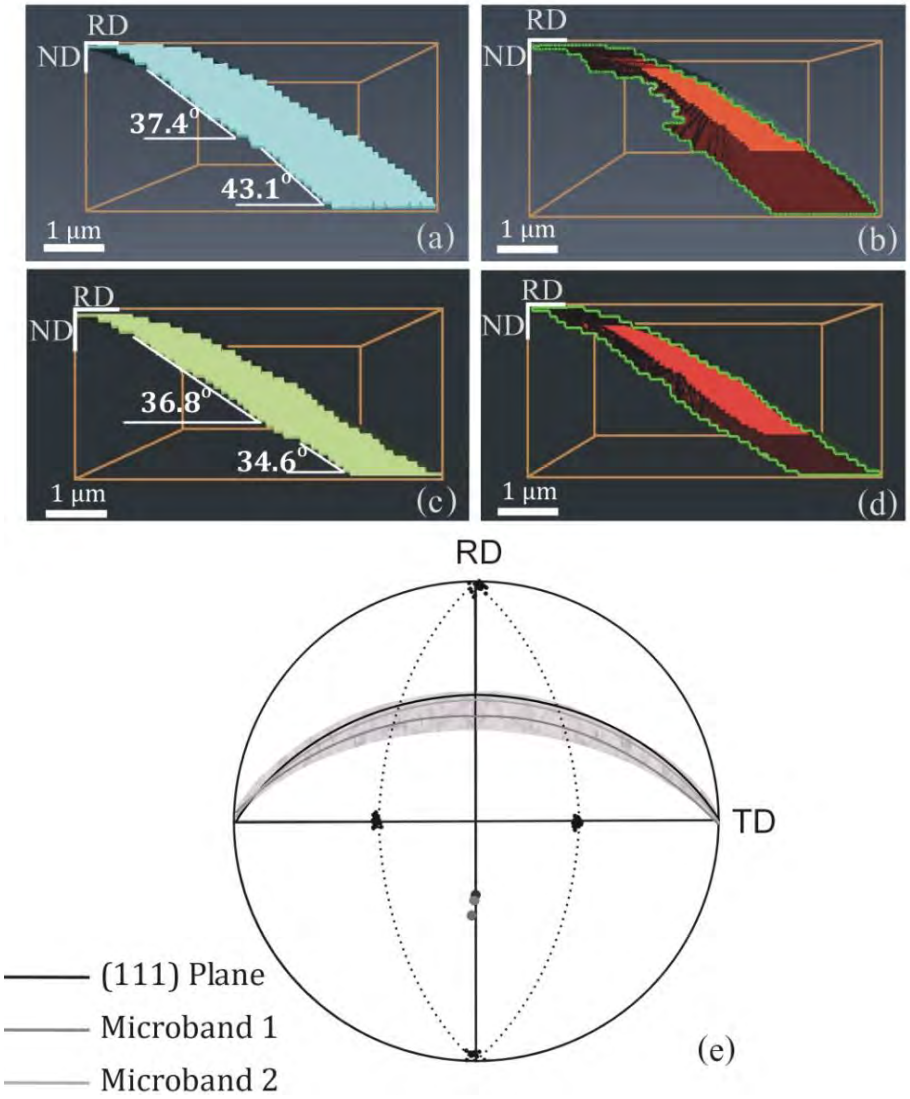

Figure 4.7: ND–RD sections through the two reconstructed microbands (a–b is microband 1 and c–d is microband 2). (e) Stereographic projection showing both the traces and normals of the range of orientations of the microband surfaces. Superimposed on the projection is both the trace and normal of the nearby (111) slip plane.

The shaded traces in Figure 4.7c correspond to the range of orientations of the microband surfaces 1 and 2. It can be seen that the surfaces of microband 2 coincides closely with the operative slip plane whereas the surfaces of microband 1 are inclined more closely to the plane of maximum resolved shear stress, that is, 45° to RD. Crystallographic and non–crystallographic variants of microbands have been discussed in various studies [Bay *et al*. 1992, Albou *et al.* 2010]. In an early investigation, Bay *et al.* [1992] showed the evidence of both kinds as a function of orientation of the

deforming grains in the same sample. Recently, Albou *et al*. [2010] showed that, in Al–Mn alloys, the crystallographic alignment of microbands was facilitated at low deformation strains (<0.15) by the solute content. In their study, microbands started to align along crystallographic slip planes at moderate strains and again become non-crystallographic by aligning along RD at higher strains when typical lamellar bands were formed. The present work demonstrated that small segments of a given microband boundary are approximately aligned parallel to the highly stressed crystallographic slip plane, although it was also found that surface irregularities may be associated with that microband [Quadir *et al.* 2007].

As the above information was limited to small segments of a given boundary, it was deemed necessary to extend the investigation to a larger volume of material containing numerous microbands. The reconstructions in 3D are shown in Figure 4.8a and b, in RD–ND and TD–ND projections. There are 35 microbands in this volume and each of them were constructed by outlining >1.5° misorientation boundaries. It is important to note that, among the two microband sets only the predominant set is plotted because the second set experiences extreme fragmentations to small segments and therefore it is difficult to trace the connectivity between them over a reasonable distance of several microns. It should be noted that the microbands in Figure 4.8 are not perfectly flat. They contain various degrees of undulations. In the RD–ND projections (in Figure 4.8a) sharp curvatures are obvious. However, it is still possible to find the average alignment of these traces with the RD, which vary between 30 to 35°. When microbands are viewed in the TD–ND projections, Figure 4.8b, the traces were found to be aligned along the TD. However, in some cases these traces were found to have up to a 12° inclinations with TD.

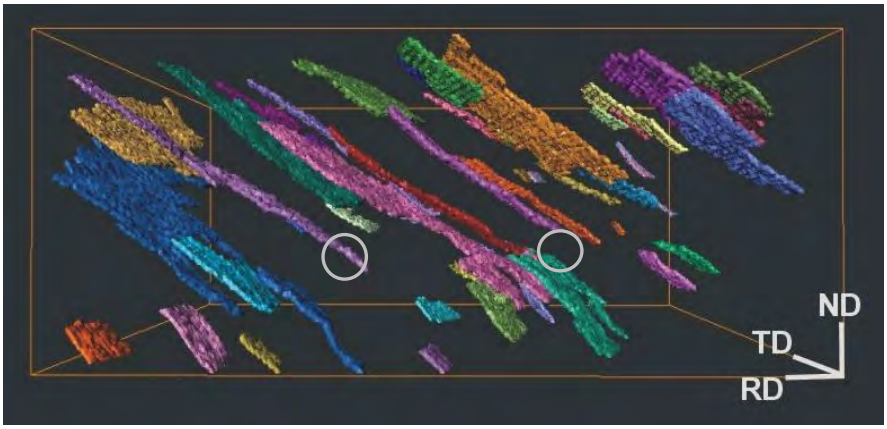

(a)

(b)

Figure 4.8: 3D reconstruction of 35 microband boundaries (at >1.5° misorientation) showing their inclinations and curvatures when viewed from (a) RD–ND section and (b) ND–TD section.

A closer inspection of the microband surfaces reveals many curved features (circled); this makes it difficult to assign a local normal at every position along a given microband boundary surface. Hence, the average alignment of a given microband was taken as the best fit of a flat surface and these data are plotted (×) in the <111> pole figure in Figure 4.9. Of the 25 reconstructed microbands, 20 surfaces are aligned within 5° of the $[11\bar{1}]$ pole of the original Goss orientation, that is, close to the $(11\bar{1})$ slip plane. While the averaged microband normal fall close to this $[11\bar{1}]$ pole, it is clear that the curved segments of many microbands (some are circled in Figure 4.8a) deviate from this orientation. These rotated microband segments appear to be the connecting bridges between the parallel segments of adjacent microbands.

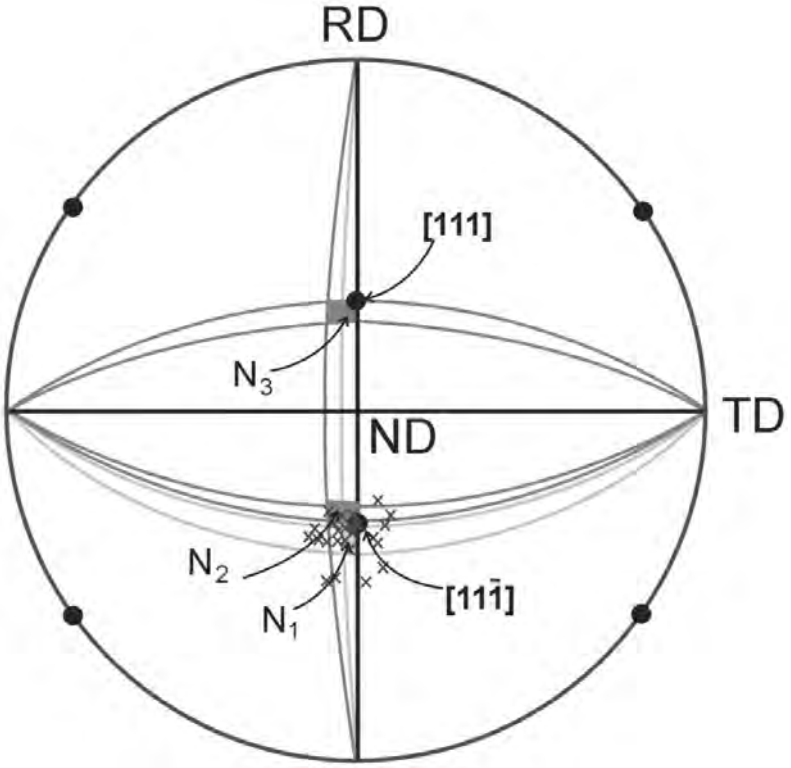

Figure 4.9: <111> pole figure showing the plot of the average normal of the 25 microband boundaries (× symbols) showing their close proximity to the [11$\bar{1}$] pole of the Goss orientation ((110)[001]). The average normal of the flat segments of the microband boundaries in Figures 4.11 and 4.12 are also plotted from their traces as N1, N2 and N3 (in the shaded ranges), to show their close correspondence with the poles of {111} potential slip planes.

The curvatures on the microband surfaces create larger local deviations from their crystallographic alignments. Among the reconstructed microbands in Figure 4.8, two examples were extracted to represent a flat and curved microband surface (see the example of the flat surface in Figure 4.10a). On each surface, the normal of 2×2 μm^2 segments were measured and plotted in the upper half of <111> pole figures to show their coincident, Figure 4.10b and c. The data points from the flat surface (in Figure 4.10b) have a small spread of ~7°. In contrast, a larger spread (~20°) is found between the points of the curved boundary interface, Figure 4.10c. In this figure one point is singled out, and excluding this point the deviation is ~15°. This matter also indicates that the highly deviated points originating from intense local curvatures may be due to the interactions by the second set of microbands. The segments in the flat surface nicely coincide with the {111} slip plane whereas there are TD rotations in the data points

from the curved surfaces. This can therefore be treated as a 3D evidence of the theory proposed by Withter *et al*. [2004], which describes microband surfaces deviating from crystallographic orientations by rotating away around the TD axis.

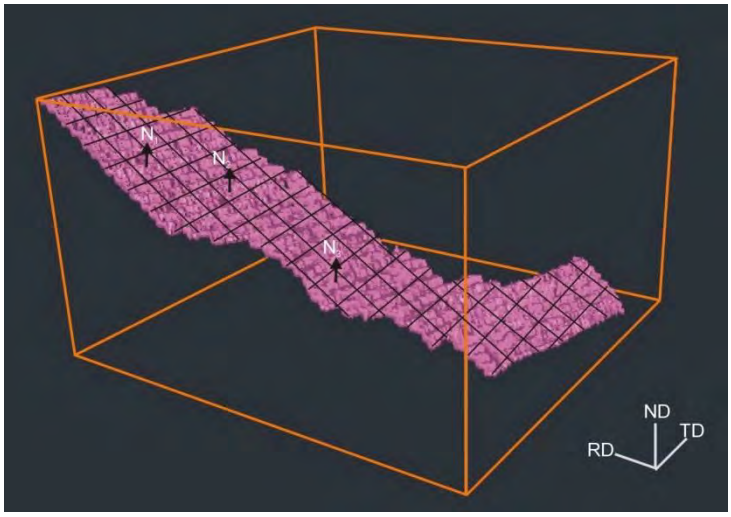

(a)

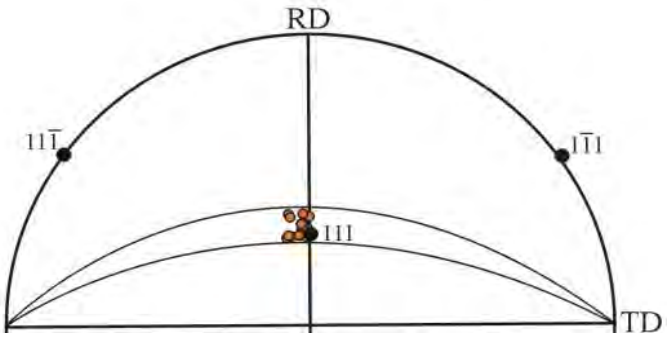

(b)

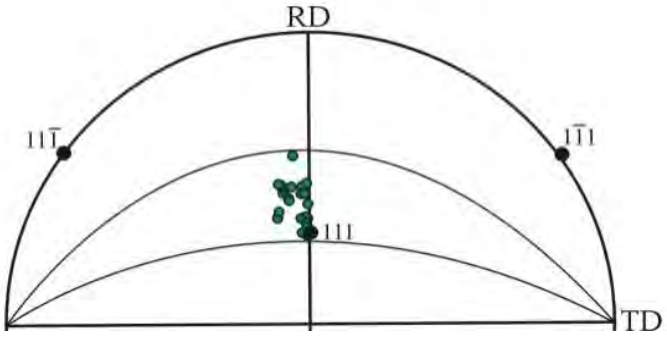

(c)

Figure 4.10: Example of a (a) flat microband interface. <111> pole figures showing the normal of the segments in (b) flat and (c) curved surfaces.

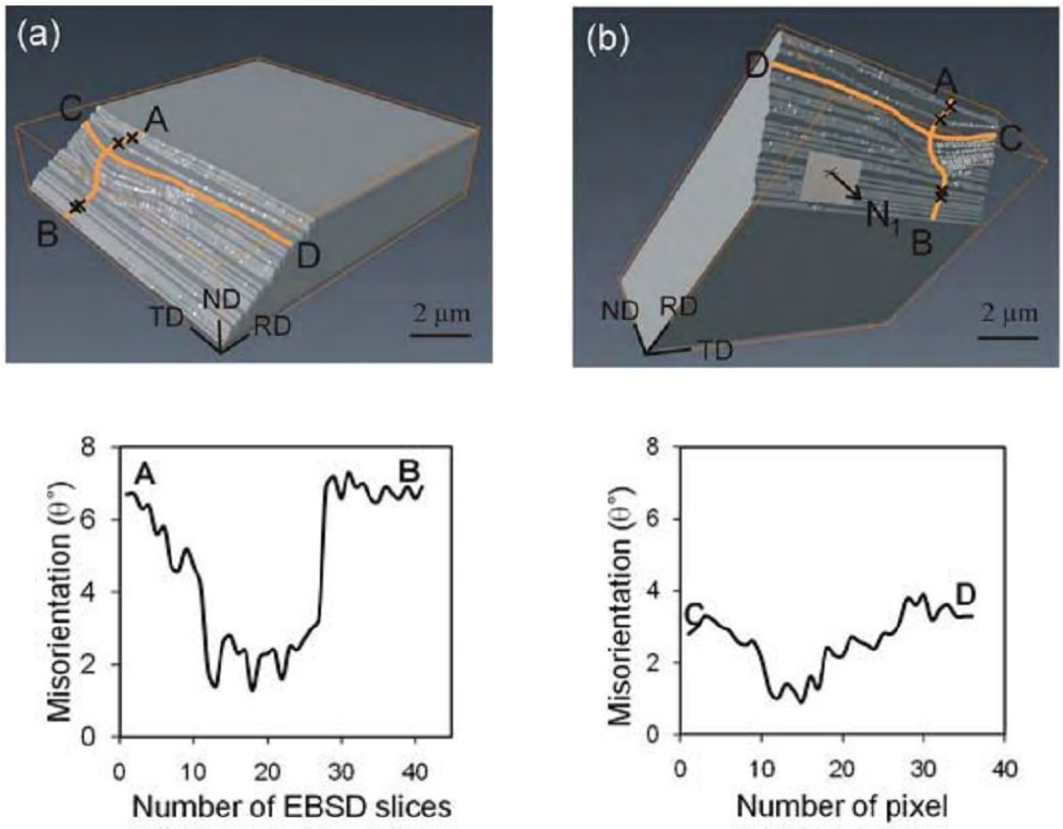

Figure 4.11: 3D-EBSD reconstruction showing a dented structure in a microband boundary interface. The misorientation profile is between the neighboring points, across the interface, along the A–B and C–D lines. N1 represents the average normal of the flat segment of the boundary interface.

The misorientation across each microband boundary was found to be reasonably uniform along a straight segment, but altered locally due to the irregularities in the form of bumps and curves. Evidence of these boundary features were also revealed in a recent 3D–EBSD investigation of cold rolled polycrystalline iron [Quadir *et al.* 2007]. In the present study, a microband–containing reconstructed block is split along the microband boundary interface (of that in Figure 4.5b), as shown in Figure 4.11a and b. The steps in the image are a result of analyzing the raw data (no boundary smoothing) and correspond to the thickness (100 nm) of each ion–milled layer during serial sectioning. Figure 4.11 shows the plot of misorientation data across the microband boundary, at each point in line A–B and C–D, through these undulated regions. Across the boundary points on A–B, misorientation increases by up to 7° in the flat region then

decreases to 2° in the undulated region, and along C–D, misorientations are ~4° in the peripheral region (which is almost flat) of the dent and decreases to ~2° near the centre of undulated region. The intersecting point of A–B and C–D is the same data point and, hence, the misorientation is equal. The low misorientations across the points in/near the undulated region are extended in C–D than A–B and, thus, it is demonstrated by this 3D–EBSD analysis that an asymmetry in misorientation exists in association with the undulations. It is worth noting that, since the distance between adjacent EBSD maps by serial sectioning is 100 nm, the irregularities in the boundary surface result in non–uniform distances between consecutive data points along A–B in Figure 4.11 (*i.e.* the distance between points between the two layers at A (marked) is much larger than at B). This serial sectioning effect is not an issue along C–D.

Table 4.1: The misorientation spread towards RD and TD (in <110> pole figures) over ~8 μm distance in undulated and liner region of the same microband.

Slices	Misorientations spread (°)			
	Linear region		Undulated region	
	along RD	along TD	along RD	along TD
1	4.96	3.25	3.73	4.04
2	4.91	2.74	3.47	4.22
3	5.79	2.78	3.21	4.82
4	5.50	2.86	4.48	4.20
-----	-----	-----	-----	-----
-----	-----	-----	-----	-----
Average	5.50	2.80	4.00	4.50

The orientation spread along the length of the microband through the bumped region in Figure 4.11 was measured over a distance of ~8 μm. This was carried out on several slices. Table 4.1 shows representative data from other EBSD slices as well as the averages from many slices. Along the undisturbed region of the microband, the average orientation spread towards RD (5.5°) is almost double than that towards TD (2.8°). However, the undulated region shows a larger orientation spread towards TD (4.5°), and very close to the spread towards RD (4.0°). The average normal direction

(N1) of the overall microband surface in Figure 4.11b is shown in Figure 4.9 to be close to [$11\bar{1}$], thereby indicating a close coincidence with one of the {111} slip planes.

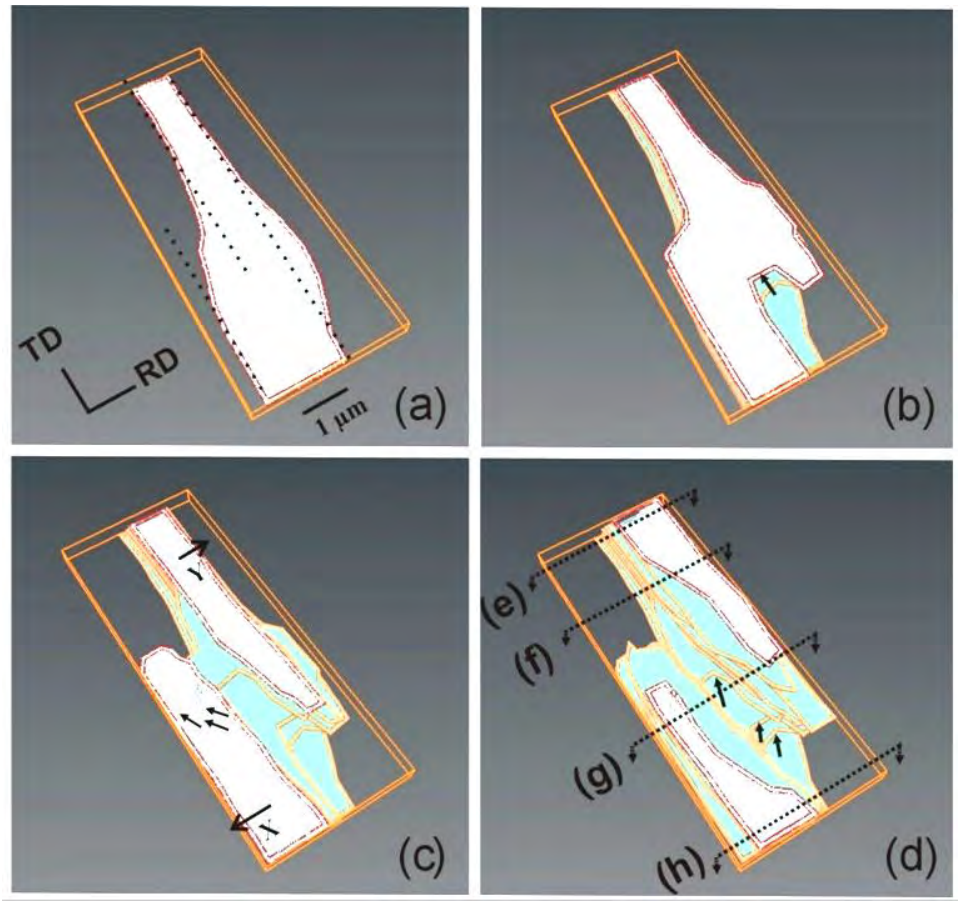

Figure 4.12 a–d: Cross–sectional images in the TD–RD section from a 3D–EBSD reconstructed volume showing the complex curvatures in the microband boundary and splitting/merging events.

4.3.2 Nature of the interactions between non-coplanar microbands

The intersection of two sets of microbands was also studied in this investigation. Figures in 4.12a–d show a series of sections through a small reconstructed volume. The consecutive sections in 3D clearly reveal the complicated nature of microbands showing splitting/merging events not clearly revealed in standard 2D EBSD maps. The first EBSD slice in Figure 4.12a, as viewed in the RD–TD cross section, shows two boundaries of the microband having both straight and curved segments. For the right–hand boundary, the straight segments (represented by dotted lines) are aligned

parallel to the TD and there is a curved segment near the middle. For the left–hand boundary, there are two straight segments aligned parallel to the TD connected by a curved segment. For the right boundary, the curved segment is of higher misorientation than the straight segments, but the opposite is the case for the left boundary. Figures 4.12b and c show the third and fifth slices of the volume showing the splitting of the single microband (Figure 4.12a) into separate bands. At the intermediate stage of microband splitting (Figure 4.12b), the edges of the connecting segments are almost parallel to the RD (arrowed). Such an event was almost never visible in the RD–ND section. Finally, Figure 4.12d shows the ninth slice revealing the close alignment to the TD of the straight segments of the two separate microbands. The various slices shown in Figure 4.12 also reveal the complicated nature of the boundary curvatures in the RD–TD section (arrowed in Figure 4.12c–d).

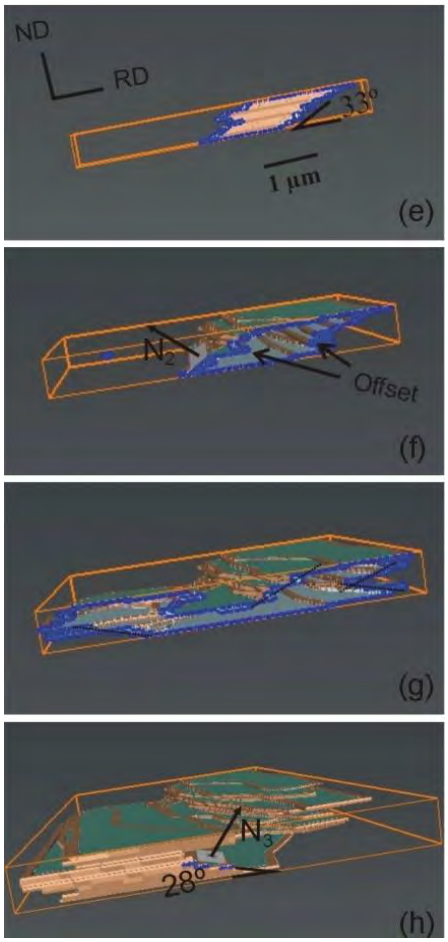

Figure 4.12e–h: Cross–sectional images in the RD–ND section from a 3D–EBSD reconstructed volume showing the complex curvatures in the microband boundary and splitting/merging events.

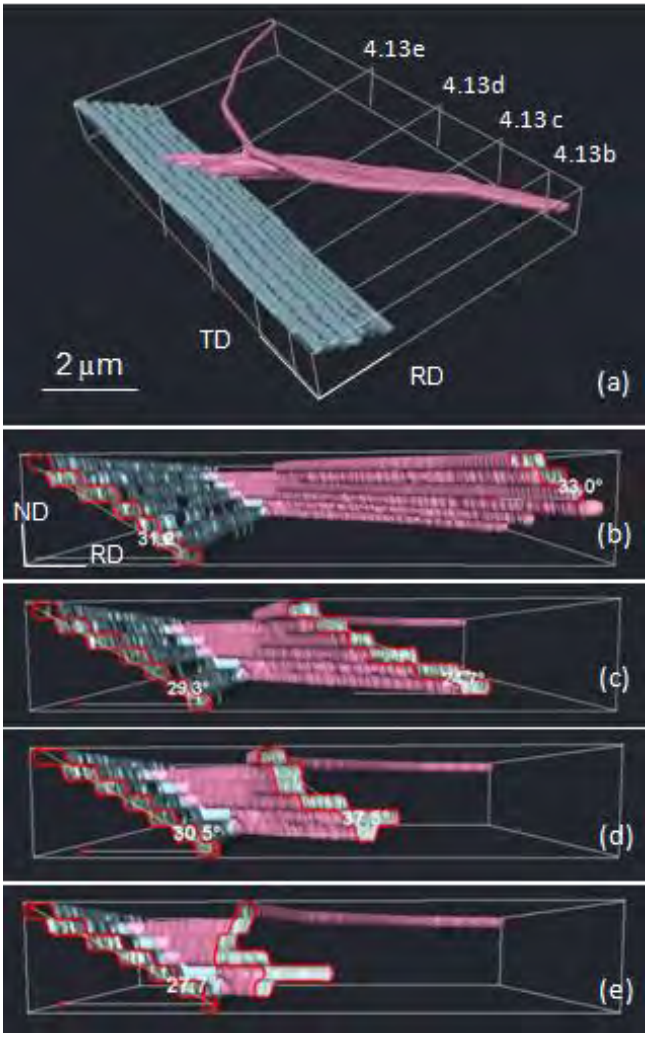

Figure 4.13: 3D reconstruction of an area containing an intersection in microband structures. (b)–(e) series of RD–ND cross section images showing the changes in microband inclination angles.

The reconstructed microbands in Figure 4.12 reveal important information on the interaction of microbands when viewed in RD–ND cross sections. Figures 4.12e–h show four sections along the marked locations in Figure 4.12d. Figure 4.12e shows the microband boundaries to be classically aligned at +33° from the RD, although the left–hand boundary contains a small offset. This boundary offset is seen to increase in Figure 4.12f (arrowed) although the general boundary inclination (given as N2) remains unchanged. In Figure 4.12g, the interaction between two microband sets now becomes apparent although the situation is complicated with the presence of offsets and connections. Nevertheless, the two microbands still contain short straight segments that are classically inclined from the RD. Finally, Figure 4.12h reveals the other set of

microbands showing one of its boundaries inclined –28° with the RD. The average normals of microband 1 and microband 2 (given as N2 and N3 in Figure 4.12g and h) are plotted in Figure 4.9 showing they are within 5° and 8° of the $[11\bar{1}]$ and [111] and poles, respectively. Overall, sectioning along the TD reveals the complex interactions that can occur between non–coplanar microbands during plastic deformation whereby highly localized curvatures between the microband aligned close to $(11\bar{1})$ and other microband aligned close to (111) are generated.

Figure 4.13 demonstrates another example of interactions in 3D reconstruction. Only seven layers of EBSD map was stacked in this volume because it is difficult to trace the boundaries further with good confidence. In Figure 4.13a, a junction of two microband boundaries is shown. In the top layer there is a misorientation line, which was hardly traced, but without further continuity, and therefore it was not possible to reconstruct the associated microband boundary surface. The reason will be highlighted in the description of the series of images in Figure 4.13b–e, which are taken at the marked sections in Figure 4.13a. In Figure 4.13b, two microband traces are highlighted at 31.2° and 33.0° inclinations with the RD. The left microband continues to remain within 31.2–27.7° inclinations in the subsequent sections in Figure 4.13c–e. In Figure 4.13e the trace of the left microband approaches the junction point. The right microband changes inclination to higher angles (from 33° and 37.5°) as it approaches the junction point (see Figure 4.13b–e). When it approaches the junction point, in Figure 4.13e, the upper part of the right microband starts changing the inclination towards the opposite angle with RD. In other words, the upper part becomes a segment of another microband set (inclined in the opposite angle). Therefore, in this particular occasion, the microband boundary is twisted near the junction, and this happens in the region between Figure 4.13d and the junction point (arrowed). Now, the nature of the sitting alone curved boundary in the top surface can be realized. It has been seen in TEM (Figure 4.17) that boundary disintegration happens as a result of interactions. Therefore, it is reasonable to assume that the boundary associated with this trace has dissolved. How boundary dissolution occurs is not clear, but has been reported by Albou *et al*. [2010] in a Al–Mn alloy. The dissolution phenomenon is also understandable from the global perspective that, irrespective of the accumulative strain, microbands are always in their 25–25°

inclinations. This indicates that the earlier formed microbands have dissolved and fresh microbands formed either in the same way as microbands form in this metal or by a rearrangement of the disintegrated segments.

4.4 Transmission electron microscopy

Additional important details of microband structure were revealed by TEM, whereby the evidence of various development stages of microband formation was obvious and, hence, the argument supporting their crystallographic alignment with the operative slip planes becomes convincing. Figure 4.14 shows a representative bright–field TEM micrograph showing a prominent set of microbands intersected by a complementary set of less well–defined microbands. In general, there were a number of areas containing a single set of microbands, although this does not appear to be frequent. In this image, the parallel arrangement of the dense dislocation walls (DDWs) is also evident, as well as signs of the classical mash and cell structures in the interior of the predominant set of microbands and, finally, evidence of the early stages of formation in the other set of microbands. Examples of the interactions between the boundaries of these complementary sets of microbands are encircled in A and B. In C, evidence of boundary fragmentation is also highlighted. The microband boundaries consist of two types: (i) the white arrowed boundaries are thin and straight, whereas (ii) the black arrowed boundaries are more complex. Selected area electron diffraction (SAED) of this area reveals a ~7° spread in orientation. Convergent beam electron diffraction (CBED) was used to measure the orientation of individual microbands and for determining how orientation varies both across their boundaries and along their length. It was found that the variation in orientation across the curved segments was generally lower than for the straight segments. Figure 4.14 also shows a CBED pattern from one of the more prominent microbands clearly showing its boundaries to be aligned parallel to {111} planes.

Figure 4.15a is a bright field TEM image of an area containing one parallel set of microbands. The misorientations across the microband boundaries were measured by CBED pattern and are plotted schematically in Figure 4.15b. There are boundaries in this region as high as 9.2°, while there are also boundaries having misorientation as low

as 2.3°. The band interiors contain a classical distribution of cell boundaries. Further details of cell architecture in the microband interior are shown in Figure 4.16, demonstrating the alignment of cell boundaries along the microband boundaries. This image is accompanied by a schematic image, showing the CBED measure misorientations across the cell boundaries. The highest and lowest measured misorientation in this area is 2.7° and 0.6°, respectively. Figure 4.15 and 4.16 demonstrate a general tendency of cell boundaries to have their long axis along the microband boundaries, and this indicates the existence of some sort of relationship in their evolution sequence. In the TEM images the spacing between microband boundaries varies between 1–2 μm, which is generally a strain dependent factor [Winther *et al*. 2004]. Also in these images the microbands are inclined classically at 25–35° with RD.

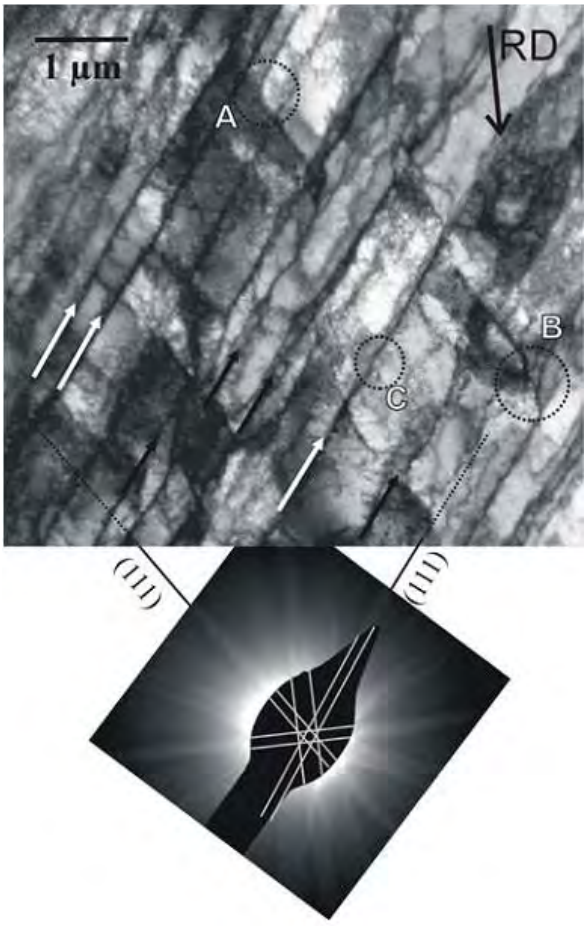

Figure 4.14: Bright field TEM micrograph and corresponding CBED patter of the RD–ND section showing an interaction between two sets of microband boundary and their alignment with the {111} planes.

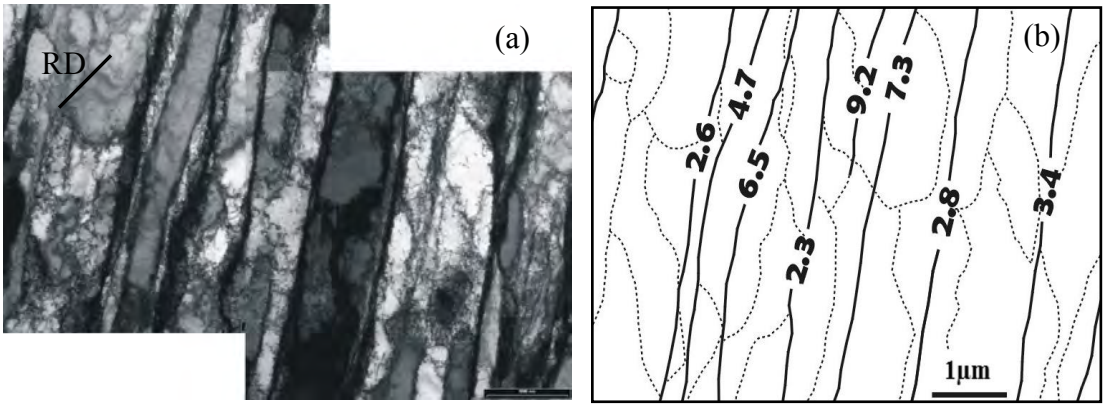

Figure 4.15: TEM bright field images of RD–ND section showing (a) small interactions of two microband sets. The misorientations of the microband and cell boundaries are shown in the schematic in (b).

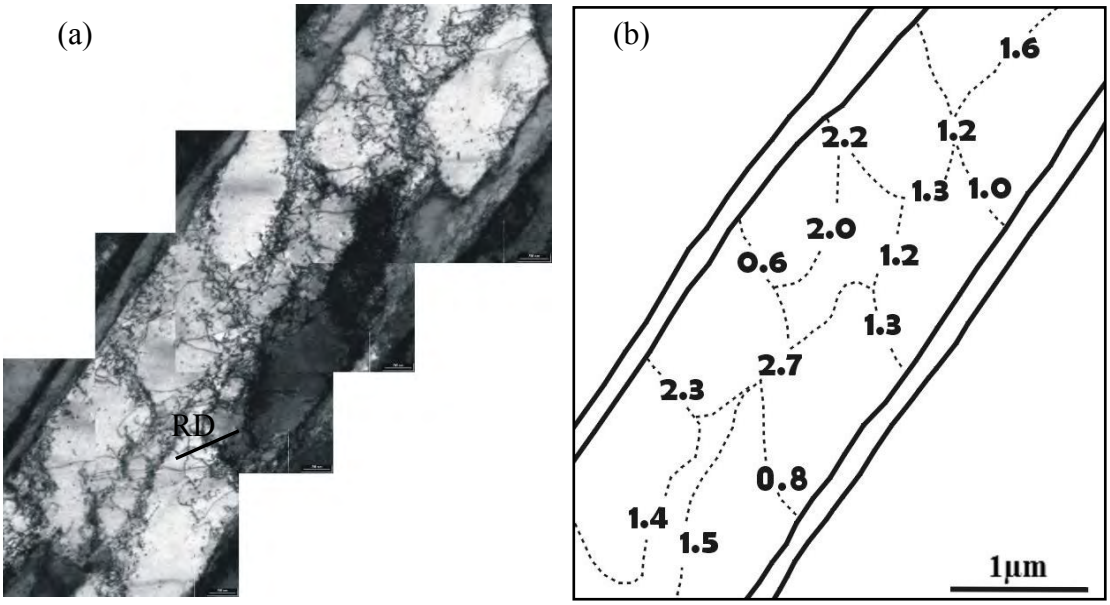

Figure 4.16: TEM bright field image and corresponding schematic of RD–ND section showing the distributions of cell boundaries and their misorientations measured by CBED.

Figure 4.17a shows a TEM micrograph of an area at an advanced stage of microband interactions. The second set of microband boundaries are operating in segments along the X–Y line showing how they clearly generate the curvature of the first microband boundaries at the point of their interaction. The variation in orientation across these curved boundaries was 2.5°, 8.0° and 3.1° at A–A′, B–B′ and C–C′, respectively. An extensive TEM analysis revealed that the relatively sharper segments

of the cell boundaries are often aligned parallel to the exiting microband boundaries. Also in Figure 4.17a, the alignments of the arrowed cell boundary segments are parallel with the microband boundaries and this phenomenon implies that the cell boundaries play an important role within the microband boundary formation steps. The variation in θ across these cell boundaries is less than 1°, in most cases. However, some cell boundaries that are well–aligned with the existing microband boundaries may have higher misorientations. An example is shown in Figure 4.17b where misorientations as large as ~2° were measured between the points located across the microband–aligned cell boundaries. This occurred in a region where the interactions with the second microband set are nominal, but exists. Again in this micrograph, identical inclinations of the cell boundaries as the microband boundaries were found. Figure 4.17c is a TEM micrograph showing intense interactions between two sets of microbands. Set B is likely to have formed earlier due to the local steps along the boundaries, which was made by pulling out at the point of interactions. At the interesting points, the microband boundary segments are smeared, and some obvious examples are found in Figure 4.17c, showing concurrent smearing of the existing microband boundary (along B) and intensifying the newly forming microband boundary (along A). This also implies that, during the interactions, dislocations from the existing microband boundary migrate to the newly forming microband boundary. It is also obvious that the microband boundary segments along a–b–c are sharper than those along both a'–b'–c' and a"–b"–c", respectively. Furthermore, the orientation differences along these sharp segments (a/b and b/c) are also higher. This indicates that set B microbands also have an influence on the boundary characteristics in set A, and vice versa.

For a further generic test of microband boundary crystallography, a larger area was imaged (Figure 4.18a) in which the beam was aligned parallel to one of the {111} set of planes (see inset). This figure shows a sharp boundary being segmented at the encircled spots at the centre of the micrograph. Evidence of boundary merging and relaxation are also encircled in the upper region of the figure. For this diffraction condition, the projected boundary thicknesses were found to be a minimum, as examined by tilting the foil along the direction in the inset. In Figure 4.18a, the average projected thickness of the boundaries becomes lowest because of their edge–on

alignment with the electron beam. When the sample is tilted away from {111} (see inset in Figure 4.18b), there is an increase in the projected thickness of the microband boundaries. This finding was appropriately confirmed both for short, straight microband segments and freshly formed microband boundaries.

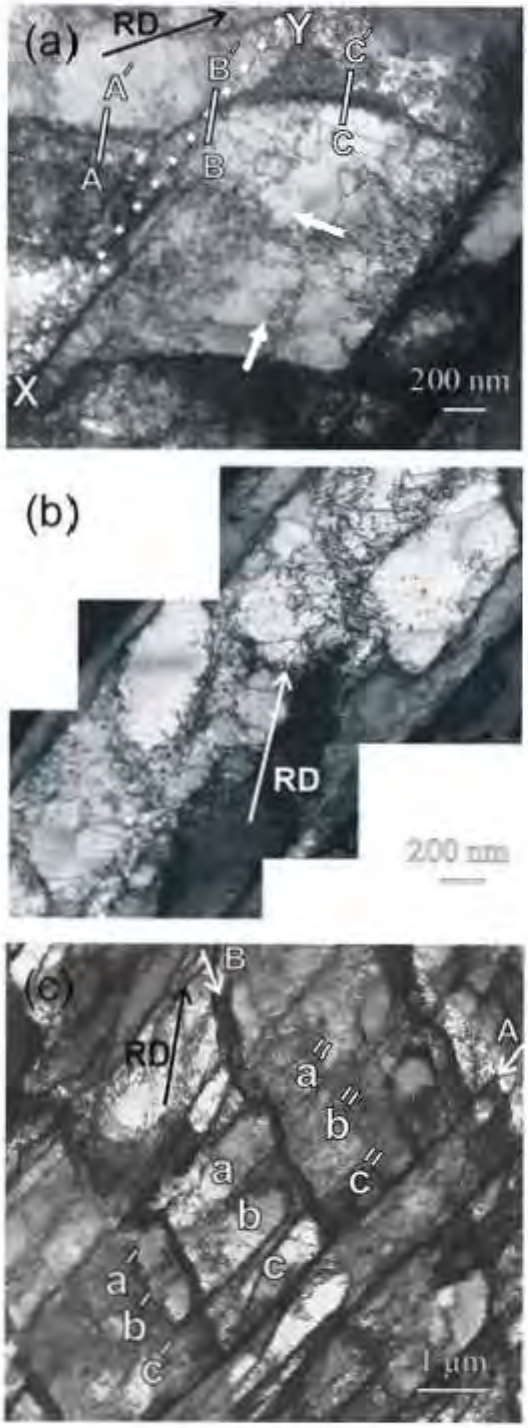

Figure 4.17: TEM micrographs of RD–ND section showing the influence of interactions on cell structures and microband boundaries.

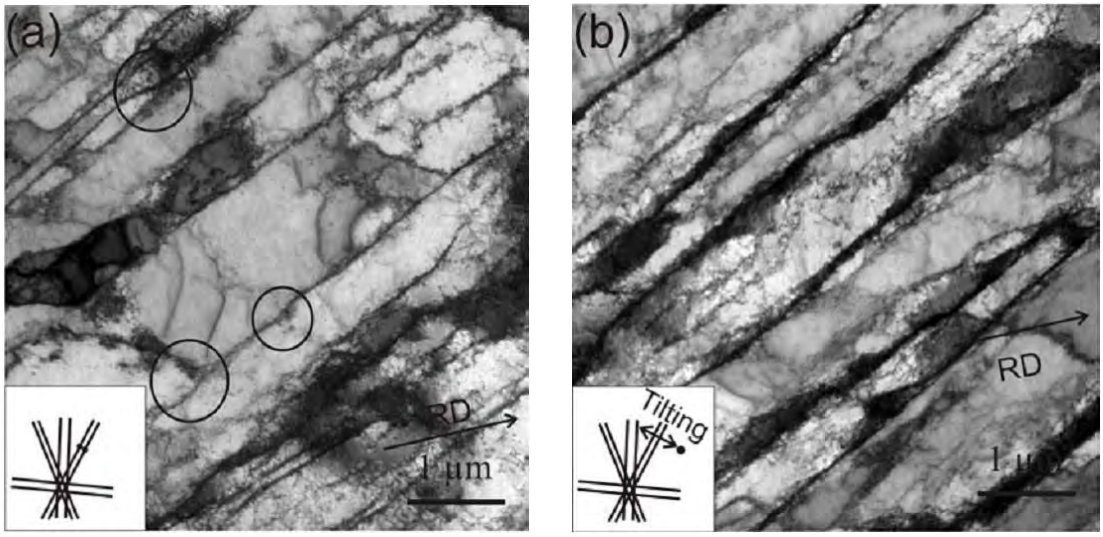

Figure 4.18: TEM micrograph of the RD–ND section showing the change of projected microband boundary thickness: (a) thin boundaries at an edge–on condition when the beam is almost parallel to the (111) set of planes, and (b) widened boundaries when the beam is rastered away from (111).

4.5 TEM and EBSD characterizations on the same microband containing region

The early microband characterizations were done by TEM, whereas more recent investigations were extensively conducted by EBSD. EBSD data are more acceptable in terms of statistics because large area scans over many regions are trivial. On the other hand, TEM reveals insight detail, some of which do not appear in EBSD studies. This section demonstrates the discrepancies that may arise from the differences in characterizing techniques, on the same area of microband containing structures.

In Figures 4.19, a high resolution EBSD map and a low magnification TEM image are shown. These data are taken from the same microband containing area in an edge of an electron beam transparent thin TEM foil. Some dimensions from sample landmarks are presented to locate the relevant features between these images. The TEM image reveals many obvious microband boundaries in Figure 4.19b, many of which do not appear in the EBSD map in Figure 4.19a. The areas within the square blocks are presented in higher magnifications in Figures 4.20a and b. Again, the misorientation between two consecutive microbands was measured from CBED patterns and it was

found that most of the boundaries in this region are of low angle nature (0.5–4^{o}). A comparison between Figure 4.20a and b shows that some microband boundaries are obvious in the TEM image but do not have adequate misorientations across them and therefore are missing in the EBSD map. It is worth noting that no post processing filtering of EBSD data has been carried out. Boundary A and B have unusually high misorientations of 6.7^{o} and 10.3^{o}, respectively, but they appear same as the other low angle boundaries in the TEM image. The A–B distance is ~2.5μm, within which there are at least another 6 microband boundaries as per the TEM image, but EBSD only detects small segments of two of them (pointed by white arrows). Therefore for a complete characterization of microband structures, and in general of deformed microstructures a complementary TEM investigation is vital.

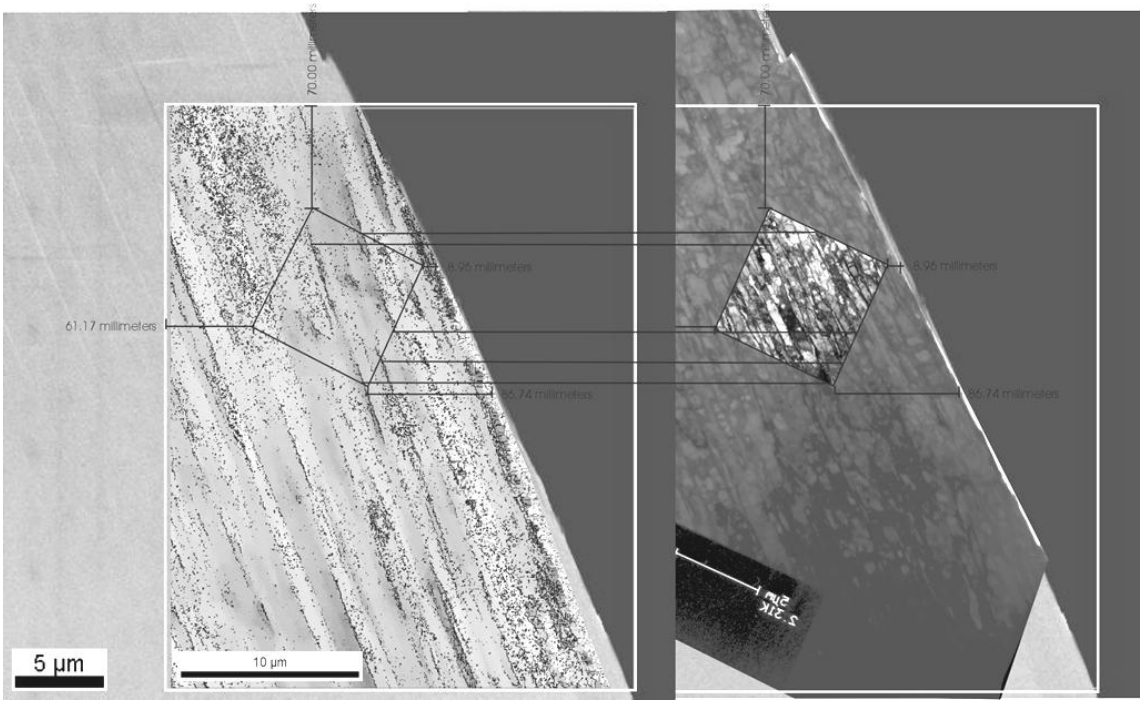

(a) EBSD map (b) TEM image

Figure 4.19: (a) EBSD measured orientation map and (b) low magnification TEM image on the same area near an edge of a TEM foil of 30% deformed Goss orientated Ni crystal. The edge dimensions are marked for locating the same area.

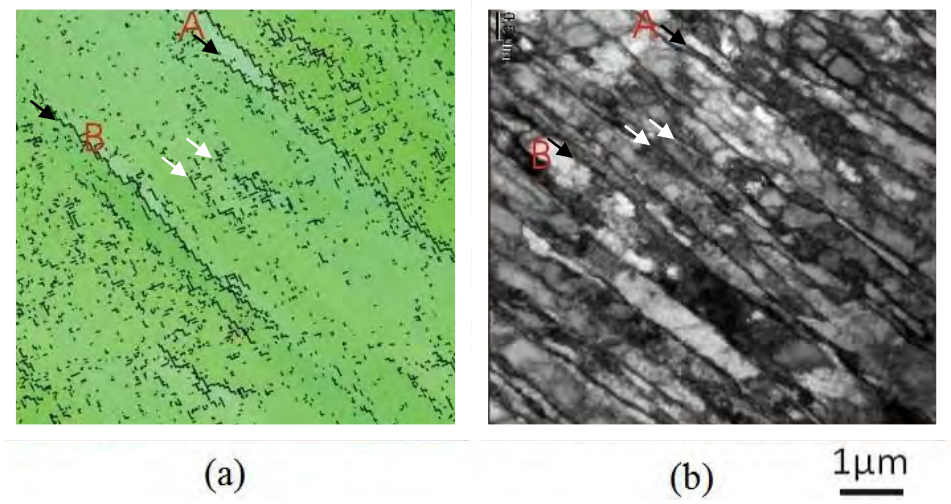

Figure 4.20 (a) EBSD maps showing 1° misorientation boundaries in black lines (b) TEM micrograph on the same area. The A and B boundaries has misorientation of 6.7° and 10.3°, respectively.

The distance between microband boundaries (*i.e.* width of microband channels) were measured by the line intercept method on both the TEM image and EBSD map. Lines were drawn at 1µm repeat distances perpendicular to their length. The result is plotted in Figures 4.21a and b. In case of EBSD most of the microbands are found to have thickness in the range of 0.5 to 1µm. On the other majority data varies in the range of 0.2 to 0.7 µm in the TEM measurement.

TEM images represent projection of the structural elements (except those that are in invisibility) within the foil thickness, which is typically ~100 nm. Whereas EBSD is a surface technique, in which the signals within ~50 nm depth (depending on the voltage of incident electron beam) are measured. Therefore in this investigation effort was dedicated to measuring the foil thickness at a location within Figure 4.20b. The sample was tilted to a two beam condition with only one strongly excited *hkl* reflection. In this condition parallel fringes are produced, which are known as Kossel–Möllenstedt (K–M) fringes, shown in Figure 4.22. The distance of those fringes from the centre line of the disk varies with specimen thickness. Therefore, to extract the thickness from the K–M fringes (schematically shown in Figure 4.23a) first the deviation parameter (s) was calculated from the following equation:

$$S_i = \frac{\Delta\theta i}{2\theta_B d^2} \qquad \text{(Eq 4.1)}$$

where, θ_B is the Bragg angle for the diffracting *hkl* plane, *d* the *hkl* interplanar spacing and λ is the wavelength of the electron beam.

The calculated values are shown in Table 4.2. Then by plotting $\left(\frac{S_i}{n_k}\right)^2$ against $\left(\frac{1}{n_k}\right)^2$, where n_k is an integer, the thickness was calculated from the intercept for a straight line, shown in the schematic in Figure 4.23a and b. The calculated value shows that the thickness of the foil was ±127 nm.

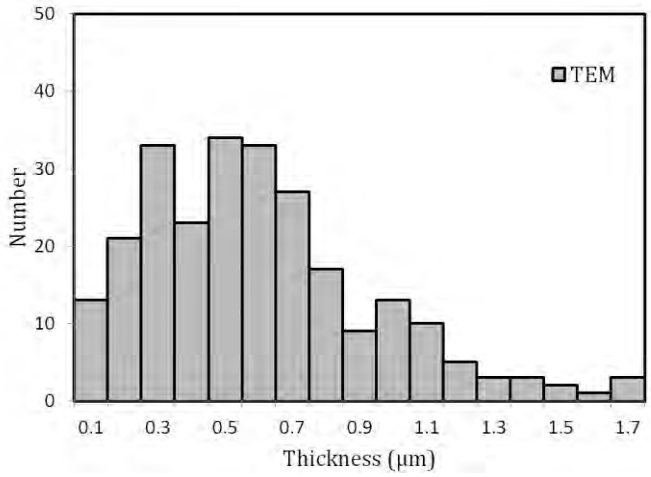

(a)

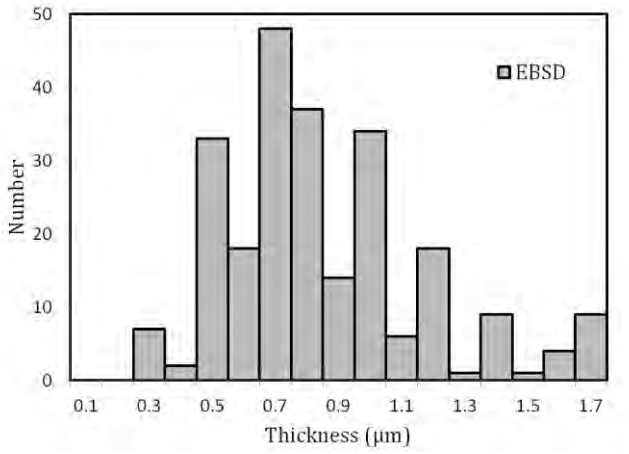

(b)

Figure 4.21: Frequency distribution of microband boundary distances showing high population of data to vary in 0.5 to 1µm range in EBSD and 0.2 to 0.7 µm range in TEM measurement.

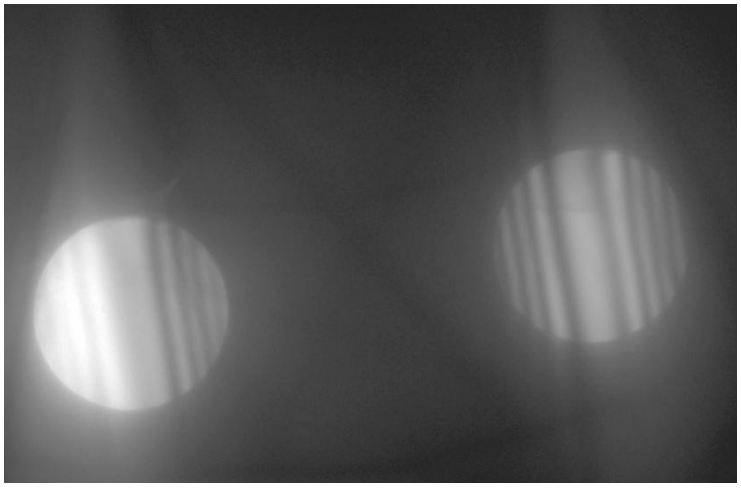

Figure 4.22: Parallel K–M fringes in a Zero Order Laue Zone CBED pattern from 30% deformed Ni single crystal under two beam conditions with (220) strongly excited.

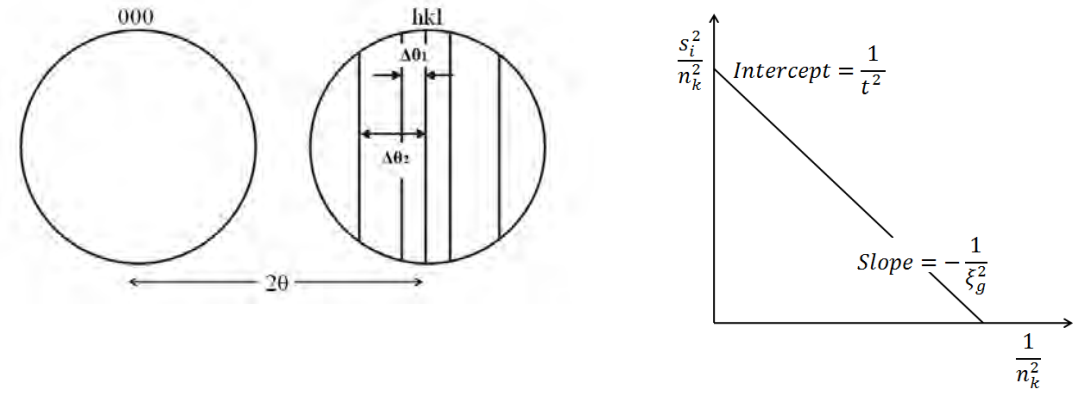

(a) (b)

Figure 4.23: (a) Schematic representation of the measurement procedure to extract thickness from the K–M fringes (b) plot $\left(\frac{S_i}{n_k}\right)^2$ against $\left(\frac{1}{n_k}\right)^2$.

Table 4.2: CBED data for thickness measurement.

S_i	n_k	$\left(\frac{S_i}{n_k}\right)^2$	$\left(\frac{1}{n_k}\right)^2$
0.00846	1	7.15×10^{-5}	1
0.01616	2	6.52×10^{-5}	0.25
0.02370	3	6.24×10^{-5}	0.11

From the foil thickness measurement it is now clear that in Figure 4.20b the microband boundaries within 127nm thickness was projected. This image is therefore more crowded with microband boundaries than the EBSD map in Figure 4.20a, which is typically expected to draw information down to 35 nm (from Monte Carlo simulation) with a 15 kV electron beam. Therefore, information from ~4 times volume was included in the TEM image than the EBSD. Within this thickness, new microband boundaries appear in the TEM foil that is not registered in the EBSD measurement. This also indicates that the continuity of microband boundaries in TD direction (along the TEM beam) is short, unlike their long axis in RD–ND section. Therefore, microband boundaries are asymmetric. This finding is also consistent with the EBSD measurement involving three orthogonal surfaces shown in the discussion section. It is to be noted that when a uniform lattice continuity is not present, diffraction takes place within a shallow thickness near the exit (at the bottom) of the TEM foil.

4.6 Discussion

4.6.1 General crystallography of microband boundaries

Microbands are ubiquitous in the RD–ND section of many fcc metals and alloys after either PSC or rolling [Winther *et al.* 1997, Winther *et al.* 2000, Godfrey *et al.* 1998, Winther *et al.* 2004, Lin *et al*. 2009]. They generally occur as two sets, inclined at ±30±5° with the RD, although in the present material, one set of microbands is predominant (Figures 4.1, 4.8 and 4.14). Microband formation is usually explained by plastic deformation involving certain crystallographic planes, whereby the dislocations

associated with the process relax on a parallel set of boundaries to form an array of DDWs [Huang and Hansen 1991, Hansen and Juul Jansen 1992, Winther *et al*. 1997, Winther *et al*. 2000, Godfrey *et al.* 1998, Winther *et al*. 2004, Lin *et al.* 2009]. Since deformation is a dynamic process, an image of any deformation microstructure captures the microbands in both their mature (plus some modifications) and early stages of formation. The mature microbands are easy to observe by optical microscopy, SEM and TEM due to their classical striped appearance. While newly created microbands are obvious in the TEM, they are usually only vaguely visible in the SEM (and EBSD) as faint traces between mature microbands. Microbands continue to form as the dislocation density increases due to the deformation with their boundaries aligned parallel (and between) to the existing microbands. This is the manner by which microband density increases to a limiting value below 1 μm separating distances [Hughes and Hansen 2000] and, thus, the microstructure reaches a situation whereby stability of the these deformation features becomes an issue. This is the general picture of microband evolution that found in many fcc and bcc metals and alloys [Humphreys and Hatherly 2004, Hughes and Hansen 2000, Bay *et al*. 1992, Hughes and Nix 1989, Hughes and Hansen 1993, Lee and Duggan 1993, Chen *et al.* 2003, Ferry and Humphreys 1996, Park and Parker 1989, Huang and Hansen 1991, Hansen and Juul Jansen 1992, Winther *et al.* 1997, Winther *et al.* 2000. Godfrey *et al*. 1998, Winther *et al*. 2004], including that observed in the present work.

There are two broad approaches for assessing the crystallographic nature of microbands. The first is based on their orientation selectivity in polycrystalline fcc and bcc metals. For example, in rolled bcc metals, microbands do not form in those grains orientated with <110> parallel to the RD (so−called α grains) since 4−6 slip systems are operative and, hence, deformation occurs homogenously to accomplish any shape change imposed by the relatively harder neighboring grains orientated with <111> parallel to the ND (so−called γ grains). It is pertinent to note that any shape change can be achieved by the operation of five independent slip systems [Reid 1973]. For γ grains, only 1 to 2 slip systems carry the deformation process thereby creating microbands aligned with their traces parallel to these planes. The same analogy also appears to be sustained for fcc metals, whereby microbands are common in Goss

({110}<001>), Brass ({011}<211>), Cube ({001}<100>), Copper ({112}<111>) and S ({123}<634>) orientations after cold rolling [Humphreys and Hatherly 2004]. Furthermore, microbands rarely operate across a grain boundary from a grain containing microbands into a microband–free grain. Thus, the first approach is versatile, but can only be utilized for judging the crystallographic nature of microbands in polycrystalline metals. The second approach is based on the characterization of individual microbands where various testing methods have been developed. In the present investigation, both conventional and advanced characterization methods were used: (i) 2D and 3D–EBSD and (ii) TEM.

3D–EBSD has enabled the direct visualization of both the structure and crystallographic nature of individual microbands and their boundaries in the Goss–oriented Ni crystal deformed in PSC to 30% reduction (Figures 4.4–4.13). In summary, both 2D– and 3D–EBSD showed that:

- a single set of microbands was predominant and these were classically aligned in the RD–ND section at +30±5° from the RD (Figures 4.1 and 4.8), but appear wavy in the RD–TD section (Figure 4.4);
- the average plane of 80% of the reconstructed microband boundaries was within ±5° of the active $(11\bar{1})$ and (111) slip planes (Figure 4.9);
- the average plane of the remaining reconstructed microbands are within 15° of the active $(11\bar{1})$ and (111) slip planes (Figure 4.9);
- there was a gradual, but cyclic, change in cumulative misorientation along the length of a given microband (Figure 4.2);
- the surfaces of the reconstructed microbands were largely planar but frequently interrupted by local distortions and undulations (Figure 4.8a and b), and
- significant interactions were associated with intersecting, non–coplanar microbands and these were complex (Figures 4.11and 4.13).

Similarly, TEM showed that:

- microbands were aligned parallel to the traces of $(11\bar{1})$ and (111) planes (Figures 4.14 and 4.18);

- the internal cell boundaries of microbands are often aligned parallel to the existing boundaries (Figures 4.16 and 4.17);
- the interactions between non–coplanar sets of microbands can either be intense (Figure 4.17c) or moderate (Figure 4.18);
- at the microband intersections, the misorientation across the boundaries varies depending on the nature of the interaction, and may increase for a rigid body rotation or decrease if a short boundary segment disintegrates (Figure 4.17), and
- Microband boundaries are asymmetric *i.e.* they have short axis along the TD and long axis long the ±30±5° direction with RD (Figure 4.20).

The combined EBSD/TEM investigation has clearly revealed the crystallographic nature of microband boundaries as well as non–crystallographic features in the form of curves and bumps, thereby resulting in their deviation away from the active slip planes. Because of these disturbances, measuring the microband alignment in short segments is only approximate and may lead to confusion. Therefore, microband boundaries should be investigated over a wider length scale by combining a set of characterizing techniques, such as EBSD by which analysis is possible over longer distances (e.g. Figure 4.8) and TEM by which the minute details within small segments can be clarified (e.g. Figures 4.14, 4.17–5.18). This combined approach is undeniably the best, as adopted by the key researchers in the field. An understanding of the sequential development of microband boundaries is also important, and in this regard 30% deformation provides a good snapshot of the deformation microstructure since both mature and freshly forming microbands are present.

4.6.2 Active slip systems and orientation spread

Certain crystal orientations in polycrystalline metals remain stable during rolling deformation. That means once a crystal rotates to this orientation it will not keep rotating with further deformation. The Goss orientation is known as a stable orientation in both bcc and fcc crystal systems. However, stable orientations also experience small rotations within a short angular range about their ideal orientation positions [Nakayama and Morii 1982, Morii *et al.* 1985]. Such behavior was explained with the “geometric

orientation stability" theory by Kocks and Chandra [1982]. Since deformation is a dynamic process and microstructural techniques provide a snapshot of the deformation at a particular instance, the maximum variation in lattice orientations over a distance (*i.e.* lattice curvatures) shown in EBSD and TEM micrographs may be regarded as a fingerprint of the orientation spread (i.e. the rotation path) [Ferry and Humphreys, 1996b]. The initial orientation of the Ni crystal was very close to Goss, and deformation generated a spread in orientations towards RD and TD of ±7.5° and ±3.5°, respectively (Figures 4.1 and 4.3). These values are readily found by the average spread in the <110> pole figure (Figure 4.24a) towards both RD and TD at 3° intervals. The spread is plotted in Figure 4.24b as a function of rotation angle starting from ND–RD to ND–TD. The <110> pole at the ND is selected for conducting this measurement in order to avoid stereographic effect on angular measurements.

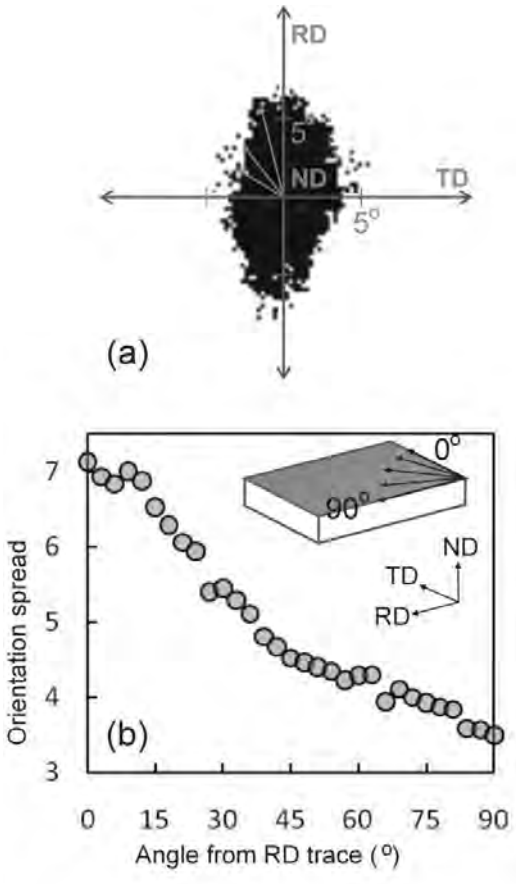

Figure 4.24: (a) The spread of [110] poles towards both the TD and RD in the deformed microstructures, and (b) an average plot from four EBSD measurements covering large areas showing that this spread is a general trend.

Although orientation oscillation is an extensively observed phenomenon, the mechanism is not completely understood. It was shown by Lee and Duggan [1991] that a friction driven shear component, which is high near the surface and gradually diminishes near the middle of a sample, triggers the RD oscillation during rolling. This phenomenon has been refined recently for a Goss−oriented Al crystal, where it was shown that the friction component occurs in a sinusoidal manner along the sheet thickness direction and, hence, a cyclic orientation oscillation towards RD was found [Liu *et al.* 2000]. The central volume of the present crystal was investigated after PSC, thereby ruling out any frictional effects causing the localized oscillations about the RD. Regardless of the origin of the oscillations, they bring the crystal into a range of orientations, in which the deformation behavior (which is governed by orientation dependent slip system selectivity) may vary on a local scale.

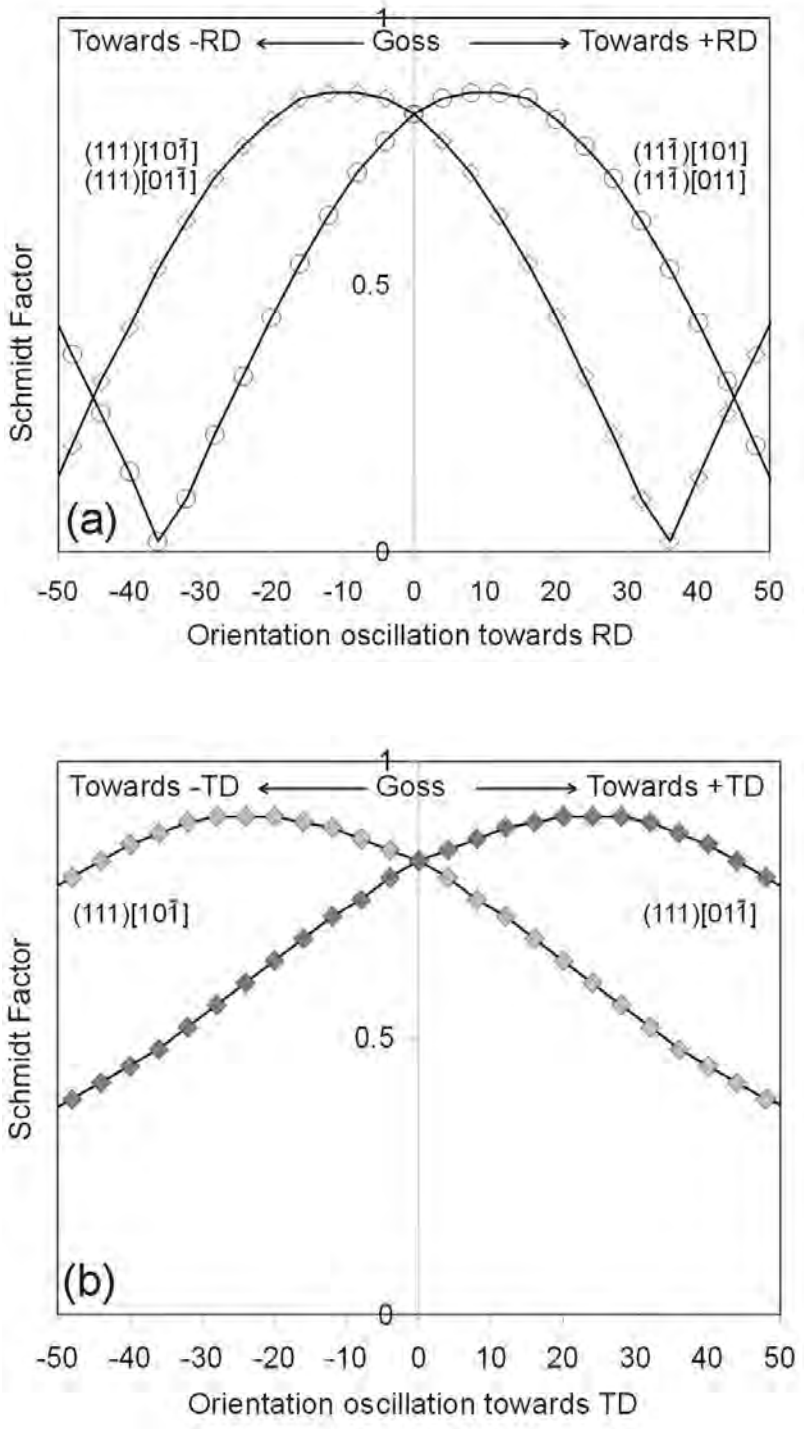

Figure 4.25: The variation of Schmidt factor of the slip components in (111) and (11$\bar{1}$) planes showing the oscillations towards: (a) RD and (b) TD. In (b), the [10$\bar{1}$] and [01$\bar{1}$] components of the (111) plane are plotted as the same occurs for the [10$\bar{1}$] and [011] components in (11$\bar{1}$) plane.

Table 4.3: Calculated Schmidt factors for the slip systems operating in a perfect Goss-oriented crystal and for those orientations deviating +5° towards both RD and TD.

Slip plane	(111)			($\bar{1}$11)			(1$\bar{1}$1)			(11$\bar{1}$)		
Slip directions	[1$\bar{1}$0]	[10$\bar{1}$]	[01$\bar{1}$]	[110]	[01$\bar{1}$]	[10$\bar{1}$]	[110]	[01$\bar{1}$]	[011]	[10$\bar{1}$]	[011]	[1$\bar{1}$0]
Slip systems	a_1	a_2	a_3	b_1	b_2	b_3	c_1	c_2	c_3	d_1	d_2	d_3
Ideal Goss (110)[001]	0	**0.82**	**0.82**	0	0.41	0.41	0	0.41	0.41	**0.82**	**0.82**	0
+5° rotation towards RD	0	**0.75**	**0.75**	0.1	0.45	0.35	0.1	0.45	0.35	**0.85**	**0.85**	0
+5° rotation towards TD	0.07	**0.78**	**0.85**	0.07	0.45	0.38	0.07	0.38	0.45	**0.78**	**0.85**	0.07

For a perfectly Goss–oriented crystal, the two complementary {111} slip planes carry equal amounts of deformation on each of two equally operative <110> directions, thereby resulting in high stability in PSC [Reid 1973]. This can be shown by calculating the Schmidt factor for each of these four {111}<110> slip systems [Reid 1973]. Table 4.3 highlights those slip systems that are most highly stressed and, hence, the alignment of the intersecting microbands along {111} and $\{11\bar{1}\}$ planes, at ±35° with the RD, is readily explained [Ferry and Humphreys 1996b]. However, there are imbalances in the distribution of slip in the other orientations within the range shown in Figure 4.24. For example, +5° rotation towards RD takes the initial Goss crystal to a new orientation, in which a_2 and a_3 components in the (111) plane become less stressed whereas the d_1 and d_2 components in $(11\bar{1})$ plane become more stressed. This is highlighted in Table 4.3. The opposite occurs for a −5° rotation towards the RD. The effect of these oscillations on the Schmidt factor of the slip systems are given in Figure 4.25a, whereby the left curve represents both a_2 and a_3 of (111) plane and the right curve represents both d_1 and d_2 of $(11\bar{1})$ plane. On the other hand, a rotation towards the TD results in the slip components becoming unequal within a given {111} plane, although the total slip within a given plane remains unchanged (Table 4.3). For example, the effect of oscillating on the a_2 and a_3 components of (111) plane is given in Figure 4.25b. In pertinence, the small (3.5°) $11\bar{1}$ TD spread is associated with the bumps and curves in the microband boundaries. Evidence of TD spread near the bump area can be seen in Figure 4.11, and a measurement of this spread was given in Table 4.1.

4.6.3 Effects of orientation oscillations on microband interactions

Orientation changes along the length of a given microband were observed in the present investigation in a Goss oriented Ni crystal. The misorientation is cumulative and gradually builds up to a maximum of ~5° over distances of ~7 μm (Figure 4.2a). This phenomenon may be explained by the measured orientation oscillations in Figure 4.24. The principal oscillation occurs about TD by ±7.5°. Such oscillations alternatingly bring the (111) and $(11\bar{1})$ slip planes to favorable orientations for either single or coplanar slip (Figure 4.25a). In local regions of microstructure conforming to the perfect Goss orientation, the two strain components associated with each slip plane remain equal, thereby resulting in coplanar slip, which is noted as a key criterion for generating

microband structures [Winther *et al.* 1997]. These microbands forming on the two operating slip planes in equal fraction results in intense intersections (Figure 4.17c). In other regions away from Goss, slip is expected to occur predominantly on a single slip plane, thereby leading to the strengthening of a one set of microbands and the breakup of the second existing set. This slip imbalance also results in a crystallographic rotation about the TD towards the RD. Overall, the RD oscillations continually activate and deactivate the two intersecting slip planes over a distance of ~7μm and, hence, the orientation changes built up over this distance are eventually interrupted by the operation of microbands on the other slip plane; this results in a rotation of the crystal back to the original Goss orientation. The overall microstructural effect is an alternating transition from intersecting microbands to single microband. The maximum deviation of only ±7.5° from Goss (Figure 4.24) is not likely to be sufficient to completely diminish slip on the secondary slip plane and, as such, there are no large areas of microstructure containing only a single set of microbands. It is worth noting that the ±3.5° TD spread observed near the undulated microband surfaces (Figure 4.10) is not an intrinsic rotation feature in PSC [Liu *et al.* 2000], but is a result of the local interactions between the two sets of microbands.

4.6.4 Asymmetry in microband interactions, their appearances in the three orthogonal sections and origin of non crystallographic microband characteristics

Figures 4.26a–c are EBSD micrographs showing the features of typical microbands when viewing three orthogonal sections [Hurley *et al*. 2003, Humphreys and Bate 2007, Quadir and Duggan 2006]. In these sections, the microbands are either aligned at an acute angle to the RD (in RD–ND section, Figure 4.26a) or wavy in the RD–TD section (Figure 4.26b). These differences in the structure of microbands when viewed in different sections can be explained by the complex nature of microband interactions, as revealed in Figures 4.8, 4.12 and 4.13. As it has been quoted that microband boundaries are composed of densely packed dislocations [Hughes and Hansen 1993, Lee and Duggan 1993, Chen *et al.* 2003]. When a second microband set operates across an existing microband set, the misorientation of the boundary may either increase or decrease (Figures 4.10, 4.11 and 4.17a). If the existing microband boundary experiences a rigid body rotation, as shown in Figure 4.17a, there is an increase in

misorientation. On the other hand, the misorientation may decrease if the existing boundary breaks up and dislocation dissolution occurs at the breaking points. Indeed, both Winther *et al.* [2004] and Albou *et al.* [2010] have argued that a loose packing of dislocations in a microband boundary may be easily broken up and dissolve. Overall, the nature of the generated misorientation depends on the nature of both the interactions and the boundary. While there is no direct evidence of boundary dissolution in the present Ni crystal, the smeared segments of microband boundaries in Figures 4.14, 4.17–4.18 also indicate this possibility.

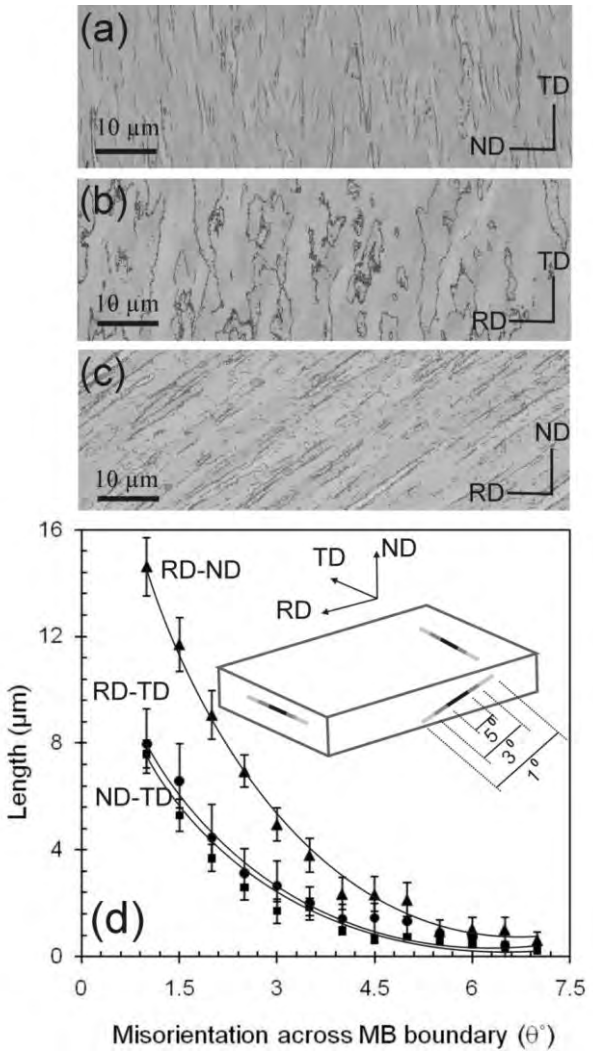

Figure 4.26: (a–c) EBSD micrographs of three orthogonal surfaces showing the 1.5° microband boundaries as black lines. (d) Plot of the microband boundary length as a function of misorientation showing that the microband boundary lengths with higher misorientations are short. The average microband length at a given misorientation is double in the RD–ND section than in the RD–TD section.

On a more global scale, microband boundaries are generally aligned at 25–35° to the RD irrespective of the degree of deformation, thereby implying that the boundaries that form in the early stages of deformation disintegrate and go through boundary rearrangements, and it is the freshly–formed microbands that generate the final configuration. Therefore, microband boundary segmentation commonly occurs due to the interaction of two sets of microbands on different slip planes and this often results in their deviation from perfect crystallographic alignment. On this basis, the Risø researchers [e.g. Winther *et al*. 2004] insist that only short segments of microband boundary should be examined by TEM when investigating their crystallographic alignment. Such complex microband interactions during plastic deformation are difficult to reveal by standard EBSD and TEM techniques. In this investigation, 3D–EBSD has revealed that the irregularities created by these microband interactions (and associated segmentations) are asymmetric in nature, that is, they are more complex in the RD–ND section compared with the RD–TD section (see Figure 4.26). Also, the bump on the microband boundary shown in Figure 4.11 has a longer axis along the TD and, therefore, this feature appears as having longer curved segments when viewed in the RD–TD section. These observations clearly reveal the complex nature of microbands when viewed in the RD–TD section.

It is apparent from the foregoing discussion that the asymmetric nature of the interacting region of two non–coplanar microbands allows their boundaries to be traced over reasonably long distances when viewed in the RD–ND section (Figure 4.26a) but much shorter distances in the RD–TD section (Figure 4.26b). Since 3D–EBSD only covers a small volume of material, the global evidence for this argument was achieved by carrying out large EBSD scans on the three orthogonal surfaces (part of each are shown in Figures 4.26a–c). From each of these plots the average length of the microband segments was measured as a function of misorientation across them. These measurements were carried out at 100 nm step size and, therefore, a boundary containing at least three consecutive data points (0.3 μm lengths) was considered, arbitrarily, to arise from a microband boundary. Figure 4.26d gives as a function of misorientation (at 0.25° intervals from 0.75° to 6.75°) showing that, for a given θ–value, the average microband length in the RD–ND section is twice the value in the

RD–TD section. While this trend continues down to the 0.3 μm length, the data up to 1 μm is reasonable to accept to avoid any noise related artifacts. Overall, the shorter straight segments (Figure 4.26) and longer curved segments (Figure 4.11) of the microbands in the RD–TD section makes their boundaries appear wavy and, hence, explains why such well–formed microband boundaries in this section do not appear to be crystallographic, that is, they are not always aligned parallel to the expected slip planes.

4.7 Conclusions

A Goss-oriented Ni single crystal was deformed by channel die plane strain compression for conducting a two- and three–dimensional study on the crystallographic alignment of the microband structures. The important conclusions of the study are summarized below:

- Two interacting microbands are the prime microstructural feature in this sample. They are crystallographically inclined at ±30±5° with the RD in the RD–ND section. The microband boundaries are composed of dense dislocation walls.
- The average flat surfaces of the microband boundaries are crystallographically inclined within ±5° to the potential {111} slip planes. The newly forming and straight segments of the boundaries are ideally crystallographic in flatness and alignment to the slip planes. After their formation, various interactions create irregular features that deviate them from their crystallographic character.
- The Goss orientation is stable under plane strain compression, but asymmetrically oscillates within ±7.5° along the RD metastable ranges. The slip components in a perfect Goss crystal are equally distributed on two systematically aligned {111} slip planes, each of which have two components to carry an equal magnitude of slip. By the RD oscillation, the slip components within a given plane remain equal but the total slip between the planes varies.
- The TD orientation spread observed in the crystal is not intrinsic of PSC deformation, but it arises from the orientation spread adjacent to the undulations created by intense interactions between two sets of microbands.

- The orientation oscillations along the RD influence the degree of interactions between the two microband sets. The latter interaction creates irregularities in the form of bumps and curves on their boundaries and intensifies/homogenizes the boundary misorientation from their ~1.5° average values.
- The curved irregularities in microband boundaries are of complex and asymmetric morphology. They have a longer axis in the TD and, hence, the straight segments of microband boundaries in RD–TD sections are shorter. Due to the interactions, the microband boundaries appear more curved and non–crystallographic in both the RD–TD and ND–TD sections, whereas their crystallographic character is well sustained in longer straight segments of the RD–ND sections.
- The straight segment of microband boundaries along the TD is significantly short as compared to their dimensions along 25–25° with RD. This results discrepancy in the TEM and EBSD measurements in the distance between microband boundaries. TEM shows closer spacing than EBSD measurement.

It can be summarized that the interactions between two sets of microbands occur in different degrees due to RD oscillations, and these also influence the microband structures and are also the major source of the deviation of microbands away from crystallographic planes. However, it is confirmed that microbands are largely crystallographic because: (i) their average planar orientations are close to the expected slip planes, and (ii) their straight segments are aligned crystallographically.

Chapter 5

Result and discussion–Part II

Microstructure evolution at low strain deformation in a Goss oriented Ni single crystal

5.1 Introduction

Similar to that described in Chapter 4, a Goss–oriented {110}<001> Ni single crystal was deformed by channel–die plane strain compression (PSC). For the work in this Chapter, a lower true strain of ε =0.10 (~10% reduction) was generated in order to investigate the early stages of microband evolution.

5.2 Results and discussion

5.2.1 EBSD investigation

Figure 5.1a shows an EBSD orientation map of a large area in the RD–ND section. In this map the ideal Goss orientation is plotted in yellow and the gradient towards dark colours denote orientations away from this orientation within a 4.5° spread. The black lines represent boundaries having >0.6° misorientations. Overall, the majority of the boundaries are low angle <1.2°. This is highlighted in the misorientation angle histogram in Figure 5.1c. Two sets of elongated and straight bands become apparent in the EBSD map. They are inclined at ±45° with the RD. This is highlighted by the lines drawn along the boundary traces. These boundaries might represent the DDW boundaries of concern. The traces of {111} crystallographic planes (dotted lines) are also superimposed on this figure and they do not match with the overall alignment of DDW traces. The orientation data of the entire scanned area is presented in a <001> pole figure in Figure 5.1b. Like the 30% deformed sample, this plot also shows a TD spread that makes the <100> pole plot elongated towards the RD. The spread is ±2.5°, which is 40% of the ±7.5° spread found in the 30% deformed sample. Another major difference with the 30% deformed sample is in the distance between DDWs which is large (5–10 μm) in the current sample. There are various other interesting boundary features in this sample and these are discussed in the following sections.

The interactions between two sets of DDWs may result in dissolution of boundary segments in any given set. Such an event is encircled in Figure 5.1a, whereby the arrow pointed boundary segment X is dissolved because of the evolution of the Y boundary. Another interesting feature also found in the evolution of the second set of DDWs within a DDW channel in the first set. It is found that a string of new DDWs

evolve in the arrow pointed spots in the DDW in channel B. Similar patterns are also found in DDW evolution in channel A and C. Whereas in the channels just above A and B (pointed by black arrows) there is no sign of new boundary evolution, and therefore have less orientation variation along the length.

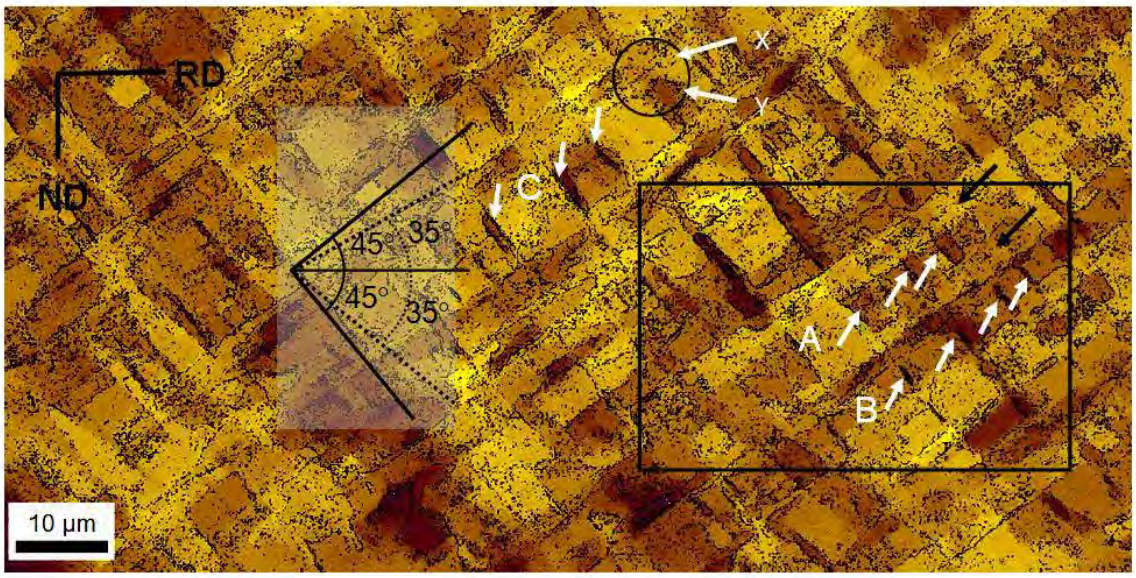

(a)

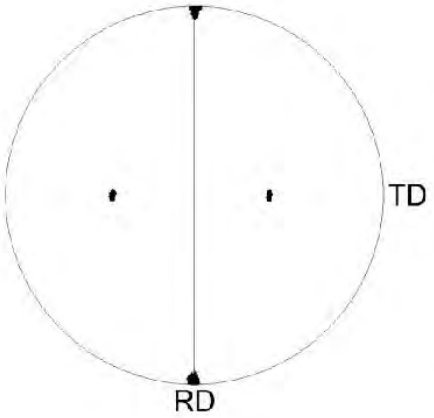

(b)

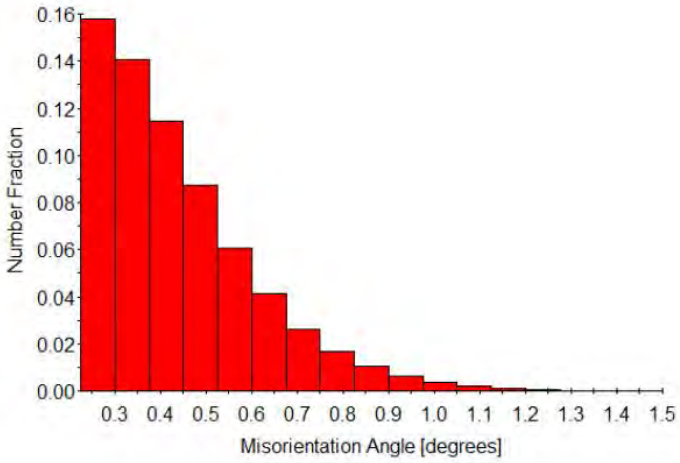

(c)

Figure 5.1: (a) EBSD orientation map; (b) <001> pole figure, and (c) misorientation histogram of a large area in RD–ND section in the 10% deformed Goss–oriented Ni single crystal.

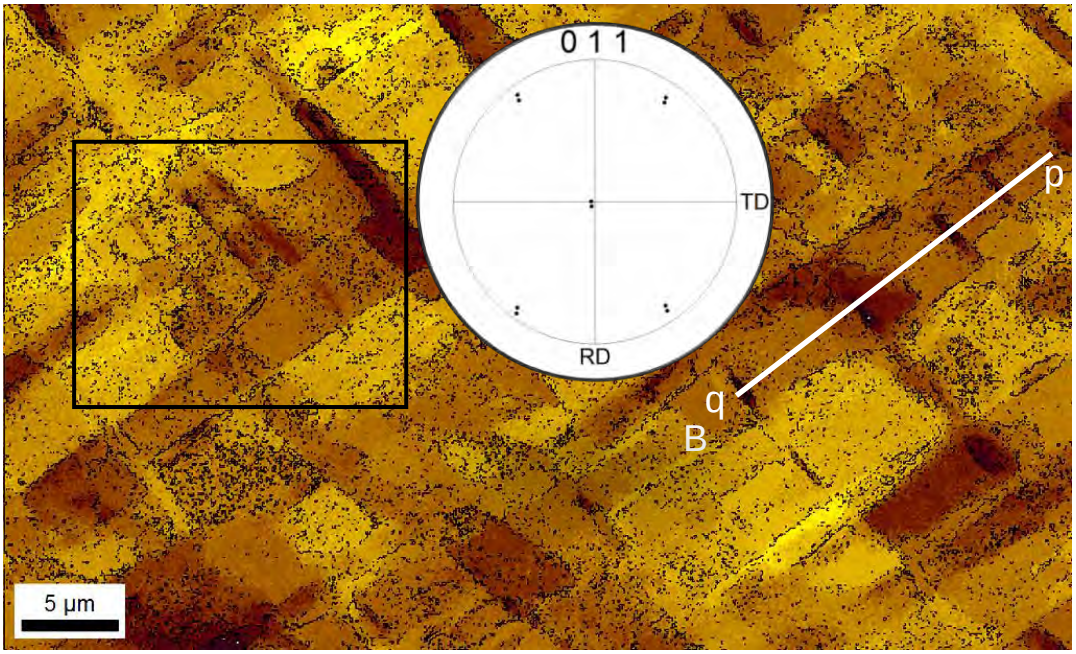

(a)

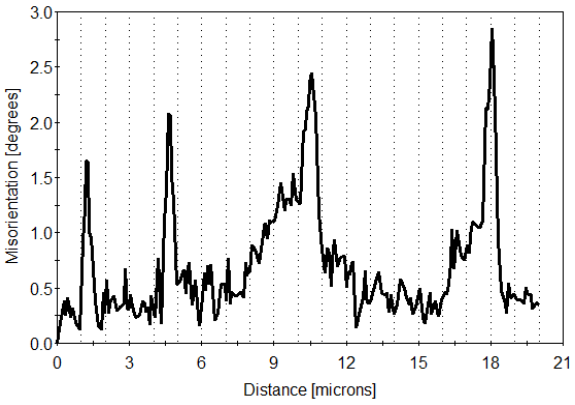

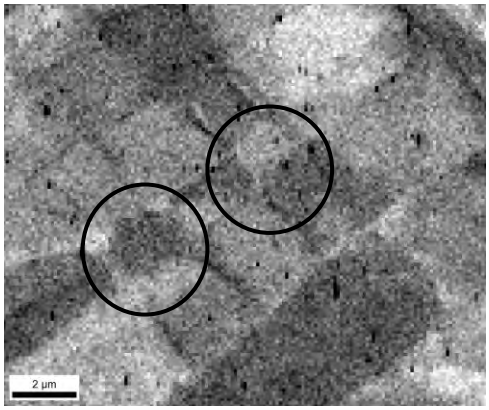

(b) (c)

Figure 5.2: (a) High resolution orientation map of the rectangular area in Figure 5.1a; (b) orientation profile along p–q in Figure 5.2a, and (c) band contrast map showing the variation in defect density at the intersecting points.

A high resolution EBSD scan was conducted within the rectangular area in Figure 5.1a, and shown in Figure 5.2a. An orientation profile (in Figure 5.2b) along p–q line includes the newly evolving boundaries in channel B, and they have generated 1.5–2.5° orientation differences corresponding to the DDWs with the point of origin (p). A complementary TEM investigation in the next section will provide insight into the dislocation structures associated with these types of events. The rectangular area in Figure 5.2a are re–plotted in Figure 5.2c to highlight the band contrast, whereby it is apparent that the contrast is prominent at the intersections (encircles). This indicates that

dislocation density varies at the intersections, and this conversely implies that existing DDWs contribute dislocations for generating new DDWs and vice versa. The embedded <110> pole figure shows the orientation relationship across one of these DDWs to have a shift around the TD. To save space this pole figure is plotted up to 65° angular range from the ND.

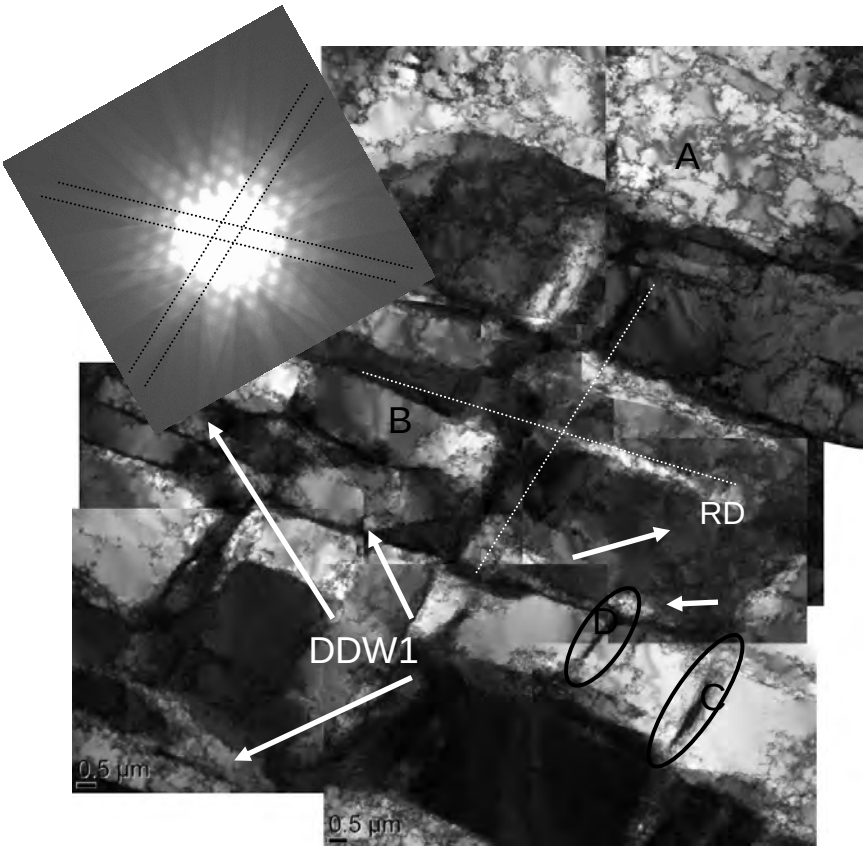

Figure 5.3: Bright field TEM micrograph with a CBED pattern showing two intersecting sets of DDWs in the RD–ND section.

5.2.2 Transmission electron microscopy

Figure 5.3 shows a montage of bright field TEM images of a large area in the RD–ND section of the 10% deformed Ni sample. The beam direction is close to a <110> crystal axis. In this image the two intersecting sets of DDWs are apparent. The included angle between them is well matching with that in their {111} crystallographic traces (see the attached CBED, which is taken from one of the DDW sets within this area). The high sharpness in one set of DDW boundaries (arrow pointed DDW1) indicates that they are aligned closely parallel to the beam axis. Based on these findings,

DDWs can be classified as crystallographic entities, which is in contradiction with the EBSD maps in Figures 5.1 and 5.2, whereby the included angle between two DDW sets was ~90° and, hence, they appear non–crystallographic.

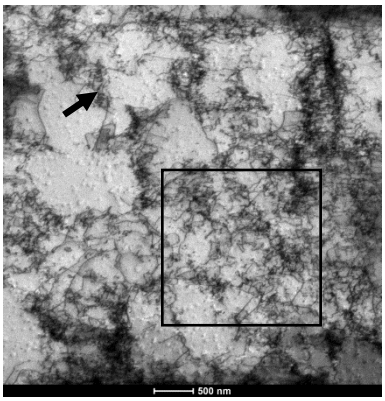

(a) Mash and cell

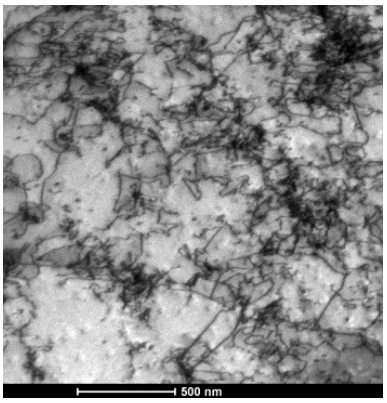

(b) Mash

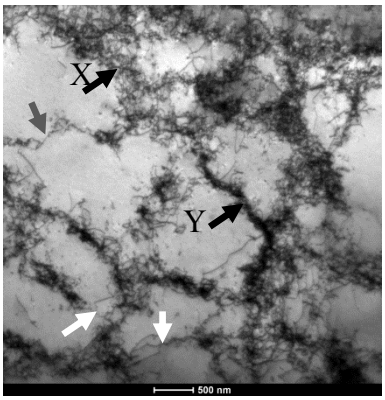

(c) Cell

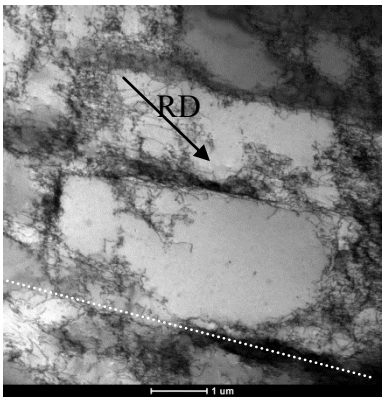

(d) Loosely packed dislocation boundaries and cleaner interior.

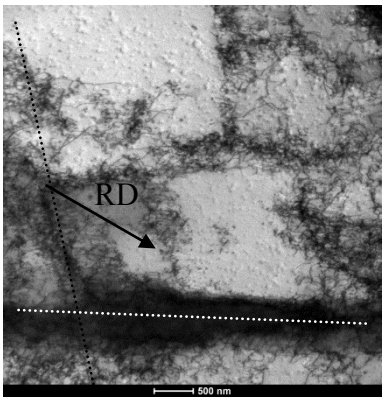

(e) Loosely packed dislocation boundaries and cleaner interior.

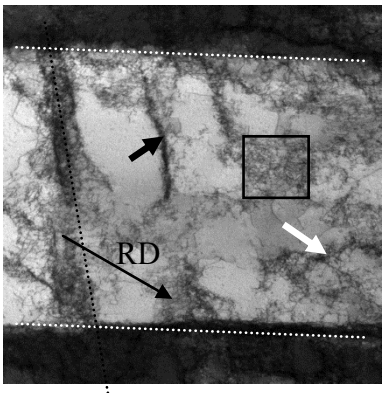

(f) Evolution of dense and sharp boundaires.

Figure 5.4: Dislocation decorations prior to DDW formation: (a) combination of mash and cell structures; (b) dislocation mash structures; (c) cell structures, and (d)–(f) dislocations structures in existing DDW structures.

There are other important features in the TEM image in Figure 5.3. For example, area A is an interior space between two DDWs and is decorated with well–defined cell structures. The density of cell structures is less in the other areas having denser DDWs. For example, in area B there is a denser distribution of DDWs. In this area cell and mash structures are not present. Therefore, the dislocations within cell boundaries may have contributions in the formation of new DDWs. An example is encircled as C, where

it is obvious that the surrounding of the newly forming DDW is clean (free from cell or mash dislocation structures). The newly forming DDW D is growing from an existing DDW and thus the dislocations from existing DDWs also contribute to generate new DDWs. The details of these features will be highlighted in the following higher resolution TEM studies.

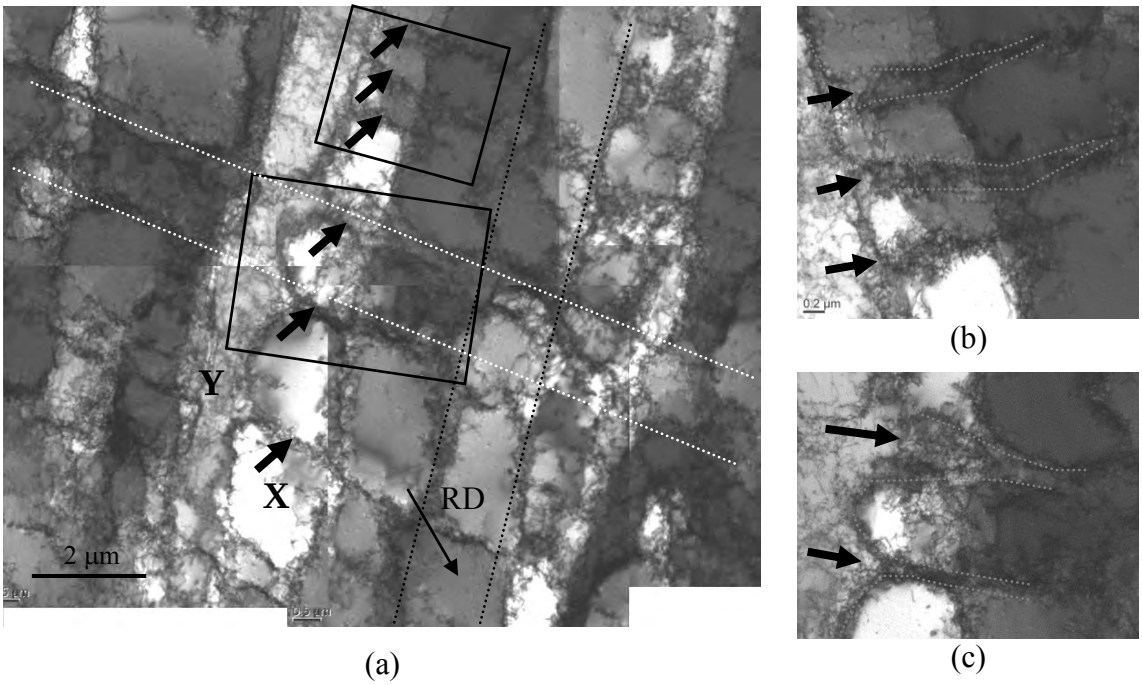

Figure 5.5: Evolution of string of microbands from the existing dense dislocation walls.

Figure 5.4 shows a series of TEM images to demonstrate dislocation decorations in the deformed structures in RD–ND section of the 10% deformed sample. Figure 5.4a covers an area that includes the very initial stage of cell boundary formation (a less compacted cell boundary is arrow pointed) in the matrix of mash dislocations matrix. The mash region in Figure 5.4a is expanded in Figure 5.4b to show the random distribution of dislocations in the mash structures. The orientation/alignment of the dislocations lines do not have a specific pattern. Also, all the dislocations in the mash matrix do not turn invisible in a single diffraction condition. In Figure 5.4c the cell structures become well developed. The cell width varies between 1–2 μm and no/negligible dislocations are visible in their interiors. In this micrograph both loosely packed (X arrowed) and densely packed (Y arrowed) cell boundaries are present. At some locations the connectivity of cell boundaries are completed by single dislocation

lines (at white arrows). Therefore at this stage of deformation, cell boundary width can be as fine as the width of a single dislocation and as wide as that in the loosely pack boundary X (~400nm). A well−formed cell boundary, such as Y, is ~150 nm wide. Within cell boundaries there are evidences of dislocation jogs. Examples of jog structures are found in the boundary pointed by a gray arrow. In this region the cell boundaries are largely equiaxed. Non−equiaxed cell boundaries, aligned along existing DDWs, are also found in this sample.

Figure 5.4d−f show densification of dislocation structures along the DDW boundaries (along white and black dotted lines). At this stage, the areas enclosed by DDWs are reasonably clean. Within a boundary pair (white dotted lines in Figure 5.4f), mash (see the area in the rectangle), cell boundaries (pointed by a white arrow) and evolution of DDW (pointed by a black arrow) parallel to the existing DDWs are found. Therefore, it can be concluded that mash and cell structures continue evolving in the DDW structures, and densification of DDWs occurs through their rearrangements. It is therefore a cyclic process.

Series of microband evolution from a DDW:

Figure 5.5a shows two sets of intersecting DDWs along the black and white dotted lines. Within the DDW enclosed channel, marked as X (parallel to black lines), a series of DDWs have started forming parallel to the white lines (arrow pointed). It is important to note that they start forming from a string of points on an existing DDW. It has been previously shown that microbands start forming on grain boundaries in a similar way [Chen *et al*. 2003; Chen and Duggan, 2004], and that finding led to a conclusion that the dislocations in the pre−existing grain boundary contribute to form new microbands. Likewise, it is plausible that the preexisting DDW helps to form the pair of dislocation boundaries of the newly forming microbands. In terms of boundary arrangement this image is comparable with Figure 5.1a, whereby a series of new DDWs started forming along channel A and B. In between the newly forming boundaries the spaces are free from dislocations. No DDW evolve in the upper channel, marked as Y, within which the structure is largely made of dislocation mash structures. The rectangular areas in Figure 5.5a are expanded in Figure 5.5b and c. In Figure 5.5b the new DDWs (arrowed) have not affected the topography of the existing DDW, whereas

in Figure 5.5c segments of existing DDWs have dissolved at the points where the new DDWs started forming. Both Figure 5.5b and c show that during propagation the newly forming DDWs are splitting to form a pair of boundaries of microband channel (see the dotted lines in gray).

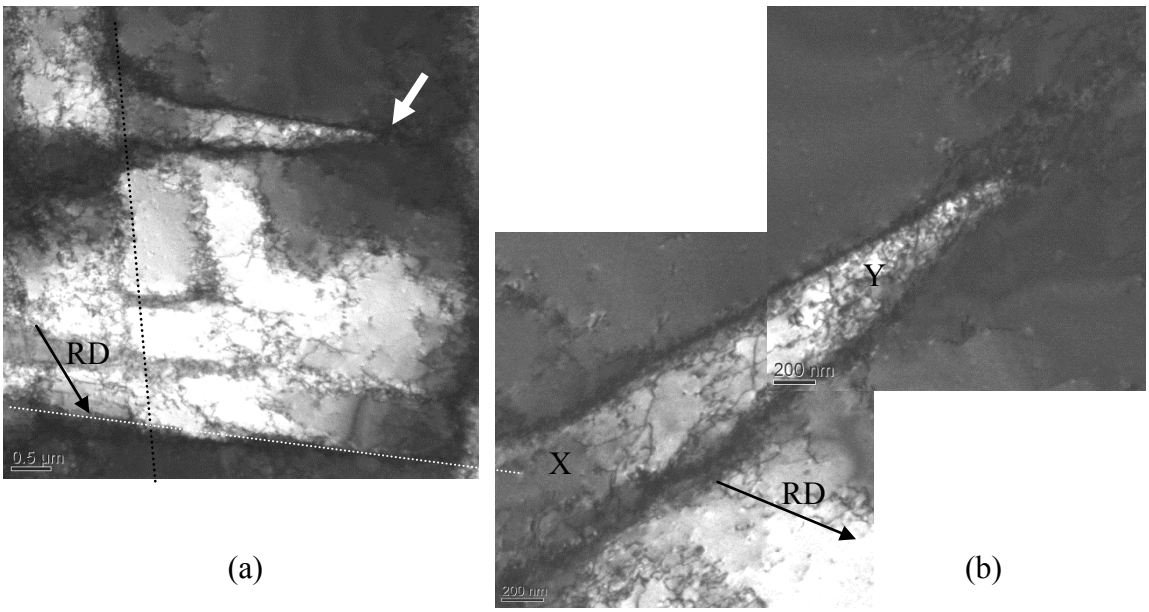

Figure 5.6: Bright field TEM images showing the formation of a microband channel by splitting an existing DDW.

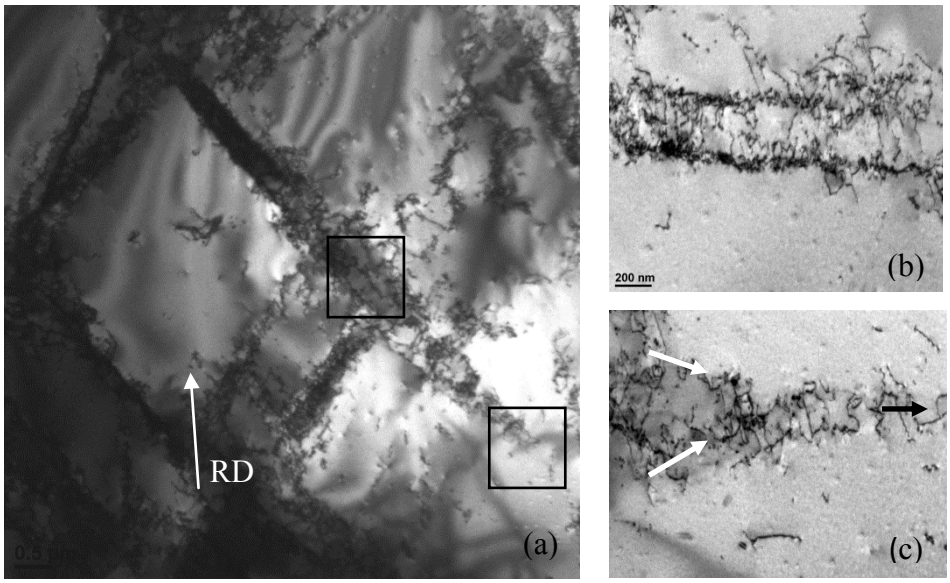

Figure 5.7: Dislocation structure in the advancing tip of a microband.

Figure 5.6a shows an example of the formation of a pair of dislocation boundaries of a microband channel by splitting a DDW. The detail of this event is shown in the magnified image in Figure 5.6b. The interior dislocation structures between the newly forming pair also varies along the length. In region X, where the splitting is already well advanced, a small number of dislocations are present, whereas, in region Y, which is close to the splitting head, the dislocation density is relatively high. The thickness of the newly forming microband channel is ~1 μm, which is equal to the typical width of microbands measured in many investigations. Splitting therefore considered as the mechanism of microband boundary formation in this material.

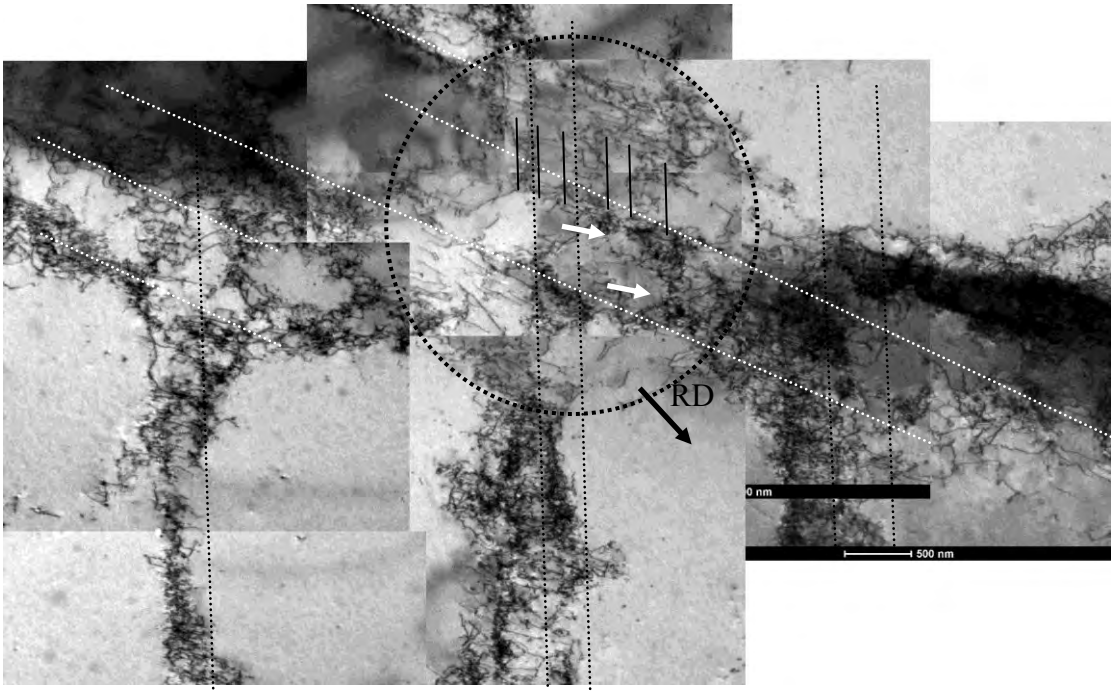

Figure 5.8: Dissolution in dislocation structures in DDWs as a result of interactions.

Microband tip:

Figure 5.7a shows a microband propagation in a dislocation free region. The magnified images in Figure 5.7b and c show the detail of the rectangular areas in Figure 5.7a. In figure 5.7b, a boundary pair becomes obvious. In Figure 5.7c, it is obvious that the tip progresses in a region having no existing dislocation structure. At the tip, a single dislocation boundary propagates along the black arrow trailing behind a pair of boundaries (indicated by white arrows).

Interaction between dislocation boundaries:

In Figure 5.8 the traces of two intersecting DDWs are outlined by the white and black dotted lines. Within the encircled region the dislocation structures of existing DDWs are severely disrupted by each other. In this region the boundaries almost turned to cell structures (white arrows pointed cell boundaries), some of which have aligned along the pre−existing DDWs (see the solid lines enclosing short segments of dislocation boundaries).

5.3 Conclusions

The deformation features in 10% deformed Goss−oriented Ni single crystal (by plane strain compression) were characterized by 2D−EBSD and TEM. The significant findings are listed in the following,

- There is a discrepancy between the EBSD and TEM measurement in the inclination of DDWs in RD−ND sections. The measured inclinations by EBSD and TEM are ±45° and ±35°, respectively.
- DDWs form by arranging the dislocations from the mash and cell structures. The spacing between DDWs is large in 10% deformed sample (5−10μm). Evolution of new dislocation structures within existing DDWs continue in the form of mash and cell structures, and later these turn into new DDWs. Through this evolution cycle densification of DDWs occurs.
- Microband formation occurs by splitting existing DDWs. Microband channels that form by splitting DDWs have the typical dimension of <1 μm.
- At the growing head of a microband channel, a single DDW propagate and then it splits into a pair of boundaries to generate a microband channel. These microbands are also with the typical dimension of <1 μm.
- Dissolution of DDW is possible when two sets of DDWs intersect. The dislocations involved in such an event get rearranged into mash and cell strcutures.

Chapter 6

Result and discussion–Part III

Unusual high angle microband boundaries in a 50% cold rolled IF steel

6.1 Introduction

Based on the extensive analyses and discussion in chapters 2 and 4, it is now clear that microband is a common deformation feature in medium to high stacking fault energy alloys. They appear in parallel arrangements of dense dislocation walls (DDWs) that separate <1μm dislocation–free channels [Humphreys and Hatherly 2004, Hughes and Hansen, 2000, Bay *et al*. 1992, Hughes and Nix 1989, Hughes and Hansen 1993]. The misorientations across microband boundaries are of low angle nature. This has been known for long time from the earlier TEM diffraction analyses and recent EBSD measurements. For example, Albou *et al.* [2010] recently reported 0.8°, 1.0° and 2.0° average misorientations across microband boundaries within the deformed grains of both high purity Al and Al–0.1%Mn after 14, 40 and 80% deformation in plane strain compression. Likewise, Hurley *et al.* [2003, 2003a] and Humphreys and Bate [2007] observed <2.5° mean orientation differences between adjacent microbands within deformed grains of Al–Mg alloys deformed up to 90% reduction by cold rolling. Among the recent TEM investigations, Chen *et al.* [2003] and Huang and Winther [2007a–b] reconfirmed that microbands are low–angle microscopic features in the deformation microstructures.

Based on extensive research over many years, 8° appears to be the upper limit for the misorientations associated with microband boundaries. In the present work, microbands with classic structural features, but exhibiting misorientations much greater than 8°, have been discovered in the deformation microstructure of cold rolled interstitial free (IF) steel. They exclusively form in some {111}<110>–oriented grains, while other γ–oriented (<111> || ND) microband–containing grains generate the typical low–angle version of microbands.

6.2 Sample processing and preparation

A Ti–bearing IF steel in the form of hot band, and containing a 40 μm average grain size, was homogenously cold rolled by successive 10% reductions in thickness to a total strain of ~50%. After appropriate electropolishing in a 90% acetic acid and 10% perchloric acid mixture, the RD–ND sections of the sample were characterized using a Tecnai TEM (operating at 200 keV) and a TSL^{TM} EBSD (attached to a JEOL 7001

FEGSEM). Comparable TEM images were captured for each EBSD area to ensure that the features under investigation are typical microbands, and because the original microband characterizations by the Risø workers were performed by TEM.

6.3 EBSD and TEM characterization

Figure 6.1a is a typical EBSD map of an RD–ND section containing an array of classical microbands inclined at ~25° to the RD. Here, the black lines represent boundaries between adjacent microbands with >12° misorientation. A >20° misorientation plot detects shorter boundary segments, but they still appear in acceptable lengths of more than five continuous data pairs. In this area, there are adjacent microbands exhibiting very large misorientations, as compared to the usual <8° values. An orientation profile across many boundaries reveals the frequency of occurrence of such high–angle boundaries (HABs). An example is shown in Figure 6.1b, in which the black and grey lines represent the 'point–to–origin' and 'point–to–point' misorientations along X–Y in Figure 6.1a. Here, the misorientations across microband boundaries vary up to an unusually high value of 20°. There is also a cyclic trend in the orientation changes, which is realized from the increment in the point–to–origin profile in one boundary and a reduction (by the same amount) in the other boundary of a given microband. This is highlighted by the encircled region of the EBSD map and the corresponding orientation profile. Across this boundary pair the point–to–point misorientation is almost equal. Thus, in a given microband array an orientation pair appears in an alternating sequence.

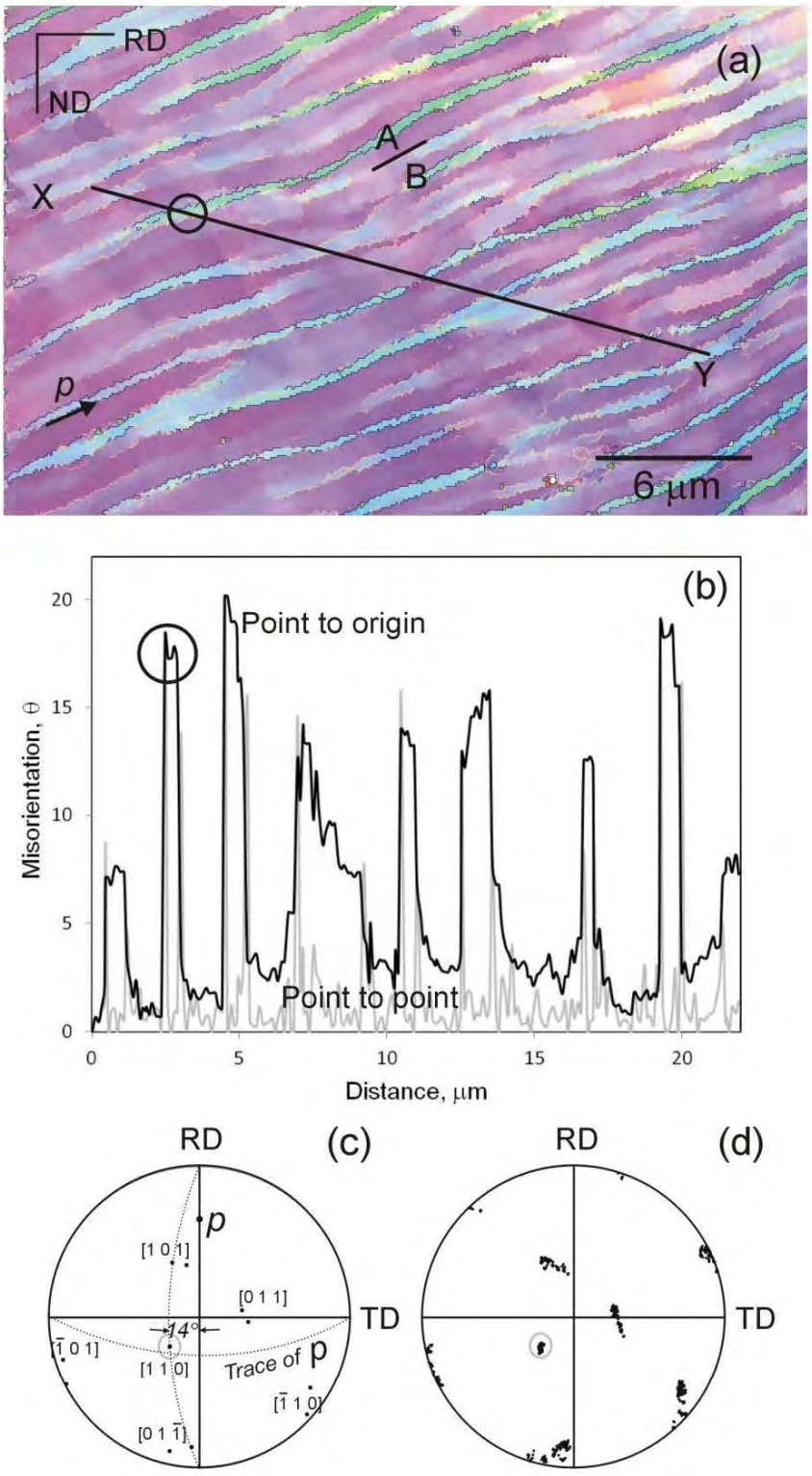

Figure 6.1: ESBD map with corresponding orientation profile and <110> pole figures showing: (a) the >12° microband boundaries (in dark lines) in a RD–ND section; (b) a cyclic orientation profile along the X–Y line, and (c)–(d) minimum spread at a <110> pole (encircled) of microband orientation pairs.

The significant color contrast between the lower–left and upper–right corners of Figure 6.1a is a typical indicator of the large variation in orientation within the grain containing the microband structures. Therefore, an orientation plot of the entire dataset shows a large spread, in which the average orientation is centered at (1 1 1)[0 1 $\bar{1}$]. In order to be precise at the local scale, the orientation dataset along X–Y in Figure 6.1a (covering ~20 microband channels) is plotted as a <110> pole figure in Figure 6.1d. The encircled [110] pole shows minimum spread, as compared to the other five <110> poles. This indicates that the rotation axes across the microband boundaries lie close to this pole. To be more specific, the orientation data across the A/B boundary segment in Figure 6.1a is plotted in a <110> pole figure (Figure 6.1c) showing a precise coincidence at the [110] pole. Many of these orientation pairs were tested within Figure 6.1a, whereby perfect coincidence, like that shown in Figure 6.1c, was not always found, but nevertheless remain within 5° angular distances. Similarly, <002> and <112> pole figures were plotted (not shown), but no such convincing coincidence was found. The bright field TEM image in Figure 6.2 (ND–RD section) shows that the microbands shown in Figure 6.1a have typical microband features similar to that observed by the Risø group, i.e., with the following three main characteristics. They:

- consist of dense dislocation walls (parallel dark lines) separated by an average distance of ~0.75 μm;
- are inclined ~28° with the RD, and
- are relatively dislocation–free.

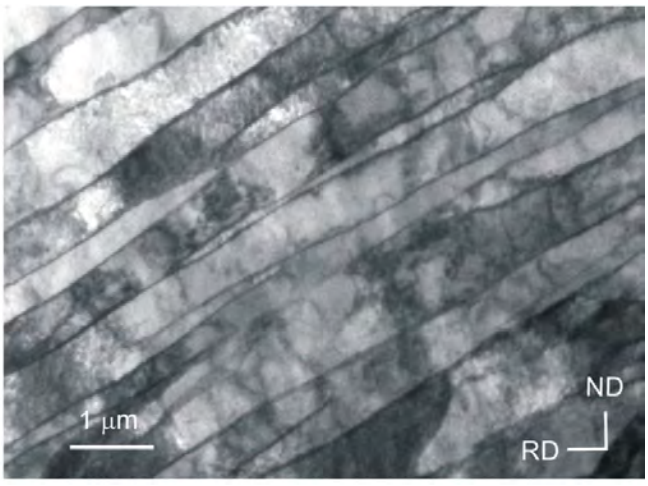

Figure 6.2: Bright field TEM micrograph of microband structures in RD–ND section showing the close resemblance with the EBSD map in Figure 6.1a.

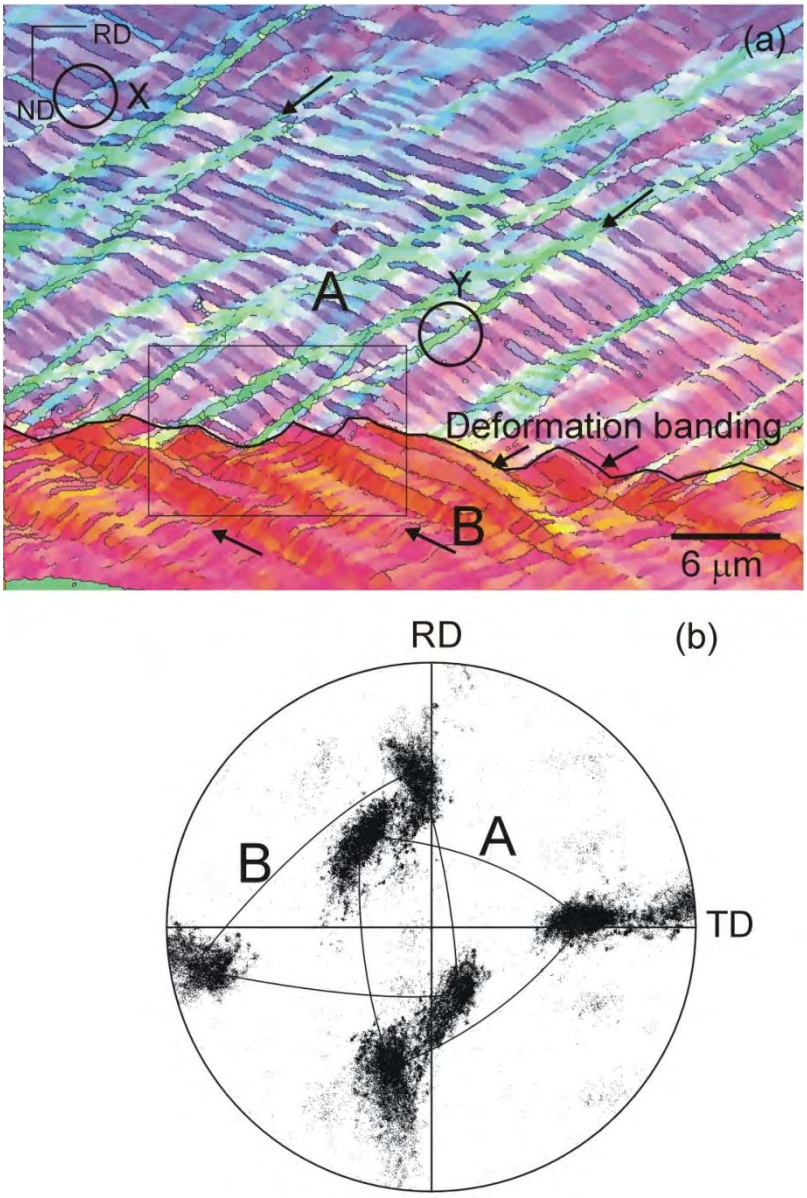

Figure 6.3: RD–ND section EBSD map (a) and corresponding <200> pole figure (b) showing deformation– and in–grain shear banding structures in a microband matrix having alternating orientation contrasts and high–angle boundary interfaces (>12° boundaries are given as dark lines).

The large area EBSD map presented in Figure 6.3a reveals numerous micro–shear bands (arrowed) within a microband–containing grain, as well as evidence of a deformation band that divides the upper (A) and lower (B) regions by a high–angle interface (represented by the black superimposed line). It is generally reported that deformation bands break up large initial grains into segments, each of which later adopt

a unique deformation mode and, hence, develop microstructures as independent grains [Tse and Duggan 2006, Quadir and Duggan 2004]. In regions A and B of Figure 6.3a, the microbands appear in alternating color contrasts, and in opposite inclinations with the RD. The overall orientations of the upper and lower regions are shown in the <200> pole figure in Figure 6.3b to be centered at (1 1 1) [1 0 $\bar{1}$] and (1 0 1) [1 0 $\bar{1}$] orientations, respectively. While the latter orientation is not part of the γ–fibre, it is generally found to be present with fairly strong intensities (*i.e.* 4–5× random for a maximum intensity of 8× random) in the rolling texture of micro–alloyed and ultra–low carbon steels [Nave and Barnett 2004]. In the upper left–hand corner of region A (encircled area X) there is clear evidence of the classic kink–like structures associated with so–called *S*–bands. These *S*–bands appear in opposite inclination angles to the microband matrix. In the areas close to the deformation band (encircled area Y) they become enclosed by a pair of >8° boundaries. Their chronological transitions from that in area X to Y are described in detail by Quadir and Duggan [2006]. These bands remain restricted within original hot–band grains and carry large shear strains and, therefore, are frequently called by 'micro–shear bands'. The average width of these bands (~0.5 μm) is about half of that of microbands. In region B of Figure 6.3a, the microbands are crossed by the thicker version of micro–shear bands and their thickening mechanism is also described by Quadir and Duggan [2006]. Although shear banding and deformation banding are not the principal focus of this chapter, the area shown in Figures 6.3 is important to study for representing another classical scenario of microband structures containing *S*– and micro–shear banding. Previously, Chen *et al.* [2003] argued that the microband structure is a precursor for *S*– and micro–shear band formation in the γ–oriented grains of the rolling microstructures of micro–alloyed and ultra–low carbon steels.

Figure 6.4a is a high resolution EBSD map of the rectangular area shown in Figure 6.3a. An orientation profile along A–B (in Figure 6.4b) shows that the misorientations across the microband boundaries vary from 8 to 20° (see the point–to–point profile, grey line). Similar to Figure 6.1c, a cyclic orientation profile is also present in the point–to–origin plot. Likewise, the curves in Figure 6.4c represent the same characteristics for the line C–D. The orientation data associated with the A–B

and C–D lines are plotted as <1 1 0> pole figures in Figure 6.5a and c, where it is clear that the rotation axes lie close to the encircled <1 1 0> poles. A more precise orientation plot across X/X′ and Y/Y′ microband boundaries are given in Figure 6.5b and d, respectively, showing that the rotation axes are consistently close to a <1 1 0> pole.

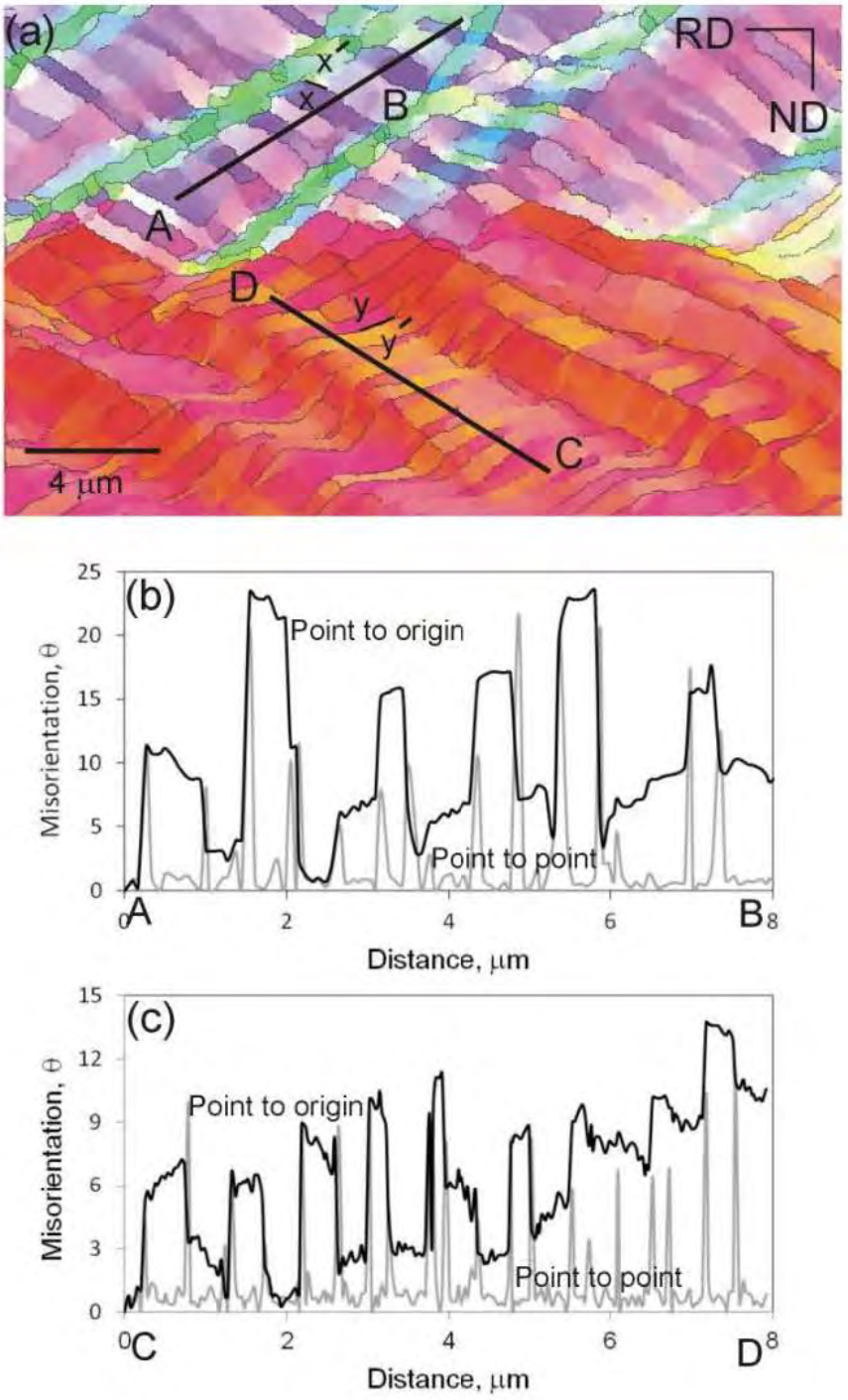

Figure 6.4: (a) High resolution EBSD map of the rectangular area in Figure 6.3a, and (b)–(c) orientation profiles along A–B and C–D in (a).

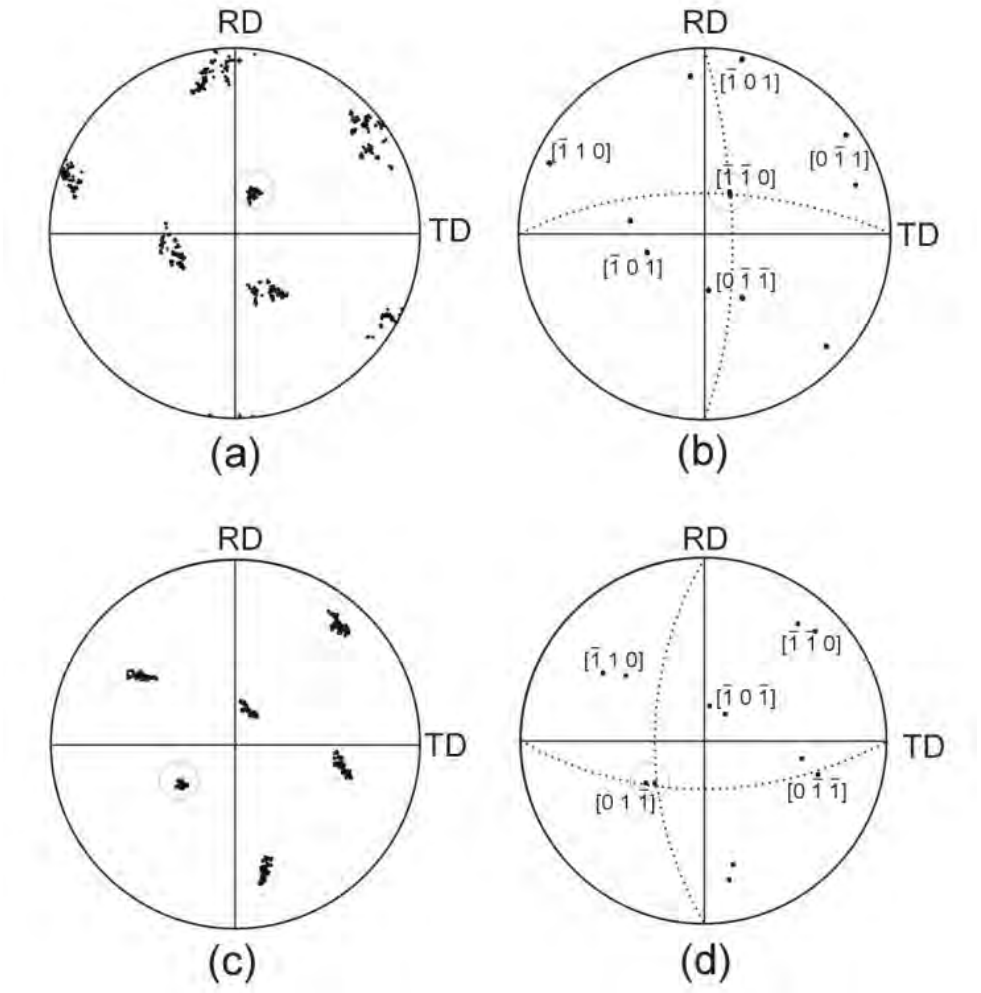

Figure 6.5: <110> pole figures showing the orientation plot of the line scans along (a) A–B and (c) C–D, and data points across (b) x/x′ and (d) y/y′ interfaces in Figure 6.4.

Finally, two bright field TEM images are given in Figures 6.6a and b to compare the *S*–band and micro–shear band structures between TEM and EBSD observations. Figure 6.6a is consistent with region A in Figure 6.3 containing *S*–bands within a region of microbands. The overall orientation of this area is centered at (116 148 $\overline{120}$) [13 $\overline{11}$ 1], *i.e.* close to (1 1 $\bar{1}$)[1 $\bar{1}$ 0], as determined by CBED (see inset in Figure 6.6a). The kinked segment in the *S*–band is misoriented by 7–10° from the straight microband segments. The microband and *S*–band boundary traces were found to align with [5 $\overline{16}$ 5] and [$\overline{16}$ 5 5] directions and, hence, they coincide with the (1 0 $\bar{1}$) and (0 1 $\bar{1}$) plane traces. In this image there is a grey–scale contrast between neighbouring microbands, which evolve from orientation dependent electron channelling (*i.e.* diffraction contrast). An alternating arrangement of this feature in the microband array is therefore

significant. Figure 6.6b is consistent with the microband structures in region B of Figure 6.3a, whereby a microband array is intercepted by wider (~1.5 μm) micro–shear bands. The microband boundary segments inside the shear band deviate from that in their matrix, the overall orientation of which is centered at (20 $\overline{27}$ 21)[$\overline{34}$ $\overline{21}$ 4], *i.e.* close to (1 $\bar{1}$ 1)[$\bar{1}$ $\bar{1}$ 0]. The traces along the microband ([$\overline{39}$ 6 6] ≈ [$\bar{1}$ 0 0]) and shear band ([$\overline{16}$ $\overline{32}$ 16] ≈ [$\bar{1}$ $\bar{2}$ 1]) boundaries coincide with the traces of (011) and (101) planes.

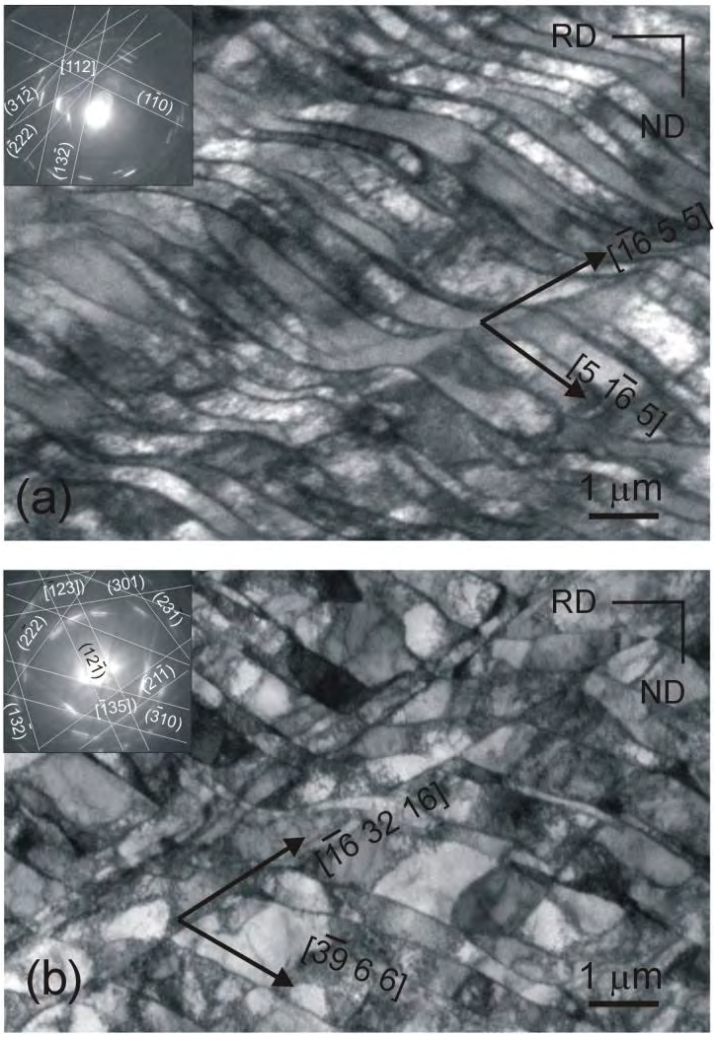

Figure 6.6: Bright field TEM micrographs of RD–ND sections showing (a) *S*– and (b) micro–shear bands in microband matrix structures. The CBED-measured Kikuchi patterns (insets) represent matrix orientations.

6.4 Discussion

In this investigation, unusual features have been found in typical microband structures in cold rolled IF steel. The typical characteristics of these microbands include the presence of dense dislocation walls at <1 μm repeat distances, 25–35° inclinations with the RD and the crystallographic alignment with the highly–stressed slip planes. The unusual microband features are discovered from their boundary crystallography, including: (i) high misorientations up to ~20° between adjacent microbands, and (ii) equal and opposite rotations with neighbouring microbands around a <110> pole. These characteristics are exclusive to {111}<110> orientations in cold rolled IF steel.

Microbands are commonly observed in the microstructures of γ–fibre grains of many types of cold rolled steel. The γ–fibre consists of (2×) {111}<110>, (2×) {111}<112> and (3×) {111}<123> texture components. A connection between these variants constitutes the complete γ–fibre skeleton, as shown in the ϕ_2=45° section of Euler space (Figure 6.7a). The rolling texture of the steel is shown in Figure 6.7b, has the {111}<110> orientation as the peak intensity, thereby indicating the high orientation stability of this component. It is important to note that {111}<110> is a common texture component of both the α– and γ–fibres. Consequently, grains of this orientation comprise both smooth 'α–type' and fragmented 'γ–type' microstructures. It has been explained from a rotation trajectory that, if a grain rotates to {111}<110> through the α–fibre components, it generates an α–type smooth substructure. Conversely, if it rotates through the γ–fibre orientations then complex γ–type substructures are generated. Therefore, the coexistence of both microstructures in a given grain is rare after medium to high levels of rolling (>50% reduction). Although the {111}<110> orientations are easy to locate in the deformation microstructure due to their high intensity and wide variations in structures, the unusually high–angle microband boundaries highlighted in the present investigation have not been reported.

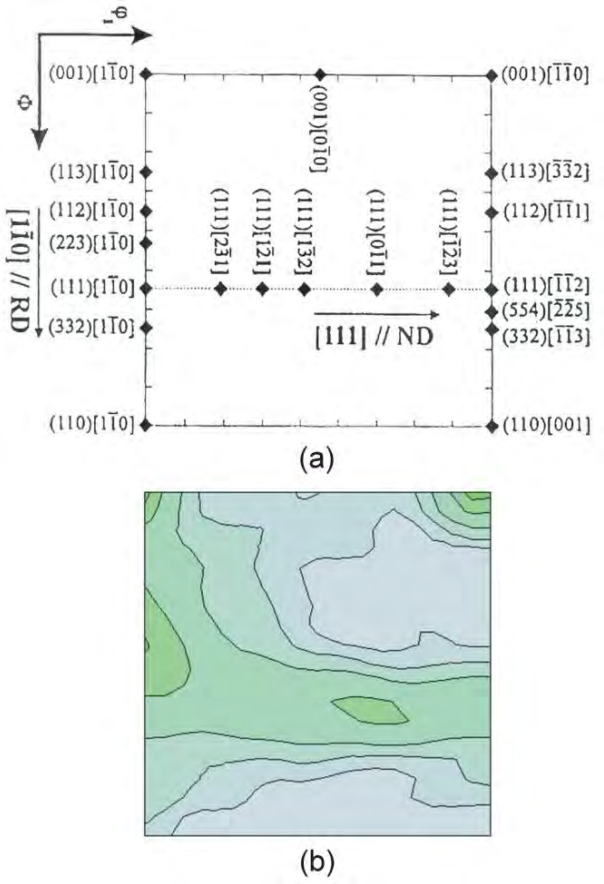

Figure 6.7: ϕ_2 = 45° section of Euler space showing: (a) predominant orientation positions of BCC rolling textures, and (b) x–ray measured rolling texture of the 50% cold rolled IF steel (Intensity levels: 1, 2, 4, 6 and 8).

There are two main theories for addressing the evolution of microband boundaries. These are described in chapter 2 and 4. The earlier theory is based on dislocation cross–slip and it was proposed by Jackson [1983a-b]. Briefly on this theory, at the growth head of a microband channel one set of dislocations experiences cross–slip and gets separated from the remaining dislocations and, thus, they form a pair of dislocation walls. Therefore, freshly–formed microbands generate dislocations in their walls with identical configurations. Across the walls, rotations by an equal and opposite angle have been observed, *i.e.* the rotation generated by the first wall is balanced by an opposite rotation across the second wall. In this theory, the axis of the rotation was also predicted as the normal of the most highly stressed slip system. Experimental evidence of this theory is provided in the monograph by Basinski and Basinski [1979] and Foxall *et al.* [1967].

According to the later theory, a dense dislocation boundary tends to split after generating a considerable misorientation (>1.5°) and, thus, a pair of microband boundaries evolves [Bay *et al.* 1992, Hughes and Nix 1989, Hughes and Hansen 1991]. The resultant misorientations of the newly–formed pair remain equal to the original boundary and, therefore, they are related by opposite rotations to each other. Evidence of boundary splitting has been observed in a wide range of metals and alloys [Bay *et al.* 1992, Hughes and Nix 1989, Hughes and Hansen 1991]. In the present work, there is also evidence of boundary splitting in several locations of the deformation microstructure (see Figures 6.1–6.4). In chapter 5 it has been demonstrated that splitting is a major source of convoluted microband interfaces in 10% deformed Ni single crystal. In both theories described herein, the alternating rotation phenomenon with neighbouring microbands can be explained, although only a few degrees of misorientation is possible for the double cross–slip mechanism [Jackson 1983A, 1983B]. The slightly larger misorientations can be explained by the boundary splitting mechanism [Hughes and Hansen 1991]. Overall, while the current theories are capable of explaining the origin of reasonably small misorientations between adjacent microbands, they cannot account for the large microband boundary misorientations observed in the present investigation.

The large microband boundary misorientations (up to 20°) observed herein have an important ramification on the question of their crystallographic alignment, *i.e.* a boundary interface separating two widely misoriented lattices cannot be in mutual crystallographic alignment with both, except for two situations. The first situation may arise due to the presence of a coincident site lattice (CSL) interface. However, CSLs are specific in misorientation and boundary interface parameters, which are not found in the current dataset. In the second situation, if the rotation axis between adjacent microband orientations coincides with their boundary surface normal then the formation of a high–angle crystallographic interface is possible. Therefore, this is a three dimensional problem. The 3D–EBSD results in chapter 4 showed that microband boundaries were irregular and curved but crystallographically aligned [Quadir *et al.* 2007]. In these investigations, typical low misoriented (~5°) microbands were studied and, hence, the misorientation axis was not a major concern. Using a combination of conventional 2D–EBSD and TEM techniques, it is also possible to approximately deduce microband

surface alignments through conventional trace analyses. For example, direction '*p*' in Figure 6.1a lies along a microband boundary trace. From the angular relationships with RD and ND, *p* (and its trace) can be potted in the pole figure (Figure 6.1c), whereby the pole of the microband interface should lie on the 'trace of *p*'. The precise location can be worked out from the boundary alignments in the other orthogonal cross sections, RD–TD or TD–ND. It is inspiring to find that the common <110> pole falls on this trace at a distance of 14° from the RD–ND axis (which is the trace of the TD). This indicates that if the microband boundary trace has ~14° inclinations with the TD in the TD–ND cross section (an angle which is within the range of commonly reported inclinations [Chen *et al.* 2003, Hurley *et al.* 2003, Humphreys and Bate 2007, Quadir and Duggan 2004, Quadir and Duggan 2006, Tse and Duggan 2006], then the interface normal coincides with the common <110> pole. Similarly, the common <110> poles observed in Figure 6.5 possibly coincide with the corresponding boundary interface normal. Therefore, it can be concluded that the rotation axis across a given microband interface closely coincides with its surface normal.

Table 6.1: Calculated Schmidt Factors on highly stressed {110}<111> and {112}<111> slip systems of the orientations shown in Figures 6.1 and 6.4, and three supplementary examples having comparable microband features.

Orientation pair	High Schmidt factor containing slip systems, {110}<111> and {112}<111>							
	{110}<111>					{112}<111>		
	1	2	3	4	5	6	7	8
Figure 6.1 (11 19 14)[$\bar{1}$ 5 $\bar{6}$] (13 16 14)[$\bar{4}$ 19 $\bar{18}$]	(101)[11$\bar{1}$] 0.7 0.69	**(110)[1$\bar{1}$1]** **0.42** **0.57**	(101)[$\bar{1}$11] 0.33 0.37	(1$\bar{1}$0) [11$\bar{1}$] 0.32 0.39	(10$\bar{1}$) [1$\bar{1}$1] 0.38 0.33	(2$\bar{1}$1)[11$\bar{1}$] 0.59 0.64	(112)[11$\bar{1}$] 0.63 0.56	(21$\bar{1}$)[1$\bar{1}$1] 0.47 0.52
Figure 6.5b ($\bar{11}$ $\bar{7}$ $\bar{8}$)[11 1 $\bar{16}$] ($\bar{20}$ $\bar{15}$ $\bar{19}$)[19 0 $\bar{20}$]	(011)[11$\bar{1}$] 0.72 0.64	**(110)[$\bar{1}$11]** **0.46** **0.6**	(01$\bar{1}$) [$\bar{1}$11] 0.47 0.4	(101)[11$\bar{1}$] 0.48 0.28	(1$\bar{1}$0) [11$\bar{1}$] 0.23 0.36	(112)[11$\bar{1}$] 0.69 0.53	($\bar{1}$21)[11$\bar{1}$] 0.55 0.58	(12$\bar{1}$) [$\bar{1}$11] 0.54 0.57
Figure 6.5d ($\bar{16}$ $\bar{1}$ $\bar{15}$)[15 0 $\bar{16}$] ($\bar{4}$ 0 $\bar{3}$)[12 1 $\bar{16}$]	(110)[1$\bar{1}$1] 0.44 0.52	**(01$\bar{1}$) [$\bar{1}$11]** **0.42** **0.52**	(011)[11$\bar{1}$] 0.45 0.49	(110)[$\bar{1}$11] 0.39 0.29	(011) [1$\bar{1}$1] 0.39 0.27	(121)[1$\bar{1}$1] 0.48 0.46	(12$\bar{1}$)[$\bar{1}$11] 0.47 0.47	($\bar{1}$12) [11$\bar{1}$] 0.47 0.43
Other case 1 ($\bar{13}$ 16 12)[$\bar{4}$ $\bar{4}$ 1] ($\bar{12}$ 13 13)[$\bar{13}$ $\bar{19}$ 7]	(10$\bar{1}$)[111] 0.7 0.65	**(011)[11$\bar{1}$]** **0.51** **0.59**	(01$\bar{1}$) [111] 0.39 0.46	(10$\bar{1}$)[1$\bar{1}$1] 0.37 0.44	(1$\bar{1}$0) [11$\bar{1}$] 0.19 0.42	(11$\bar{2}$)[111] 0.63 0.64	($\bar{2}$11)[111] 0.59 0.48	($\bar{1}$21)[11$\bar{1}$] 0.41 0.59
Other case 2 ($\bar{5}$ $\bar{4}$ $\bar{4}$)[0 $\bar{1}$ 1] ($\bar{7}$ $\bar{5}$ $\bar{8}$)[3 $\bar{25}$ 13]	**(110)[1$\bar{1}$1]** **0.73** **0.81**	(1$\bar{1}$0) [11$\bar{1}$] 0.44 0.52	(10$\bar{1}$)[1$\bar{1}$1] 0.44 0.18	(011) [1$\bar{1}$1] 0.29 0.63	(101)[11$\bar{1}$] 0.73 0.46	(21$\bar{1}$)[1$\bar{1}$1] 0.68 0.57	(121)[1$\bar{1}$1] 0.59 0.84	(2$\bar{1}$1)[11$\bar{1}$] 0.68 0.57
Other case 3 (5 4 6)[14 $\bar{1}$ $\bar{11}$] (14 10 19)[15 $\bar{2}$ $\bar{10}$]	(110)[$\bar{1}$11] 0.67 0.66	**(011) [11$\bar{1}$]** **0.53** **0.43**	**(011) [1$\bar{1}$1]** **0.43** **0.52**	(101)[$\bar{1}$11] 0.39 0.48	(110)[1$\bar{1}$1] 0.27 0.23	(211)[$\bar{1}$11] 0.61 0.65	(12$\bar{1}$)[$\bar{1}$11] 0.55 0.49	($\bar{1}$21)[11$\bar{1}$] 0.56 0.52

The well–documented characteristic showing the close coincidence of microband boundary surfaces with the highly stressed slip planes can be checked for the current microband boundaries. The resolved shear stresses (in the form of Schmidt factors) on the (12×) {110}<111> and (12×) {112}<111> slip systems are calculated for six microband orientation pairs [Reid 1973]. It is to be noted that, in a given microband array, there are two sets of microbands (Figures. 6.1 and 6.3). In each set there are also orientation spreads of up to 10° (primarily along the microband length). Therefore, the central orientation of each set is taken as their representative orientation data and listed in pairs in the first column of Table 6.1. Here, rows 1–3 display the orientation data from Figures 6.1 and 6.5 and rows 4–6 show three other orientation pairs (figures are not included) having identical high–angle boundary characteristics. Of the possible {110}<111> slip systems, five of the highest stressed systems are tabulated in descending order in columns 1 to 5. Likewise, the three of the most highly stressed {112}<111> slip systems are tabulated in columns 6 to 8. It turns out that the planes representing the common poles in Figures 6.1 and 6.5 are either the first or second (shown in bold) most highly stressed slip planes. Therefore, this finding leads to the conclusion that the microband interfaces, which are previously found to accommodate rotations around their normal, also align with the most highly stressed slip planes. Several other {112}<111> slip systems were also found to have high Schmidt factors (as shown by the values in columns 6 to 8), but none of these show coincidence with microband boundary interfaces. This outcome also matches the finding of Chen *et al*. [2003, 2006] who showed that the {110}<111> slip systems accommodate shear processes in IF steel during low levels of deformation (~10% reduction) at room temperature.

The foregoing discussion confirms that high–angle microband features evolve in two stages. In stage one, typical low–angle microband boundaries form on highly stressed slip planes, followed by stage two where the high–angle features develop by a relative rigid body rotation between neighboring microbands about the normal of their boundary interface. The first stage occurs early in the deformation process and is considered to be a generic event in all microband–containing grains, while the second stage occurs in some {111}<110> grains in the latter stages of deformation. Grains with {111}<110> orientations are the most stable in the γ–fibre (peak intensity component in

the rolling texture, Figure 6.7b) and, unlike other unstable/metastable orientations, they remain in place without experiencing rotations during further deformation. Therefore, in {111}<110> grains, the maximum shear stresses remain restricted onto the existing microband boundaries. As a result, further deformation proceeds by achieving rotations at the microband boundary interfaces and around their surface normal directions, as shown in Figures 6.1, 6.3 and 6.4. The mechanism associated with this particular type of rotation is now known. A similar type of process has been observed previously during the generation of deformation banding interfaces [Lee and Duggan 1991, Liu *et al.* 2000], which operates in coarser length scales than the microband boundary spacing. It is pertinent to note that, due to the low–angle interfaces associated with classical microband boundaries, they are not expected to have a significant influence on recrystallization. However, the high–angle microband boundaries observed in this work may exhibit high mobility during recrystallization if the stored energy criterion is fulfilled. Thus, in a given microband array consisting of highly alternating orientations, it is possible that any one of these microbands may expand laterally during annealing, although their growth will cease when another microband of the same orientation is encountered due to 'orientation pinning' [Humphreys and Hatherly 2004]. Hence, recrystallization in these regions of {111}<110>–oriented grains is difficult despite the high–angle microband boundaries. This may also explain why {111}<110> texture components do not dominate the recrystallization texture in cold rolled and annealed steels despite these components dominating the rolling texture.

6.5 Conclusions

High–angle microband boundaries with misorientations up to ~20° between adjacent microbands were identified in the microstructures of cold–rolled IF steel. The following is a summary of the salient features of these deformation structures:

- Both {111}<112>– and {111}<110>–oriented grains comprise microband structures after moderate amounts of rolling reduction. The other microstructural constituents are deformation bands and in–grain shear bands. Microbands are normally low angle deformation features but, in some {111}<110>–oriented grains, high angle microbands were found to form.
- The high angle microbands have identical characteristics to that of typical low angle microband structures in terms of inclinations with the RD, boundary constitutions with dense dislocation walls and act as matrix structures for generating kink band and micro–shear bands.
- Across the high angle microband boundaries the orientations rotate around the axes lying along the surface normal of their interfaces, *i.e.* similar to a crystallographic twist boundary.
- Orientation variations occur in a cyclic nature across many high angle microband boundaries.
- High angle microband boundary interfaces coincide with the most highly stressed crystallographic lattice planes.

Chapter 7

Result and discussion–Part IV

Three dimensional EBSD characterization of grain boundary deformation structures in IF steel

7.1 Introduction

An understanding on the deformation features that are generated across grain boundaries is important because many metallurgical events occur at or near grain boundaries. For example, nucleation of recrystallization, chemical segregation and localized oxidation are common events that take place in the vicinity of grain boundaries. From numerous investigations it has been found that recovery and recrystallization occurs at faster rates near grain boundary regions [Hall 1951, Burke and Turnbull 1952, Saylor *et al*. 2004, Randle *et al*. 2008]. In those investigations, conventional two dimensional characterization tools were utilized. Therefore, it is of great interest to elucidate grain boundary deformation features by using high resolution 3D capabilities of modern EBSD systems.

In this investigation, a 3D–EBSD study was conducted to study grain boundary deformation features in an interstitial free (IF) steel following 75% rolling deformation. From 2D investigations the deformation grains can be distinctively classified in terms of the grain interior substructures. One set shows highly fragmented structures that originate from frequent presences of sharp low/high angle misorientation boundaries. The other set shows smooth substructures from gradual/gentle orientation changes. In the earlier set, the {111} crystallographic planes orient parallel to the rolling plane. These grains are generally known as the γ–fibre grains. The latter set of grains has <110> directions parallel to the rolling direction and are known as α–fibre grains.

In steel research, the γ grains are of particular interest because early recrystallization occurs within these grains during annealing. In low carbon and micro–alloyed steels (e.g. IF steel) the early recrystallization stage determines the final annealing textures and, therefore, understanding this stage is important for acquiring better control on recrystallization textures. Within the γ grains, recrystallization takes place in certain microstructural features, such as, in–grain shear bands and deformation bands. These bands were found to form on the microband matrix structures within γ oriented grains. The structural details of microbands were discussed in chapters 4–6.

Apart from the aforementioned recrystallization sites, it has been unanimously found that a large fraction of recrystallization takes place near the original hot band

boundaries of γ grains [Inagaki 1966]. It is to be noted that, this class of recrystallization does not fall within the strain induced boundary migration (SIBM) mechanism, whereby a high angle grain boundary segment of a sub−grain block migrates to grow. This process normally takes place at original hot−band grain boundaries and, therefore, SIBM has been primarily understood as a grain boundary involved recrystallization phenomenon. In contrast, in the form of the recrystallization being discussed here nucleation takes place in the grain boundary vicinity without involving the hot−band grain boundaries. In the literature, there are no quantitative data describing the fraction of recrystallization that falls within this category. The early study by Inagaki [1966] shows that almost 90% recrystallization occurs in the grain boundary regions in a low carbon steel. However, because of limited microscopy resolution at that time, this data may also include some of the grains that formed through SIBM mechanism. Later, Hayakaya and Szpunar [1997a-b] portrayed a model to describe how recrystallization occurs in the vicinity of grain boundaries without involving the pre−existing hot band grain boundaries. Further details of the model are included in the discussion section of this chapter.

In this investigation grain boundary regions in a 75% cold rolled IF steel are analyzed by 3D−EBSD to elucidate the local micro−orientation distributions to find out if they comprise essential features for recrystallization.

7.2 Characterization by two dimensional techniques

Figure 7.1a shows a SEM electron channelling contrast (ECC) image of a stack of elongated grains in a RD−ND section to demonstrate different types of grain boundaries that form after 75% cold rolling reduction. Based on extensive literatures on the distinctiveness of α and γ microstructures, the grains labeled as A, C and D can be categorized as α grains and B, E and F as γ grains. The abrupt changes in gray scale contract in the γ grains represent sharp orientation fluctuations. On the other hand, the gentle−smeary changes in contrast in the α grains represent gradual orientation gradients. Slip system selectivity during deformation, which is governed by grain orientation, is the origin of the microstructural differences between these two types. Briefly, many available slip systems in the α grains allow them to accommodate easy

shape change and, hence, generate smooth substructures. Conversely, restricted slip processes in a few operating slip systems in the γ grains results complex substructures.

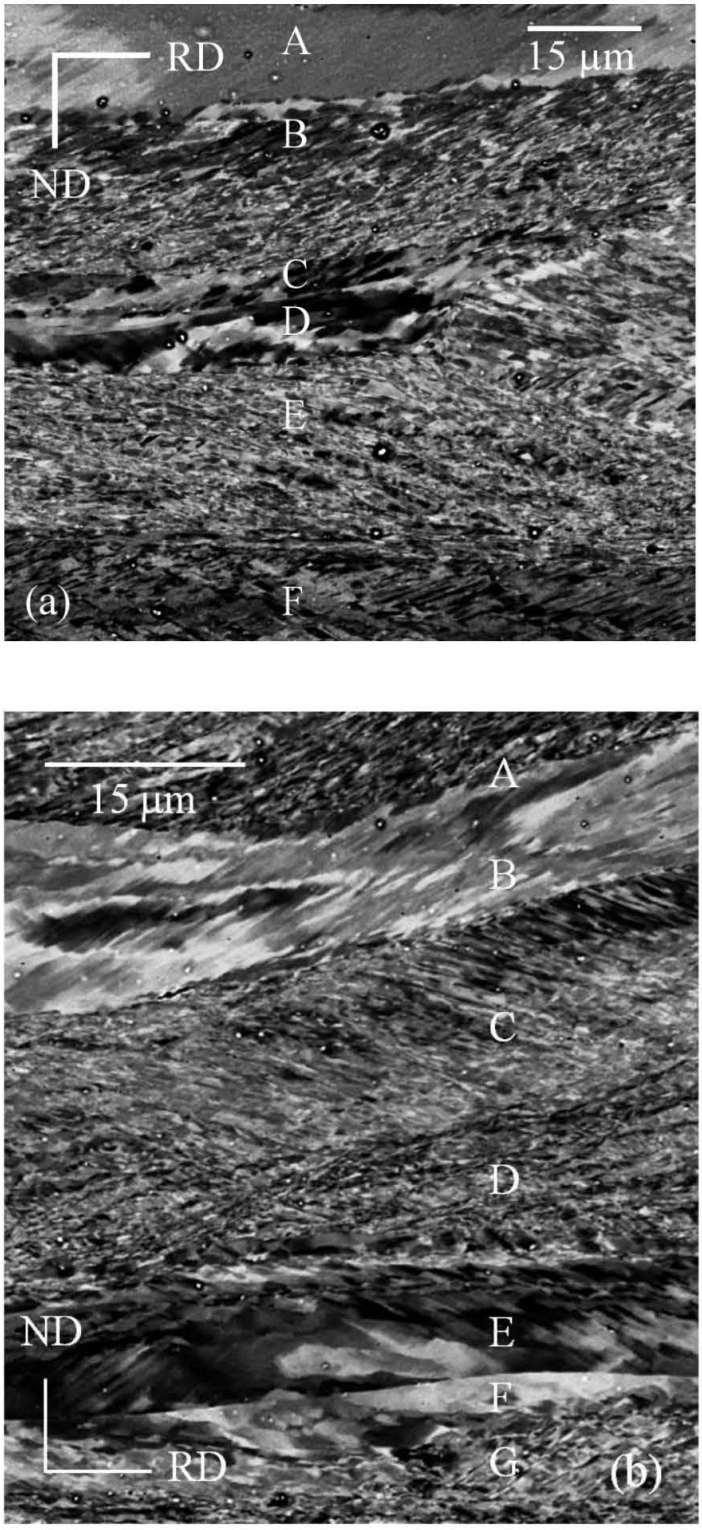

Figure 7.1(a–b): SEM ECC images in RD–ND section of 75% cold rolled IF steel showing: the nature of grain boundaries as a function of grain substructure.

The detail is described in the study of microband structures in chapters 4 and 6. It is important to highlight that the α/α and α/γ (e.g. A/B, B/C, C/D and D/E) boundaries are well defined and relatively simpler than the γ/γ boundaries (e.g. E/F). Figure 7.1b shows another example of deformation microstructures in a SEM ECC image, whereby α/α (E/F) and α/γ (A/B, B/C and D/E) boundaries are also sharp, and as it was seen before, γ/γ boundaries (e.g. C/D) are relatively complex and difficult to track.

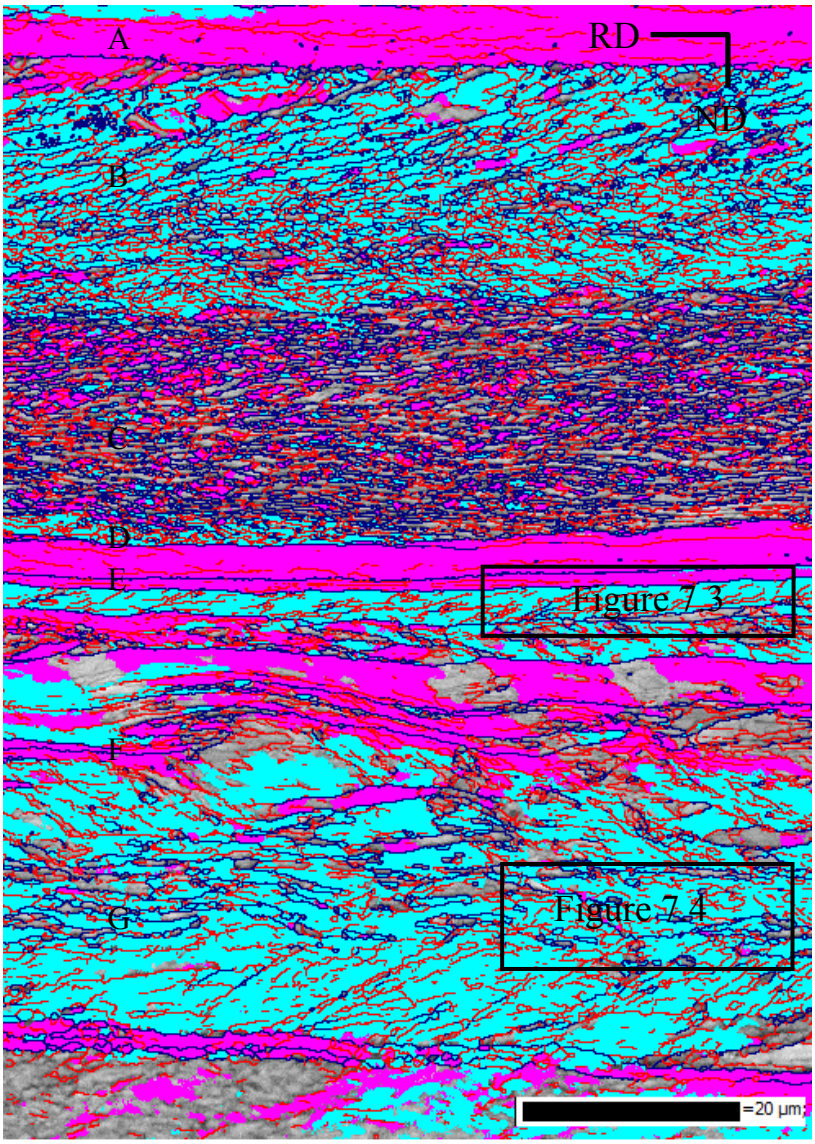

Figure 7.2: EBSD map of a larger scan in the RD–ND sections of 75% cold rolled IF steel to show the nature of grain boundaries between the γ and α oriented deformation grains.

Figure 7.2 shows an EBSD map of a stack of along RD elongated grains to show the characteristics of boundaries as a function of grain orientation. The grains are color coded according to their orientation *i.e.* the γ fibre grains in Acua and α fibre grains in Fuchsia. The high (>15°) and low (5–15°) angle misorientation boundaries are plotted in blue and red lines, respectively. Frequent presence of boundaries in the γ grains implies the existence of highly fragmented structures, and this is typical of the γ grains. 25–30° inclinations of these boundaries indicates that these features belong to classical microbands and micro–shear bands. Details of these features are described in the literature review (chapter 2) and during the extensive study on microband structures in chapter 4. The rare presence of misorientation boundaries in the α grains are also typical in this material. In some locations of the micrograph the hot–band grain boundary are not obvious. Nevertheless the deformation grains are labeled as A to G. From this micrograph it is obvious that the α/α and α/γ boundaries are relatively simpler than the γ/γ boundaries. Example of α/γ boundaries are A/B and D/E, and example of γ/γ boundary is F/G.

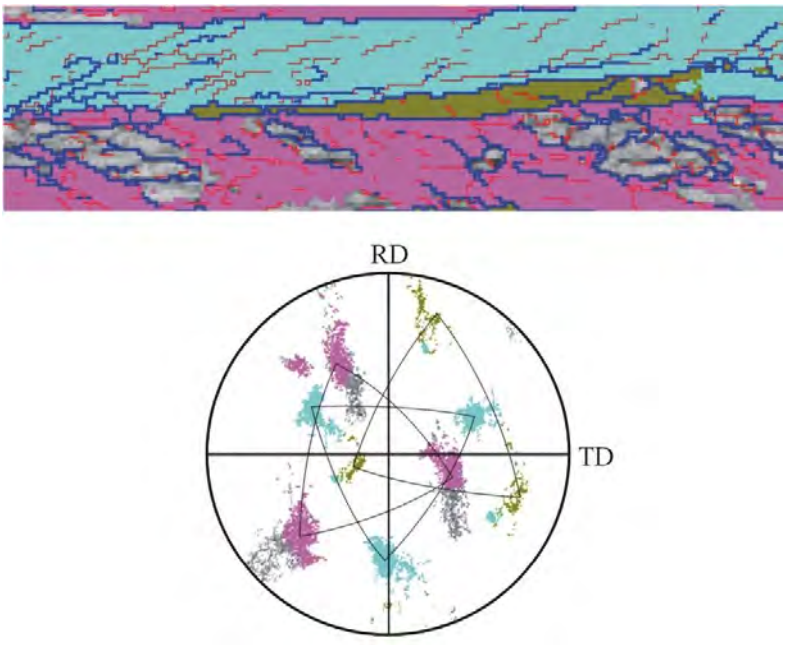

Figure 7.3: EBSD map of a γ/γ boundary and corresponding color coded <200> pole figure showing the presence of thin blocks of material with dissimilar orientation.

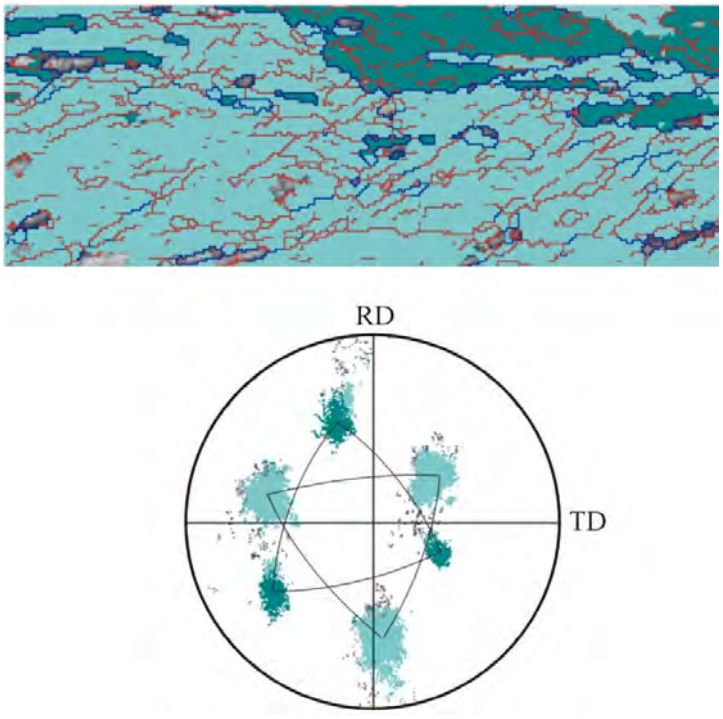

Figure 7.4: EBSD map and corresponding color coded <200> pole figure showing a complex boundary interface between two γ oriented grains.

The complexities in the γ/γ boundaries in Figure 7.2 (in rectangular boxes) are highlighted in Figure 7.3 and 7.4. In Figure 7.3 the color coded map and corresponding pole figure indicate that the upper and lower grains have ~{111}<112> and ~{111}<123> orientations, respectively. There is a thin grain separated by high angle boundaries and at their interface. Figure 7.4 highlights the complexities in an interface between two γ oriented grains. The corresponding color coded <200> pole figure shows that the upper and lower grains have ~{111}<123> and~{111}<112> orientations. They are separated by an irregular and complex boundary interface (in blue color). From these findings it is concluded that γ/γ boundaries may often turn complex in terms of grain boundary topography and presence of materials of other orientations.

7.3 Characterization by 3D–EBSD

For conducting the 3D–EBSD investigation, an area was selected having several grain boundaries, including a complex grain boundary between two microband containing grains. As described in chapter 3 on the 3D–EBSD procedures, a rectangular protrusion of 25×45 μm^2 area was fabricated by FIB milling. Figure 7.5 shows a SEM

micrograph of the protrusion. As described in chapter 3, the fiducial marks, EBSD surface and slicing directions are labeled in the micrograph. 3D–EBSD data collection was carried out by an automated system of Oxford Instrument HKL EBSD fitted into a Dual Beam platform of Carl Zeiss Augira machine. EBSD scanning at 100 nm step size and FIB serial sectioning by 100 nm slice thickness were conducted in alternating sequences up to 45 cycles. The acquired data were analyzed by HKL CHANNEL 5 data analysis software.

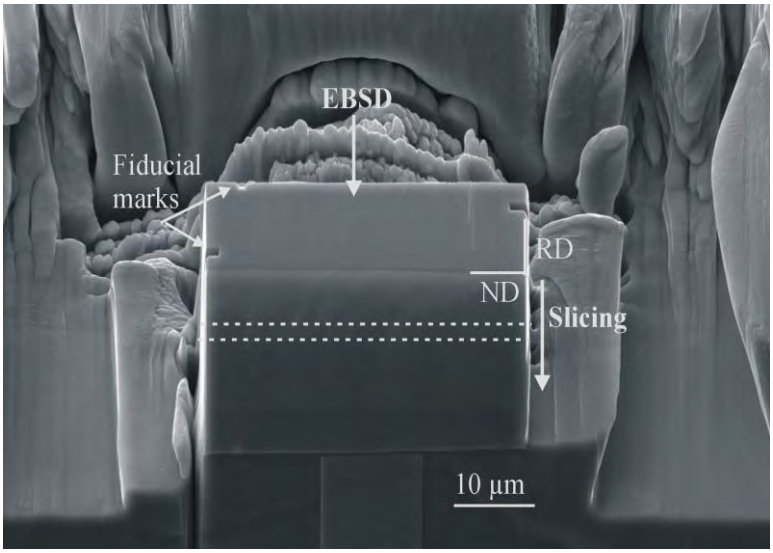

Figure 7.5: SEM micrograph of the protrusion in a 75% cold rolled IF steel. The milling direction, EBSD surface and fiducial marks are labeled.

7.3.1 General description

EBSD maps from the 10th, 20th, 30th and 40th slices are shown in Figure 7.6a–d. In these maps the >10° and 2–10° misoriented boundaries are plotted in yellow and black lines, respectively. Overall, there are five major regions separated by >10° boundaries, marked as A, B, C, D and E in Figure 7.6a. At this stage, each of them is considered as individual deformed hot–band grain. Within each grain low and high angle boundaries are distributed in different densities. In Grain A and C there are parallel lines of low angle misorientation boundaries. These are probably representing the microband boundaries, as shown in chapter 4. In grain A, these boundaries are inclined at +20° with the RD and in grain C, there are two intersecting sets inclined at ±23° with the RD. These are arrow pointed in the micrographs.

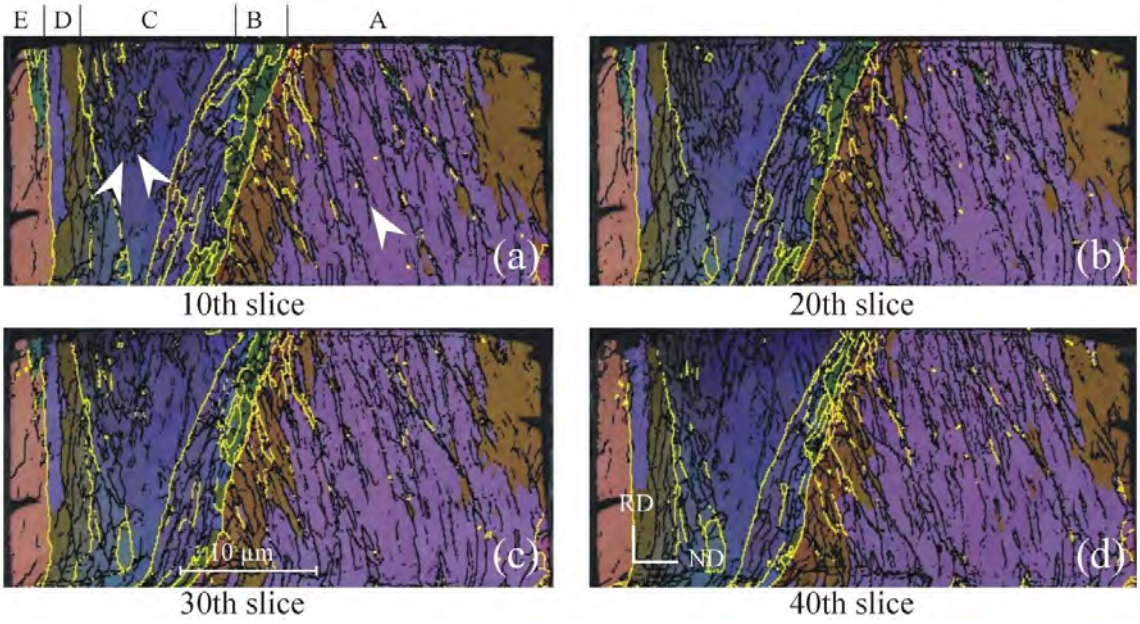

Figure 7.6: All Euler orientation plots of 10th, 20th, 30th and 40th slices showing >10° boundaries in yellow and 2–10° boundaries in black lines.

The orientation data of grains A, B and C are plotted in a color coded orientation map corresponding to the attached <200> pole figure in Figure 7.7. Within each grain (A, B, and C) there are large orientation spreads. The magnitude in spread are measured as 24°, 30°and 15° in grain A, B and C, respectively. These are marked by enclosing the pole points corresponding to the grains in the pole figure. The orientation data are also tabulated below in Table 7.1 to show the central orientation and the nearby standard rolling texture components. The orientation spread and distance from the standard rolling component are also included in the table.

In Grain A and C the primary source of orientation spread is the microband boundaries and variations within microband channels. Their orientations are centered at A(7 8 10)[4 $\overline{11}$ 6] and B(3 7 4)[1 $\bar{5}$ 8], which are close to (1 1 1)[1 $\bar{2}$ 1] and(1 1 1)[0 $\bar{1}$ 1] standard orientations, respectively (see Table 7.1). In Grain B, co–existing of high and low angle boundaries create a large spread of ~30° *i.e.* from (17 11 24)[3 $\bar{9}$ 2] to (14 11 26)[$\overline{23}$ 8 9] orientations. These orientations are 17.6° away from (1 1 1)[1 $\bar{2}$ 1] and 21.7° away from (1 1 1)[$\bar{2}$ 1 1] orientations, respectively (see the <200> pole figures corresponding to slice 1 in Figure 7.8). A gradual transition between these orientations indicates the presence of all the intermediate orientation components. It should be noted that (1 1 1)[1 $\bar{2}$ 1] and (1 1 1)[$\bar{2}$ 1 1] are complementary rolling texture components.

Within grain E there is negligible presence of misorientation boundaries and within grain D there are some low angle boundaries parallel to the adjacent original hot–band grain boundary (see Figure 7.6).

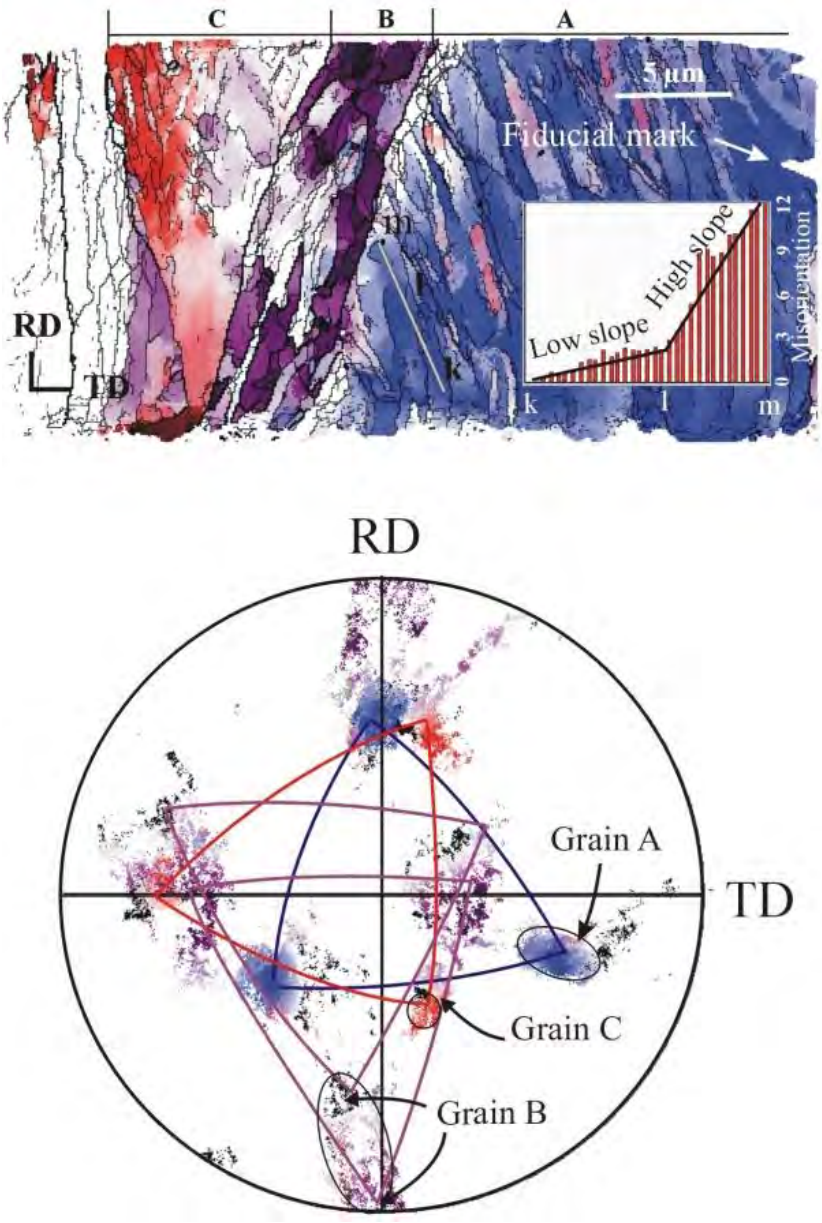

Figure 7.7: Color coded orientation plot of slice 4, along with <200> pole figure, to highlight the orientation position and spread in grain A, B and C. The black thick and thin lines represent >15° and 3–15° misoriented boundaries, respectively.

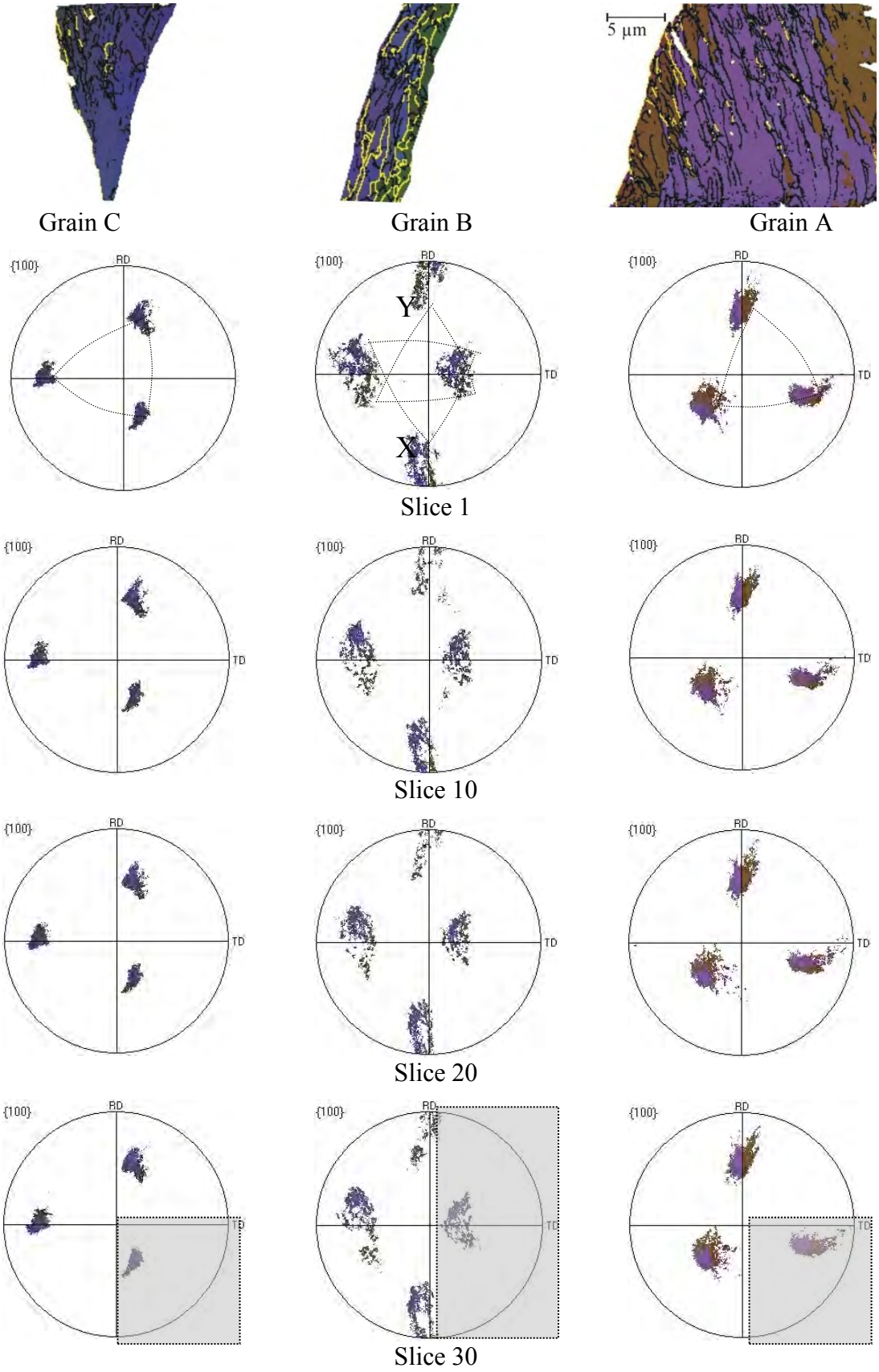

Figure 7.8: <200> pole figures showing orientation variations of Grain A, B and C across 1st, 10th, 20th and 30th slices.

Table 7.1: Orientation data of grain A, B and C.

Grain	Orientation spread	Central orientation	Close bcc rolling orientation	Misoriented by
A	24°	(7 8 10)[4 $\overline{11}$ 6]	(1 1 1)[1 $\bar{2}$ 1]	10.7°
B	30°	X: (17 11 24)[3 $\bar{9}$ 2]	(1 1 1)[1 $\bar{2}$ 1]	17.6°
		Y: (14 11 26)[$\overline{23}$ 8 9]	(1 1 1)[$\bar{2}$ 1 1]	21.7°
C	15°	(3 7 4)[1 $\bar{5}$ 8]	(1 1 1)[0 $\bar{1}$ 1]	19.8

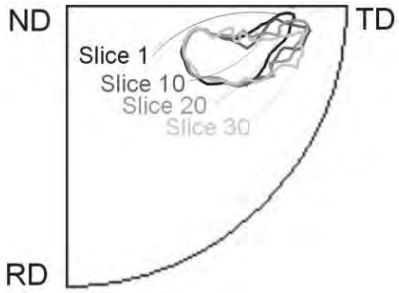

(a) Grain A

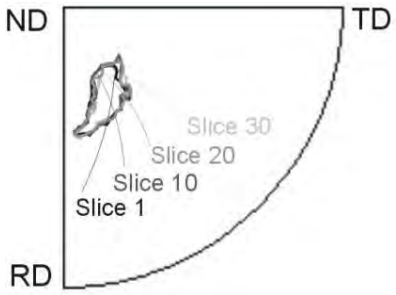

(b) Grain C

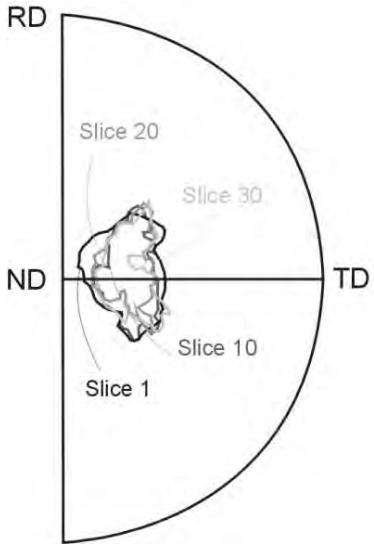

(c) Grain B

Figure 7.9: The orientation spreads found in Figure 7.8 are superimposed for showing variations across slices.

It is possible to track the orientation variations across the slices within a given grain by comparing the pole figures between successive layers. The <200> pole figure plots of the data from Grain A, B and C (in the 1st, 10th, 20th and 30th slices) are plotted in Figure 7.8, from which it become obvious that none of the grains show significant change in orientations. To find out subtle changes across a given pole the orientation spreads around the highlighted pole figure regions in Figure 7.8 are

re–plotted in Figure 7.9. From this plot it turns out that, within Grain C, the shift is less than that in Grain A and B. In grain A, the shift is larger near the TD, and this is relevant to the steep orientation gradient region next to the A/B grain boundary.

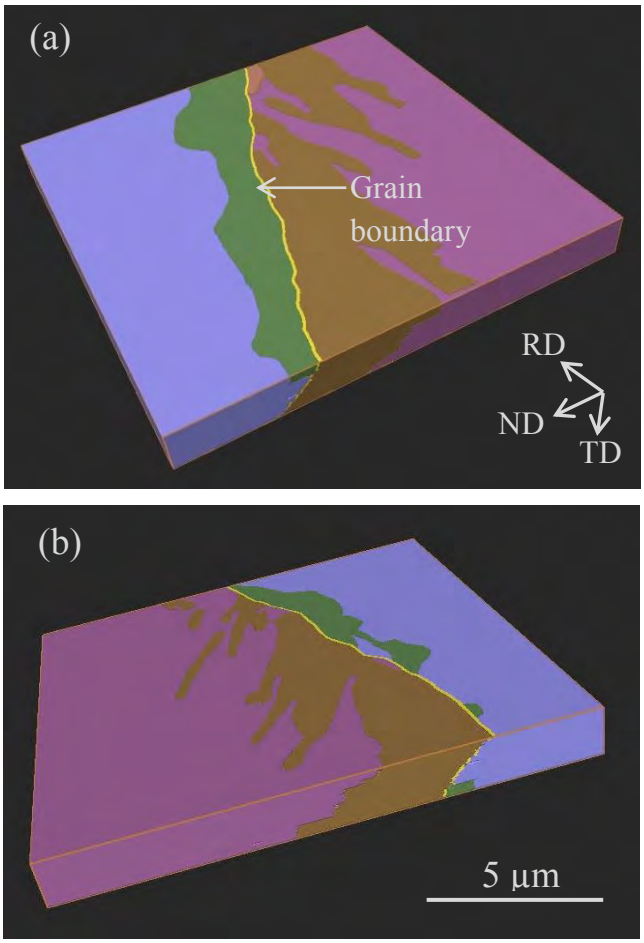

Figure 7.10: (a) Front and (b) rear projection of the 3D reconstructions across A/B grain boundary (in yellow).

7.3.2 Thee dimensional reconstructions

To reconstruct a feature in 3D space from 2D scans, the continuity of the feature is tracked across the slices. Then, the feature was outlined in each slices by Corel draw and reconstructed in 3D using Avizo Fire 7.0 3D software. For example, the A/B boundary features are important to understand in 3D, because both A and B grains comprise classical fragmented substructures, whereby early recrystallization can potentially take place. In each slice, the A/B boundary adjacent regions were plotted as TD inverse pole figure maps. These maps were assigned color by Corel draw according

to orientation variation. In a given area, if the TD variation is small and gradual it was assigned a uniform color, but if the variation is large (>15°), it was assigned a different color. Finally, the slices were reconstructed by stacking them onto their fiducial marks. The front and rear projections of the reconstructions are shown in Figure 7.10a and b. In these images the original hot band grain boundary is marked by a yellow line, across which a significantly large volume of material is affected. In Figure 7.11 a and b, the morphology of A/B boundary is revealed by splitting apart grain A and B and, thus, it becomes obvious that a typical irregular and curved grain boundary interface is present. The overall alignment of the grain boundary interface is along the RD–TD section. This is expected to happen because of flattening of the grains after 75% rolling reduction. In the following discussion, some specific features are separated out from the 3D reconstruction.

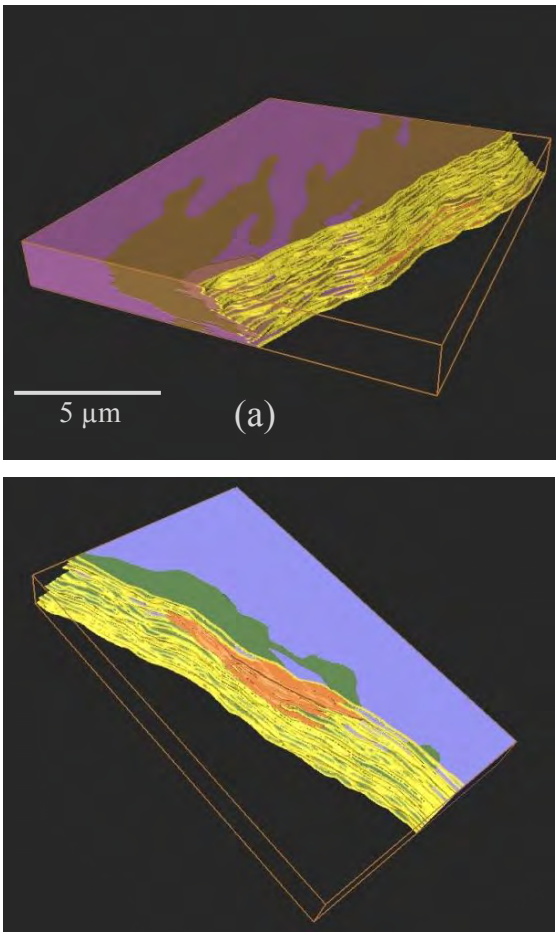

Figure 7.11: 3D reconstruction showing the grain boundary interface across A and B grains.

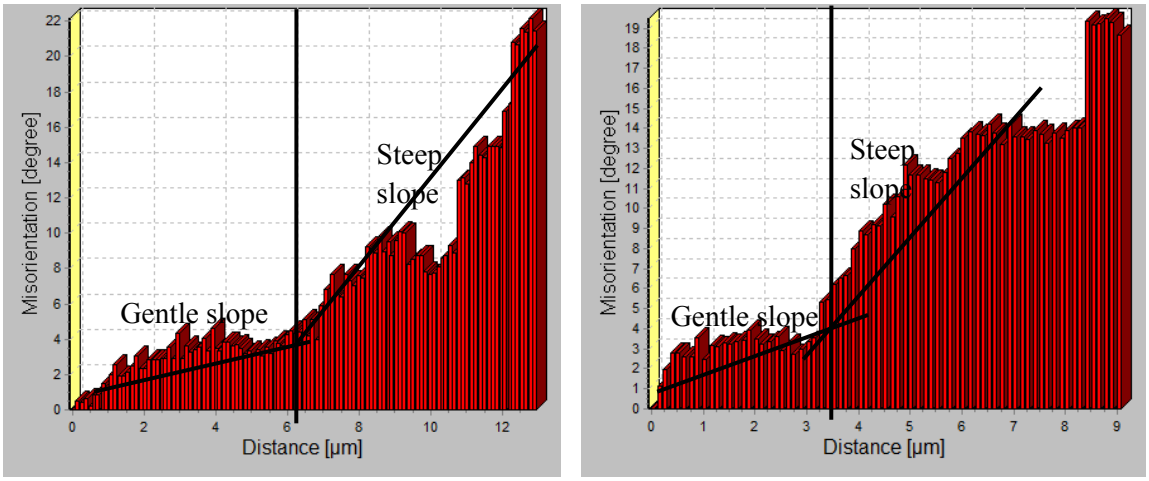

(a) (b)

Figure 7.12: Examples of orientation gradients along microband channels. From left to right orientation data are plotted from the grain interior to the A/B boudnary interface.

Highly misoriented regions across A/B boundary

In Grain A the change in orientation between consecutive points along microband channels is low. However, on approach to the A/B boundary the orientation difference increases. In an inset in Figure 7.7 the orientation profile along k–l–m microband channels is plotted and therefore it becomes clear that there is a sharp change in orientation gradient from 0.8°/µm in k–l segment to 3.8°/µm in l–m segment. A similar plot was found in most of the traceable microband channels. In Figures 7.12a and b, two other examples are plotted from the 10th and 20th slices. In both, the trend is similar *i.e.* steep orientation gradients near the boundary interface and gentle gradients in grain interiors.

In the B side of A/B boundary, a high angle boundary is formed almost parallel to the A/B boundary (see the yellow lines in Figure 7.6a and thick black lines in Figure 7.7). This boundary is more curved and irregular than the A/B boundary. In some locations the orientation difference across this boundary becomes as low as 5–8°. This nature of misorientation variation along the length of the boundary indicates that this boundary has evolved during the deformation. In Figure 7.6, this boundary becomes rather complex in the 20th, 30th and 40th slices. Nevertheless, continuity of this boundary in parallel to the original A/B interface across the slices indicates that this boundary was formed during deformation as an effect of pre–existing A/B boundary.

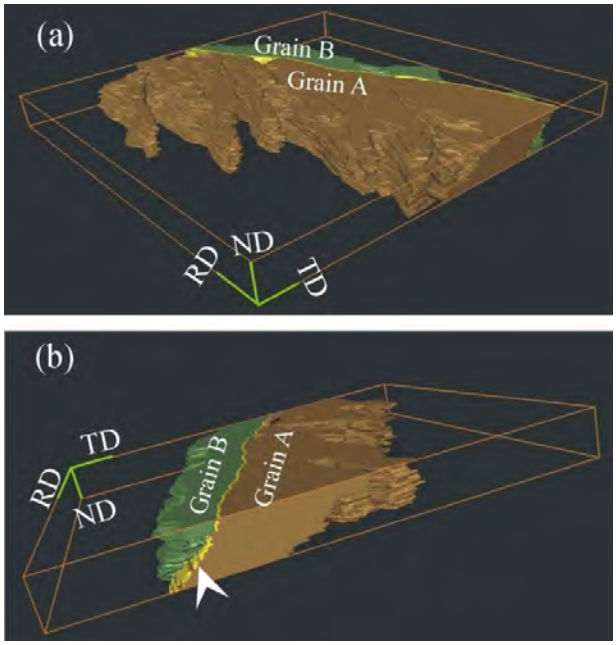

Figure 7.13: 3D reconstruction of the region effected by A/B grain boundary.

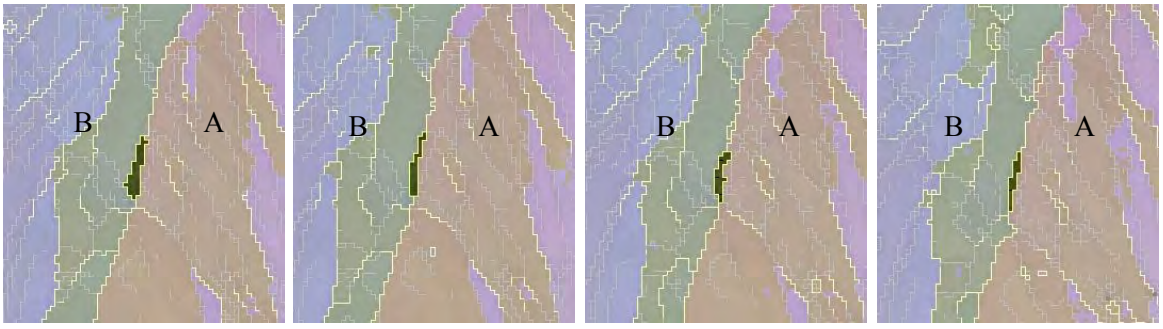

(a) Slice 2 (b) Slice 4 (c) Slice 6 (d) Slice 8

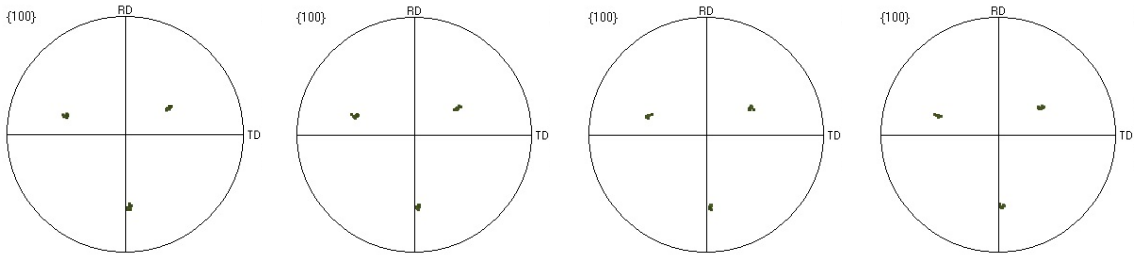

(e) Internal spread=4.5° (f) Internal spread=2.8° (g) Internal spread=2.2° (h) Internal spread=3.6°

Misorientations=1.2° 0.6° 2.8°

Figure 7.14: A thin strip of material continued across many slices in A/B boundary. The orientation of this strip is dissimilar to either side of the boundary (A and B).

From the aforementioned description it is conclusively shown that steep orientation gradients are present near A/B boundary in grain A along the microband channels and sharp high angle boundary formed in grain B. It is possible to separate this region over the entire 45 slices and reconstruct a 3D volume (Figure 7.13a and b). This block has a complex morphology. The serrated appearance in the microband containing side (in grain A) implies that microband channels/boundaries experience orientation changes when they approach the original hot band grain boundary. The average width of this region is ~2.3 μm in grain B and ~4.8 μm in grain A and, therefore, this region is considered to be of significantly large volume.

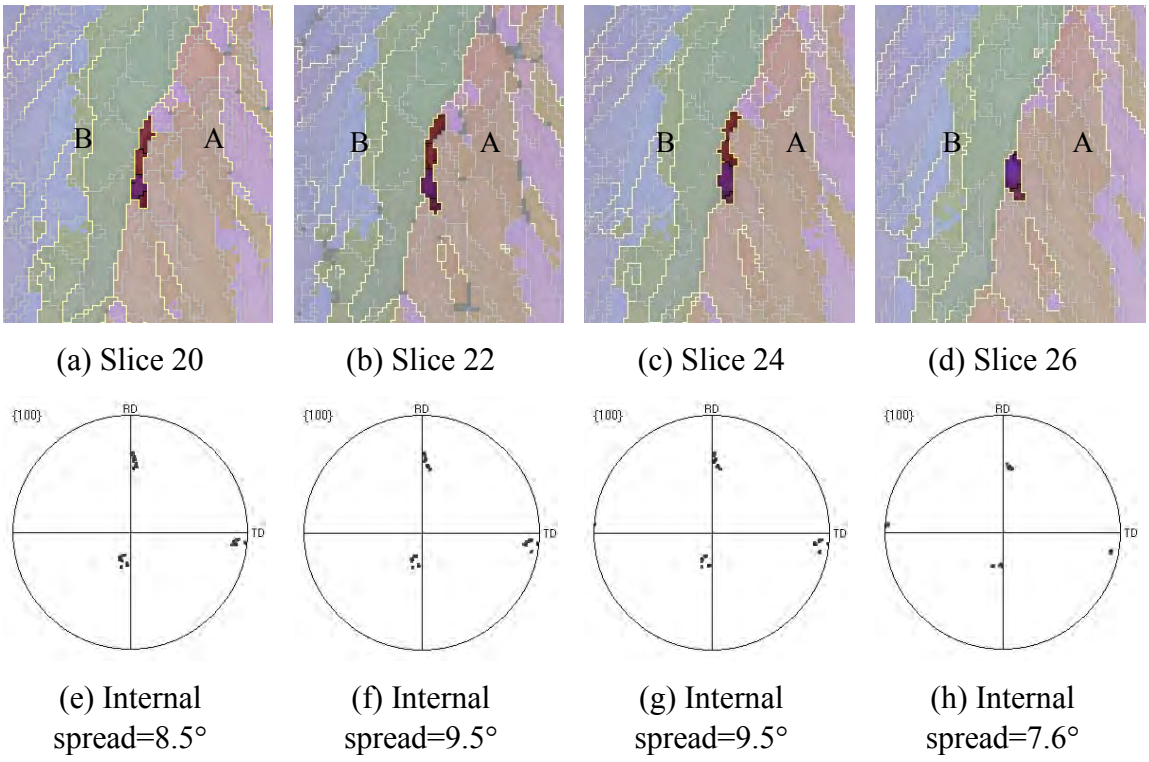

(a) Slice 20 (b) Slice 22 (c) Slice 24 (d) Slice 26

(e) Internal spread=8.5° (f) Internal spread=9.5° (g) Internal spread=9.5° (h) Internal spread=7.6°

Figure 7.15: A second example of thin strip at A/B boundary, having dissimilar orientation from both A and B.

Distribution of thin blocks in the immediate vicinity of A/B grain boundary

On a finer scale, in the immediate grain boundary vicinity there are thin strips of material having large orientation differences with both A and B grains. For example, in slice 2 (see Figure 7.14a**)** the highlighted thin block of material has a maximum width of 400 nm. This block continued in the 4th, 6th and 8th slice with 300, 300 and 200 nm maximum widths, respectively (see Figures 7.14b, c and d). The orientations of this

strip across the slices are plotted in the accompanied <200> pole figures in Figure 7.14 e, f, g and h. The overall orientation of this block is centered at (15 12 16)[4 $\bar{1}3$ 6], which is 8.9° away from the commonly found (111)[1 $\bar{2}$1] rolling texture component. This means that the orientation of this block is close to the interior of grain A, but is further away from the local orientations of the steep gradient region near A/B boundary. There are small orientation variations along the length of the thin strip. The magnitude in each slice is included in Figure 7.14.

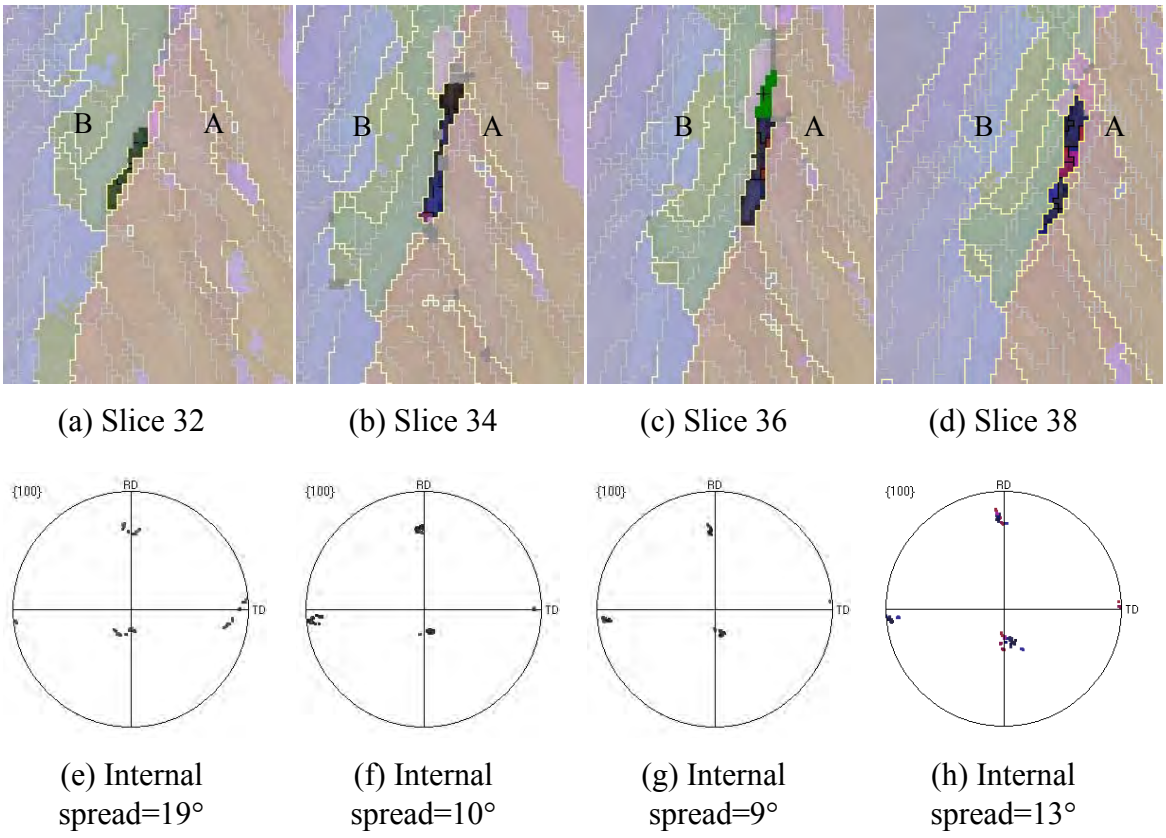

(a) Slice 32 (b) Slice 34 (c) Slice 36 (d) Slice 38

(e) Internal spread=19° (f) Internal spread=10° (g) Internal spread=9° (h) Internal spread=13°

Figure 7.16: A third example is highlighted at A/B boundary to demonstrate the formation of thin strips having dissimilar orientation from both grain A and B.

Figure 7.15 shows another example of thin strip at A/B boundary in the 20th, 22th, 24th and 26th slices. This block is wider than the previous example, in the range of 400–700 nm, at the widest region. Within each slice, there is an orientation variation along the length of the block and, therefore, it is not possible to measure the change in orientation between slices. Nevertheless, orientation shifts between the slices are obvious from the corresponding <200> pole figure plots in Figure 7.15e–h. The overall orientation of these bocks are centered at (0 $\bar{3}$ $\bar{5}$) [1 10 $\bar{6}$], which is 6.6° away from (0 $\bar{1}$ $\bar{2}$)[0 2 $\bar{1}$] orientation.

For being a new finding, for statistical validation a third example of the same phenomenon is presented in Figure 7.16. Similar to the previous examples, four slices are presented across A/B boundary. Along the length within each slice there are orientation variations. The orientation of this block is close to that shown in Figure 7.15, and, therefore, it is possible that the same block has been disrupted during subsequent deformation following its formation during earlier deformation stages.

From the aforementioned results it is conclusive that, during deformation, thin blocks form along original hot-band boundaries. Within the A/B boundary several other strips were identified and these are reconstructed and displayed as Q, R, S, T and U in 3D in Figure 7.17. The grain boundary interface is shown in yellow background. Among them, block S is much longer than the others. The central orientation of each block is plotted in <200> pole figures in Figures 7.18a and b. The orientations of these blocks are Q: (12 3 17)[21 1 $\overline{15}$0], R: (19 3 20)[20 0 $\overline{19}$], S: (8 1 22)[25 $\bar{2}$ $\bar{9}$], T: (15 12 16)[4 $\overline{13}$ 6] and U: (11 12 20)[$\overline{20}$ 15 2]. The orientations of Q, R and S are close to the orientation of Grain C.

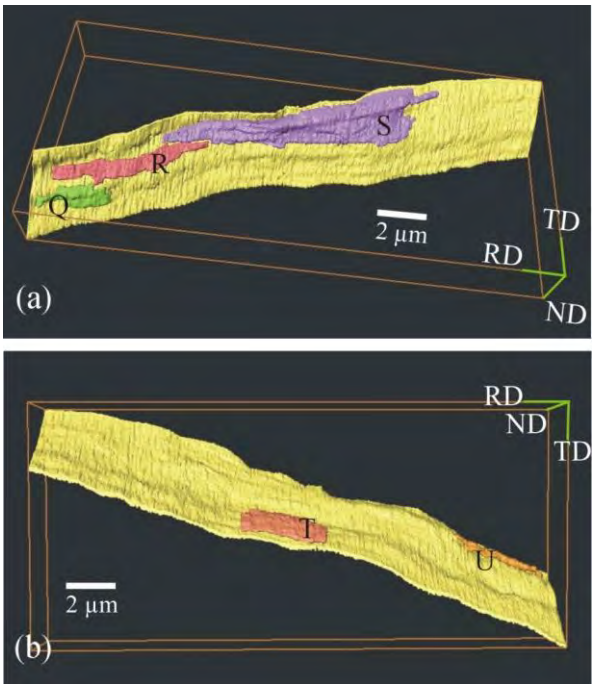

Figure 7.17: 3D reconstruction of thin blocks on the yellow background of A/B grain boundary interface.

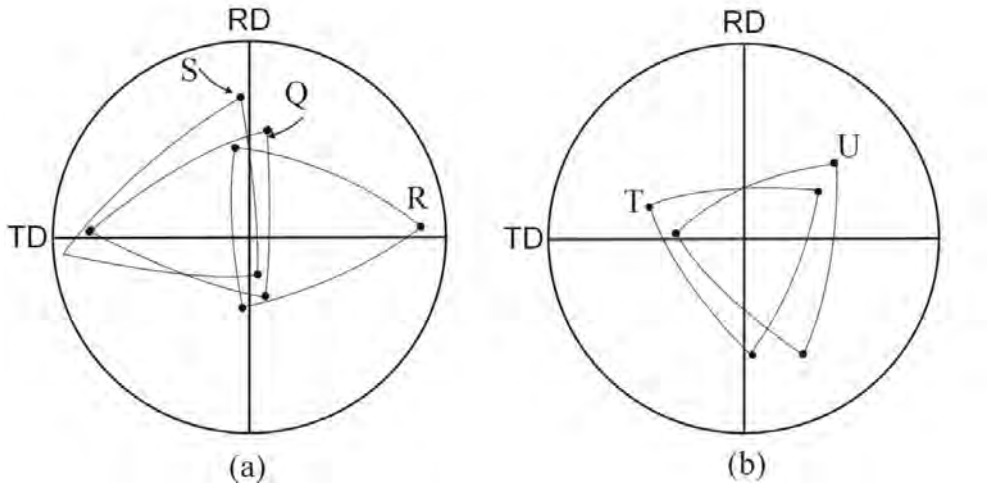

Figure 7.18: <200> pole figure to represent the central orientations of the thin blocks at the A/B grain boundary interface.

7.4 Discussion

The influence of the aforementioned grain boundary regions on deformation and recrystallization textures are discussed in the following sections.

7.4.1 Grain boundary influences on rolling textures

Grain boundary regions are different from grain interiors in terms of crystallographic orientations and microstructures and, therefore, they may have significant influence in the generation of rolling textures. It has been noted in numerous investigations that without taking these features into account texture prediction may be incomplete and unpractical. For example, in the early experimental data of Barrett and Levenson [1941] it was demonstrated that single crystal deformation data are not collectively representative of their polycrystalline constituent's data. In their experiment, a single crystal disk was embedded into a close fitted hole in a polycrystalline copper plate and subsequently cold rolled to 90% reduction in thickness. They conducted this experiment on 26 differently oriented crystals, and it turned out that <110> parallel to the RD and <111> parallel to the ND are stable orientations. Later, with the development of orientation distribution functions these orientations are now known as the α– and γ–fibres, respectively. Currently, these fibre textures are unanimously obtained by many researchers in the rolling texture of bcc iron [Humphreys and Hatherly 2004]. In Barrett and Levenson's [1941] experiment, however, a larger spread

around the stable orientations was measured in comparison to polycrystalline samples. Therefore, it is concluded that the constraints surrounding a given grain in a polycrystalline sample influences the deformation texture, in terms of orientation sharpening.

Inagaki and Suda [1972] also observed that the rolling textures of a polycrystalline metal are different to that generated in single crystals. They demonstrated this phenomenon by determining crystal rotation paths through measuring relative stability of various important orientations of rolling orientations in steel. They rolled highly textured fine grained samples to various reductions. After each deformation cycle the orientation changes was tracked from ODF data [Inagaki and Suda 1972, Inagaki 1987a–b] and, finally, two principal rotation paths were determined. These are as follows:

Path 1: {001}<100> → {001}<110> → {112}<110> → {223}<110>

Path 2: {110}<001> → {554}<225> → {111}<112> → {111}<110> → {223}<110>

Thus it turned out that {001}<110> orientation is a metastable component (see path 1) in a polycrystalline sample but this was earlier demonstrated by Koh and Dunn [1955] as a stable orientation component in single crystal experiments. Therefore, it has been concluded that the orientation stability can significantly vary in the presence of grain boundary constrains. Therefore, the regions across the A/B boundary in Figure 7.13 behave differently from the grain interiors as a result of the constraints imposed by the boundary.

Inagaki [1994] also proposed a model of deformation textures in steel that includes the influence of grain boundaries. An essential hypothesis in his model is that the metastable orientations obtain stability under the influence of grain boundary constraints. This can be justified from the fact that {111}<112> is a commonly found texture component in 60–95% rolled polycrystalline steel samples, but this is expected not to present for being a metastable component according to the rotation path 2 (above), and expected to rotate towards {111}<110> and then {223}<110>. In general terms, in highly rolled samples {223}<110> single component texture should form according to path 1 and 2 instead of forming all the components along the α– and γ–fibres. Based on this argument, it was concluded by Inagaki [1994] that grain

boundary interactions turn metastable orientation components into stable orientations. Without this assumption the well–examined experimental fibre texture is not possible to imagine in polycrystalline samples. According to this notion, the boundary regions of two γ oriented (<111>//ND) grains are assumed to rotate around <111> to satisfy stress and strain compatibilities between the grains. A schematics view of the theme is shown in Figure 7.19 [Inagaki 1994].

According to Inagaki's [1994] hypothesis, an accelerated rate of rotation is also assumed to occur if one of these grains has already reached to a stable end orientation *i.e.* {111}<110>. This suggests that, in the present data, a strong interaction is likely to occur between grain A and C in Figure 7.7, for one being close to a metastable (*i.e.*{111}<112>) and one to a highly stable (*i.e.* {111}<110>) orientation. The steep gradient region in grain A adjacent to the A/B boundary is therefore considered to form as a result of grain boundary interactions. However, the rotation axis is not as systematic as indicated by Inagaki *i.e.* to be around <111>//ND, between γ orientation components.

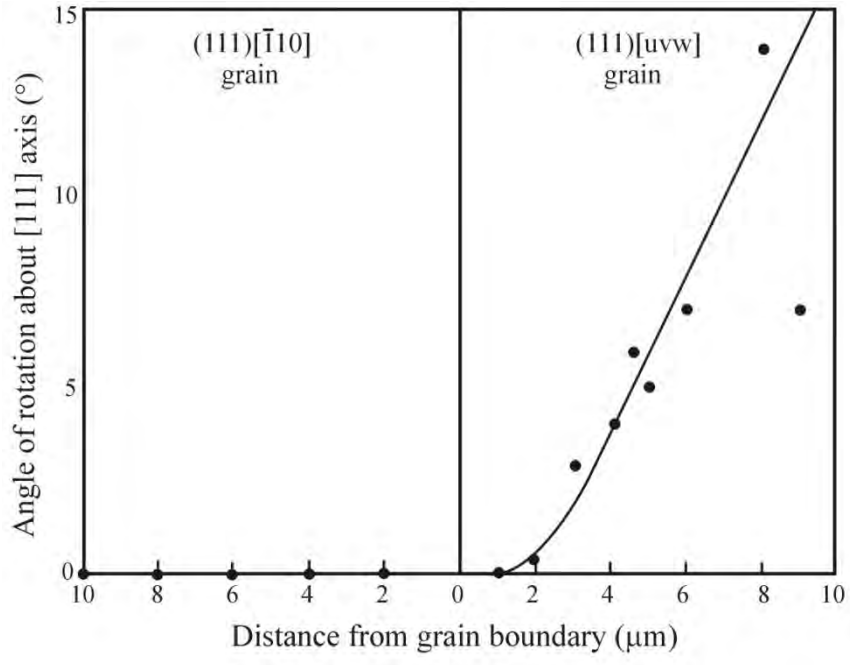

Figure 7.19: Rotation about [111]||ND axis observed in the boundary regions between (1 1 1) [$\bar{1}$ 1 0] and (1 1 1) [uvw] deformed grains. Angles of rotation measured from (1 1 1)[$\bar{1}$ 1 0] is indicated as a function of distance from grain boundary. *Reproduced from* [Inagaki 1994].

The presence of many high angle boundaries in the interior of Grain B is indicative of highly constrained deformation. As a consequence, grain block B is probably separated from the neighboring grain C during deformation. This assumption is justified through the findings that show some of the thin blocks (Q and S at A/B boundary) have orientations close to grain C. Therefore, it is possible that during deformation grain B and C were formed by the division of a single hot–band grain, and during this process small debris were left over in the form of thin blocks at the A/B boundary. The availability of many slip systems on {110}, {112} and {123} slip planes also makes bcc metals prone to inhomogeneous deformation in constrained situations, such as the grain boundary region in the present case.

Although Inagaki's experimental findings and physical model generated a qualitative basis of grain boundary influence on deformation texture modeling, this does not provide a quantitative measure. In recent times, VanHoutte's texture simulation team made significant improvements in texture predictions by utilizing the grain interaction concept, which is known as Lamel model [Dellannay *et al.* 2001 and Liu *et al.* 2002]. Briefly on this model, the grain boundary regions are assumed to adopt dissimilar deformation modes to that of the grain interior: shear deformation in the grain boundary regions of a given grain was found to be influenced by the top and bottom neighboring grains in RD–ND section. This is the key concept in the so called pancake model whereby grain boundary influence is assumed to be significant because of substantial flattening of deforming grains after large rolling reductions (>60%). Through this model, the fcc rolling texture was better predicted over Finite Element (FE) and Relaxed Constrain (RC) models. In the case of bcc texture prediction, this model yields closer approximation to experimental data over all other simulation conducted so far. More specifically, the γ–fibre texture is better predicted through this model than the α–fibre components. This has been also reflected in the current data showing that the α/α grain boundary (C/D in Figure 7.1a and E/F in Figure 7.1b) region is much simpler than the γ/γ (E/F in Figure 7.1a, C/D in Figure 7.1b, Figures 7.3 and 7.4.) boundaries. Finally, the size and shape of the grain boundary affected regions (in Figure 7.13a and b) between two principal rolling components (~{111}<112> and ~{111}<110>) provide an important experimental basis for texture simulations.

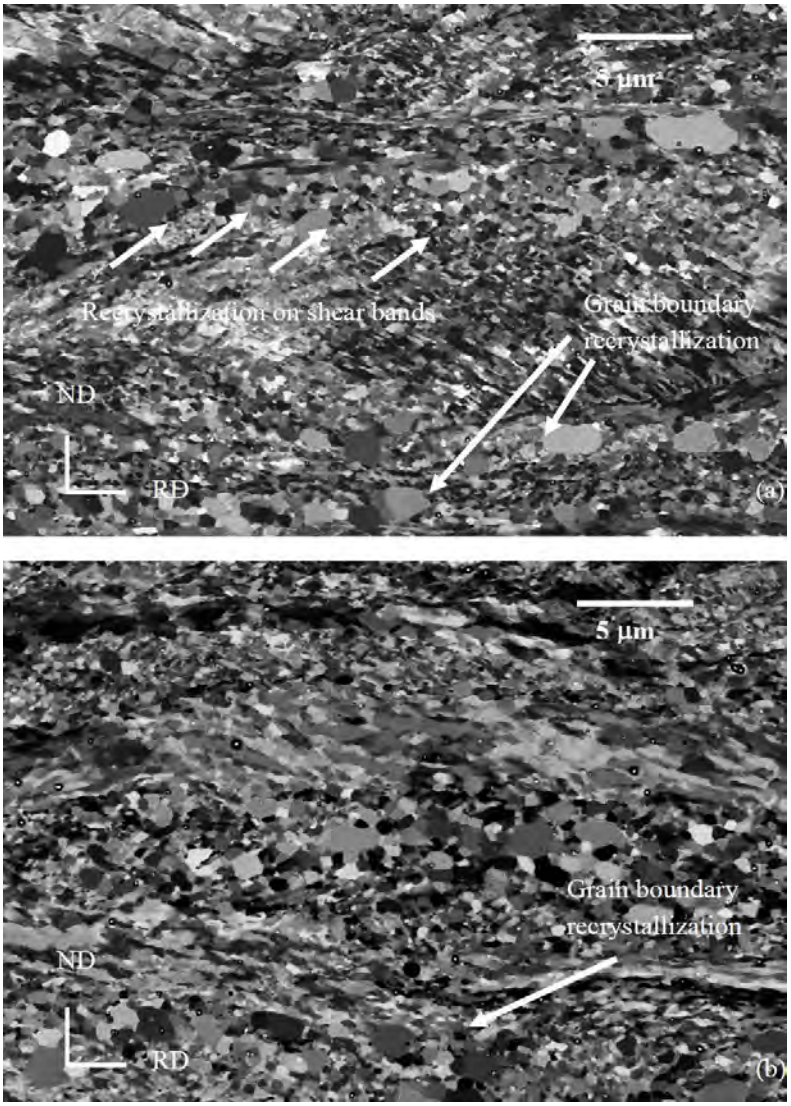

Figure 7.20: SEM ECC images of RD–ND section of partly recrystallized cold rolled IF steel showing recrystallization at or near grain boundary regions.

7.4.2 Grain boundary influences on recrystallization textures

During annealing, early recrystallization was often found to occur near the boundaries of original hot–band grains. Examples of such events are shown in Figures 7.20a and b, whereby the grain boundary regions become populated with recrystallization nuclei. Some recrystallization also occurs in grain interiors on shear and deformation bands. It is difficult to quantify grain boundary contributions to recrystallization, in terms of number or area fractions. This is because, after considerably high rolling reductions (e.g. 75% in thickness) the hot band grains resemble a pancake shape and, therefore, a large area fraction of the grains belongs to

the grain boundary regions. As a consequence it often turns into a confusing situation to judge if successfully recrystallized grains (of 3−5 μm in diameter) originate from the immediate grain boundary vicinity or not. Nevertheless, Inagaki [1966] demonstrated that 90% recrystallization occurs in the grain boundary regions in a cold rolled low carbon steel. Although this number appears exceptionally high, it at least provides evidence of significantly larger recrystallization events near grain boundaries. In the current investigation, although Figures 7.20a and b demonstrate near (or at) grain boundary recrystallizations, the principal recrystallization sites in this material are the highly fragmented substructures (shear bands [Barnett and Jonas 1997, Barnett and Jonas 1999] and deformation bands [Tse *et al*. 1999 and Tse *et al*. 2006]) within the γ oriented grains.

In principle, recrystallization commences by moving crystallographic interfaces. For an interface to be mobile in a given microstructural region, two essential requirements need to be fulfilled. One is the misorientation across the interface, which needs to be high angle and the other is the difference in stored energy across the interface, which must be high enough to overcome the associated dragging forces. There has been extensive research on these factors. In the literature, the well−established data are based on x−ray and neutron diffraction techniques, whereby orientation dependent stored energy data was used to explain the origin of certain recrystallization textures in steel. However, these techniques do not provide microtexture information, which is essential for understanding recrystallization for being a site specific phenomenon, such as grain boundary regions.

Based on local characteristics, Hayakawa and Szpunar (1997a) proposed a grain boundary recrystallization model for IF steels. The schematic of the model is shown in Figure 7.21, whereby recrystallization nucleation is assumed to take place in the grain boundary vicinity, where both the abovementioned criteria are assumed to be fulfilled through the accommodation of stress and strain in the form of gradual and sharp lattice curvatures. According to this model the steep orientation gradient region in grain 1 may act as ideal recrystallization sites.

In the deformation microstructures of steels the grain boundary regions are made of subgrains, as that also in the grain interiors. During recrystallization certain subgrains

achieve preferential growth. The subgrains near grain boundaries have some advantages in this regard. They may experience faster recovery than those in the grain interior because grain boundaries act as sinking sites of defects (vacancy and dislocations). Also, more heterogeneities in subgrain structures near grain boundaries promote faster recovery [Hayakawa and Szpunar 1997b].

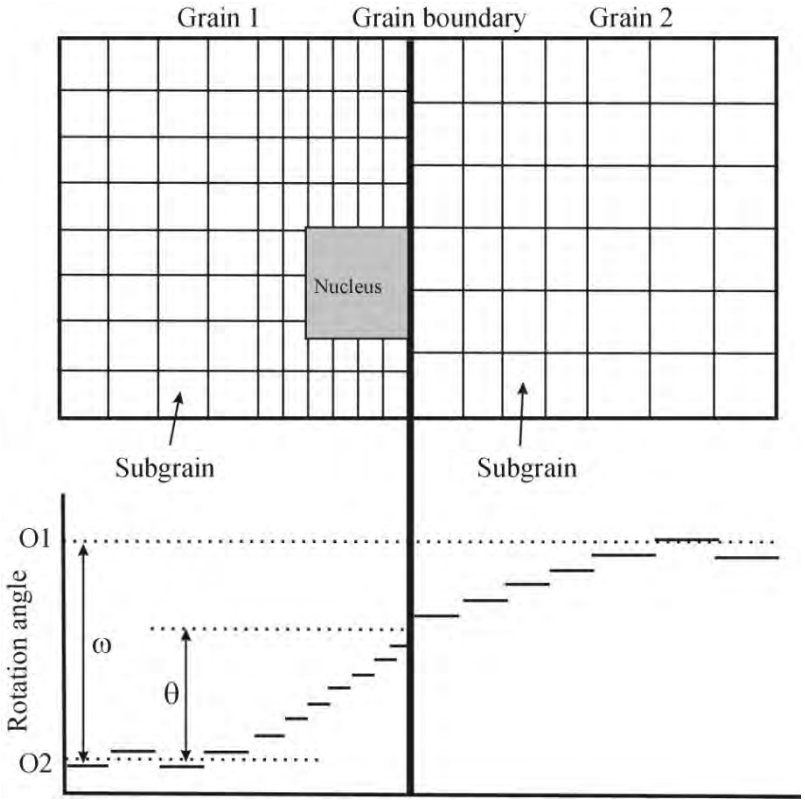

Figure 7.21: Schematic drawing of lattice rotation across a grain boundary. Stored energy of grain 1 is higher than that of grain 2. O1 represents the orientation of grain 1 and O2 represents that of grain 2. *Reproduced from* [Hayakawa and Szpunar 1997b].

When recrystallization kinetics is evaluated in terms of subgrain size, the grain boundary regions are thought to have advantages for having smaller subgrain distributions that store more energy and, therefore, respond faster to recovery and recrystallization processes. It is pertinent to note that subgrain size distribution in rolled steel is also an orientation dependent factor. For example, in {111}<112> oriented grains the average subgrain size is 0.35 μm, which is much finer than the {111}<110> oriented grains [Hayakawa and Szpunar 1997a]. From numerous investigations it has been found that the average subgrain size in the γ grains varies between 0.3–0.7 μm

after 70–80% rolling reductions [Goodenow 1970, Dillamore *et al.* 1967, Inagaki 1966]. Although subgrain size is not a measurable parameter from the current experimental data, this is a factor that should be included in this discussion for being an important driving force for recrystallization.

Growth of a subgrain to successful recrystallization may occur in two principal ways. If the subgrains reside at a high angle boundary, such as those at the sharp boundaries in grain B in Figure 7.7, they may grow by migration of the subgrain segment on the high angle boundary, according to the model outlined by Jones *et al.* [1979]. This event is unlikely to occur in the existing hot-band grain boundaries, because of the dragging forces from the nano–particles that form as a result of the addition of stabilizing elements (Ti) by combining with the interstitial carbon atoms [Hua *et al.* 1997 and Hua *et al.* 1993]. However, high angle boundaries that evolve during deformation (in grain B in Figure 7.7) do not contain those particles and therefore may act as potential sites for recrystallization.

According to the second mechanism recrystallization may occur in the steep orientation gradient region in Grain A in Figure 7.7. This mechanism was described by Hayakawa and Szpunar [1997a] in the form of a model (see Figure 7.21). An essential requirement of the model is a steep orientation gradient, whereby only a small number of subgrains are required to coalesce to evolve a mobile high angle (>15°) interface. For instance, a 15° interface may form if the subgrains within a 3 μm distance in a 5°/μm orientation gradient region combine together. This may require only 3 to 4 subgrains to combine if the average subgrain size varies in 0.7 to 1.0 μm range, which has been found in many steels [Goodenow 1970, Dillamore *et al.* 1967, Inagaki 1966]. In this model the subgrain coalescence step is the slowest and, therefore, the process becomes viable when less number of subgrains are required to coalesce. The steep orientation gradient near the grain boundary in grain A of Figure 7.7 may act as an excellent region for generating recrystallization nuclei.

Finally and very importantly, the thin blocks in the immediate grain boundary vicinity of Figure 7.17 are wide, long and enclosed by high angle boundaries. Therefore these blocks well may act as recrystallization nuclei. They do not have size advantages in the thickness directions over the average subgrain sizes. Nevertheless, these

components have been found to be present in small intensities in the recrystallization textures of IF steels. For instance, {110}<110> (which is close to the complementary Q and R in Figure 7.18) and {001}<100> (which is close to S in Figure 7.18) have been found in small intensities in the annealing textures of cold/warm rolled IF steels, although these orientations were not found in the rolling textures [Barnett and Jonas 1997, Barnett and Jonas 1999]. Therefore, it is more likely that these orientations originate in the recrystallization textures by growing from the thin blocks that reside in grain boundary interfaces in the deformation microstructures.

7.5 Conclusions

The deformation features at the boundaries between {111}<uvw>–oriented deformed grains were characterized by 2D– and 3D–EBSD. The following conclusions are deduced from the study,

- Highly fragmented (γ–fibre) and smooth (α–fibre) microstructures developed in the grains in RD–ND section in a 75% rolled IF steel. In terms of boundary, the α/α boundaries are relatively simple with sharp interface and γ/γ boundaries are complex with a diffused interface. The α/γ boundaries have intermediate complexities.
- Regions of steep orientation gradients form near the γ/γ boundaries. The volume of the regions is significantly large as compare to the volume of the hot–band grains. These regions comprise essential features to be potential sites for nucleation of recrystallization.
- Fragmentation in the vicinity of γ/γ grain boundaries also occurs. The volume of these fragmented blocks is also large and, hence, may act as potential sites for recrystallization.
- Thin crystals of other orientations were discovered on the deformed grain boundaries. They have dissimilar orientations with both the grains sharing a given boundary. These blocks are thin along the boundary interface normal (ND), and elongated along the RD and TD directions. There are either small or large orientation differences within a thin block at the grain boundary.

Chapter 8

Concluding summary and future work

8.1 Concluding summary

The deformation features in a Goss−oriented Ni single crystals and interstitial free (IF) steels were investigated by high resolution two and three dimensional EBSD and conventional TEM techniques. In the Ni single crystals, the evolution sequence of microbands at different strains and their crystallographic aspects were evaluated, and the observed phenomena are explained in light of the existing theories of microband formation. Unusual microband features and unknown grain boundary characteristics were also discovered in the cold rolled IF steels. The following are the major findings deduced from these studies:

8.1.1 Chapter 4: Microband crystallography in a 30% deformed Ni single crystal

Two intersecting microbands are the prime microstructural features in this sample. The average alignments of these boundaries show good matching with the {111} crystallographic slip planes. After their formation, various interactions generate irregularities in microband interface that deviate them from their crystallographic alignments. During deformation, the Goss orientation oscillates around the transverse direction, and this influences the degree of interactions between the two sets of microbands. These effects appear in the microstructures in the form of fragmentations, dissolutions, turning and twisting of the microband boundaries.

8.1.2 Chapter 5: Dislocation structures in a 10% deformed Ni Single crystal

In this sample, dense dislocation walls (DDWs) appear at ±45° and ±35° inclinations with RD in EBSD and TEM measurements, respectively and, therefore, this investigation generates a puzzle that needs to be studied further. TEM showed that mash and cell structures form prior to the formation of DDWs, with microband formation occurring via the splitting of these DDWs. It was also found that microband boundaries initiate from DDWs and propagate into the dislocation−free regions.

8.1.3 Chapter 6: Unusual microband boundary misorientations in 50% cold rolled IF steel

High–angle microband boundaries, with misorientations up to ~20°, were identified in the {111}<110>–oriented grains in the deformation microstructure of the cold rolled IF steel. These microbands rotate with the two neighbouring bands by equal and opposite angles, around the axes lying along the surface normal of their interfaces. Thus, an alternating orientation pair forms in a given microband array. Like typical low–angle microband boundaries, these microband boundary interfaces also coincide with the highly–stressed crystallographic slip planes.

8.1.4 Chapter 7: Grain boundary deformation features in a 75% cold rolled IF steel

Rolling the IF steel to 75% reduction in thickness generated complex structures in the grain boundary regions between two principal γ–oriented grains, *i.e.* ~{111}<112> and ~{111}<110>. These structures appear in the form of steep orientation gradients up to 5°/μm, high angle boundary networks and thin, elongated blocks on the actual grain boundary. Overall, deformation creates highly complex grain boundary regions that are irregular and diffuse and, hence, are potential sites for nucleation of recrystallization on subsequent annealing.

8.2 Future studies

8.2.1 Goss orienated Ni single crystals

The crystallographic nature of microbands have been studied extensively, and significant conclusions were made on the basis of detailed 3D–EBSD and TEM analyses. However, the early stages of microband formation in the 10% deformed Ni sample requires further investigation to elucidate the following:

- There were discrepancies in the EBSD and TEM measurements concerning the the crystallogaphic alignments of DDWs (Figures 5.1–5.2 vs 5.3 and 5.6).

- The dislocation configurations at the growing head of a microband tip, and their configurations when they split into two boundaries to form a dislocation free microband channel (Figure 5.7).

- The dislocation configurations in the mash and cell structures, and their contributing mechanisms in constituting microband boundaries (Figure 5.4).

- The differences in dislocation structures within DDW channels that enables some DDWs to instigate new microbands, while other DDWs remain inert with internal cell structures (Figure 5.5).

8.2.2 Grain boundary characterizations by 3D EBSD and ex–situ annealing study

The grain boundaries in a 75% rolled IF steel were found to be very complex. Further studies and analyses are required to investigate the following matters:

- The 3D distribution of stored energy in the grain boundary vicinity regions is required. Here, a correlation between stored energy and the spatial distribution of microstructures will provide a 3D understanding of subsequent recrystallization processes.

- The differences between grain boundary regions and grain interiors needs further work for explaining the mechanism that makes the grain boundary regions special. A thorough examination, in light of existing simulation data of deformation textures, is required to determine if the thin, elongated blocks found on the grain boundaries are part of the original grains or generated by mutual rotations between the grains shearing along a common boundary interface.

- A better understanding of the role of grain boundaries on recrystallization can be achieved by careful experimentation. For example, cyclic heating in a vacuum furnace and intermediate 2D–EBSD studies of pre–polished 65–80% deformed IF steel samples would be effective for conducting such a study.

References

Aghan R. L. and Nutting J. *Structure and properties of low carbon steel after deformation to high strains*, J. Metal Science, 14 (6), 233–237 (1980).

Albou A., Driver J. H. and Maurice C. *Microband evolution during large plastic strains of stable {110}<112> Al and Al–Mn crystals*, Acta Materialia, 58 (8), 3022–3034 (2010).

Baba-Kishi K. Z. *Electron backscatter Kikuchi diffraction in the scanning electron microscope for crystallographic analysis*, Journal of Matar Sci. 37, 1715–1746 (2002).

Backofen W. A. *Deformation processing,* Metallurgical Transactions, 4 (12), 2679–2699 (1973).

Barnett M. R. and Jonas J. J. *Distinctive aspects of the physical metallurgy of warm rolling,* ISIJ Int. 39, 856–873 (1999).

Barnett M. R. and Jonas J. J. *Influence of ferrite rolling temperature on grain size and texture in annealed low C and IF steels,* ISIJ Int. 37, 706–714 (1997).

Barrett C. S. and Levenson L. H. Trans AIME, 145, 281–288 (1941)

Barrett C. S. and Massalski T. B. *Structure of Metals*, McGraw Hill, (1966).

Barrett C. S. Trans. Metall. Soc. AIME, 135, 296-352 (1939)

Basinski S. J. and Basinski Z. S. *Dislocations in Solid*, 4, North–Holland, Amsterdam, (1979).

Bay B., Hansen N., Hughes D. A. and Kulmann-Wilsdorf D. *Overview no. 96 evolution of f.c.c. deformation structures in polyslip*, Acta Metall Mater., 40, 205–219 (1992).

Birosca S., Buffiere J. Y., Garcia–Pastor F. A., Karadge M. Babout M. and Preuss M. *Three–dimensional characterization of fatigue cracks in Ti-6246 using X-ray tomography and electron backscatter diffraction.* Acta Mater., 57, 5834–5847 (2009).

Borbély A., Maurice C. I., Piot D. and Driver J. H. *Spatial characterisation of the orientation distributions in a stable plane strain-compressed Cu crystal: A statistical analysis*, Acta Mater., 55, 487–496 (2007).

Bunge H. J. *On representation of prepared orientation*, Acta Crystallographica, S21, A249 (1966).

Bunge H. J. *Texture Analysis in Materials Science*, Butterworths, London (1982).

Burke J. E. and Turnbull D. *Recrystallization and grain growth*, Progress in metal science. Phys. 3, 220–292 (1952).

Cerezo A., Godfrey T. J., Grovenor C. R. M. and Smith, G. D. W. *Surface analysis with a position-sensitive atom probe*, Journal of Physics: Condensed Matter 1: SB99–SB103 (1989).

Chen Q. Z. and Duggan B. J. *On cells and microbands formed in an interstitial-free steel during cold rolling at low to medium reductions*, Metall Mater Trans A, 35 (A), 3423–3430 (2004).

Chen Q. Z., Ngan A. H. W. and Duggan B. J. *Microstructure evolution in interstitial-free steel during cold rolling at low strain levels*, Proc R Soc Lond A., 459, 1661–1685 (2003).

Chen Q. Z., Quadir M. Z. and Duggan B. J. *Shear band formation in if steel during cold rolling at medium reduction levels*, Philosophical Magazine, 23, 3633–3646 (2006).

Day A., Trimby P., Mehnert K. and Neumann B. *Channel 5, HKL Technology* (2004).

DeHoff R. T. *Quantitative serial sectioning analysis – preview*, Journal of Microscopy 131, 259–263 (1983).

Delannay L., Mishin O. V., JuulJensen D. and VanHoutte P., *Quantitative analysis of grain subdivision in cold rolled aluminum,* Acta Mater., 49, 2441–2452 (2001).

Dillamore I. L., Smith C. J. E. and Watson T. W., *Oriented Nucleation in the Formation of Annealing Textures in Iron*, Metal Science, 1, 49–54 (1967).

Dillamore I. L., Roberts J. G. and Busch A. C., *Occurrence of shear bands in heavily rolled cubic metals,* Metal Science, 13, 73–77 (1979).

Doodenow R. H. and Held F. J. *Recrystallization of low-carbon titanium stabilized steel* Metallurgical Transactions, 1, 1507–2515 (1970)

Dorner D., Zaefferer S. and Raabe D., *Retention of the Goss orientation between microbands during cold rolling of an Fe–3%Si single crystal*, Acta Mater., 55, 2519–2530 (2007).

Duggan B. J. and Jones I. P., *Texture Crystall. Solids*, 2, 205 (1977).

Duggan B. J. and Tse Y. Y. *Crystal growth in deformed metals by an impingement and spheroidisation process*, Acta Mater., 52 (2), 387–393 (2004).

Duggan B. J., Hatherly M., Hutchinson W. B. and Wakefield P. T. *Deformation structures and texture in cold rolled 70:30 Brass*, Met. Sci. 12, 343–351 (1978).

Dunn D. N. and Hull R. *Reconstruction of three–dimensional chemistry and geometry using focused ion beam microscopy*, Applied Physics Letters, 75 (21), 3414–3416(1999).

Ferry M. and Humphreys F. J. *Discontinuous subgrain growth in deformed and annealed {110}<001> aluminium single crystal*, Acta Mater., 44, 1293–1308 (1996a).

Ferry M. and Humphreys F. J. *The deformation and recrystallization of particle–containing {011}<100> aluminium crystals*, Acta Mater, 44, 3089–3103 (1996b).

Ferry M., Xu W., Mateescu N., Cairney J. M. and Humphreys F. J. Keynote paper: *On the viability of FIB tomography for generating 3-D orientation maps in deformed and annealed metals,* International Symposium on Fundamentals of Deformation and Annealing, Eds. P.B. Prangnell and P.S. Bate, Manchester, UK, 55–64 (2006).

Foresman O. *Undersokning av rymdstrukturen hos ett kolstal av hypereutektoid sammansattning*, Jernkontorets Ann. 102, 1–30 (1984).

Foxall R. A., Duesbery M. S. and Hirsch P. B., Can. J. Phys., 45, 607–29 (1967).

Fu X., Poulsen H. F., Schmidt S., Nielsen S. F. Lauridsen E. M. and Juul Jensen D., *Non–destructive mapping of grains in three dimensions*, Scripta Materialia 49 (11), 1093–1096 (2003).

Gault B., Moody M. P., Cairney J. M. and Ringer S.P. *Atom probe microscopy,* Springer book series in Materials Science (2012).

Godfrey A., Juul Jensen D. and Hansen N. *Slip pattern, microstructure and local crystallography in an aluminium single crystal of brass orientation {110}<112>*, Acta Mater., 46, 823–833 (1998).

Gourgues–Lorenzon A. F. *Application of electron backscatter diffraction to study of phase treasformations,* Int. Mat. Reviews, 52, 65–128 (2007).

Groeber M., Ghosh S., Uchic M. D. and Dimiduk D. M. *A framework for automated analysis and simulation of 3D polycrystalline microstructures.: Part1: Statistical characterization,* Acta Materialia 56 (6), 1257–1273 (2008a).

Groeber M., Ghosh S., Uchic M. D. and Dimiduk D. M. *A framework for automated analysis and simulation of 3D polycrystalline microstructures. Part 2: Synthetic structure generation*, Acta Materialia 56 (6): 1274–1287 (2008b).

Guzzo R., Ball M. D. and Lloyd D. J. *Development of roping in an aluminum automotive alloy AA6111*, Acta Mater., 48 (13), 3361–3376 (2000).

Hall E. O. *The deformation and ageing of mild steel: III discussion of results,* Proc. Phys. Soc. Lond. Sect B 64, 747–753 (1951).

Hansen N. and Juul Jensen D. *Flow stress anisotropy caused by geometrically necessary boundaries,* Acta Metallurgica et Materialia, 49, 3265 (1992).

Hansen N. and Juul Jensen D. *Hot deformation in aluminum alloys*, Eds Longdon et al. TMS, Warrendale, 3, (1991)

Hatherly M. and Hutchinson W. B. *An introduction to textures in metals*, Chameleon Press, London (1979).

Hatherly M. and Malin A. S. *Deformation of copper and low stacking fault energy, copper ase alloy*, Metals Technology, 6, 308–319 (1979).

Hayakawa H. and Szpunar J. A. *A comprehensive model of recrystallization for interstitial free steel*, Acta Mater., 45, 3721–3730 (1997a).

Hayakawa H. and Szpunar J. A.*, Modeling of texture development during recrystallization of interstitial free steel*, Acta Mater., 45, 2425–2434 (1997b).

He D., Zaefferer S., Zhu J. and Lai Z., *Three dimensional morphological and crystallographical investigation of lamellar alpha and retained beta in a near alpha titanium alloy by combination of focused ion beam and electron back scatter diffraction,* Steel Research International, 83, 496–500 (2012)

Hillert M. and Lange N. *Decomposition of austenite by diffusional processes*, New York: Interscience (1962).

Hirsch J. and Lücke K., *Overview no: 76, Mechanism of deformation and development of rolling textures in polycrystalline fcc metals–I. Description of rolling texture development in homogeneous CuZn alloy,* Acta Metall., 36, 2863–2882 (1988a).

Hirsch J. and Lücke K., *Overview no: 76, Mechanism of deformation and development of rolling textures in polycrystalline fcc metals–II. Simulation and interpretation of experiments on the basis of Taylor type theories,* Acta Metall., 36, 2883–2904 (1988b).

Hopkins R. H. and Kraft R. W. *A rapid technique for observation of 3- dimensional microstructures-application to analysis of fault structure in eutectic alloy,* Transactions AIME 233, 1526–1532 (1965).

Hu H. *Recovery and Recrystallization of Metals*, Ed L. Himmel, Interscience, New York, 311–362 (1963).

Hua M., Garcia C. I. and DeArDo A. J. *Multiphase precipitates in interstitial–free steels* Scripta Metallurgica et Materialia., 28, 973–978 (1993).

Hua M., Garcia C. I. and DeArDo A. J. *Precipitation behavior in ultra–low–carbon steels containing titanium and niobium* Metallurgical and Materials Transactions A. 28, 1769–1780 (1997)

Huang X. and Hansen N. *Microstructural evolution in nickel during rolling and torsion*, Mater. Sci. Tech., 7, 544–553 (1991).

Huang X. and Winther G. *Dislocation structures. Part I. Grain orientation dependence*, Phil Mag., 87, 5189–5214 (2007a).

Huang X. and Winther G. *Dislocation structures. Part I. Slip system dependence,* Phil Mag., 87, 5215–5235 (2007b).

Hughes D. A. and Hansen N. *High angle boudnary formed by grain subdivision mechanism,* Acta Mater., 45, 3871–3886, (1997).

Hughes D. A. and Hansen N. *Microstructural evolution in nickel during rolling to large strains*, Metall Trans., A, 24, 2021–2037 (1993).

Hughes D. A. and Hansen N. *Microstructure and strength of nickel at large Strains*, Acta Mater., 48 (11), 2985–3004 (2000).

Hughes D. A. and Nix W. D. *Strain hardening and substructural evolution in Ni-Co solid solutions at large strains*, Mater Sci Eng A., 122, 153–172 (1989).

Hull D. A. McCammond, D., Hoeppner, D. W. and Hellier, W. G., *Titanium prior–beta grain volume distribution by quantitative serial sectioning techniques,* Materials Characterization, 26 (2), 63–71 (1991).

Humphreys F. J. and Bate P. S. *The microstructures of polycrystalline Al–0.1Mg after hot plane strain compression*, Acta Mater, 55, 5630–5645 (2007).

Humphreys F. J. and Hatherly M., *Recrystallization and Related Annealing Phenomena*. Oxford, Pergamon Press. (2004).

Humphreys F. J. *Grain and subgrain characterisation by electron backscattered Diffraction,* Journal Material Science 36, 3833 (2001).

Humphreys F. J. Proceeding of the 4th Int. Riso Symposium, Riso National Laboratory (1983).

Hurley P. J. and Humphreys F. J. *The application of EBSD to the study of substructural development in a cold rolled single-phase aluminium alloy*, Acta Mater., 51, 1087–1102 (2003a).

Hurley P. J., Bate P. S. and Humphreys F. J. *An objective study of substructural boundary alignment in aluminium*, Acta Mater., 51, 4737–4750 (2003).

Hutter H. A. G. M. *Development and application of a new imaging system for SIMS*. Conference on SIMS VIII, Amsterdam, Wiley, New York, (1992).

Inagaki H. and Suda T. *The development of rolling textures in low-carbon steels*, Texture, 1, 129–140 (1972).

Inagaki H. *Cracking of cementite particles and its influences on the development of the rolling texture in low carbon steels,* Z. Metallkd. 78, 630–638 (1987).

Inagaki H. J. Jap. Inst. Metals. 50, 250 (1966).

Inagaki H. *Stable end orientations in the rolling textures of the polycrystalline iron,* Z. Metallkd. 78 431–439 (1987).

Inkson B. J., Mulvihill M. and Möbus G. *3D determination of grain shape in a FeAl-based nanocomposite by 3D FIB tomography*, Scripta Materialia 45, 753–758 (2001a).

Jackson P. J. *The formation of microbands by cross slip*, Scripta Metall., 17, 199–202 (1983).

Jackson P. J. *The role of cross-slip in the plastic deformation of crystal, Mat. Sci. and Engg.,* 57, 39–47 (1983).

Jones A. R., Ralph B. and Hansen N., *Subgrain coalescence and the nucleation of recrystallization at grain boundaries in aluminium.* Proc. R. Soc. Lond. A, 368, 345–357. (1979).

Khorashadizadeh A., Raabe D., Winning M. and Pippan R. *Recrystallization and grain growth in ultrafine–grained materials produced by high pressure torsion,* Advanced Engineering Materials, 13, 245–250 (2011).

King, K., Liu B. Y., Quadir M. Z., Ferry M. and Bassman L. *Novel method for indentifying low angle sub grain boundaries*, CTMS 2009 138TH Annual Meeting & Exhibition-Supplemental Proceedings, 3, 669–676 (2009).

Knudsen T. A. *An experimental study of plastic deformation of materials*, PhD thesis, Risø National Laboratory for Sustainable Energy, Technical University of Denmark (2008).

Kocks U. F. and Chandra H. *Slip geometry in partially constrained deformation,* Acta Metall, 30, 695–709 (1982).

Koh P. K. and Dunn C. G., AIME, 203, 401–406 (1955).

Konrad J., Zaefferer S. and Raabe D. *Investigation of orientation gradients around a hard Laves particle in a warm-rolled Fe3Al-based alloy using a 3D EBSD–FIB technique.*, Acta Mater., 54, 1369–1380 (2006).

Kosel T. and Washburn J., ICSMA. II, American Soc. of Metals, 459 (1970).

Kral M. V. and Spanos G. *Three–dimensional analysis of proeutectoid cementite precipitates,* Acta Materialia 47 (2), 711–724 (1999).

Kuhlmann-Wilsdorf D. and Hansen N. *Geometrically necessary, incidental and subgrain boundaries*, Scripta Metallurgica et Materialia, 25 (7), 1557–1562 (1991).

Larsen A. W., Poulsen H. F., Margulies L., Gundlach C., Xing Q., Huang X. and Juul Jensen D., *Nucleation of recrystallization observed in situ in the bulk of a deformed metal*, Scripta Materialia 53, 553–557 (2005).

Lee C. S. and Duggan B. J. *A simple theory for the development of inhomogeneous rolling textures*, J Metall Trans A, 22, 2637–2643 (1991).

Lee C. S. and Duggan B. J. *Deformation banding and copper–type rolling textures*, Acta Mater, 41, 2691–2699 (1993).

Lee S. B., Rickman J. M. and Rollett A. D., *Three-dimensional simulation of isotropic coarsening in liquid phase sintering I: A model*, Acta Materialia, 55 (2), 615–626 (2007).

Lin F. X., Godfrey A. and Winther G. *Grain orientation dependence of extended planar dislocation boundaries in rolled aluminium*, Scripta Mater, 61, 237–240 (2009).

Lin F. X., Godfrey A., Juul Jensen D. and Winther G. *3D EBSD characterization of deformation structures in commercial purity aluminum.* Mat. Charac. 61, 1203–1210 (2010).

Liu Q., Wert J. and Hansen N. *Location-dependent lattice rotation and shear strain in rolled aluminium single crystals of cube and Goss orientations*, Acta Mater, 48, 4267–4279 (2000).

Liu T., Raabe D. and Zaefferer S. *A 3D tomographic EBSD analysis of a CVD diamond thin film,* Science and technology of advanced materials, 9, 035013 (2008).

Liu W. C., Juul Jensen D. and Morris J. G. *Effect of grain orientation on microstructures during hot deformation of AA 3104 aluminium alloy by plane strain compression*, Acta Mater, 49, 3347–3367 (2001).

Liu Y. S., Delannay L. and Van Houtte P. *Application of the Lamel model for simulating cold rolling texture in molybdenum sheet,* Acta Mater., 50, 1849–1856 (2002).

Maitland T. and Sitzman S. *Electron backscatter diffraction technique and materials characterization examples, in* Scanning microscopy for nanotechnology, Techniques and applications. Ed. Zhou W. Wang Z. L. *et al*. (2007).

Malin A. S. and Hatherly M. *Microstructure of cold rolled copper,* Metal Science, 13, 463–473, (1979)

Mangan M. A. and Shiflet G. J. *Three–dimensional reconstruction of pearlite colonis in Fe-0.8C-12Mn*., International Conference on Solid-Solid Phase Transformations, Warrendale, PA, TMS, (1994).

Mateescu N. M. *PhD Thesis: Development of 3D-EBSD and its application to the study of various deformation and annealing phenomena*, The University of New South Wales (2008).

Mateescu N., Ferry M., Xu W. and Cairney J.M., *Some factors affecting EBSD pattern quality of Ga+ ion-milled face centred cubic metal surfaces*. Materials Chemistry and Physics, 106, 142–148 (2007).

Midgley P. A., Weyland M., Thomas J. M. and Johnson B. F. G. *Z–Contrast tomography: a technique in three-dimensional nanostructural analysis based on Rutherford scattering*, Chemical Communications 10, 907 – 908 (2001).

Miller M. K., *Atom Probe Tomography–analysis at the atomic level*, Springer, New York (2000).

Miller M. K., Jayaram R. and Russell K. F*., Characterization of phosphorus segregation in neutron-irradiated pressure vessel steels by atom probe field ion microscopy,* Conference Information: Symposium on Microstructure of Irradiated Materials, 373, 113–118 (1995).

Morii K., Mecking H. and Nakayama Y. *Development of shear bands in f.c.c. single crystals*, Acta Metall, 33, 379–386 (1985).

Muller D. *Introduction to Electron Microscopy* (2008).

Nakayama Y, Morii K. *Transmission electron microscopy of shear band formation in rolled copper single crystals*, Trans. Jpn. Inst. Met, 23, 422–431 (1982).

Nave M. D. and Barnett M. R. *The influence of solute carbon in cold-rolled steels on shear band formation and recrystallization texture*, ISIJ Int., 44, 187–96 (2004).

Nielsen S. F., Lauridsen E. M., Juul Jensen D. and Poulsen H. F. *A threedimensional X-ray diffraction microscope for deformation studies of polycrystals*, Materials Science and Engineering A 319–321: 179–181 (2001).

Park N. K. and Parker B. A. *The development of the deformed microstructure in commercially pure nickel*, Mater. Sci. Eng. A, 113, 431–439 (1989).

Parniere P. and Sauzay C. *Determination of the yield loci of bcc metals deforming by crystallographic slip (pencil glide),* Materials Science and Engineering, 22, 271–280 (1976).

Piehler H. R. Thesis Doctor of Science, Massachusetts Institute of Technology, USA. (1967).

Poulsen H. F., *3DXRD microscopy – a comparisonwith neutron diffraction,* Appl. Phys. A 74, 1673–1675 (2002).

Poulsen H. F., *Three-Dimensional X–Ray diffraction microscopy–mapping polycrystals and theirdynamics,* Springer (2004).

Prangnell P. B., Hayes J. S., Bowen J. R., Apps P. J. and Bate P. S. *Continuous recrystallisation of lamellar deformation structures produced by severe deformation* Acta Mater., 52, 3193–3206, (2004)**.**

Prior J. D., Bouyle A. P., Cheadle M. C., Day A., Lopez G., Peruzzo L., Potts J. G., Reddy S., Spiess R., Timms N. E., Trimby P., Wheeler J. and Zetterström L. *The application of electron backscatter diffraction and orientation contrast imaging in the SEM to textural problems in rocks*, American Mineralogist, 84, 1741–1759 (1999).

Quadir M. Z. and Duggan B. J. *Deformation banding and recrystallization of α fibre componentsin heavily rolled IF steels,* Acta Mater., 52, 4011–4021 (2004).

Quadir M. Z. and Duggan B. J. *Shear band thickening during rolling of interstitial free steel*, ISIJ Int., 46, 1495– 1499 (2006).

Quadir M. Z., Mateescu N., Bassman L., Xu W. and Ferry M. *Three dimensional structure of microbands in a cold rolled steel*. Scripta Materialia, 57, 977–980 (2007).

Quadir M.Z., Al–Buhamad O., L. Bassman and M. Ferry: *Development of a recovered/recrystallized multilayered Microstructure in Al Alloys by Accumulative Roll Bonding*, Acta Materialia. 55, 5438–5448 (2007a).

Randle V. and Engler O. *Introduction of texture analysis, macrotexture, microtexture and orientation mapping,* CRC press (2000).

Randle V. *Application of electron backscatter diffraction to grain boundary characterisation*, International Materials Reviews 49 (1), 1–11 (2004).

Randle V., Rohrer G. S., Miller H. M., M. Coleman and Owen G. T., *Five-parameter grain boundary distribution of commercially grain boundary engineered nickel and* copper, Acta Mater., 56, 2363–2373 (2008).

Reid C. N. *Deformation Geometry for Materials Scientists*, 1st ed, Pergamon Press, Oxford, UK (1973).

Rhines F. N., Craig K. R. and Rousse D. A., *Measurement of average grain volume and certain topological parameters by serial sectioning analysis*, Metallurgical and materials transactions A, 7, 1729–1734 (1976).

Rollett A. D., Lee S. B., Campman R. and Rohrer G. S., *Three–dimensional characterization of microstructure by electron back–scatter diffraction*, Annu. Rev. Mater. Res. 37, 627–58 (2007).

Rosenberg J. M. and Piehler H. R., *Calculation of the Taylor factor and lattice rotations for bcc metals deforming by pencil glide,* Metallurgical Transactions. 2 (1), 257–259 (1971).

Rosier D. J. and Klug A. *Reconstruction of three dimensional structures from electron micrographs*, Nature, 217, 130–134 (1968).

Rosner M., Pöckl G., Danninger H. and Hutter H., *2D– and 3D– SIMS investigations on hot–pressed steel powder HS 6–5–3–8*, Analytical and Bioanalytical Chemistry 374, 597–601 (2002).

Rowenhorst D. J., Gupta A., Feng C. R. and Spanos G., *3D crystallographic and morphological analysis of coarse martensite: combining EBSD and serial sectioning,* Scripta Materialia, 55 (1), 11–16 (2006).

Saowadee N., Agersted K., Ubhi H. S. and Bowen J. R. *Ion beam polishing for three–dimensional electron backscattered diffraction,* J. Microsc., 249, 36–40 (2013).

Saylor D. M., El–Dasher B. S., Adams B. L. and Rohrer G. S. *Measuring the five–parameter grain–boundary distribution from observations of planar sections,* Metall. Mater. Trans. A, 35, 1981–1989 (2004).

Schmidt S., Nielsen S. F., Gundlach C., Margulies L., Huang X. and Juul Jensen D. *Watching the Growth of Bulk Grains During Recrystallization of Deformed Metals*, Science 305, 229 (2004).

Schwartz A. J., Kumar M. and Adams B. L. *Electron backscatter diffraction in materials science*, Springer (2000).

Schwarzer R. A. *Measurement of local textures with transmission and scanning electron microscopes,* Textures and Microstructures, 13, 15–30 (1990).

Shen K. and Duggan B. J., *Microbands and crystal orientation metastability in cold rolled interstitial-free steel*, Acta Materialia, 55 (4), 2237–1144 (2007).

Sluytman J. V., Fontaine A. L., Cairney J. M. and Pollock T. *Atom probe study of elemental partitioning in Ni–based superalloys with PGM additions*, Acta Materialia, 58, 1952–1962 (2010).

Tang F., Ringer S.P., Bendavid A., Martin P. and Cairney J. M., *Atomic scale microstructural details of nanocomposite TiSiN film*, Scripta Materialia, 63, 192–194 (2010).

Trimby P. W. *Orientation mapping of nanostructured materials using transmission Kikuchi diffraction in the scanning electron microscope,* Ultramicroscopy, 120, 16–24 (2012).

Tse Y. Y. and Duggan B. J. *Orientation imaging microscopy study of recrystallization in IF steels*, Met. and Mat. Trans. A. 37, 1055–1064 (2006).

Tse Y. Y., Lie G. L. and Duggan B. J., *Deformation banding and formation of nucleation in IF steel,* Scripta Materialia, 17, 25–30 (1999).

Watanabe R. *Possible slip systems in body centered cubic iron,* Materials Transactions, 47 (8), 1886–1889 (2006).

Willis D. J. *Substructure develoopement in cold worked metals*, J. Structural Geology, 1 (4), 334 (1979).

Winther G. and Huang X. *Dislocation structures. Part II. Slip system dependence*, Phil Mag, 87, 5215–5235 (2007).

Winther G., Huang X. and Hansen N. *Crystallographic and microscopic orientation of planner dislocation boundaries–correlation with grain orientation*, Acta Mater, 48, 2187–2198 (2000).

Winther G., Huang X., Godfrey A. and Hansen N. *Critical comparison of dislocation boundary alignment studied by TEM and EBSD: technical issues and theoretical consequences*, Acta Mater, 52, 4437–4446 (2004).

Winther G., Juul Jensen D. and Hansen N. *Dense dislocaion walls and microbands aligned with slip planes-theoretical consideration*, Acta mater. 45 (12), 5059–5068 (1997).

Xu W., Ferry M., Cairney J. M. and Humphreys F. J. *Application of FIB–EBSD tomography for understanding annealing phenomena in a cold rolled particle containing Nickel alloy,* Materials Characterization 58 (10), 961–967 (2007c).

Xu W., Ferry M., Cairney J. M. and Humphreys F. J. *Three-dimensional investigation of particle-stimulated nucleation in a nickel alloy,* Acta Materialia 55 (15), 5157–5167 (2007b).

Xu W., Ferry M., Mateescu N., Cairney J. M. and Humphreys F. J., *Techniques for generating 3–D EBSD microstructures by FIB tomography,* Materials Characterization, 58 (10), 961–967 (2007a).

Xu W., Quadir M. Z. and Ferry M. *A High–resolution three–dimensional electron backscatter diffraction study of the nucleation of recrystallization in cold–Rolled extra–low–carbon Steel,* Metallurgical and Materials Transaction **A**. 40A, 1547–1556 (2009).

Zaafarani N., Raabe D., Singh R. N., Roters F. and Zaefferer S. *Three–dimensional investigation of the texture and microstructure below a nanoindent in a Cu single crystal using 3D EBSD and crystal plasticity finite element simulations*, Acta Materialia, 54, 1863–1876 (2006).

Zaefferer S., Wright S. I. and Raabe D. *Three dimensional microscopy in a focused ion beam-scanning electron microscope: A new dimension of microstructure characterization,* Metallurgical and Materials Transactions, 39A (2), 374–389 (2008).